

USING GLOBULAR CLUSTERS TO UNVEIL THE
PROPERTIES OF THE LIGHT AND DARK
GALAXY HALO

Meghan Emily Hughes

A thesis submitted in partial fulfilment of the requirements of
Liverpool John Moores University
for the degree of
Doctor of Philosophy.
May 2021

Declaration

The work presented in this thesis was carried out at the Astrophysics Research Institute, Liverpool John Moores University. Unless otherwise stated, it is the original work of the author.

While registered as a candidate for the degree of Doctor of Philosophy, for which submission is now made, the author has not been registered as a candidate for any other award. This thesis has not been submitted in whole, or in part, for any other degree.

Meghan Emily Hughes
Astrophysics Research Institute
Liverpool John Moores University
IC2, Liverpool Science Park
146 Brownlow Hill
Liverpool
L3 5RF
UK

SEPTEMBER 23, 2021

Abstract

Galaxies encode fossil records of their formation histories. While in the Milky Way there is the opportunity to observe individual stars, in other galaxies this is not always possible. Low surface brightness in the outskirts and crowding in the centre makes it challenging to determine the age, chemical composition, kinematics and spatial sub-structure of an external galaxy. Globular clusters however, are collections of stars that are bright and reach far out into a galaxy halo, making them ideal candidates to unveil hidden properties of the galaxy in which they reside, including their formation histories and dark matter distributions.

To use GCs as tracers of the formation history of a galaxy, one must first understand how these objects form and evolve alongside their host galaxies. The Modelling Star cluster population Assembly in Cosmological Simulations within EAGLE (E-MOSAICS) simulations, are a tool to do just that. The simulations are a suite of 25 zoom-in Milky Way-mass galaxies and, more recently, a 34 Mpc volume that follow the co-formation and evolution of galaxies and their GC populations. In this thesis, the simulations are used to address multiple questions of GC and galaxy co-formation.

The mass function of globular cluster (GC) populations is a fundamental observable that encodes the physical conditions under which these massive stellar clusters formed and evolved. In this thesis I show that the cluster formation model in E-MOSAICS reproduces the observed shapes of GC mass functions. Furthermore, I examine the origin of the shape and relate it to the mass and the formation history of galaxies, concluding that it is a combination of nature and nurture that sets this shape.

Stellar streams are the most direct evidence of accretion onto a galaxy halo. In this

thesis I examine the properties of GCs associated with stellar streams. More massive accreted galaxies typically contribute younger and more metal rich GCs. Furthermore, GCs associated with stellar streams have systematically lower $[\alpha/\text{Fe}]$ at fixed $[\text{Fe}/\text{H}]$ than other GCs in a galaxy halo. This lower age results from a more extended cluster formation history in more massive galaxies. In addition, at fixed stellar mass, galaxies that are accreted later host younger clusters, because they can continue to form GCs without being subjected to environmental influences for longer. This explains the large range of ages observed for clusters associated with the Sagittarius dwarf galaxy in the halo of the Milky Way compared to clusters which are thought to have formed in satellites accreted early in the Milky Way's formation history.

The α -element abundances of the globular cluster (GC) and field star populations of galaxies encode information about the formation of each of these components. The $[\alpha/\text{Fe}]-[\text{Fe}/\text{H}]$ distribution of GCs largely follows that of the field stars and can also therefore be used as tracers of the $[\alpha/\text{Fe}]-[\text{Fe}/\text{H}]$ evolution of the galaxy. There is a wide range of shapes for the field star $[\alpha/\text{Fe}]-[\text{Fe}/\text{H}]$ distribution, with a notable subset of galaxies exhibiting bimodal distributions, in which the high $[\alpha/\text{Fe}]$ sequence is mostly comprised of stars in the bulge, a high fraction of which are from disrupted GCs, where this fraction correlates with the galaxy's formation time. Using this result, I suggest that the Milky Way experienced a phase of unusually rapid growth at early times.

The E-MOSAICS simulations can also be used to test other models to inform the users about any biases they should be aware of. Dynamical models allow the user to connect the motion of a set of tracers to the underlying gravitational potential, and thus to the total (luminous and dark) matter distribution. Globular clusters (GCs) are an ideal tracer population in dynamical models. This thesis tests how well Jeans-Anisotropic-MGE (JAM) models using GCs (positions and line-of-sight velocities) as tracers can constrain the mass and radial distribution of DM halos. There is a strong correlation between how well we recover the mass and the radial distribution of the DM and the number of GCs in the galaxy: the constraints get exponentially worse with fewer GCs, and at least 150 GCs are needed in order to guarantee that the JAM model will perform

well.

These results contribute to the growing body of work that recognises the close relationship between GC and galaxy formation. This thesis shows clearly that the properties of GCs can be used to investigate the formation history of both the visible and dark components of a galaxy.

Publications

In the course of completing the work presented in this thesis, the contents of Chapters 4, 5 and 6 have been submitted and accepted for publication in a refereed journal:

- *Fossil stellar streams and their globular cluster populations in the E-MOSAICS simulations*
Hughes, M.E., Pfeffer, J., Martig, M., Bastian, N., Crain, R.A., Kruijssen, J.M.D., Reina-Campos, M., 2019, MNRAS 482, 2795
- *The $[\alpha/\text{Fe}]$ - $[\text{Fe}/\text{H}]$ relation in the E-MOSAICS simulations: its connection to the birth place of globular cluster field stars in the bulge*
Hughes, M.E., Pfeffer, J.L., Martig, M., Reina-Campos, M., Bastian, N., Crain, R.A., Kruijssen, J.M.D., 2020, MNRAS 491, 4012
- *What to expect when using globular clusters as tracers of the total mass distribution in Milky Way-mass galaxies*
Hughes, M.E., Jethwa, P., Hilker, M., van de Ven, G., Martig, M., Pfeffer, J.L., Bastian, N., Kruijssen, J.M.D., Trujillo-Gomez, S., Reina-Campos, M., Crain, R.A., 2021, MNRAS 502, 2828

The contents of Chapter 3 correspond to a fourth study submitted to MNRAS:

- *The physics governing the upper truncation mass of the globular cluster mass function*
Hughes, M.E., Pfeffer, J.L., Bastian, N., Martig, M., Kruijssen, J.M.D., Crain, R.A., Reina-Campos, M., Trujillo-Gomez, S., 2021, MNRAS, Submitted

Other work I have contributed to during the preparation of this thesis appears in:

- *The kinematics of globular cluster populations in the E-MOSAICS simulations and their implications for the assembly history of the Milky Way*
Trujillo-Gomez, S., Kruijssen, J.M.D., Reina-Campos, M., Pfeffer, J.L., Keller, B.W., Crain, R.A., Bastian, N., **Hughes, M.E.**, 2021, MNRAS 503, 31
- *Linking globular cluster formation at low and high redshift through the age-metallicity relation in E-MOSAICS*
Horta, D., **Hughes, M.E.**, Pfeffer, J.L., Bastian, N., Kruijssen, J.M.D., Reina-Campos, M., Crain, R.A., 2021, MNRAS 500, 4768
- *Where did the globular clusters of the Milky Way form? Insights from the E-MOSAICS simulations*
Keller, B.W., Kruijssen, J.M.D., Pfeffer, J.L., Reina-Campos, M., Bastian, N., Trujillo-Gomez, S., **Hughes, M.E.**, Crain, R.A., 2020, MNRAS 495, 4248
- *Predicting accreted satellite galaxy masses and accretion redshifts based on globular cluster orbits in the E-MOSAICS simulations*
Pfeffer, J.L., Trujillo-Gomez, S., Kruijssen, J.M.D., Crain, R.A., **Hughes, M.E.**, Reina-Campos, M., Bastian, N., 2020, MNRAS 499, 4863
- *Kraken reveals itself – the merger history of the Milky Way reconstructed with the E-MOSAICS simulations*
Kruijssen, J.M.D., Pfeffer, J.L., Chevance, M., Bonaca, A., Trujillo-Gomez, S., Bastian, N., Reina-Campos, M., Crain, R.A., **Hughes, M.E.**, 2020, MNRAS 498, 2472
- *The mass fraction of halo stars contributed by the disruption of globular clusters in the E-MOSAICS simulations*
Reina-Campos, M., **Hughes, M.E.**, Kruijssen, J.M.D., Pfeffer, J.L., Bastian, N., Crain, R.A., Koch, A., Grebel, E.K., 2020, MNRAS 493, 3422

- *The evolution of the UV luminosity function of globular clusters in the E-MOSAICS simulations*

Pfeffer, J., Bastian, N., Crain, R.A., Kruijssen, J.M.D., **Hughes, M.E.**, Reina-Campos, M., 2019, MNRAS 487, 4550

Acknowledgements

First and foremost a huge amount of thanks goes to my three mentors, who have given me an immeasurable amount of support. To Marie, for always knowing what to say, for greatly improving my writing skills and for always making me a priority. You helped me to realise that it is OK for a plan to change and it not be a failure and for that I extend my deepest thanks. To Nate, thank you for introducing me to the wonderful marriage between globular clusters and galaxy formation. Your down-to-earth, honest advice and words of encouragement have been invaluable to me. Last but far from least, Joel, it is hard to find the words to say how important you have been to this work and to my development as a scientist. Thank you for taking me on as your masters student and turning my weak coding skills into something I could confidently start a PhD with and since then for always finding time for my ‘quick questions’ which were scarcely quick and often repeated.

This work would not have been possible without my collaborators. Thanks to Rob Crain, Diederik Kruijssen, Marta Reina-Campos and Sebastian Trujillo-Gomez for welcoming me into the E-MOSAICS team, listening to my ideas and sharing insightful discussions. To Prashin Jethwa, thank you for never tiring of my questions and for the many beers, my experience in Germany would have been lonelier without you. Thank you to Michael Hilker, who greeted me with a warm smile and kindness every day at ESO and kept my theoretical mind observationally focussed when it needed to be. A huge thanks also goes to Glenn van de Ven for supporting my application to ESO when we hadn’t met and for making me feel welcome and valued in your research group from the start.

The ARI is a wonderful place to be a part of and it contains so many great people. Thank you to Anna, Danielle and Phil who keep the place afloat and for whom nothing is too much trouble. Thank you to the stellar pops group, past and present, for a lively and supportive scientific environment. My time at the ARI would not have been as enjoyable if it were not for the students, thank you all for the tea breaks, support and many a beer along the way. A special thanks to Tom, Sarah, Jon, Joaquín, Conor, Al, Danny, Joe and Charlotte for always being up for a chat and for keeping me smiling and laughing, especially this past year.

I am incredibly grateful to my family and friends, who have always supported me. To Paige and Liz, for being there from the start, cheering me on and bringing a little bit of Manchester to Munich when I really needed it. To Rachel, for celebrating every achievement with me, big or small, thank you for always being a phone call away. Jess, I'm not sure I would have made it through undergraduate without you, thank you for being the best housemate. To Olivia, you never fail to brighten my day, thank you for the walks, honest chats, early morning gym sessions and for offering me a place to stay when I had a long commute. Aunty Ann, Aunty Clare, Aunty Lynnette and Uncle Gary you have filled my life with love, lifted my spirits when they needed lifting and made me laugh until my belly hurts, thank you for always being proud of me. Grandma, I am immensely proud to be the granddaughter of a such a strong woman, I am so happy to have you. Nana and Granddad, it has been my motivation to continue to make you proud.

This experience would have been twice as difficult and half as fun were it not for Jonathan Stott. Thank you for not complaining (ok, only complaining a little) when I drag you on long walks, supplying me with endless cups of tea (and the occasional glass of wine), making me laugh when it seemed so hard, reassuring me that it will all be fine and for always being there. Your calm nature and unwavering love, support and belief has given me courage in times I needed it most. Here's to the next chapter.

Finally, to the two people who have always been there, my best friends, my taxi, my therapists, my house movers, occasionally my bank, mum and dad. From the moment I declared I wanted to be a 'doctor in space' and you said 'well they must need doctors

up there' I knew I could be whatever I wanted, yet I've always known that all you want for me is happiness and for that I am eternally grateful. Thank you for all the support, material and emotional, and for always believing in me. I dedicate this thesis to you, for giving me the tools to reach for the stars.

For Denise and Tony

*“Today is your day!
Your mountain is waiting.
So...get on your way!”*

- Dr Seuss, Oh, the places you'll go!

Contents

Declaration	ii
Abstract	iii
Publications	vi
Acknowledgements	ix
Contents	xiii
List of Tables	xviii
List of Figures	xix
1 Introduction	1
1.1 Galaxy demographics	2
1.2 A model for the formation and evolution of the Universe	4
1.3 Galaxy formation in the Λ CDM Universe	7
1.3.1 Star formation and feedback processes	8
1.3.2 Dynamical evolution	9
1.3.3 Chemical evolution	14

1.4	Globular cluster populations	16
1.4.1	The Milky Way	17
1.4.2	M31	22
1.4.3	Beyond the local group	26
1.5	Globular cluster formation and evolution	31
1.5.1	Globular cluster formation	31
1.5.2	Globular cluster evolution	34
1.5.3	Simulating GC and galaxy populations	37
1.6	This thesis	40
2	Methods	42
2.1	Simulations	42
2.1.1	EAGLE	44
2.1.2	E-MOSAICS	46
2.2	Dynamical modelling	50
2.2.1	Assumptions and important concepts	51
2.2.2	Jeans modelling	52
2.3	The Markov-Chain-Monte-Carlo technique	56
3	The physics governing the upper truncation mass of the globular cluster mass function	59
3.1	Introduction	59
3.2	Comparison between simulations and observations	63
3.2.1	Virgo Cluster Data	63

3.2.2	Simulation Data	64
3.2.3	Model results vs. Observations	68
3.3	Alternative cluster formation physics	71
3.4	Dependence on GC formation and evolution	73
3.4.1	GC mass loss cases	73
3.5	Conclusions	81
4	Fossil stellar streams and their globular cluster populations in the E-MOSAICS simulations	84
4.1	Introduction	84
4.2	Identifying stellar streams and their associated GCs in E-MOSAICS .	87
4.2.1	Stellar stream identification	87
4.2.2	Definitions	91
4.3	GCs in stellar streams	92
4.3.1	Properties of GCs associated with stellar streams	92
4.3.2	Comparisons of GC properties on and off streams	96
4.4	The Relationship Between GC Formation History, Galaxy Mass and Infall Time	99
4.4.1	Total age range of GCs	99
4.4.2	GC formation after infall	101
4.5	Comparisons With Observations	104
4.6	Conclusions	106
5	The $[\alpha/\text{Fe}]$-$[\text{Fe}/\text{H}]$ relation in the E-MOSAICS simulations: its connection	

to the birth place of globular clusters and the fraction of globular cluster field stars in the bulge	108
5.1 Introduction	108
5.2 The α abundances of globular clusters and field stars	111
5.3 The $[\alpha/\text{Fe}] - [\text{Fe}/\text{H}]$ distribution of field stars and its connection to the formation and disruption of globular clusters	116
5.3.1 Cluster formation and disruption across the $[\alpha/\text{Fe}]-[\text{Fe}/\text{H}]$ plane	116
5.3.2 Galactocentric position in the $[\alpha/\text{Fe}]-[\text{Fe}/\text{H}]$ plane	123
5.4 The fraction of field stars in the bulge originating in GCs	123
5.4.1 Bulge stars from disrupted GCs in E-MOSAICS	123
5.4.2 Comparison with the Milky Way	127
5.5 Conclusions	130
6 What to expect when using globular clusters as tracers of the total mass distribution in Milky Way-mass galaxies	132
6.1 Introduction	132
6.2 The Jeans Model	138
6.2.1 Introducing the coordinate system	138
6.2.2 Jeans-Anisotropic-MGE	138
6.2.3 Markov-chain-Monte-Carlo	142
6.3 JAM outputs	144
6.3.1 Recovery of free parameters	144
6.3.2 Recovery of velocity moments	149
6.3.3 Recovery of dark matter mass distribution	151

6.4	Investigation of the effects of the GC system	156
6.4.1	Effect of GC distribution sphericity	156
6.4.2	Number of GCs	159
6.4.3	Line-of-sight velocity error	163
6.4.4	Number of GCs and velocity error combined	165
6.5	Dependence on additional galaxy properties	167
6.6	Summary and Conclusions	168
7	Summary	172
7.1	Future prospects	174
	Bibliography	177

List of Tables

2.1	Properties of the 25 simulated Milky Way-mass, L^* galaxies at $z = 0$. The number of GCs includes all GCs with a mass greater than $10^5 M_{\odot}$.	47
3.1	The number of galaxies and GCs in each galaxy mass bin and GC sub-population. The highest galaxy mass bins contain just one galaxy, so in this case we give the galaxy's mass.	68
6.1	The total and stellar mass of each galaxy simulation along with the number of GCs in each of the 25 simulated galaxies for 3 different GC parameter restrictions. Note that the radius cut is based on projected x and y coordinates after the galaxy has been aligned as edge-on.	137

List of Figures

1.1	The Hubble tuning fork diagram. Image taken from the National Schools’ Observatory.	2
1.2	Metallicity distribution for 137 Milky Way GCs as listed in the Harris (1996) catalogue. Figure taken from (Harris, 1999).	18
1.3	The observed age-metallicity relation of GCs in the Milky Way. As in Kruijssen et al. (2019b) , the sample is the mean of the compilations by Forbes & Bridges (2010) ; Dotter et al. (2010, 2011) and VandenBerg et al. (2013) . The symbol colour indicates the galactocentric radius given by Harris (1996, 2010) where any cluster with a distance greater than 30 kpc is given a yellow colour. The errorbar in the lower left corner indicates the typical error on the measurement of the age. . . .	19
1.4	PAndAS metal-poor stellar density map. The map shows the red giant branch stars with the positions of all GCs overplotted. The two dashed circles centred on M31 represent $R_{\text{proj}} = 25$ and 150 kpc. The white ellipse represents the indicates the central stellar disc. M33 lies to the south-east of M31 and the dashed circle centred on this galaxy represents $R_{\text{proj}} = 50$ kpc. This figure is figure 6 in Mackey et al. (2019)	23

- 1.5 This figure shows the similarities between the Galactic GC M80 (left) and the most massive YMC in the nearby dwarf starburst galaxy NGC 1569 (right). The ages are 11 Gyr and 15 Myr respectively. The masses and half light radii are very similar but the ages differ. This shows that GC-like YMCs are still forming today. Left image credit: NASA and The Hubble Heritage Team (STScI/AURA). Right image credit: NASA, ESA, the Hubble Heritage Team (STScI/AURA), and A. Aloisi (STScI/ESA). Image taken from ([Kruijssen, 2014](#)). 32
- 1.6 A comparison between the mass functions of two GC populations. The left hand panels show that of the Milky Way, which has an evolved GC population, the data is taken from [Baumgardt & Hilker \(2018\)](#). The right hand panels show the young clusters of M51, which contains a young GC population, the data is taken from [Messa et al. \(2018\)](#). The top and bottom panels represent two ways of presenting the mass functions: as a histogram (top panels) and as a cumulative function (bottom panels). 35
- 2.1 Figure 1 of [Kruijssen et al. \(2019a\)](#) to visualise the nature of the E-MOSAICS simulations. The main panel shows the dark matter distribution of the EAGLE Recal-L025N0752 simulation at $z = 0$, the yellow circles highlight the 25 Milky Way-mass galaxies in the simulation. The two solid circles indicate the galaxies in the top right panel, which shows gas density coloured by temperature ($T = 10^5 - 10^6 K$, red to white). The two middle right panels show mock-optical images of one galaxy, with the bottom panel including GCs ($M > 5 \times 10^4$) as dots coloured by their origin. The bottom row visualises the assembly of the same galaxy and its star cluster population, with gas shown in grey scale and dots again showing the positions of the GCs, coloured by their metallicities ($-2.5 < [\text{Fe}/\text{H}] < 0.5$). 43

3.1	An example of a Schechter function fit to the simulation data. The blue line shows a cumulative distribution function of the GC masses. The orange dotted line shows the median Schechter function fit from the MCMC and the dotted lines show the 16th and 84th percentiles. . . .	65
3.2	The dependence of $M_{c,*}$ on galaxy stellar mass in the Virgo galaxy cluster and the most-massive E-MOSAICS galaxy group. The black stars represent the data taken from Fig. 16 of Jordán et al. (2007) . The blue points show the fits to the E-MOSAICS fiducial model at $z=0$, where the error bar represents the 16th-84th percentile range of the posterior distribution. The blue E-MOSAICS points match well with the Jordán et al. (2007) sample.	69
3.3	The dependence of $M_{c,*}$ on galaxy stellar mass in the Virgo galaxy cluster and the most-massive E-MOSAICS galaxy group. The black stars represent the data taken from Fig. 16 of Jordán et al. (2007) . The coloured points show the fits to the E-MOSAICS volume, split by the group mass. We just include the quiescent galaxies from the simulations to be able to compare to the observed galaxy cluster. . . .	70
3.4	The dependence of $M_{c,*}$ on galaxy stellar mass in the Virgo galaxy cluster and the most-massive E-MOSAICS galaxy group. The fiducial model, the ‘no formation’ model, the ‘CFE only’ model and the ‘Mc only’ model are represented by blue, orange, green and pink circles respectively.	71

3.5	The dependence of $M_{c,*}$ on galaxy stellar mass in the Virgo galaxy cluster and the E-MOSAICS galaxy cluster. The black stars represent the data taken from Fig. 16 of Jordán et al. (2007) . The blue points show the E-MOSAICS fiducial model at $z=0$. The orange points show the E-MOSAICS model with no dynamical friction taken into account. Finally, the green points show the E-MOSAICS with no mass loss (stellar evolution or dynamical) taken into account. Full dynamical evolution must be included in the simulation to match well with the Jordán et al. (2007) sample.	74
3.6	The dependence of GC birth pressure on galaxy stellar mass in the E-MOSAICS galaxy cluster. The shaded regions show the 16th-84th percentile range.	75
3.7	The ratio of the median initial parent galaxy stellar mass to the initial stellar mass of the $z = 0$ galaxy as a function of the $z = 0$ galaxy mass. The black points and line show the median and 16th-84th percentile ranges in galaxy mass bins of 1 dex.	76
3.8	The dependence on the median time a GC spends in its parent galaxy as a function of galaxy stellar mass. The colours of the three subsamples are the same as in Fig. 3.5 and the shaded regions show the 16th-84th percentile range.	77
3.9	The dependence of α on galaxy stellar mass in the E-MOSAICS galaxy cluster. The blue points show the E-MOSAICS fiducial model at $z=0$. The orange points show the E-MOSAICS model with no dynamical friction taken into account. Finally, the green points show the E-MOSAICS clusters that survive to $z=0$ within our mass cut but with no mass loss (stellar evolution or dynamical) taken into account. . . .	80

4.1	Stellar density plots of 3 of the haloes which show clear streams. From top to bottom, we show galaxies MW03, MW09 and MW17. From left to right, the plots show the main galaxy, the accreted component (everything that did not form in the central galaxy) and one clear stream. Each panel is 200 kpc on a side.	88
4.2	Examples of stellar substructure generated during the accretion of a single galaxy. These panels highlight the high diversity in the classification of a stellar stream. All of these events were placed into the stream category. From panel (a)–(d) these are accretion events from MW12, MW17, MW05 and MW13.	89
4.3	Median ages and metallicities of GCs on and off the streams shown with their 16th and 84th percentile bars. Each pair of points represents one simulated halo, where ‘stream’ refers to the median of all the GCs which are associated with all of the streams in a given halo, and ‘non-stream’ refers to the median of all the GCs which are not associated with a stream in this halo. The GCs have undergone the mass, age and radius cuts mentioned previously. Note the large variation from halo to halo.	93

- 4.4 Host galaxy properties (lookback time of the crossing of the virial radius, i.e. the 'infall time', and stellar mass) are plotted against the GC properties (median metallicity and median age) in order to highlight key trends. Here, each point represents an individual stream progenitor galaxy across all simulated haloes. The black lines represent the fit and the grey band represents the 1σ scatter of the data around the fit. The red stars represent where the Sagittarius dwarf, the SMC and the LMC (from low to high mass) lie in this parameter space – see the text for age and metallicity references. The mass-metallicity relation of [Peng et al. \(2006\)](#) for all GCs is shown by the light blue line in the top right panel- this has been extrapolated below stellar masses of $5 \times 10^8 M_{\odot}$. Age and metallicity show a clear dependence on the parent galaxy properties, indicated by the Pearson coefficients quoted in each panel. 94
- 4.5 The difference in the median GC ages between the stream and non stream GCs, within the same halo, plotted as a function of the difference in their median metallicities. Each point represents one stream. The non-stream population refers to all the GCs which survive the various property cuts which do not lie on this particular stream; it therefore includes GCs which lie on other streams in this halo, GCs which have been accreted but do not lie on a stream and GCs formed in the main galaxy. Left panel: the colours represent the host galaxy's stellar mass. Right panel: the colours represent the virial radius crossing time. There is an anti correlation between age and metallicity. More massive galaxies which crossed the virial radius more recently are more likely to have GCs on streams which are younger and more metal rich. . . . 97

- 4.6 Left panel: the age range of the GCs which have been accreted with a satellite galaxy as a function of the parent galaxy’s stellar mass, the solid black line represents the best fit line for satellite galaxies with a stellar mass greater than $10^8 M_{\odot}$, the red symbol with error bar represents the position of the Sagittarius dwarf galaxy. Right panel: the difference from the line of best fit for each satellite galaxy above $10^8 M_{\odot}$, the solid grey line represents the best fit line and the grey band represents the 1σ scatter of the data around the fit, the red dotted line represents the method for estimating an infall time for the Sagittarius dwarf galaxy, discussed in Section 6.6. Each point represents an accreted galaxy, those accretion events that are seen as streams at $z = 0$ are represented by circles and the rest of the accreted galaxies are represented by squares. The points labelled 1 and 2 will be used in Fig. 4.7 to investigate the star formation histories of two galaxies at the same mass but with different age ranges. 98
- 4.7 The star formation histories of two accreted galaxies that produce streams. The orange lines correspond to the galaxy labelled 1 in Fig. 4.6 and the purple lines correspond to the galaxy labelled 2 in Fig. 4.6. The gas is split up into star forming (dashed lines) and non star forming (dotted lines). Note how the galaxy which crossed the virial radius (shown by the vertical lines) longer ago also stopped forming GCs longer ago, which is due to gas stripping. 99
- 4.8 Time for which GCs continue to form after they have crossed the virial radius as a function of galaxy mass. The points are coloured by the infall time (left panel) and the time for which the galaxy retains its star forming gas after falling into the halo of the main galaxy (right panel) . 102

4.9	Time for which GCs continue to form after they have crossed the virial radius as a function of how long the satellite galaxy takes to completely merge with the main galaxy after it has crossed the virial radius. Only galaxies with $M > 10^8 M_{\odot}$ are shown. The points are coloured by infall time. We see that faster mergers happen at earlier times.	103
5.1	Five of the E-MOSAICS galaxies in $[\alpha/\text{Fe}]-[\text{Fe}/\text{H}]$ space, chosen to illustrate the diversity of the $z = 0$ $[\alpha/\text{Fe}]-[\text{Fe}/\text{H}]$ distributions. The contours represent the field stars and the points represent the in-situ (red) and ex-situ (blue) GCs.	112
5.2	Top left: the median $[\text{O}/\text{Fe}]$ as a function of metallicity of the in-situ and ex-situ field stars and GCs in all 25 galaxies. Top middle: the median $[\text{O}/\text{Fe}]$ as a function of metallicity of the in-situ and ex-situ GCs in all 25 galaxies. Top right: the median $[\text{O}/\text{Fe}]$ as a function of metallicity of the GCs on streams and not on streams in the 15 MW-like galaxies identified in Hughes et al. (2019) . The shaded regions show the 16th and 84th percentiles and the lines are a running median of $[\text{O}/\text{Fe}]$ in $[\text{Fe}/\text{H}]$ bins of 0.5 dex with a difference of 0.125 dex between each bin. The bottom panels show the differences in $[\text{O}/\text{Fe}]$ between the subsets of stars or GCs for each $[\text{Fe}/\text{H}]$ bin. All panels only include bins with more than 5 GCs to avoid poor sampling issues.	114
5.3	The $[\text{O}/\text{Fe}] - [\text{Fe}/\text{H}]$ relation for five of the simulated galaxies. Each panel shows a 2D histogram of the stars in the galaxy coloured by, the cluster formation efficiency (CFE), the fraction of stars which were born in GCs but now reside in the field (f) and the galactocentric radius of the stars at $z = 0$ (R). In the last row, only the stars from the inner 30 kpc are shown.	117

5.4 Top row: the $[O/Fe]$ - $[Fe/H]$ relation for GCs grouped by their galaxy's degree of bimodality. The solid black lines represent the running medians of the individual galaxies, computed using the LOWESS method. Each point represents one $z = 0$ GC coloured by its difference from the running median of the t_g - $[Fe/H]$ relation of its host galaxy. Bottom row: the Spearman rank correlation coefficient of the Δt_g - $\Delta[O/Fe]$ relation. Each line represents present day GCs ($GC_{S_z=0}$, black), any GC that formed ($GC_{S_{init}}$, red) and the field stars (blue). The shaded regions highlight the metallicity bins in which the Spearman correlation coefficient for $GC_{S_z=0}$ is not significant (Spearman p-value > 0.01). The other populations have significant correlations in all $[Fe/H]$ bins. The $[Fe/H]$ bins are wider in the clearly bimodal case to account for lower number statistics. 119

5.5 The fraction of field stars in the bulge which were born in GCs (f_{bulge}) as a function of the redshift ($z_{formation}$) at which all progenitors together have attained half of the $z = 0$ stellar mass (this is effectively the median age or median formation redshift of all stars in the galaxy at $z = 0$). The different symbols represent the degree of bimodality the field stars show in the $[O/Fe]$ - $[Fe/H]$ plane, from definite bimodality (stars), to intermediate bimodality (squares) to no bimodality at all (circles). The data are shown as lower limits due the under disruption of GCs in E-MOSAICS. The upper limits (at the tips of the arrows) show the extreme assumption that no GC survives in the bulge. Top panel: f_{bulge} across all field stars in the bulge. Bottom panel: f_{bulge} for field stars below $[Fe/H] < -0.7$ to match the selection when deriving f_{bulge} for the MW. The grey data point indicates the bulge mass fraction from GCs derived by [Schiavon et al. \(2017\)](#) for the formation redshift of the Milky Way inferred from the age-metallicity distribution of its GC population by [Kruijssen et al. \(2019b\)](#). 124

5.6	The fraction of field stars in the bulge which were contributed by GCs (f_{bulge}) in 0.5 dex $[\text{Fe}/\text{H}]$ bins. The solid lines show the running median and the shaded regions represent the 16th-84th percentile range. The galaxies are stacked by the level of bimodality their stars show in the $[\alpha/\text{Fe}]-[\text{Fe}/\text{H}]$ plane, coloured as in Fig. 5.5. f_{bulge} peaks higher and at lower metallicities in galaxies with clear $[\alpha/\text{Fe}]$ bimodality. . .	126
5.7	The metallicity distribution function of field stars in the bulges of the three E-MOSAICS galaxies that show bimodal $[\alpha/\text{Fe}]$ at a given $[\text{Fe}/\text{H}]$, these are MW13 (solid line), MW18 (dashed line) and MW21 (dotted line). The stars are split by whether they were born in a GC (blue lines) or not (red lines).	129
6.1	MGE fits for all 25 galaxies. The black contours show the distribution of baryons in the galaxies and the red ellipses show the MGE fits to the simulations. The galaxies are ordered from left to right and then top to bottom in increasing number, with MW00 in the top left and MW24 in the bottom right. The galaxies are projected at a distance of 1Mpc and we show the inner 100 arcsec square (100 arcsec equates to ≈ 480 pc).	139
6.2	The posterior distributions for the four free parameters shown for one of the simulated galaxies (MW02). The grey 1D and 2D histograms represent the recovered values from the JAM model and the blue 1D histograms and vertical lines represent the fit directly to the simulated data.	145
6.3	The posterior distributions for the four free parameters shown for one of the simulated galaxies (MW04). The grey 1D and 2D histograms represent the recovered values from the JAM model and the blue 1D histograms and vertical lines represent the fit directly to the simulated data.	146

6.4	A demonstration of how we assign GCs to the major or minor axes for MW16. Each point represents one GC, coloured by whether it belongs to the major or minor axis population, with the minor axis shown in blue and the major axis shown in orange. The void in the centre is due to the inner 2 kpc radius cut.	147
6.5	The line of sight velocity dispersion ($\sigma_{z'}$) recovered from JAM and directly from the simulations as a function of projected radius for 6 of the simulated galaxies. The continuous solid line shows the median JAM output and the dotted lines represent the 1σ spread in the predictions. The points with error bars show the true $\sigma_{z'}$ calculated directly from the simulations. To calculate the true GC $\sigma_{z'}$ we binned the GCs in groups of 20. In the top right corner I indicate the disc to total mass ratio (D/T) for each galaxy.	148
6.6	Projected radial profiles of the mass enclosed for the 25 galaxies, using all clusters at $z = 0$ with a mass $> 10^5 M_\odot$, an age $> 8\text{Gyr}$ and a galactocentric radius $R > 2\text{kpc}$. The solid black line represents the true mass calculated directly from the simulations. The blue-shaded regions represent the 1 and 2σ bounds on the recovered mass from the JAM model. Each panel also contains a histogram of the 2D projected GC positions.	152
6.7	Estimators of the performance of the JAM model. From top to bottom, they quantify the DM mass difference, the spread in the DM mass difference and the maximum values of the KS test, for all the galaxies in the suite of 25 Milky Way-mass zoom simulations. Data points correspond to different samples of GC tracers as indicated in the legend. The grey-shaded region contains the averages and 1σ spreads for each of the GC sub-samples, indicated by the stars with errorbars.	153

6.8	Estimators of the performance of the JAM model as in Fig. 6.7, as a function of the sphericity (s) of the GC distribution, with $s = 1$ being a spherical distribution. The points are also coloured by the number of GCs used in the JAM model.	157
6.9	Mass enclosed profiles for MW002 with it's GCs randomly sampled to include 10-100 percent of them. We show the D_{KS} value of each JAM model in the relevant panel. The number in the top left of each panel shows the number of GCs used in the JAM model. The lines and shaded regions correspond to the description in Fig. 6.6	159
6.10	Estimators of the performance of the JAM model as in Fig. 6.7, as a function of the number of GCs used in the model. Here we show four galaxies: MW00, MW02, MW12 and MW13 indicated by the legend.	160
6.11	Estimators of the performance of the JAM model as in Fig. 6.7, as a function of the total number of GCs in the galaxy and used in the JAM model. Each point represents one of the 25 simulated galaxies.	161
6.12	Estimators of the performance of the JAM model as in Fig. 6.7, as a function of the line-of-sight velocity error. Here we show five galaxies: MW00, MW02, MW03, MW12 and MW13 as indicated by the legend.	164
6.13	The accuracy and precision of the mass enclosed at the maximum GC radius for all 25 galaxies plotted as a function of the number of GCs in that galaxy. Each colour represents the results for three different line of sight velocity errors.	166

Chapter 1

Introduction

On a clear, dark night, away from towns and cities, there is a magnificent structure to be seen: a stream of millions of stars across the sky, cloaked in clouds of dust and gas. The 'Milky Way', the 'Silver River' or the 'Backbone of Night' are just some of the names given to the galaxy that holds within it billions of stars, one of which our Earth orbits. As our home, the Milky Way has long fascinated astronomers and until about 100 years ago was thought to be the entire Universe. Charles Messier had identified objects in the sky that had a spiral like structure, but classified them as being part of our own Galaxy. Messier compiled a list of these 'spiral nebulae' in the 17th Century and some people argued that these nebulae were 'island universes' - objects like the Milky Way but external to it. It wasn't until 1923 when Edwin Hubble used Cepheid variable stars as standard candles to measure the distance to these 'nebulae' that it became clear that they weren't nebulae at all. Hubble's distance to the Andromeda 'Nebula' placed it at such a distance that ended the debate, proving that they were unquestionably other galaxies.

Advances in technology and telescopes has led to the discovery that there are, in fact, billions of other galaxies. Each with its own unique properties in size, colour and morphology. We also now understand that these galaxies do not evolve in isolation like an 'island universe' would, rather that the Universe is dynamic and galaxies are constantly interacting with each other. Therefore, the new question is how do these

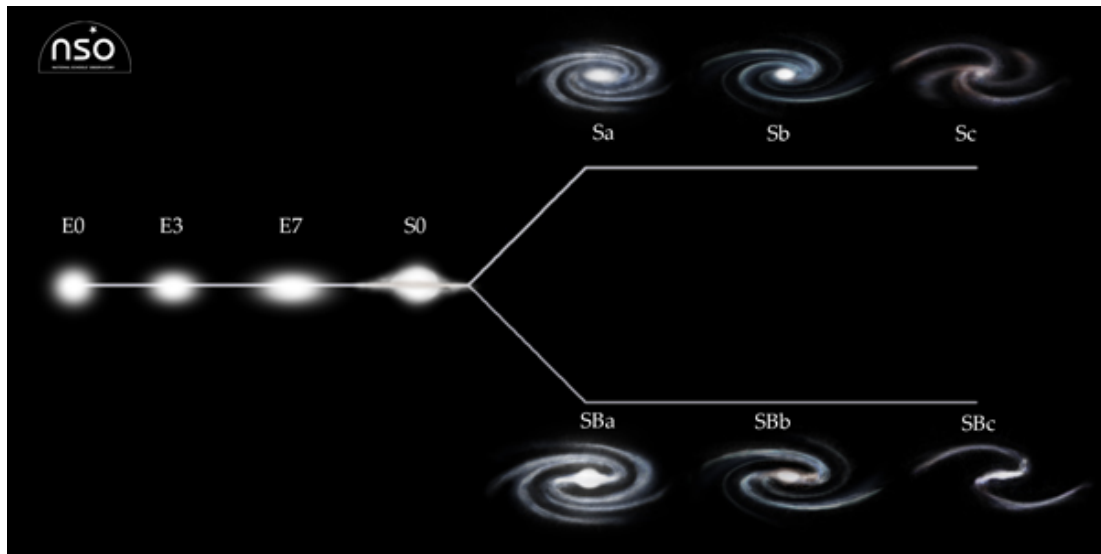


Figure 1.1: The Hubble tuning fork diagram. Image taken from the National Schools’ Observatory.

interactions shape the galaxies, and what has occurred in one galaxy’s history that makes it appear different to its neighbour now?

In 1930 Harlow Shapley already recognised the significance of stellar clusters in answering this question, noting “The typical star clusters are in themselves numerous and widely distributed, and their problems are intimately interwoven with some of the most significant questions of stellar organisation and galactic evolution” (Shapley, 1930). This thesis builds on the notion that stellar clusters and galaxies share an intimate formation history and uses “the most magnificent objects that can be seen in the heavens” (Herschel 1802, referring to star clusters) to disentangle the history and reveal otherwise hidden properties of galaxies.

1.1 Galaxy demographics

Since the original discovery of fuzzy and spiral ‘nebulae’ it has been known that galaxies show a range in their morphological types (Hubble, 1926). Galaxy morphology encompasses many complexities of galaxy structure including the presence of bulges, thin and thick discs, bars and spiral arms. One of the first steps to understand different

formation mechanisms of galaxies is to categorise them into different morphological types. Edwin Hubble did this for the first time in 1926 and although the picture is now deemed too simple the basic ideas presented still hold. [Hubble \(1926\)](#) developed a classification scheme in what is known as the ‘tuning fork diagram’ (see Fig. 1.1). The diagram is divided into two parts: ellipticals (spheroidal galaxies) and spirals (galaxies with spiral arms). The elliptical galaxies have numbers from 0 to 7 depending on their shape, with E0 galaxies being perfectly round and E7 galaxies being very elliptical. The spiral galaxies are classified into two groups, spirals without bars (given the notation S) and spirals with central bars, from which the spiral arms usually originate (given the notation SB). The spirals are also assigned letters a to c, which characterise how tightly wound the spiral arms are. Sa and SBa spirals have large bulges and very tightly wound spiral arms. Sc and SBc spirals have small bulges and loosely wound spiral arms. There are some galaxies that do not fit into any of these categories and these were termed ‘irregulars’ and consist of galaxies with odd shapes and sizes.

This discussion can be simplified by considering the fraction of a galaxy’s light or mass contained in a pressure supported spheroid or bulge and the fraction that is contained in a flattened, rotationally supported disc. This bulge to disc ratio is broadly correlated with classical Hubble type. It is often difficult to robustly decompose the galaxy light into a spheroid and disc component and therefore other metrics such as the concentration (the ratio of the radius containing 90% of the light to the radius containing 50% of the light), the half light radius (the radius at which the luminosity drops to half of that at the centre) or the Sérsic index ([Sérsic 1963](#) a measure of the ‘slope’ of the light profile e.g. [Blanton & Moustakas 2009](#)) are frequently used as rough proxies for morphology.

Galaxies can also be characterised by their radial size and internal velocity. For disc-dominated galaxies the radial size is usually characterised by the scale radius r_s (the scale radius in the exponential function characterising the radial light profile) and the characteristic velocity is the rotation velocity at the maximum of the rotation curve V_{rot} . For spheroid-dominated galaxies the radial size is characterised by the half light radius r_e (the radius that contains half of the total luminosity) and the internal velocity

is characterised by the velocity dispersion σ . Both discs and spheroids exhibit correlations between their stellar mass or luminosity (L), radial size (r) and internal velocity (V) (Faber & Jackson, 1976; Kormendy, 1977; Tully & Fisher, 1977; Shen et al., 2003; Courteau et al., 2007; Bernardi et al., 2010). A combination of these three quantities forms a fundamental plane, meaning that the galaxies populate a relatively thin plane in the three-dimensional $L - r - V$ space (Faber et al., 1987; Djorgovski & Davis, 1987; Bender et al., 1992; Burstein et al., 1997). Projections of this plane forms some of the well-known relations such as the Tully-Fisher relation for discs ($L - V_{rot}$; Tully & Fisher 1977), the Faber-Jackson relation for spheroids ($L - \sigma$; Faber & Jackson 1976) and the Kormendy relation also for spheroids ($L - r_e$; Kormendy 1977). The slope, scatter and evolution of these relations with redshift carry important clues about the formation history of galaxies of different morphological types (e.g. Shen et al. 2003; Trujillo et al. 2006; Kassin et al. 2007; Cappellari et al. 2009; Bernardi et al. 2010; van der Wel et al. 2014).

Disc dominated galaxies are predominantly blue and star forming while spheroid dominated galaxies are red and quiescent (e.g. Roberts & Haynes 1994; Kauffmann et al. 2003; Blanton & Moustakas 2009). The mass functions of the two classes of galaxies are also different, the spheroid dominated galaxies contribute a larger fraction of the galaxies at higher galaxy stellar mass than the disc dominated galaxies (e.g. Bernardi et al. 2010).

The probability for a galaxy to be quiescent depends both on its stellar mass and large scale environment. It therefore becomes apparent that galaxy properties are also dependent on their place in the Universe.

1.2 A model for the formation and evolution of the Universe

To be able to model galaxy formation, one must adopt a model for the Universe itself. Observations have revealed that our Universe is geometrically flat (e.g. Planck

[Collaboration et al. 2020](#)) and dominated by dark energy and dark matter.

The model must be able to account for the observation of the 3K cosmic microwave background (CMB) radiation ([Penzias & Wilson, 1965](#)). The all-sky microwave observations that detected the CMB provide a snapshot of the Universe at $z \approx 1100$. The Differential Microwave Radiometer instrument aboard the COBE satellite showed that small temperature anisotropies existed in the CMB ([Smoot et al., 1992](#); [Bennett et al., 1996](#)). Subsequent missions including WMAP ([Bennett et al., 2003, 2013](#)) and Planck ([Planck Collaboration et al., 2014, 2016](#)) confirmed these small amplitude fluctuations, which are the seed for large scale structure in the Universe. A popular way to quantify how well the models of the Universe can match the CMB is the calculation of an ‘angular power spectra’, which measures the correlations between the small fluctuations of the CMB temperature from different directions. As the angle between the directions increases, the amount of correlation will change. The angular power spectra as seen from observations can be compared to theory and the discrepancy between the two can be quantified (e.g. [Planck Collaboration et al. 2016](#)).

Additionally, the model must contain some matter that interacts only via gravity. This ‘dark’ matter is inferred through several phenomena that, to be explained, require some additional mass. These include the velocities of galaxies in clusters ([Zwicky, 1937](#)), flat rotation curves in galaxies ([Rubin & Ford, 1970](#); [Rubin et al., 1980](#)) and strong gravitational lensing observed around galaxy clusters ([Walsh et al., 1979](#)).

The model must also be able to explain the level of galaxy clustering. The distribution of galaxies is mapped through ‘large scale structure’ surveys (e.g. [York et al. 2000](#); [Colless et al. 2001](#); [Jones et al. 2004](#); [Blake et al. 2010](#)) and angular power spectra of matter can be constructed and compared to models in the same way as for the CMB. Perhaps one of the most surprising discoveries in cosmology is that the Universe is not only expanding, but this expansion is accelerating ([Riess et al., 1998](#); [Perlmutter et al., 1999](#)), therefore any model of the Universe must also include a parameter that can account for this acceleration.

Currently, the best fitting model to the [Planck Collaboration et al. \(2016\)](#) power spec-

tra, and one that can also account for large scale structure and accelerating expansion, is the Λ CDM model. The model has three major components: Λ , a cosmological constant that includes dark energy and is responsible for the accelerating expansion of the universe ($\approx 70\%$ of the energy density); cold dark matter (CDM, $\approx 25\%$ of the energy density); and baryonic or visible matter that makes up just 5% of the energy density. Λ CDM is successful at reproducing the detailed properties of galaxies including, but not limited to, their numbers, clustering, colours and morphologies. Some alternative models challenge the assumptions of Λ CDM (such as modified Newtonian dynamics [Milgrom 1983](#)) and can reproduce some aspects of the $z = 0$ universe. However, for the purposes of this thesis, I assume Λ CDM to be the correct parameterisation of the Universe.

I now briefly outline the simplified timeline of the early Universe in the context of this model.

1. **Inflation**—The very early Universe was an extremely hot, dense and nearly homogeneous mixture of photons, electrons, baryons (in the form of protons and alpha particles), CDM and neutrinos. The photons and baryons were tightly coupled together as a plasma. The initial conditions of this plasma are thought to be established during a period of rapid expansion known as inflation (e.g. [Tsujiikawa 2003](#); [Baumann 2009](#)). Density fluctuations in the plasma are seeded by quantum fluctuations in the field driving inflation. The small perturbations propagate through the plasma collisionally as a sound wave, producing under and over densities in the plasma with simultaneous changes in density of matter and radiation. CDM doesn't partake in these pressure induced collisions, but does act gravitationally, either enhancing or negating the fluctuations of the photons and baryons.
2. **Recombination and decoupling**—Eventually, the plasma expands and cools enough for electrons and baryons to recombine, forming neutral atoms. The photons decouple from the baryons i.e. the mean free path of photons becomes larger than the size of the Universe, meaning that this snapshot of the density fluctuations

is preserved in the CMB anisotropies (Eisenstein & Hu, 1998). Recombination produces a neutral universe which is unobservable throughout most of the electromagnetic spectrum, an era sometimes referred to as the ‘Dark Ages’. During this era, CDM begins gravitational collapse in overdense regions.

3. **Reionisation**–Baryonic matter gravitationally collapses into these CDM halos where its pressure and density increases. This allows the first stars to form and ‘Cosmic Dawn’ begins. Radiation from these objects reionises the intergalactic medium.
4. **Structure formation and acceleration**– Denser than average regions will attract their surroundings more strongly than average. This allows the denser regions to become even more dense as matter is drawn away from the already under dense regions. This results in a vast cosmic web of dark matter that is then traced by luminous matter. As the Universe continues to expand over time, the negative pressure associated with dark energy increasingly dominates over opposing gravitational forces and the expansion of the Universe accelerates.

1.3 Galaxy formation in the Λ CDM Universe

Evidence of dark matter came before any evidence for the accelerating expansion of the Universe, but still models were put forward to explain structure formation (Press & Schechter, 1974; White & Rees, 1978; Fall & Efstathiou, 1980). In these early models structure is seeded prior to recombination through the gravitational collapse of CDM and following recombination neutral gas falls into the gravitational potentials caused by the CDM. These systems then merge together to form larger and larger structures. This is a hypothesis that is not dissimilar to the one accepted for galaxy formation today, with the addition of an expanding Universe.

The landscape of the CDM has many small scale peaks superimposed on top of the medium and large scale peaks. As the Universe expands the background density decreases. When a peak exceeds a critical over-density relative to the background, the

region within that peak becomes gravitationally self bound. These self bound regions are often referred to as dark matter haloes. The baryons can then be considered as falling into the dark matter haloes and clusters of galaxies are found in the most massive haloes at $z = 0$.

1.3.1 Star formation and feedback processes

The collapse of dark matter will eventually stop as it reaches virial equilibrium, whereas baryons can radiate away their binding energy and collapse further in the centres of the dark matter haloes. If the cooling time is less than the collapse time, the gas can fragment into small, high-density cores that may form stars and give rise to a visible galaxy (Silk, 1977; Rees & Ostriker, 1977; Hunter, 1992; Williams et al., 2000).

To continue to form stars, galaxies must be continually fed with gas. This gas accretion transpires in two ways: ‘hot’ and ‘cold’ accretion. If the gas infall velocity is supersonic it will experience a shock and heat to the virial temperature of the halo, gas can then cool radiatively and settle into a rotationally supported disc and form stars (e.g. Fall & Efstathiou 1980; Kereš et al. 2005), this is the hot accretion mode. Cold accretion takes place when the gas does not become shock heated (e.g. Kereš et al. 2005), filaments of the cosmic web feed the galaxy preferentially through cold accretion. Both modes of gas accretion can coexist (e.g. Kereš et al. 2005; Dekel & Birnboim 2006; Ocvirk et al. 2008) and provide the galaxy with its interstellar medium (ISM) that fuels continuous star formation. The rate at which a galaxy forms stars is known as the star formation rate (SFR) and is related to the gas surface density in the ISM (Kennicutt, 1998).

The cooling of gas within small, dense dark matter haloes is predicted to be very efficient and the need to inject energy to regulate galaxy growth was recognised even in the earliest galaxy formation models (e.g. White & Rees 1978). Simulations without this extra energy injection produced stellar discs that were too massive and compact compared to observations (Katz & Gunn, 1991; Navarro & Benz, 1991; White & Frenk, 1991; Balogh et al., 2001). Some physical feedback processes must be at play to pre-

vent the gas from cooling or to reheat it.

First of all, is the process of star formation itself. Feedback in the form of protostellar winds and supernova explosions produce large amounts of energy that can heat surrounding gas and potentially blow it out of the galaxy (Matzner & McKee, 2000). The energy injected through stellar feedback increases as the SFR increases, allowing for the self-regulation of galaxy formation. In cosmological simulations, the inclusion of this feedback ensures there is no overproduction of galaxies of Milky Way-mass and below (Mitchell et al., 2020) and ensures the production of realistically sized spiral galaxies (e.g. Governato et al. 2007; Marinacci et al. 2014; Agertz & Kravtsov 2016).

For galaxies above Milky Way mass, feedback provided by the active galactic nuclei (AGN) becomes important. Most massive spheroidal galaxies contain a supermassive black hole at their centre (e.g. Kormendy & Ho 2013) that can accrete gas and subsequently release energy (e.g. Silk & Rees 1998; Bower et al. 2006; Croton et al. 2006). This channel of energy injection becomes important when stellar feedback becomes inefficient in massive galaxies. Simulations have shown that AGN activity has a significant influence on the SFR of massive galaxies and can lead to galaxy quenching (e.g. Springel 2005; Bower et al. 2006; Booth & Schaye 2009).

From this discussion it is clear that galaxy formation is full of complexities. Cooling, star formation and AGN accretion can all alter the phases of the baryonic component in a galaxy and all are intertwined. For example, if cooling becomes efficient, the star formation rate of the galaxy increases which in turn produces more stellar winds and supernovae that act against efficient cooling of the gas. Understanding these various feedback loops is one of the most important issues in modern theoretical galaxy formation physics.

1.3.2 Dynamical evolution

Galaxy formation is far from a closed box process. Galaxies can accrete new material (both dark and baryonic matter) from the intergalactic medium and can lose material

through feedback processes or through the gravitational attraction of a more massive galaxy. Galaxies can also merge to form a new galaxy with different properties from its progenitors. In fact, in the CDM models of galaxy formation galaxy haloes grow hierarchically: larger haloes are formed by the merging of smaller ones (e.g. [Blumenthal et al. 1984](#)). Halo or galaxy growth through this hierarchical process usually takes one of three forms (e.g. [L'Huillier et al. 2012](#)):

1. **Smooth accretion**– Part of the growth of a massive halo is the merging with a large number of smaller haloes and to a good approximation, such mergers can be thought of as smooth accretion. Accretion is the steady flow of dark matter and gas onto the galaxy from the surrounding filaments of the cosmic web.
2. **Minor mergers**– If two merging haloes have very different masses (usually a mass ratio of less than 1:3) the smaller system can orbit within the larger one for an extended period of time. Dynamical friction causes an energy transfer and the smaller object falls inwards towards the larger. Tidal effects then remove mass from its outer regions and may dissolve it completely. If the smaller system is massive enough, it may retain its identity for a long period of time.
3. **Major mergers**– The rare process of two haloes of similar mass merging is a more violent process. Usually the process disturbs the structure of the two progenitors to create a galaxy with a different morphology to the ones from which it formed. The process can trigger a burst of star formation or AGN activity if the two progenitor galaxies contained enough cold gas.

Through the theory of hierarchical galaxy formation every galaxy we observe today should have undergone some sort of merger in its lifetime. [Li et al. \(2007\)](#) showed that galaxies experience ~ 3 major mergers in their life time, independent of their mass. Mergers have a significant impact on the morphologies, SFR and chemical composition of galaxies and therefore understanding their nature and frequency is a fundamental part of understanding galaxy formation and evolution.

When a smaller galaxy enters the potential well of a more massive galaxy it undergoes

mass loss. The mass loss usually occurs in the form of tidal stripping (e.g. [Read et al. 2006](#)) and dynamical friction can cause increased tidal stripping (e.g. [Fujii et al. 2006](#)). I outline both mechanisms here.

Tidal Stripping: The matter (dark and baryonic) in the outer parts of the satellite can experience tidal forces that exceed the gravitational force binding them to their host galaxy. The gravitational attraction of the main galaxy causes the satellite to accelerate towards it, the material that is closest to the main galaxy will feel a different acceleration to the material furthest away from it. If the difference between these accelerations and that of the centre of the satellite is larger than the binding force per unit mass then material will be stripped and become bound to the main galaxy instead of the satellite ([Binney & Tremaine, 1987](#); [Read et al., 2006](#)). This, when combined with the motion of the satellite on its orbit, can create streams of stripped stars and gas ([Helmi et al., 1999](#)). Some of the most well known streams are the Magellanic stream, a stream of stripped neutral hydrogen from the Magellanic clouds ([Wannier & Wrixon, 1972](#)) and the stream of stars associated with the dissolution of the Sagittarius dwarf galaxy ([Newberg et al., 2002](#)). Streams are powerful tools in galactic archaeology, they can be used to constrain the gravitational potential of their host galaxy (e.g. [Johnston et al. 1999](#)) and also constrain the merger history of the galaxy because the stream can survive even after the bound satellite has been destroyed (e.g. [Helmi 2008](#)).

Dynamical Friction: When an object moves through a large collisionless system of field particles it experiences a drag force. This drag force is known as dynamical friction and transfers energy from the object to the field particles. One way to think about dynamical friction is that the moving object causes the field particles to accelerate towards the object. As a result, the particle number density behind the object is higher than that in front of it and the net effect is a drag force on the object. Consequently, the object loses energy and angular momentum to the field particles and the orbit of the massive object decays with time, meaning it moves towards the centre of the potential well ([Fujii et al., 2006](#)). In the case of a satellite galaxy orbiting in the dark matter halo of a more massive galaxy, dynamical friction moves it closer to the centre of the galaxy where tidal stripping is more efficient ([Chandrasekhar, 1943](#)). However, mass

loss from tidal stripping can cause an increase in the dynamical friction time scale by a factor of 2-3 (Colpi et al., 1999; Fujii et al., 2006; Boylan-Kolchin et al., 2008).

The merging of two galaxies with comparable mass cannot be treated analytically. Their orbital energy is transferred to the internal energy of the merger product and some of the orbital energy can be carried away by material ejected from the progenitors. The system settles into a new equilibrium via violent relaxation (Toomre, 1977; Barnes, 1998). The outcome of such relaxation is near-impossible to predict theoretically and therefore numerical simulations are used to make predictions (e.g. Springel 2005; Cox et al. 2006; Naab et al. 2006; Lotz et al. 2008; Solanes et al. 2018). Even the earliest simulations revealed that mergers between disc galaxies of approximately equal mass can result in the formation of an elliptical galaxy (Farouki & Shapiro, 1982; Negroponte & White, 1983). Therefore it is postulated that some elliptical galaxies are the result of a major merger that included at least one disc galaxy.

The structure of the remnant between two galaxies depends primarily on four properties:

- The progenitor mass ratio. Major mergers are destructive to both galaxies and result in an entirely new galaxy. On the contrary, minor mergers are less destructive and the remnant often still resembles the most massive progenitor.
- The morphologies of the progenitors. Discs are fragile structures that can be thickened even during a minor merger. During a major merger of two disc galaxies, tidal tails are often created (e.g. Wen & Zheng 2016) that are absent in the major merger of two elliptical galaxies.
- The gas mass fractions of the progenitors. Gas responds to pressure forces and can lose energy through radiative cooling. Gas-rich mergers can be responsible for triggering star bursts and AGN activity (e.g. Mihos & Hernquist 1996; Springel 2005; Croton et al. 2006; Hopkins et al. 2008).
- The orbital properties. The orbital energy, angular momentum and orientation is an important factor in determining the presence of tidal features.

This has so far been a description of the merger events between two isolated galaxies. However, denser environments, such as galaxy groups and clusters are hubs of dynamical activity that are constantly transforming galaxies. Therefore, we now outline the processes that can transform galaxies within dense environments.

Galaxy Harassment: In a cluster of galaxies, the velocity of an individual galaxy is typically larger than the internal velocity dispersion of the galaxy (Moore et al., 1996). This means that encounters with other galaxies within the galaxy cluster can be considered as high speed interactions, contrary to the tidal stripping above, that can be considered as a low speed interaction between two galaxies. When a galaxy undergoes a high speed interaction it is heated and becomes less bound, this makes the galaxy more vulnerable to subsequent tidal interactions with other galaxies and the cluster potential. The culmination of multiple high speed interactions is known as galaxy harassment (e.g. Richstone 1976; Farouki & Shapiro 1981). This can cause substantial mass loss and fragile discs may get heated and transformed into spheroids (e.g. Moore et al. 1996).

Dynamical friction: As previously discussed in the context of two merging galaxies, dynamical friction causes a satellite galaxy to sink to the centre of a potential well. In the context of a galaxy cluster, this causes the satellite galaxy to sink towards the massive, central galaxy. The satellite galaxy is unlikely to merge with other satellites of the central due to the high speed interactions. If the galaxy can remain bound as it makes its way to the centre of the potential well, it will merge with the central galaxy of the cluster (e.g. Gallagher & Ostriker 1972; Ostriker & Tremaine 1975; Malumuth & Richstone 1984).

Ram-pressure stripping: A galaxy can have its gas stripped as it moves through the intra-cluster medium (Gunn & Gott, 1972; van Gorkom, 2004). This is similar to the force felt when moving quickly through the air. Ram-pressure stripping is also an important feature of the interaction between two isolated galaxies discussed above but can be stronger in galaxy clusters due to the intra-cluster medium. When a galaxy loses its interstellar gas, it loses its potential for further star formation and becomes quenched. How quickly a galaxy loses its star forming gas depends on its mass. Higher

mass galaxies are able to hold onto their gas for longer since it is more bound to the galaxy, whereas low mass galaxies will become quenched much quicker.

Starvation: The gas consumption timescale of a galaxy is much shorter than a Hubble time (Larson et al., 1980). Therefore, star forming galaxies require sustained gas accretion (see Section 1.3.1). Once a galaxy enters a cluster the accretion is mostly shut off and continued star formation uses the gas that is left in the galaxy: the galaxy then transforms from blue and star-forming to red and quenched. This process is enhanced through ram-pressure stripping which reduces the gas reservoir the galaxy had left.

It is apparent from this section that galaxy interactions are a fundamental part of shaping the $z = 0$ galaxy. The impact of such interactions depends on many different factors. There is still a lot of uncertainty in our understanding of the impact of mergers on the morphology, SFR and other properties of galaxies. If the merger history of a galaxy can be determined, its properties could be connected to significant merger events. This is an ongoing challenge in astrophysics to which this thesis aims to contribute.

1.3.3 Chemical evolution

The early Universe contained only hydrogen and helium, with a small amount of lithium. The first stars were formed from this primordial material and created heavier elements in their cores via nuclear fusion, a process termed stellar nucleosynthesis (Harwit & Spaans, 2003; Nomoto et al., 2013). The products of stellar nucleosynthesis enrich the interstellar medium (ISM) through stellar winds and supernovae. Stellar nucleosynthesis produces elements as heavy as iron (Fe) and heavier elements are produced during the supernova event in a process termed supernova nucleosynthesis (Hoyle & Fowler, 1960).

Massive stars ($M_* > 8 M_\odot$) evolve rapidly and end their life in a core-collapse supernovae (Filippenko, 1997). This type of supernovae enriches the ISM with Fe and α elements, which are formed through a ladder of nuclear reactions, starting from carbon and consuming only helium and the product of the previous reaction. They are

so-called because their most abundant isotopes are integer multiples of four (e.g. Oxygen, Neon, Magnesium, Silicon, Argon, Calcium), the mass of the helium (or alpha) particle. Lower mass stars are longer lived and end their life as a white dwarf. This white dwarf can accrete material from a companion star, reach a critical mass and explode as a Type Ia supernova or two white dwarfs may merge and cause such an explosion (Filippenko, 1997). This type of supernovae provides significant iron enrichment to the ISM (Anders, 1959).

Some light elements that are not formed through nucleosynthesis are formed through cosmic ray spallation (Meneguzzi et al., 1971). Cosmic rays are highly energetic charged particles, such as protons, alpha particles or nuclei of other heavier elements. When a ray particle impacts with matter a large number of nucleons can be ejected from the object hit. This process contributes to the abundance of some light elements such as lithium, beryllium and boron.

The mass fraction of the baryonic component of stellar systems contained in metals (all elements heavier than helium) is referred to as its metallicity. The metallicity of a galaxy usually increases with time as more metals are synthesised and released into the ISM that then forms new stars with the enriched material. This makes the chemical composition a powerful tool to disentangle the past star formation history of the galaxy. More intense star formation leads to more ejecta from stars that then enriches the ISM quicker, so galaxies that formed relatively quickly will have a steep age-metallicity relation compared to those galaxies that formed slower.

Another constraint on the evolution of a stellar system is in the form of the α -element abundance ratio with Fe. Stars have relatively high $[\alpha/\text{Fe}]$ at low $[\text{Fe}/\text{H}]$ and form a plateau in $[\alpha/\text{Fe}] - [\text{Fe}/\text{H}]$ space. As the metallicity increases there is a ‘knee’, after which the $[\alpha/\text{Fe}]$ begins to decrease with increasing $[\text{Fe}/\text{H}]$. The knee corresponds to the time at which the Type Ia supernovae begin to enrich the ISM with Fe (Wheeler et al., 1989), thus decreasing the $[\alpha/\text{Fe}]$ ratio. How much a galaxy can enrich itself in Fe through stellar winds and core-collapse supernovae before the Type Ia supernova turn on can be an indication of the star formation rate in a stellar system. For example, low mass galaxies do not enrich as quickly as high mass galaxies and therefore the

position of the knee is shifted to lower $[\text{Fe}/\text{H}]$ (e.g. [Pritzl et al. 2005](#); [Tolstoy et al. 2009](#)).

The combination of dynamical and chemical information about a galaxy is key to unlocking the information about its past. In the Milky Way, we are in the unique position of knowing the properties of individual stars and therefore can use them to understand how the Milky Way formed and assembled. In other galaxies it is not always possible with current telescopes and observational techniques to know the properties of individual stars. Therefore, a widely accepted alternative is to use globular cluster (GC) properties to infer stellar population properties and formation histories.

1.4 Globular cluster populations

GCs are spherical collections of millions of stars held together by their mutual gravity. They are bright and dense systems that reach far out into the halo of a galaxy. GCs have been found in most observed galaxies, from low-mass dwarf galaxies to massive elliptical galaxies in all kinds of environments ([Harris, 1991](#)). A typical globular cluster is old, usually > 10 Gyr (however, GCs are seen to still be forming in the universe today e.g. [Portegies Zwart et al. 2010](#)), this makes them some of the oldest objects in the Universe. In external galaxies GCs stand out as bright entities against the background of field stars. GCs were once considered simple stellar populations, meaning they can be described by a single age and they retain the metallicity at which they form (see later discussion about light element abundance variations within GCs). The ages and metallicities of GCs can be determined at much further distances than the field star component. Together, this makes GCs ideal tools to study the formation of galaxies.

For example, the Milky Way system is home to many infalling dwarf galaxies and two such galaxies are the Large and the Small Magellanic Clouds (LMC and SMC). They will eventually deposit their GCs into the halo of the Milky Way. Both galaxies have large GC populations that span a wide range of ages. From GCs that are forming today (e.g. R136, [Crowther et al. 2016](#)), to tens of hundreds of Myr (e.g. NGC 1850, [Correnti](#)

et al. 2017 and NGC 1856, Hodge & Lee 1984), as well as large intermediate age populations (e.g. NGC 419, Lindsay 1, Glatt et al. 2008 and NGC 1978, Mucciarelli et al. 2007) ranging from 1-8 Gyr, and finally the classic GC populations > 10 Gyr. The chemical enrichment history of the LMC and the SMC can be traced based on their GC populations (Horta et al., 2021a) and, with techniques to associate the GCs with their parent galaxies (e.g. Majewski et al. 2003; Law & Majewski 2010b; Helmi et al. 2018; Belokurov et al. 2018; Myeong et al. 2019; Massari et al. 2019; Vasiliev 2019), even after accretion onto the Milky Way would still be possible. For this reason GCs are often considered fossil records of galaxy formation and evolution and many galaxy surveys include the observation of GCs in their scientific objectives.

Starting with our own Milky Way there has been a quest to understand where GCs came from and how we can use their properties to infer the formation history of galaxies, including but not limited to our own. Some of the properties of a GC system are outlined in this section.

1.4.1 The Milky Way

Historically, the starting point for studies of GC populations is the Milky Way, where some GCs can be identified by the naked eye. Individual stars within Milky Way GCs can be resolved and more precise ages and metallicities can be determined.

There are ~ 150 GCs known to reside within the Milky Way potential (Gaia Collaboration et al., 2018; Vasiliev, 2019) although the actual number could be closer to ~ 180 , because some are likely to be obscured by the dusty and dense plane of the galaxy (Binney & Wong, 2017). The Milky Way GC population has an approximately spherical distribution extending out to more than 100 kpc from the centre of the galaxy (Harris, 1996). However, their spatial distribution also contains substructures, where some GCs are grouped in space. These groupings often coincide with the positions of dwarf galaxies (e.g. Zinn 1985; Majewski 1994).

The existence of two distinct sub-populations in the GC population, based on metal-

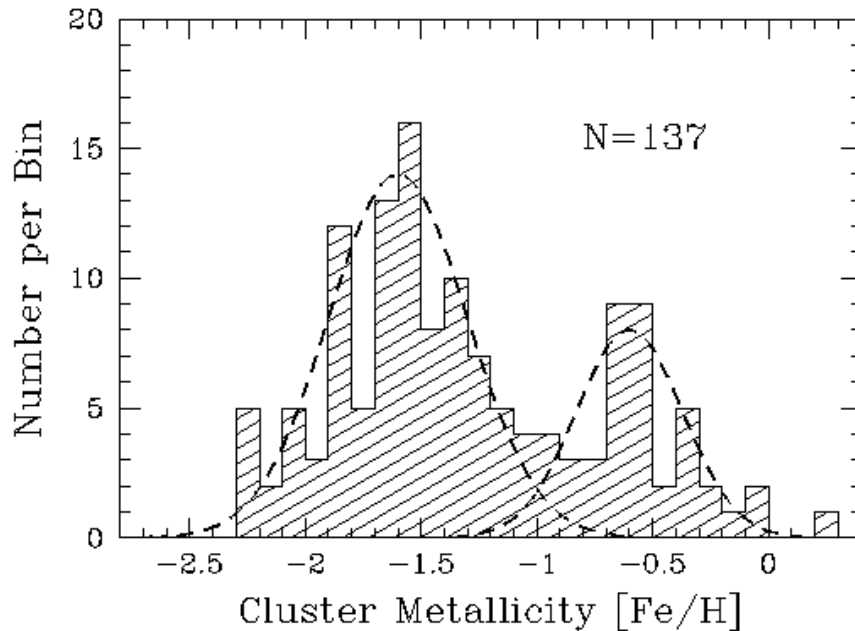


Figure 1.2: Metallicity distribution for 137 Milky Way GCs as listed in the [Harris \(1996\)](#) catalogue. Figure taken from ([Harris, 1999](#)).

licity was suspected early on in the research into Milky Way GCs ([Kinman, 1959](#)) but was firmly established by the study of [Zinn \(1985\)](#). There is a metal-poor population (comprising of $\approx 3/4$ of the GCs) and a metal-rich population (comprising of the remaining $\approx 1/4$ GCs). The total metallicity distribution function can be well described by two Gaussians in $[\text{Fe}/\text{H}]$, separated by ≈ 1 dex in metallicity, this is shown in Fig. 1.2 taken from [Harris \(1999\)](#). It was also found that the two populations have different spatial distributions, with the metal-poor component spread throughout the halo in a near-spherical distribution ([Zinn, 1985](#)), and the metal-rich component contained to the inner region of the galaxy, mostly within the solar galactocentric radius with a more flattened distribution ([Zinn, 1985](#); [Armandroff, 1989](#); [Minniti, 1995](#)).

More recently, with precise relative ages (e.g. [Marín-Franch et al. 2009](#); [VandenBerg et al. 2013](#)) it has been found that the majority of the GCs in the Milky Way are older than ~ 10 Gyr, giving them a formation redshift of $z > 2$. There are, however, a number of GCs that are somewhat younger than the majority, with ages ~ 8 Gyr.

When combining the precise ages with homogeneous metallicity measurements ([Carretta et al., 2009](#)), the age-metallicity relation (AMR) can be plotted. The combina-

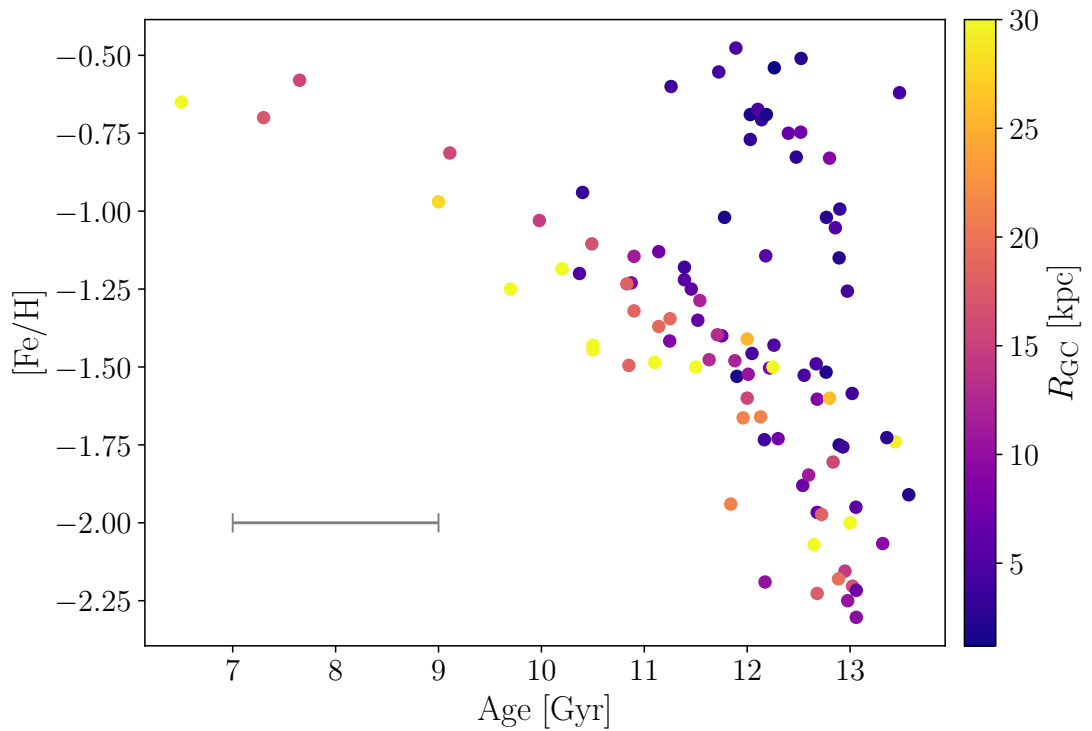


Figure 1.3: The observed age-metallicity relation of GCs in the Milky Way. As in [Kruijssen et al. \(2019b\)](#), the sample is the mean of the compilations by [Forbes & Bridges \(2010\)](#); [Dotter et al. \(2010, 2011\)](#) and [VandenBerg et al. \(2013\)](#). The symbol colour indicates the galactocentric radius given by [Harris \(1996, 2010\)](#) where any cluster with a distance greater than 30 kpc is given a yellow colour. The errorbar in the lower left corner indicates the typical error on the measurement of the age.

tion of three main compilations of Milky Way GC ages and metallicities is shown in Fig. 1.3. The three are by [Forbes & Bridges \(2010\)](#), [Dotter et al. \(2010, 2011\)](#) and [VandenBerg et al. \(2013\)](#). I have used the same compilations as in [Kruijssen et al. \(2019b\)](#) and where multiple measurements are available the mean age and metallicity is taken. What is particularly interesting, is that the AMR of Milky Way GCs is bifurcated ([Marín-Franch et al., 2009](#); [Forbes & Bridges, 2010](#); [Leaman et al., 2013](#)). There is a steep branch at old ages, covering all metallicities and a branch that extends to younger ages. The points in Fig. 1.3 are also coloured by their galactocentric radius and the GCs in the old branch have smaller galactocentric radii that are associated with the galactic bulge and disc, whereas the young branch hosts GCs that extend to larger galactocentric radii. Kinematic information helped to reveal that the GCs comprising the younger branch are more likely to be on radial orbits. By contrast, the GCs comprising the steep old branch are more likely to have orbits that are closer to circular and exhibit net rotation of order $50 - 80 \text{ kms}^{-1}$ (e.g. [Dinescu et al. 1999](#); [Massari et al. 2013](#)).

It has been suggested by [Leaman et al. \(2013\)](#) that the GCs comprising the old branch have an AMR consistent with being formed in the bulge of the Milky Way. The bulge is the old, central component of the Galaxy and therefore these GCs were likely formed along with the main part of the Milky Way. The branch of younger GCs, however, exhibits an AMR that is consistent with dwarf galaxies. Therefore, the conclusion is that these young-branch GCs formed in dwarf galaxies that were subsequently accreted into the halo of the Milky Way. It is therefore now accepted to refer to the GCs in the Milky Way as residing in the in-situ (steep, old) or accreted (shallower, younger) branch of the AMR ([Recio-Blanco, 2018](#)). These results are the first hints that detailed AMRs of GCs can be used to infer the accretion history of their host galaxy, particularly when combined with kinematic information.

Another consistently studied property of the Milky Way GCs system is the α -element abundances. In general, Galactic GCs exhibit similar $[\alpha/\text{Fe}]$ to the field stars at a given $[\text{Fe}/\text{H}]$ (e.g. [Pritzl et al. 2005](#)). However, there are some Galactic GCs that have relatively low $[\alpha/\text{Fe}]$ given their $[\text{Fe}/\text{H}]$. As discussed in Section 1.3.3 lower

mass galaxies cannot enrich their ISM as much as higher mass galaxies before Type Ia supernovae start to contribute a higher fraction of Fe, it is therefore hypothesised that these GCs have been accreted into the Milky Way alongside dwarf galaxies (Lin & Richer, 1992; Sneden, 2004; Pritzl et al., 2005; Forbes & Bridges, 2010). Metallicity and α abundances can be a powerful combination to distinguish accreted GCs from the in-situ ones.

First demonstrated by the discovery of the Sagittarius dwarf spheroidal galaxy in the process of disruption (Ibata et al., 1995) and stellar streams crossing the solar neighbourhood (Helmi et al., 1999; Dinescu et al., 1999), it has long been known that the Milky Way is home to many accreted and destroyed dwarf galaxies that would have brought with them their own GC systems. With the advent of the Gaia mission, it is possible to exploit full six-dimensional phase-space information for almost all of the Galactic GCs (Gaia Collaboration et al., 2018; Vasiliev, 2019). Enabling astronomers to derive orbits of GCs and shed light on their formation, evolution and origins. More recently, thanks to advancements in data and data analysis techniques, systems that are deeply embedded in the stellar population of the Milky Way have been discovered, such as the Gaia-Enceladus-Sausage structure (Belokurov et al., 2018; Helmi et al., 2018) and Kraken (Kruijssen et al., 2019b), which was discovered from its GCs alone. These discoveries illustrate the power the GC population has to inform us about the stellar population of galaxies.

Disrupted GCs

As I will discuss in Section 1.5.2, the GC populations we observe at $z = 0$ are subsample of all of the star clusters that ever formed in the Galaxy. Many star clusters in the Galaxy have been destroyed because of tidal shocks and tidal forces. It is sometimes possible to see this in action, in the form of cold, thin stellar streams (e.g. Odenkirchen et al. 2001; Rockosi et al. 2002; Grillmair & Dionatos 2006a,b; Bernard et al. 2016), however these streams are faint and not every disrupted GC will produce a stream that is still observable at $z = 0$. Therefore, other methods are applied to distinguish

stars that may once have been part of a star cluster, but are now mixed with the field population.

Stellar clusters have traditionally been considered single stellar populations. However, one of the key results of GC studies is that a large number of GCs contain unusual patterns in their light element abundances (e.g. [Osborn 1971](#); [Carretta et al. 2010](#); [Martocchia et al. 2018](#)), with no corresponding differences in their metallicities or ages. This rules out two separate formation epochs and thus the formation of these ‘multiple populations’ is currently unknown (for a recent review, see [Bastian & Lardo 2018](#)).

Although the cause of many debates in GC formation, when studying galaxy formation these unusual light-element patterns have proven to be particularly useful. Whilst one population of stars in GCs shows abundances very similar to that of the Milky Way field stars, the other population is sufficiently different that it can be used as a chemical ‘finger print’ for disrupted GCs. This is proven to be applicable to investigating the amount of mass contributed by disrupted GCs to the build up of various components of the galaxy (e.g. [Martell et al. 2011, 2016](#); [Schiavon et al. 2017](#); [Martell 2018](#); [Horta et al. 2021b](#)). From a GC point of view, this allows one to put constraints on how much more massive the GC system of the Milky Way was in the past.

In addition, some of the integrated light studies of extra-galactic GCs show some peculiarities in their colours ([Powalka et al., 2016](#); [Chantereau et al., 2018](#)). This could be due to these light element abundance variations and therefore the impact of multiple populations must be understood in order to use the colours of extragalactic GCs to probe galaxy formation.

1.4.2 M31

Previously, I discussed why the properties of GC systems makes them ideal targets for large surveys of galaxies outside of the Milky Way. One such survey is the Pan-Andromeda Archaeological Survey (PAndAS) of our nearest spiral galaxy M31 ([Mc-](#)

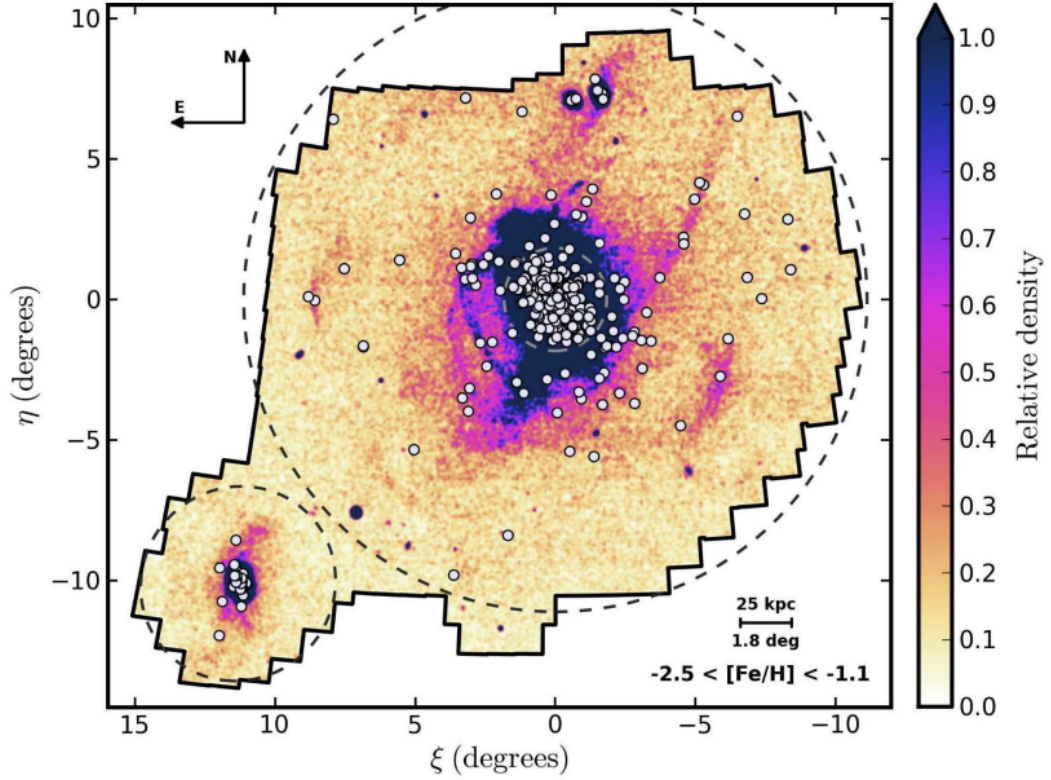


Figure 1.4: PAndAS metal-poor stellar density map. The map shows the red giant branch stars with the positions of all GCs overplotted. The two dashed circles centred on M31 represent $R_{\text{proj}} = 25$ and 150 kpc. The white ellipse represents the central stellar disc. M33 lies to the south-east of M31 and the dashed circle centred on this galaxy represents $R_{\text{proj}} = 50$ kpc. This figure is figure 6 in [Mackey et al. \(2019\)](#).

[Connachie et al., 2009](#)). Due to the proximity of M31 to the Milky Way, the PandAS survey can detect low surface brightness features such as faint satellites and substructure in the diffuse stellar halo as well as its GCs. This gives an unparalleled view of the interaction between the stellar halo and its GCs and provides an excellent comparison to our own Milky Way. In addition to the work in M31, the PandAS survey also includes some of its satellites, M33, NGC 147 and NGC 185 in which GCs are found and studied. M33 is a disc galaxy that includes young, intermediate and old age GCs ([Moretti & Held, 2007](#); [Huxor et al., 2014](#)). NGC 147 and NGC 185 are dwarf galaxies that host 10 and 8 GCs respectively ([Veljanoski et al., 2013](#)).

Using the PAndAS survey, [Huxor et al. \(2008, 2014\)](#) reported the discovery of ~ 100 GCs in the halo of M31 as the first uniform census of GCs across the M31 halo, out

to 150 kpc (previous studies had not covered such a wide field of view and had been comparatively closer to the centre of M31 < 25 kpc, [Crampton et al. 1985](#); [Battistini et al. 1987](#); [Barmby et al. 2000](#); [Caldwell et al. 2009](#); [Fan et al. 2010](#); [Caldwell et al. 2011](#)). The catalogue presented by [Huxor et al. \(2014\)](#) includes GCs out to the edge of the PandAS footprint confirming the suspicion that the M31 GC system is very extended ([Mackey et al., 2010](#)) and it is likely that there are more GCs associated with M31 outside the field of view of the observations.

91 of the ~ 100 GCs in M31 lie outside of the projected radius $R_{\text{proj}} > 25$ kpc including 12 at distances $R_{\text{proj}} > 100$ kpc ([Huxor et al., 2008, 2014](#)). This is in contrast with the Milky Way GC system where there are only 13 known objects with Galactocentric radii greater than 30 kpc ([Harris, 1991](#)). Outside of 25 kpc there is a factor of 7 more GCs in the M31 halo than the Milky Way and inside this radius M31 has a factor of 3 more. This difference could be accentuated when considering that there are detections of very faint GCs in the halo of the Milky Way that would lie below the completeness limit of the PandAS data and therefore would be likely missed if they are present. The reason for this discrepancy in the numbers of GCs is somewhat down to M31 being more massive than the Milky Way. The differences in the radial distributions is likely due to differences in their formation histories.

The stellar halo of M31 shows direct evidence for accretion events in the form of tidal debris, or stellar streams ([Ferguson et al., 2002](#); [Ibata et al., 2007](#)) and it is therefore possible to connect some of these tidal features with the GC population. [Mackey et al. \(2010\)](#) presented the positions of the M31 GCs overlaid onto a metal-poor stellar density map and found a striking correlation between the positions of the halo GCs and the stellar over-densities. They confirmed that this alignment was statistically significant, with just a $\approx 0.25\%$ probability that the alignment occurs by chance. This provides evidence that a significant portion of the outer-halo GCs in M31 were accreted alongside satellite galaxies and is a direct illustration of the assembly of a GC system in action. Additionally, [Mackey et al. \(2019\)](#) classified the outer halo GCs into those that are associated with a stellar substructure and those that are not. Their ‘substructure’ clusters have a strong spatial and/or kinematic link with a halo substructure and their

‘non-substructure’ clusters do not. They also assign an ‘ambiguous’ category into which clusters that have conflicting or weak association with a substructure are placed. They find that between $\approx 35 - 62\%$ of GCs at $R_{\text{proj}} > 25$ kpc have some substructure connection, making them consistent with having been accreted into the M31 halo.

The luminosity function of the M31 GCs outside a radius $R_{\text{proj}} = 30$ kpc is bimodal (Huxor et al., 2014). Mackey et al. (2010) argue that a substantial fraction of the halo GCs have been accreted and therefore Huxor et al. (2014) postulate that the fainter peak of the luminosity function is due to these accreted GCs. This postulation is further strengthened with the finding that the GCs associated with the accreted Sagittarius dwarf galaxy in the Milky Way are relatively faint when compared with the other halo GCs in the Milky Way (Law & Majewski, 2010b). Mackey & van den Bergh (2005) also found a fainter peak in the luminosity function of the young GCs in the Milky Way halo, which they argued are likely to be accreted objects.

The M31 GCs subsamples (substructure, non-substructure and ambiguous) all show a bimodal luminosity distribution (Mackey et al., 2019). If the low-luminosity peak is indicative of an ex-situ origin then some of the non-substructure GCs must also have been accreted. Supporting this hypothesis, the radial distribution of the ‘non-substructure’ GCs shows a smooth decline with radius, with a slope that is extremely similar to the metal-poor field star population (Mackey et al., 2019) that is likely a product of completely disrupted low-mass dwarfs. Additionally, the colours of the non-substructure GCs are almost exclusively bluer (and therefore likely more metal-poor) than the substructure sample compounding the notion that most of the halo GCs are accreted, but those that are not associated with substructure originated from less massive hosts that were accreted early (Mackey et al., 2019).

Finally, the ages of the GCs associated with the substructure class of GCs are, on average, younger than the GCs in the non-substructure class of GCs (Mackey et al., 2019). Since the GCs are now in an environment that lacks the required densities for them to form, this is indicative of more recent accretion events. This, when combined with the fact that they are also more metal-rich means that they were accreted more recently and alongside more massive hosts than their accreted non-substructure counterparts.

In conclusion, M31 is an excellent test case where hierarchical assembly of a GC population can be seen occurring alongside the host galaxy. It is also clear that the properties of the GCs can be used to put constraints on the build up of a galaxy halo.

1.4.3 Beyond the local group

Fully exploiting the expanse of extragalactic GCs requires large samples of spectroscopically studied GCs. Obtaining such data is observationally time expensive, however, their power is well respected and extensive catalogues of GCs exist. For example, the SAGES Legacy Unifying Globulars and GalaxieS (SLUGGS) survey (Brodie et al., 2014) has acquired radial velocities for more than 4000 GCs (Pota et al., 2013; Forbes et al., 2017) and calcium triplet based metallicities for more than 900 GCs (Usher et al., 2012) in 27 early type galaxies. The Fornax Cluster VLT Spectroscopic Survey (Pota et al., 2018) spectroscopically detected and studied GCs in the core of the Fornax galaxy cluster. Additionally the Fornax 3D (F3D) survey (Sarzi et al., 2018) made use of the wide field of view of the Multi Unit Spectroscopic Explorer (MUSE; Bacon et al. 2010) to extract spectra of a large number of GCs in 32 galaxies (irrespective of morphology) in the Fornax galaxy cluster. The work revealed the line-of-sight velocities for 722 GCs and the metallicities for 238 GCs (Fahrion et al., 2020). The ACS Virgo Cluster Survey (Côté et al., 2004) probes the brightest 90% of the GC luminosity function in 100 galaxies in the Virgo galaxy cluster, yielding a sample of $\approx 13,000$ GCs.

Such surveys are important in GC and galaxy studies since they give a statistical sample of GC populations across a range of cosmic environments. This has driven a major leap forwards in the understanding of how the environments of GC formation is imprinted in their properties. In this section I will briefly outline some of the main properties of GC populations that can link them to the formation history of their host galaxy.

Total mass of a GC system

The number of GCs in a galaxy (N_{GC}) and the total GC system mass (M_{GC}) are correlated positively with the galaxy stellar mass (e.g. [Hudson et al. 2014](#)). This suggests a link between the the GC system and the host galaxy, however both of these relations have some non-linearity. Low-mass galaxies and some galaxies of very high mass contain a higher fraction of their stars in GCs than the galaxies of intermediate mass (e.g. [Peng et al. 2008](#)).

M_{GC} can also be correlated with the dark matter mass in a galaxy (M_{halo}). In this case, a near-linear relation is found (e.g. [Blakeslee 1999](#); [Hudson et al. 2014](#)), at least above $M_{halo} \sim 5 \times 10^{11} M_{\odot}$ ([Bastian et al., 2020](#)). This is potentially a surprising result when it is more natural to connect GC formation to the stellar component of a galaxy than to expect the GC system to ‘know’ about the dark matter halo in which it resides. A relatively simple approach to understanding this surprising result is that the linear $M_{GC} - M_{halo}$ relation is because the merging of low- and high-mass haloes leads to average halo properties and GC systems which produce tight relations ([Kruijssen, 2015](#); [El-Badry et al., 2019](#)).

These results suggest an intimate relation between GC populations and their host haloes and indicate that GCs can be used to trace the properties of the dark matter content in galaxies. Dark matter halo masses have been measured using N_{GC} with consistent results to masses measured from GC dynamics and stellar velocity dispersions ([Beasley et al., 2016](#); [Beasley, 2020](#)).

Metallicity distributions and gradients

The mean metallicity of the whole GC system correlates positively with the stellar mass of the host galaxy ([Strader et al., 2005](#); [Peng et al., 2006](#)). Similar to the stars, GCs in more massive galaxies are able to achieve higher levels of metal enrichment ([Tremonti et al., 2004](#); [Kirby et al., 2013](#)).

Like the Milky Way, it has been found that many galaxies have a bimodal GC colour

distribution with a red and a blue population (e.g. [Larsen et al. 2001](#); [Peng et al. 2006](#); [Sinnott et al. 2010](#); [Pota et al. 2013](#)). This colour bimodality has been interpreted, and spectroscopically confirmed as a metallicity bimodality and used as evidence for a two-phase formation scenario of massive galaxies ([Côté et al., 1998](#); [Beasley et al., 2002](#); [Brodie & Strader, 2006](#); [Strader et al., 2007](#); [Beasley et al., 2008](#); [Alves-Brito et al., 2011](#); [Usher et al., 2012](#)). Metal-rich (red) GCs are thought to form in-situ, whereas the metal-poor (blue) population is thought to have been accreted alongside their dwarf galaxy parents. However, the translation of a colour bimodality into a metallicity bimodality is under debate with some authors suggesting that the colour bimodality is an artifact of a strongly non-linear colour-metallicity relation ([Yoon et al., 2006, 2011](#)). This would make the metallicity distribution of a GC system unimodal, but skewed towards low metallicities. This picture is in some disagreement with studies of spectroscopic metallicities and is an area of ongoing research.

[Fahrion et al. \(2020\)](#) compared the metallicities of the GCs with that of the host galaxy's centre in the F3D survey. They found that massive galaxies have GCs spanning a large range of metallicities with some almost as metal-rich as the galaxy centre. [Fahrion et al. \(2020\)](#) were also able to compare the GC metallicity to the metallicity of the galaxy light at its position in the galaxy (instead of the metallicity at the galaxy centre). They find that the red GC population traces the metallicity of the galaxy light over a range of radii and host galaxy masses. By contrast, the blue GC population shows a wide range of relative GC metallicities and can be significantly more metal-poor than their hosts at any given radius. This is consistent with the red GCs having formed alongside the main component of the galaxy light and the blue GCs having an external origin.

In agreement, [Forbes et al. \(2011\)](#) found metallicity gradients for both a red and blue GC population in NGC 1407 out to ~ 60 kpc. Beyond this radius, the metallicities flatten out, indicative of a galaxy that formed by both in-situ star formation in the inner regions and accretion in the outer parts.

Radial profiles

Another GC system property that correlates positively with the mass of the host galaxy is the radius that contains half of the GC system ('half number radius' or GC r_e ; [Forbes et al. 2017](#)). This is similar to the galaxy size-mass relation and is thought to be due to mergers 'puffing up' galaxies or adding additional material (including GCs) to their outskirts.

The number density distribution of GCs with galactocentric radius is important for a number of reasons, including as input to dynamical modelling of the GC system. It is typical to fit radial density profiles of GCs with [Sersic \(1968\)](#) profiles since they have deprojected analytic forms, they extrapolate to finite total GC numbers and both the stellar components and dark matter components of galaxies can be well fitted by Sérsic-like functions ([Strader et al., 2011](#)).

In many galaxies, the metal-poor GCs are more extended than the metal-rich ones ([Geisler et al., 1996](#); [Côté et al., 2001](#); [Bassino et al., 2006](#); [Tamura et al., 2006](#); [Forte et al., 2007](#); [Harris, 2009](#); [Faifer et al., 2011](#); [Strader et al., 2011](#); [Forbes et al., 2012](#); [Pota et al., 2013](#)) and the profile of the metal-rich population is found to match the shape of the profile of the galaxy light ([Tamura et al., 2006](#); [Strader et al., 2011](#); [Forbes et al., 2012](#); [Pota et al., 2013](#)). This supports the general idea that metal-rich GCs formed along with the bulk of the field star population in massive galaxies (e.g. [Brodie & Strader 2006](#); [Bassino et al. 2006](#)). There is however, flattening of the radial profile towards the centre of the galaxy and this is interpreted as the effect of GC disruption, which is stronger in the central regions of the galaxy ([Baumgardt, 1998](#); [Baumgardt & Makino, 2003](#)).

In the massive elliptical galaxy M87, the ellipticity of the GC radial profile has been studied. M87 is aspherical with its stellar isophotal ellipticity increasing from 0.2 near the centre to 0.45 in the outer halo ([Kormendy et al., 2009](#)). [McLaughlin et al. \(1994\)](#) estimated that the ellipticity of the GC system in the inner regions of M87 is roughly consistent with the galaxy light. By contrast, [Strader et al. \(2011\)](#) estimated that the ellipticity of the GC system as a whole is more constant than that of the galaxy light.

However, the red and the blue GCs show differing ellipticity profiles, with the red GCs following the shape of the galaxy light and the blue GCs being much more constant.

In the ACS Virgo Cluster survey it is found that in early type galaxies with visible elongation there is also an elongation of the GC system for both the red and the blue sub-population (Wang et al., 2013). This supports the notion that the red population are associated with the metal-rich field stars but also suggests that if the blue population have been accreted, they must have done so along a preferred merging axis.

Kinematics

Using spectra, line-of-sight velocities of individual GCs can be determined. This is crucial not only to confirm GC candidates, but to study the kinematics of the global GC system and potentially use GCs as tracers for dynamical modelling.

The GC system kinematics have been shown to correlate with some general properties of the host galaxy. For example, the V_{rms} of the GC system correlates with the host galaxy X-ray luminosity, central velocity dispersion of the stars and absolute K -band magnitude. These correlations hold when the kinematics of the red and blue GC sub-populations are studied separately but the relation is tighter for the red GCs (Lee et al., 2010; Pota et al., 2013). This suggests that the kinematics of the GCs are tightly linked to the galaxy in which they reside.

Due to the radial extent of GCs, their power in revealing the mass distribution of a galaxy was quickly recognised. The velocity dispersion in the GCs is in good agreement with that of the stars and therefore the GCs can be trusted as tracers of the enclosed mass (Pota et al., 2013; Forbes et al., 2017; Fahrion et al., 2020). This trend holds when splitting the populations by colour, although the blue GC populations show more scatter in their relation than the red GCs (e.g. Lee et al. 2008). The high velocity dispersion of the GCs in galaxies cannot be explained if only the observed gas and stars contribute to the mass of the galaxy. Therefore, GCs have provided some of the strongest evidence for dark matter at large galactocentric radii (e.g. Zepf et al. 2000; Côté et al. 2001; Strader et al. 2011; Zhu et al. 2014; Alabi et al. 2017).

The GC systems of galaxies have been found to have varying levels of rotation (Pota et al., 2013; Fahrion et al., 2020), but when separated into their red and blue sub-populations, the red GCs show higher rotation amplitudes and follow the stellar rotation more closely than the blue population (Romanowsky et al., 2009; Schubert et al., 2010; Strader et al., 2011; Norris et al., 2012; Pota et al., 2013; Fahrion et al., 2020). It is also found that the red population rotates more consistently with the photometric major axis than the blue sub-population, which sometimes shows a misalignment at large distances (Pota et al., 2013).

The similar kinematics of the metal-rich GC sub-population and the stellar component of the galaxy suggests a close relation between the formation processes of the two (Strader et al., 2011). The metal-poor GC sub-population shows different kinematics to that of the metal-rich GCs and the galaxy light, suggesting that they are a distinct population, likely not formed in the main galaxy. However, rotation has been detected in both the red and blue GC populations, independent of the host mass or morphology (e.g. Arnold et al. 2011; Pota et al. 2013). The accreted GC population can show rotation if the associated satellite galaxies fell into the potential of the main galaxy from a preferred direction, as has been discussed for the Local Group (Libeskind et al., 2011).

1.5 Globular cluster formation and evolution

1.5.1 Globular cluster formation

In the late 17th century William Herschel led a survey (or, as he called it, a “sweeping of the heavens”) that catalogued nebulae and stellar clusters. Herschel classified stellar clusters based on their brightness and shape and coined the term ‘globular cluster’ to refer to the brightest and most-spherical clusters of stars (Herschel, 1786, 1789, 1802).

Since these early catalogues there has been a large interest in the formation of these objects and with the determination of their distances (Shapley, 1917, 1918a,b,c) and

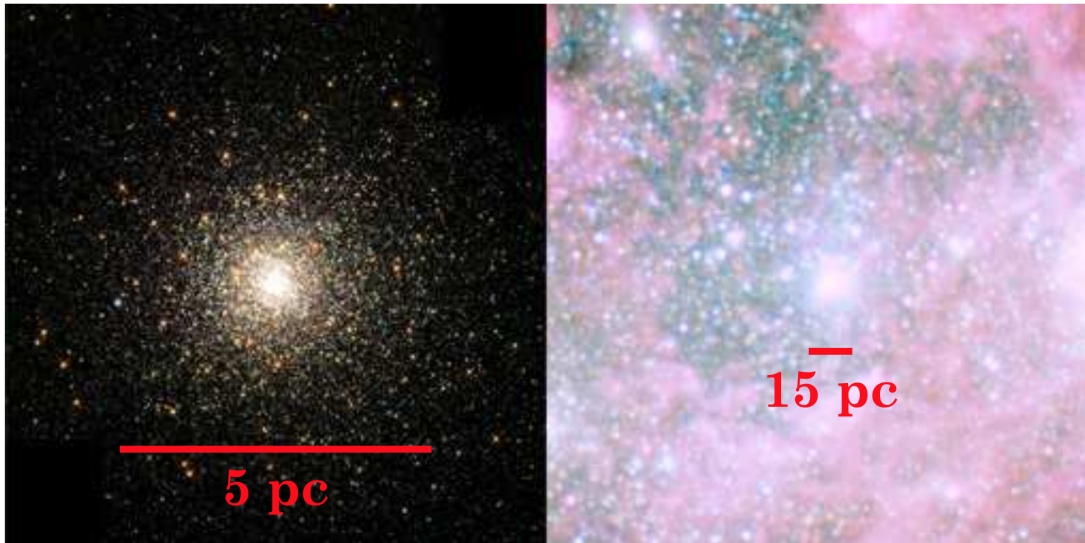


Figure 1.5: This figure shows the similarities between the Galactic GC M80 (left) and the most massive YMC in the nearby dwarf starburst galaxy NGC 1569 (right). The ages are 11 Gyr and 15 Myr respectively. The masses and half light radii are very similar but the ages differ. This shows that GC-like YMCs are still forming today. Left image credit: NASA and The Hubble Heritage Team (STScI/AURA). Right image credit: NASA, ESA, the Hubble Heritage Team (STScI/AURA), and A. Aloisi (STScI/ESA). Image taken from (Kruijssen, 2014).

colours (Shapley, 1918d) came a more advanced classification system. The ‘open’, or ‘galactic’ stellar clusters are bluer, more spatially extended and reside close to the Galactic plane. By contrast the ‘globular’ clusters are red, compact and reside in the outer regions of the galaxy (Shapley, 1930; Trumpler, 1931). The discovery of two mutually exclusive types of stellar cluster contributed to the idea that they were two separate types of object with different formation mechanisms. However, even then there was some debate, owing to the discovery of objects such as NGC5053 which resembles an ‘open’ cluster, but has a Galactic position that should place it in the ‘globular’ category (Trumpler, 1931).

From this early work, the formation of GCs has been a point of contention. One family of models suggest that the GCs had a special formation mechanism, different to normal star formation, that took place in the high-redshift Universe. Such models include: the formation of GCs from thermal instabilities when the first galaxies collapsed (Fall & Rees, 1985), high speed collisions of dark matter sub-haloes (Madau et al., 2020), high-density regions along cosmic filaments before or during galaxy collapse (Boylan-

Kolchin, 2017) or in dark matter mini-haloes (Peebles, 1984; Griffen et al., 2010)

The second family of models work on the assumption that stellar clusters are a natural consequence of normal star formation (e.g. McCrea 1961; Ashman & Zepf 1992; Elmegreen & Efremov 1997; Kravtsov & Gnedin 2005; Shapiro et al. 2010; Kruijssen 2015) and has been strengthened by the discovery of a predicted population of young and massive stellar clusters. These objects were first described as ‘super star clusters’ and discovered with ground based telescopes (e.g. Arp & Sandage 1985; Melnick et al. 1985). Then, with the advent of the Hubble Space Telescope (HST) came the discovery of many young, massive cluster (YMC) populations (e.g. Holtzman et al. 1992; Whitmore et al. 1993; O’Connell et al. 1994; Whitmore & Schweizer 1995; Larsen 2000; Longmore et al. 2014; Bastian 2016), including metal-poor YMCs in dwarf galaxies, as shown in Fig. 1.5 (Anders et al., 2004). YMCs in the local Universe have similar masses and overlapping metallicities with the old GCs and also have similar properties to proto-GCs observed at $z = 2 - 6$ through gravitational lensing studies (Johnson et al., 2017b; Vanzella et al., 2017). Therefore, it is inferred that YMCs are simply young GCs and open clusters are at the low mass end of a continuous star cluster mass distribution that shares a common formation mechanism (e.g. Harris & Pudritz 1994; Elmegreen & Efremov 1997; Portegies Zwart et al. 2010; Kruijssen 2014; Horta et al. 2021a). YMCs offer an insight into the formation of the traditional GCs residing in the halo of many galaxies. Figure 1.5 shows the similarities between a GC and a YMC.

YMCs are observed to form in environments that are gas-rich and have high pressures and therefore high star formation rates. More GCs formed at higher redshift because the gas-fraction, pressure ($P/k \approx 10^7 K cm^{-3}$ as opposed to $P/k \approx 10^4 - 10^5 K cm^{-3}$ in the Milky Way), density ($\Sigma \approx 10^2 - 10^{3.5} M_{\odot} pc^{-2}$ as opposed to $\Sigma \approx 10 M_{\odot} pc^{-2}$ in the Milky Way) and hence star formation rate at $z = 1 - 3$ (Swinbank et al., 2011) was higher than it is at present. The high pressures lead to a high fraction of star formation occurring in gravitationally bound clusters (Kruijssen, 2012) and allow for the collapse of significantly massive molecular clouds (e.g. Dekel et al. 2009). Together these two factors allow galaxies to not only form a high fraction of their stars in bound clusters, but for the resulting stellar clusters to be very massive (Harris & Pudritz, 1994). Be-

ing more massive gives a stellar cluster a greater probability to remain gravitationally bound until $z = 0$.

Another theory is that the formation of these YMCs in the early universe is enhanced by galaxy mergers (e.g. [Li et al. 2017b](#); [Kim et al. 2018](#)). Galaxy merger rates at $z > 1$ are significantly higher than at $z = 0$ (e.g. [Fakhouri et al. 2010](#)) and can enhance the gas pressure in a galaxy, therefore allowing for the formation of massive stellar clusters. However, it is also theorised that mergers could destroy clusters that have already formed in the galaxy disc ([Kruijssen et al., 2012b](#)) and the fraction of all star formation that occurs due to merger events could be reasonably low ([Rodighiero et al., 2011](#)). Therefore, although mergers could contribute to the formation of some GCs it is difficult to quantify their contribution and even if they do not contribute significantly to the formation of GCs, they can contribute to the survival fraction by ejecting GCs into a galaxy halo where they can survive for longer timescales ([Kruijssen, 2015](#); [Kravtsov & Gnedin, 2005](#)).

1.5.2 Globular cluster evolution

The total mass in GCs is an important observational constraint on galaxy formation and evolution. The $z = 0$ mass in GCs is found to have a strong correlation with galaxy halo mass (see Section 1.4.3). However, this mass is not representative of all the GCs that would have formed in a galaxy, because GCs lose mass over time and some clusters will have been completely disrupted. The evolution of the GC mass function over time can link the total mass in GCs at $z = 0$ to the total mass in GCs that ever formed.

The mass functions of young star cluster populations are well described by a power law with slope ≈ -2 at the low mass end, and an exponential cut off at the high mass end, known as a Schechter ([Schechter, 1976](#)) function ([Gieles, 2009](#); [Larsen, 2009](#); [Portegies Zwart et al., 2010](#); [Johnson et al., 2017a](#); [Li et al., 2017a](#)),

$$\frac{dN}{dM} \propto M^{-2} \exp\left(-\frac{M}{M_c}\right), \quad (1.1)$$

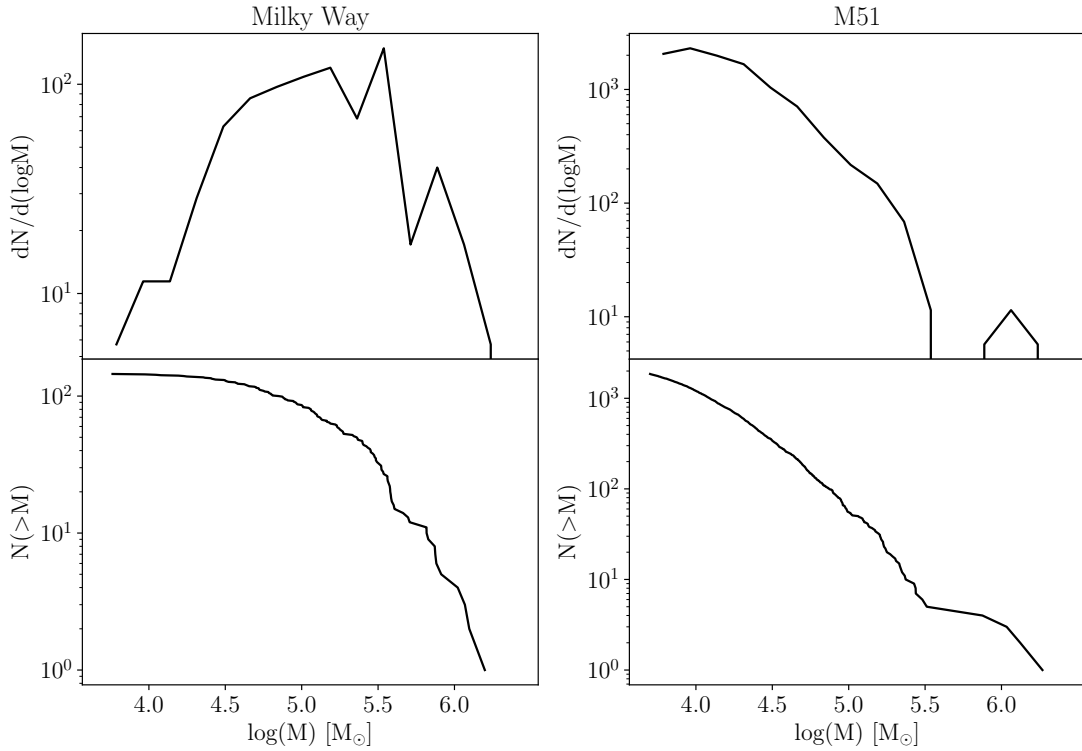


Figure 1.6: A comparison between the mass functions of two GC populations. The left hand panels show that of the Milky Way, which has an evolved GC population, the data is taken from [Baumgardt & Hilker \(2018\)](#). The right hand panels show the young clusters of M51, which contains a young GC population, the data is taken from [Messa et al. \(2018\)](#). The top and bottom panels represent two ways of presenting the mass functions: as a histogram (top panels) and as a cumulative function (bottom panels).

where M_c is the exponential truncation mass and has been observed to depend on the galactic environment (e.g. [Jordán et al. 2007](#); [Larsen 2009](#); [Adamo et al. 2015](#); [Johnson et al. 2017a](#); [Messa et al. 2018](#)), with galaxies exhibiting higher SFR (e.g. more massive galaxies, starburst galaxies etc.) forming more massive clusters. The right hand panels of Fig. 1.6 show the mass function of young ($< 200\text{Myr}$) clusters in M51 and there is a clear exponential truncation at high-mass.

In old GC populations, there is a deficit of low mass GCs and the mass function is log-normal in shape ([Brodie & Strader, 2006](#); [Jordán et al., 2007](#)). The left hand panels of Fig. 1.6 show the mass function of the Milky Way GCs, in the top panels the deficit of low-mass GCs is clearly seen when comparing to the young clusters of M51. If we take the view that GCs are simply evolved YMCs then their evolution must transform the mass function. Furthermore, as discussed in Section 1.4.1 some GC stars now belong

to the field population of galaxies and therefore GCs must lose mass over their lifetime.

GCs can lose mass through stellar evolution, two-body relaxation and tidal shocks. Dynamical friction can cause a change in orbit that promotes further mass loss. Stellar evolutionary mass loss is independent of galactic environment and cluster mass and therefore affects all GCs equally. Stellar evolution is most effective when the GC is young (< 1 Gyr; [Fall & Zhang 2001](#)), whereas dynamical evolution of the star cluster can act over longer timescales.

Two-body relaxation, or evaporation is an internal process within the cluster and is important in GCs due to their compact nature. Such compactness means that stars are tightly packed together and tidal encounters between stars are important. Two-body relaxation allows stars to exchange energy between themselves and some encounters can impart enough kinetic energy to a star that it can escape the cluster entirely. Although evaporation has a long timescale it can limit the cluster lifetime. The timescale of evaporation grows with cluster mass (e.g. [Spitzer 1940](#); [Spitzer & Harm 1958](#); [Spitzer 1987](#); [Lamers et al. 2005](#); [Gieles & Baumgardt 2008](#)) and it is the dominant mass-loss mechanism in gas-poor environments.

Shocks occur when a cluster orbits in a galactic potential that is not smooth and because a realistic galaxy contains a high amount of substructure, a cluster is subject to a non-negligible number of shocks in its lifetime. The shocks can occur due to giant molecular clouds ([Gieles et al. \(2006\)](#); [Lamers & Gieles \(2006\)](#)), spiral arm passages ([Gieles et al., 2007](#)), passages through the galaxy disc ([Gnedin & Ostriker, 1997](#); [Kruijssen & Portegies Zwart, 2009](#); [Webb et al., 2014](#)) and interactions with galaxy merger induced substructure ([Kruijssen et al., 2012b](#)). The disruption timescale associated with tidal shocks decreases with strength of the shock and the density of the cluster ([Spitzer & Harm, 1958](#); [Gnedin et al., 1999](#); [Gieles et al., 2006](#); [Prieto & Gnedin, 2008](#); [Kruijssen et al., 2011](#); [Webb et al., 2019](#)).

Tidal shocks dominate in the gas-rich environments where GCs form ([Gieles et al., 2006](#); [Lamers & Gieles, 2006](#); [Elmegreen & Hunter, 2010a](#); [Kruijssen, 2012](#); [Miholics et al., 2017](#)). This has been termed the ‘cruel cradle effect’ ([Kruijssen et al., 2012a](#))

and clusters must escape their turbulent formation environment in order to survive (Kravtsov & Gnedin, 2005; Kruijssen, 2015). There have been a few ways put forward that aid GC survival such as orbit scattering by giant molecular clouds or spiral arms (Gustafsson et al., 2016) or internal (stellar or AGN feedback) or external (ram pressure stripping) galaxy quenching. Mergers are the most easily understood ways to remove GCs from their birth environments. During mergers clusters are tidally stripped from their host galaxy and enter the halo of the more massive galaxy but also the clusters in the main galaxy can be moved out into the halo during a minor or a major merger. A caveat here is that more massive, metal-rich galaxies have fewer galaxies that are of equal mass or more massive, therefore the clusters in these kinds of galaxies experience a longer time trapped in the gas rich disc and therefore fewer clusters survive (Kruijssen et al., 2019a). Once in the halo of a galaxy, disruption happens on timescales typically greater than a Hubble time and therefore we observe these old globular clusters in the haloes of galaxies today. The GC population in the halo may continue to grow as the galaxy accretes more lower-mass galaxies.

In conclusion, GC formation is a natural consequence of star formation in high pressure and density environments and is inevitable in most galaxies. However, whether we observe the GC in the local Universe depends on its survival. This is a crucial factor in GC studies, both observational and theoretical. With advancements in observational facilities such as the James Webb Space Telescope (JWST) direct detections of young, massive star clusters in high-redshift galaxies will become possible. However, it will be unclear whether or not the young massive star cluster can be considered a proto-GC because this will require accounting for the various disruption mechanisms described above.

1.5.3 Simulating GC and galaxy populations

Massive star clusters span a wide range of ages and are the products of intense star formation episodes in galaxies. Additionally, to be observed at $z = 0$ they must survive alongside the dynamical evolution of their host galaxy. Together this indicates

an intimate relationship between galaxy and GC formation and evolution. Therefore, modelling GCs requires a self-consistent treatment of the formation and subsequent disruption of star cluster populations in a fully cosmological environment.

There have been many modelling attempts of GC systems that consider one or two aspects of the problem at a time. For example, many works focused on the explanation of the colour bimodality of GC systems (e.g. [Côté et al. 1998](#); [Muratov & Gnedin 2010](#); [Tonini 2013](#); [Li & Gnedin 2014](#); [Renaud et al. 2017](#)). Others investigated the specific frequency of GC populations (e.g. [Côté et al. 1998](#); [Hilker et al. 1999](#); [Moore et al. 2006](#); [Mistani et al. 2016](#)) or the GC-halo mass relation (e.g. [Boylan-Kolchin 2017](#)). Some modelling techniques worked to investigate the formation efficiency of GCs across cosmic time and relate this to reionisation (e.g. [Katz & Ricotti 2014](#)) and others focused only on reproducing the properties of the Milky Way GC system (e.g. [Kravtsov & Gnedin 2005](#); [Prieto & Gnedin 2008](#); [Griffen et al. 2010](#); [Renaud et al. 2017](#)).

Ideally, direct simulations would be used, where the formation and evolution of individual GCs could be followed in a cosmological context over a Hubble time. These direct simulations are self consistent so there is no need for any subgrid physics or assumptions (e.g. [Li et al. 2017b](#); [Kim et al. 2018](#); [Lahén et al. 2019, 2020](#)). They consider different galactic environments from dwarf galaxies, including merging systems ([Kim et al., 2018](#); [Lahén et al., 2019](#); [Ma et al., 2020](#)) to Milky Way mass haloes ([Li et al., 2017b, 2018](#)). These studies require spatial resolution on scales of parsecs or smaller, this places strong computational constraints on the number of simulations, the volume size and the redshift range over which the simulations are evolved. Therefore these simulations often follow the the evolution of very small cosmological volumes over brief periods of time.

A different approach is to use semi-analytic methods (e.g. [Beasley et al. 2002](#); [Kruijssen 2015](#); [Choksi et al. 2018](#); [El-Badry et al. 2019](#)). These methods determine GC system properties through galaxy properties such as merger rates ([Li & Gnedin, 2014](#)), halo growth rates ([Choksi et al., 2018](#)) and average gas surface densities ([El-Badry et al., 2019](#)), often through the post-processing of dark matter only simulations to in-

clude baryons. This approach resolves any issues with the direct simulations having a lack of statistical power, as the cosmic evolution of a range of halo masses and environments can be studied with the computational requirements for running many merger trees being much smaller. However, this family of simulations require a number of simplifying assumptions such as the influence of the cosmic environment due to lack of a spatially resolved description of the galaxy and the inability to track full GC orbits. An additional drawback of these semi-analytic methods is the simplified description of GC disruption, usually only including evaporation, with some studies not including disruption at all (e.g. [Beasley et al. 2002](#); [El-Badry et al. 2019](#)).

Furthermore, another family of models use hydrodynamical, cosmological simulations of galaxy formation to select particles as GC candidates (e.g. [Renaud et al. 2017](#); [Halbesma et al. 2020](#); [Ramos-Almendares et al. 2020](#)). They then study the properties of the resulting GC population. Such GC populations can be biased depending on the particle selection criteria used.

To be able to model a statistically significant number of realistic GC and galaxy systems a compromise needs to be made. The E-MOSAICS simulations represent a fourth family of models ([Pfeffer et al., 2018](#); [Kruijssen et al., 2019a](#)) where a semi-analytic model of star cluster formation is coupled to a cosmological, hydrodynamic simulation. These simulations work from the hypothesis that GC populations are the survivors of YMC formation that occurs during intense star formation episodes. These simulations include the effects of the ISM on the type of YMCs that can form, as well as the effect of destruction of the young clusters, cluster migration out of the cluster-forming environment, two-body relaxation and the effects of mass loss due to tidal shocks. Also, the fraction of stars that form in clusters is also explicitly tied to the conditions of the host galaxy, with low star formation rate dwarf galaxies only forming a few percent of their stars in clusters to star bursts forming 50% of their stars in clusters (e.g. [Bastian 2016](#)).

The star clusters in the E-MOSAICS simulations are formed in a subgrid fashion. Subgrid physics is a way to describe any parameter on a scale that is smaller than the element of the simulation. In this case, it describes star clusters that have a mass smaller

than the mass of the stellar particle in the simulation. In this way the star clusters become a sub-component of the stellar particle, but are not individually resolved. This approach facilitates the simulation of multiple galaxies across a range of cosmic environments with only a small amount of extra computational expense from the simulation of star clusters. The details of these simulations are outlined in Section 2.1.

1.6 This thesis

This thesis aims to place globular cluster systems in the context of galaxy formation and evolution. In previous work a general picture has been built of the co-formation and evolution of galaxies and their GC populations. The general scenario is that, as gas cools in the centre of dark matter haloes at $z > 2$ the in-situ galaxy is built. Subsequently, lower mass galaxies are accreted into more massive haloes and an ex-situ galaxy component grows.

During the in-situ phase of galaxy formation, in the densest regions of galaxies, the progenitors of $z = 0$ GCs form in environments where the star formation rate is high. This formation takes place near the centres of what will become massive galaxies producing the red, metal-rich GC sub-populations. By contrast, low metallicity GCs are preferentially formed in low-mass dwarf galaxies, where the star formation rate is likely lower and the ISM cannot reach high metallicities. If accreted onto a massive galaxy, these GCs will form part of the blue, metal-poor halo GC population of the galaxy.

As described in this chapter, recent years have shown an emerging body of work which examines GCs not as individual resolved objects, but instead sees each one as part of a wide system that is intertwined with the host galaxy. With the advancement of large scale surveys there is a plethora of observational data to be examined, but simulations and thus theoretical understanding of such systems has lagged behind due to the demanding computational requirements. This thesis uses the state-of-the-art E-MOSAICS simulations (described in Chapter 2) to make steps towards bridging this gap. The E-MOSAICS simulations follow the formation and evolution of GCs in a

cosmological context, but cannot resolve individual clusters.

There is a range of work that examines the input physics of the E-MOSAICS simulations and compares and contrasts the outputs to observational data, this is described in Chapter 2. In Chapter 3, I contribute to this body of work by investigating the mass functions of GCs as a function of galaxy stellar mass and comparing this to the observational results of [Jordán et al. \(2007\)](#). The results in Chapter 3 and other works by the E-MOSAICS team show that the simulations produce realistic GC populations and therefore can be used to gain a deeper understanding of how these systems formed and assembled in the context of the formation of their host galaxy. This thesis examines four properties of GC systems in the context of the E-MOSAICS simulations to gain theoretical understanding. The four properties are the truncation mass of the GC mass function in relation to the host galaxy mass (Chapter 3), the ages and metallicities of GCs on stellar streams (Chapter 4), the α abundances of GCs and their relation to the field star population (Chapter 5) and the fraction of field stars that are contributed by disrupted GCs in the bulge of Milky Way mass galaxies (Chapter 5).

The E-MOSAICS simulations can be used as a test data set of other astrophysical methods and techniques that require the use of GCs. This has the advantage of knowing the ‘truth’ about the simulations. In this thesis, I take advantage of the realistic GC populations in the simulations and test the use of dynamical models with GCs as tracers (Chapter 6). This is to allow the user of such dynamical models to understand the requirements of the model in terms of the data quality and also to investigate if there are any biases in the model a user should be aware of before employing it to make scientific conclusions.

Together, the chapters in this thesis reveal the power of the simulations, firstly to provide explanation and understanding of the observed properties of GCs and secondly to provide data to test other models on. In Chapter 7 I present the conclusions of this work and discuss the future prospects.

Chapter 2

Methods

In this thesis Chapters 3, 4, 5 and 6 rely on the E-MOSAICS simulations. Additionally, Chapter 6 uses dynamical modelling techniques and Chapters 3 and 6 use the Markov Chain Monte Carlo technique to estimate parameters of a model. I therefore give an outline of all of these methods in this chapter for the reader to refer back to.

2.1 Simulations

For the purpose of this thesis we use the E-MOSAICS simulations. The E-MOSAICS (MOdelling Star cluster population Assembly in Cosmological Simulations within EAGLE, [Pfeffer et al. 2018](#); [Kruijssen et al. 2019a](#)) simulations follow the co-formation and evolution of galaxies and their GC populations in a cosmological context. This is achieved by combining the MOSAICS ([Kruijssen et al., 2011](#); [Pfeffer et al., 2018](#)) sub-grid model of stellar cluster formation and evolution into the software used to conduct the EAGLE (Evolution and Assembly of GaLaxies and their Environments, [Schaye et al. 2015](#); [Crain et al. 2015](#)) galaxy formation simulations as described in [Pfeffer et al. \(2018\)](#) and [Kruijssen et al. \(2019a\)](#). The simulations were initially a volume limited sample of 25 zoom-in simulations of Milky Way mass galaxies ($7 \times 10^{11} < M_{200}/M_{\odot} < 3 \times 10^{12}$). Re-simulations were preferred to follow the target galaxies at high resolution whilst remaining computationally efficient and therefore a volume

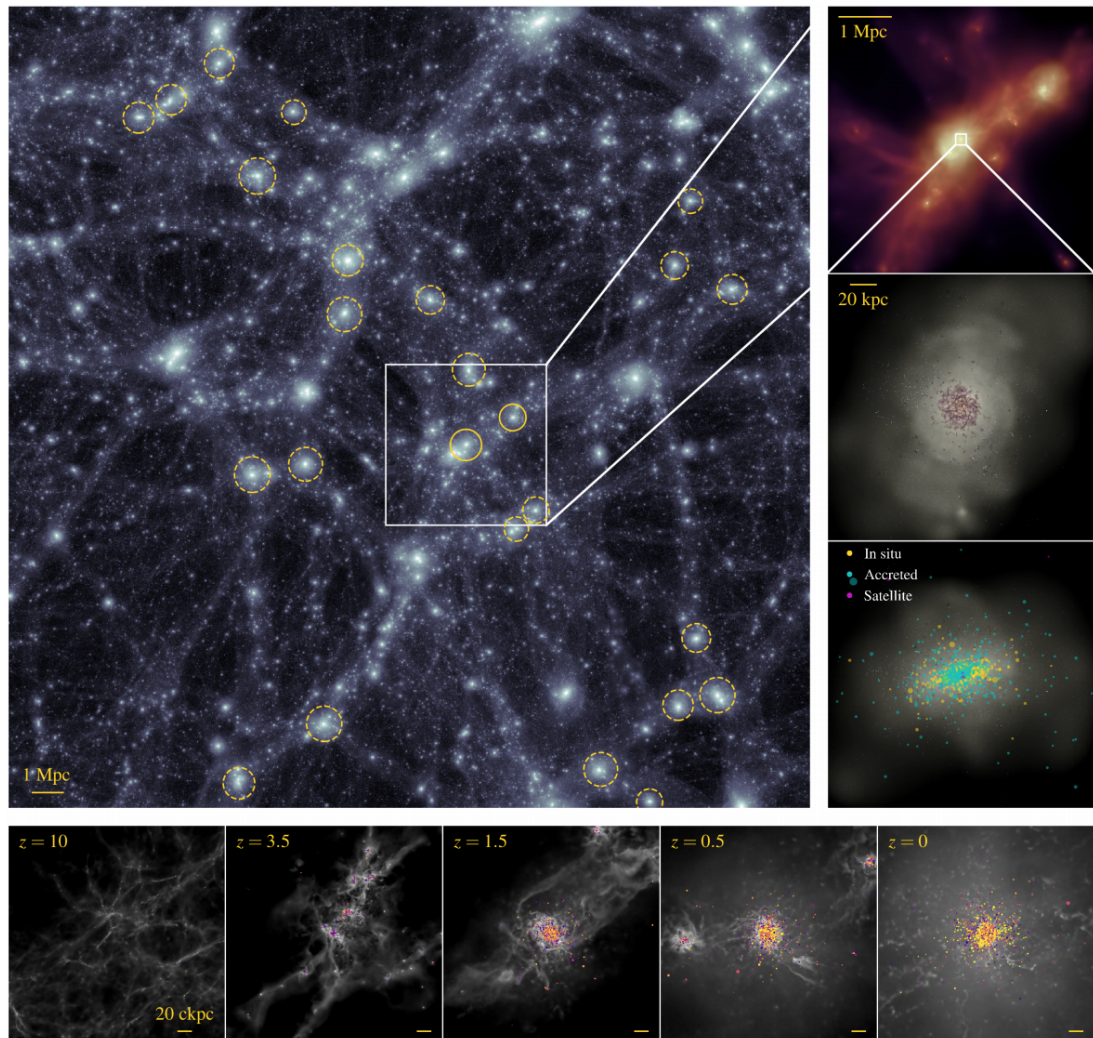


Figure 2.1: Figure 1 of [Kruijssen et al. \(2019a\)](#) to visualise the nature of the E-MOSAICS simulations. The main panel shows the dark matter distribution of the EA-GLE Recal-L025N0752 simulation at $z = 0$, the yellow circles highlight the 25 Milky Way-mass galaxies in the simulation. The two solid circles indicate the galaxies in the top right panel, which shows gas density coloured by temperature ($T = 10^5 - 10^6 K$, red to white). The two middle right panels show mock-optical images of one galaxy, with the bottom panel including GCs ($M > 5 \times 10^4$) as dots coloured by their origin. The bottom row visualises the assembly of the same galaxy and its star cluster population, with gas shown in grey scale and dots again showing the positions of the GCs, coloured by their metallicities ($-2.5 < [\text{Fe}/\text{H}] < 0.5$).

limited sample from EAGLE Recal-L025N0752 (introduced by [Schaye et al. 2015](#)) was taken. The initial conditions of the 25 zoom-ins were of similar resolution to the parent simulation and had an approximate initial gas particle mass of $m_g = 2.25 \times 10^5$ and high resolution dark matter particle mass of $m_{dm} = 1.2 \times 10^6$. More recently a 34 Mpc^3 volume has been simulated. This ‘volume’ simulation was initialised with more than 1 billion dark matter and gas particles meaning it has the same resolution as the zoom-in simulations (Crain et al., in prep.). This larger simulation gives the opportunity to analyse galaxies of different masses and also galaxy groups and clusters. For each simulation, 29 snapshots are saved between $z = 20$ and $z = 0$. The 25 Milky Way-mass E-MOSAICS simulations are visualised in Fig. 2.1 where the main panel shows the dark matter distribution of the EAGLE Recal-L025N0752 simulation at $z = 0$, where the large-scale structure of the universe can be seen, the yellow circles highlight the 25 Milky Way-mass galaxies in the simulation suite. The top right panel shows gas density coloured by temperature (purple to white hues represent temperatures of $T = 10 - 10^{5.5} \text{ K}$ respectively), here it can be seen that the two galaxies are already undergoing an interaction, they are connected by a gas bridge. The two middle right panels show mock-optical images of one galaxy, with the bottom panel including GCs ($M > 5 \times 10^4$) as dots coloured by their origin, shells and streams can be identified and GCs that have been accreted have a more extended spatial distribution, highlighting the hierarchical nature of galaxy formation. The bottom row visualises the assembly of the same galaxy and its star cluster population, with gas shown in grey scale and dots again showing the positions of the GCs, coloured by their metallicities ($-2.5 < [\text{Fe}/\text{H}] < 0.5$). This row shows clearly that accretion of smaller mass galaxies with their own GCs is taking place, resulting in a growth of the GC population.

2.1.1 EAGLE

EAGLE is a set of hydrodynamical simulations of the formation of a cosmologically representative sample of galaxies in a Λ CDM cosmogony, meaning that a wide range of galaxy environments are sampled. The simulations use a heavily-modified version of the smoothed particle hydrodynamics (SPH) code GADGET3 (last described by

Springel 2005). The main modifications are to the hydrodynamics algorithm, the time-stepping criteria (see Schaye et al. 2015 for more detail), and the addition of a suite of sub-grid models which govern processes acting on scales below the simulation’s numerical resolution. Schaller et al. (2015) investigates the impacts of these modifications on the EAGLE galaxy population. The routines include sub-grid radiative cooling (Wiersma et al., 2009), star formation (Schaye & Dalla Vecchia, 2008), stellar feedback (Dalla Vecchia & Schaye, 2012), chemical evolution (Wiersma et al., 2009), gas accretion onto, and mergers of, super massive black holes (BHs) (Rosas-Guevara et al., 2015; Schaye et al., 2015) and active galactic nuclei (AGN) feedback (Booth & Schaye, 2009; Schaye et al., 2015). EAGLE tracks the abundances of the 11 elements most important for radiative cooling (H, He, C, N, O, Ne, Mg, Si, S, Ca, Fe). The efficiency of the stellar feedback and the BH accretion is included in the simulation calibration to match the $z = 0$ galaxy stellar mass function and the sizes of disc galaxies, and the AGN feedback is calibrated to produce the known relationship between the BH mass and the galaxy stellar mass. The standard resolution EAGLE simulations yield a galaxy stellar mass function that reproduces the observed function to within 0.2 dex over the well-sampled and well-resolved mass range. The simulations also reproduce other observables, such as the galaxy specific star formation rates and the total stellar mass of galaxy clusters. For a full description of the models, see Schaye et al. (2015).

To follow the formation of a galaxy halo, the SUBFIND algorithm (Springel et al., 2001; Dolag et al., 2009) is used to identify subhaloes (galaxies) in the simulations. Dark matter structures are first identified using the friends-of-friends (FoF) algorithm (Davis et al., 1985), with a linking length 0.2 times the mean interparticle separation. Then, gas, star and black hole particles are associated with the FoF group of their nearest dark matter particles. SUBFIND then identifies the substructures that are gravitationally bound within the FoF groups.

Once haloes and subhaloes have been identified, merger trees can be constructed. These trees allow the user of these simulations to understand exactly how that galaxy formed and where its stars and GCs were born. For EAGLE and the E-MOSAICS

volume these merger trees were created with the D-trees algorithm (Jiang et al., 2014) to locate the most bound particle of a subhalo. Qu et al. (2017) then look for this most bound particle in candidate descendant subhalos for up to five of the following snapshots. Using the most bound particle of a subhalo means that it can be identified even when the outermost particles have been stripped. For the E-MOSAICS Milky Way-mass zoom-in simulations Pfeffer et al. (2018) creates subhalo merger trees by following the method in Jiang et al. (2014) and Qu et al. (2017).

2.1.2 E-MOSAICS

Modelling star cluster systems requires treatment of the star cluster formation, evolution and disruption processes. E-MOSAICS adopts a star cluster formation model based on observations of young star clusters, under the assumption that young star clusters, GCs and open clusters have a common formation mechanism (Portegies Zwart et al., 2010; Longmore et al., 2014; Kruijssen, 2015; Bastian, 2016). E-MOSAICS couples a semi-analytic model of star cluster formation to the EAGLE simulation in a subgrid manner.

Star cluster formation

Whenever a stellar particle is formed in the simulations, some fraction of the stellar mass is considered to reside in bound clusters. The fraction of the mass that is assigned to cluster formation is regulated by the local cluster formation efficiency (CFE, Bastian 2008) and is dependant on the local natal gas pressure (Kruijssen, 2012). Once the fraction of mass for cluster formation has been determined, initial cluster masses are stochastically sampled from a Schechter initial cluster mass function (Schechter, 1976) of the form given in Eq. (1.1). The truncation mass, $M_{c,*}$, of the Schechter function is environmentally dependant (Reina-Campos & Kruijssen, 2017)¹. The Reina-Campos & Kruijssen (2017) model assumes that $M_{c,*}$ is proportional to the mass of

¹So as to not impose an upper limit on the cluster mass, the cluster masses are allowed to exceed the mass of the particle. This is justified because occasionally, the truncation mass of the ICMF exceeds the mass of a stellar particle in these high resolution simulations.

Table 2.1: Properties of the 25 simulated Milky Way-mass, L^* galaxies at $z = 0$. The number of GCs includes all GCs with a mass greater than $10^5 M_\odot$.

Name	$\log M_{200}$	$\log M_*$	N_{GC}
MW00	11.95	10.28	252
MW01	12.12	10.38	642
MW02	12.29	10.56	841
MW03	12.17	10.42	547
MW04	12.02	10.11	264
MW05	12.07	10.12	951
MW06	11.96	10.31	441
MW07	11.86	10.16	251
MW08	11.87	10.12	200
MW09	11.87	10.16	255
MW10	12.36	10.48	1012
MW11	12.15	10.06	205
MW12	12.34	10.44	1013
MW13	12.38	10.37	280
MW14	12.34	10.59	827
MW15	12.16	10.15	551
MW16	12.32	10.54	504
MW17	12.29	10.49	337
MW18	12.25	10.00	121
MW19	12.20	9.93	108
MW20	11.97	10.10	385
MW21	12.12	10.03	181
MW22	12.15	10.43	365
MW23	12.19	10.53	711
MW24	12.06	10.29	340

the molecular cloud from which the star clusters form (Kruijssen, 2014), however, the simulations do not have the necessary resolution to model the molecular clouds. Therefore the masses are set by the largest gravitationally unstable mass in a differentially-rotating disc, i.e. the Toomre (1964) mass. In the models, the maximum gas mass that can collapse may decrease if the stellar feedback timescale is shorter than the gravitational collapse timescale. In the feedback limited regime $M_{c,*}$ increases with the natal gas pressure, but may decrease outside of this regime, i.e. near the centres of galaxies. Pfeffer et al. (2019b) compare the $M_{c,*}$ of young star cluster populations in the E-MOSAICS simulations with observations and find good agreement. There is a scatter in $M_{c,*}$ for the simulated galaxies at fixed star formation rate and more observations of systems with young star clusters are needed to test whether this scatter in

the simulations is consistent with observed systems.

Once formed the clusters inherit the age, metallicity, position and velocity of their parent stellar particle. Although some open clusters can have masses of just $10M_{\odot}$ the minimum mass of a globular cluster is 10^4M_{\odot} (Janes, 2000) therefore clusters with masses less than 10^3M_{\odot} are not evolved in these simulations, this reduces memory requirements.

Star cluster evolution

Clusters lose mass in the simulations by stellar and dynamical evolution. For the dynamical evolution, mass loss is included via two-body relaxation and tidal shocks. The total mass-loss rate for a cluster is the sum of the contribution from stellar evolution, two body relaxation and tidal shocks (Pfeffer et al., 2018),

$$\left(\frac{dM}{dt}\right) = \left(\frac{dM}{dt}\right)_{ev} + \left(\frac{dM}{dt}\right)_{rlx} + \left(\frac{dM}{dt}\right)_{sh}, \quad (2.1)$$

the clusters are evolved down to a minimum mass of $100M_{\odot}$ before they are assumed to be completely disrupted. Dynamical mass loss from a cluster is added back to the field star mass of the stellar particle.

The mass loss from stellar evolution in the GCs includes supernovae and stellar winds and it is proportional to that of their host star particle (Wiersma et al., 2009). Therefore the stellar evolution mass loss is encapsulated in one term in Eq. 2.1. Stellar mass loss is computed after dynamical mass loss such that it is not double-counted. A detailed description of stellar cluster mass loss is provided in Section 1.5.2, we discuss it here in the context of the simulations.

Two body relaxation occurs when two stars pass each other in the cluster. From this close encounter energy can be exchanged and occasionally one star gains enough energy to escape the cluster entirely. Two body relaxation timescale increases with cluster mass and therefore the mass-loss rate from two body relaxation in the simulations is determined by the current cluster mass and the local tidal field of the parent stellar

particle.

A tidal shock occurs when the cluster passes a large mass over a time much shorter than the dynamical timescale of the cluster. The gravitational force of the mass imparts some energy into the cluster causing it to expand and lose some of its outer stars. The mass-loss rate due to tidal shocks is dependant on the density of the cluster, and includes a correction factor for the damping of the energy injection by adiabatic expansion. The implementation of relaxation and tidal shocks are calibrated to N-body simulations of GCs ([Kruijssen et al., 2011](#)).

These mass-loss mechanisms are implemented on-the-fly, an extra process that is treated in post-processing is dynamical friction. Dynamical friction must be treated this way because stellar particles may host clusters of different masses, resulting in a range of dynamical friction timescales for a single particle. The dynamical friction timescale is calculated for all clusters at each simulation snapshot and clusters can be completely removed by dynamical friction when the dynamical friction timescale is less than the age of the cluster.

Uses and observational comparisons

The E-MOSAICS simulations have reproduced a range of observed properties of both young and old GCs. For example, the range in the number of GCs is consistent with observed ones in the MW and M31. This is discussed in more detail in [Kruijssen et al. \(2019b\)](#), where the number, metallicity distributions, and spatial density profiles of the populations are explicitly compared to the observed values of the MW and M31. The radial distribution of the birth pressure of the clusters matches that of the observations of [Leroy et al. \(2008\)](#) ([Pfeffer et al., 2018](#)). The CFE radial distribution is similar to the observed distributions of [Silva-Villa et al. \(2013\)](#); [Johnson et al. \(2016\)](#) and the global CFE at $z=0$ of all the galaxies shows the same range as that observed (1-50%, e.g. [Adamo et al., 2015](#); [Johnson et al., 2016](#)) ([Pfeffer et al., 2018](#)). The simulations also reproduce and provide explanation for the existence of a 'blue tilt' in GC populations ([Usher et al., 2018](#)), as well as reproduce the fraction of disrupted GC stars in the bulge

(Hughes et al., 2020) and the halo (Reina-Campos et al., 2018, 2020) of the Milky Way. Additionally, the simulations have shown that the irregularity in age-metallicity relations of local group galaxies can be reproduced by different formation histories and can subsequently be used to infer such formation histories (Kruijssen et al., 2019a,b, 2020). The simulations have also been used to conclude that GCs associated with stellar streams will be, on average, younger than the GC population not associated with a stellar stream (Hughes et al., 2019), a result subsequently confirmed through observations of stellar streams in the halo of M31 (Mackey et al., 2019). The ages of the GCs in the E-MOSAICS simulations reproduce those of observed systems, for example Reina-Campos et al. (2019) show that not only are the median ages of MW and extragalactic GCs reproduced, but also the observed age offset between metal-poor and metal-rich GCs (e.g. Brodie & Strader, 2006; Forbes et al., 2015). In addition, the E-MOSAICS galaxies are consistent with the specific frequency and spatial distribution of GCs in the Milky Way (Kruijssen et al., 2019b).

Although many properties of GC populations are reproduced, the number density of low mass clusters in E-MOSAICS is over predicted. This is due to the lack of a cold, dense gas phase in the EAGLE model, which would disrupt many of these clusters (as discussed in Pfeffer et al. 2018) and it will be addressed in a future generation of models. The chapters in this thesis take steps to reduce the effect of this under-disruption problem. Although under-disruption may also effect some of the high-mass GCs ($M/M_{\odot} > 10^{5.5}$), the high mass-end of the simulated GC mass functions are in agreement with observations from the Milky Way and M31 (Pfeffer et al., 2018).

2.2 Dynamical modelling

The movement of the stars in a stellar system trace the underlying potential in which they orbit, therefore by studying their dynamics we can determine how much mass is present and where it is located. Chapter 6 of this thesis uses dynamical modelling techniques to determine the dark matter mass distribution in 25 Milky Way zoom-in simulations. Here we give an outline of dynamical modelling techniques.

2.2.1 Assumptions and important concepts

The fundamental assumption in dynamical modelling of galaxies is that they are collisionless. Thus, the orbit of a star can be determined by assuming the system's mass is smoothly distributed in space, rather than concentrated into point-like sources. Galaxies can be considered collisionless because their relaxation time is much larger than the age of the Universe (e.g. [Binney & Tremaine 1987](#)).

A galaxy can contain billions of stars and modelling the position and orbit of each one is not practical. Therefore, all the information contained in a dynamical model can be summarised into the distribution function (DF) $f(x, v)$. The DF describes the density of stars over position (x), velocity (v) and time, also known as the phase-space density of the galaxy. This function must remain positive for a physical model.

The time-evolution of the DF is governed by the fundamental relation known as the collisionless Boltzmann equation and the Jeans theorem ([Jeans, 1915](#)) states that any steady-state solution of the collisionless Boltzmann equation depends on the phase-space coordinates only through integrals of motion in the given potential. An integral of motion is defined as a function of the phase-space coordinates that remains constant along any orbit.

In the case of axisymmetric potentials, which are relevant for the work in this thesis, the classical integrals of energy and angular momentum (E and L_z respectively) remain constant in all orbits. Therefore, given the Jeans theorem, it is acceptable to describe axisymmetric systems by considering two-integral DFs. However, it is often found that for astrophysically relevant axisymmetric potentials most orbits allow for an additional non-classical integral, the so-called 'third integral'. This integral, in general, does not have an analytic expression and hence it is necessary to resort to more sophisticated numerical orbit-superposition methods in order to study these kind of systems.

Orbit-superposition dynamical modelling techniques, also known as Schwarzschild modelling are very flexible due to their orbit-superposition nature and therefore require fewer assumptions of the DF. The method consists of assuming the total gravitational

potential, then computing a large number of orbits in such a potential (of the order $10^3 - 10^5$ orbits) so they have a good sampling of the phase-space. Then the orbits are weighted to reproduce observed kinematics of a tracer population. This technique has been used to model kinematic data sets, with the aim of determining the dynamical structure, mass distribution and dark matter fraction of nearby early-type galaxies (e.g. [Thomas 2010](#); [Poci et al. 2019](#)). Additionally, made-to-measure methods also return a physical solution without having to specify the distribution function. Made-to-measure dynamical models can be even more flexible than Schwarzschild models because there is no need to specify the parameterised form of the gravitational potential (e.g. [Gajda et al. 2021](#)). The drawback of these numerical techniques is that they are very computationally expensive and so far discrete versions of the models are not available and therefore data sets have to be spatially binned. For the purposes of the work in this thesis, where we wish to use GCs as tracers of the underlying potential we use Jeans modelling techniques. Jeans modelling techniques, although less sophisticated than orbit modelling techniques, are computationally faster. They have also been expanded for the use of discrete data sets ([Watkins et al., 2013](#)). In this thesis we aim to test how well the discrete Jeans modelling method performs on 25 Milky Way zoom-in simulations, when GCs are used as the tracers for the underlying galactic potential.

2.2.2 Jeans modelling

As discussed, the DF of a system in a steady state must satisfy the collisionless Boltzmann equation. For a stellar system consisting of a large number of stars, with a distribution function (DF) $f(\mathbf{x}, \mathbf{v}, t)$, moving under a smooth gravitational potential $\Phi(\mathbf{x}, t)$, the collisionless Boltzmann equation (using summation convention with $i=1$ to 3) can be written as

$$\frac{\partial f}{\partial t} + v_i \frac{\partial f}{\partial x_i} - \frac{\partial \Phi}{\partial x_i} \frac{\partial f}{\partial v_i} = 0. \quad (2.2)$$

$f(\mathbf{x}, \mathbf{v}, t)$ is a function of seven variables (3 position, 3 velocity variables and one time variable) and so a large amount of variable combinations satisfies the collisionless Boltzmann equation. Therefore, the Jeans modelling approach to drastically reducing

the problem and one that leads to the Jeans equations is take moments of the collisionless Boltzmann equation. The zeroth moment is obtained by integrating equation 2.2 over $d^3\mathbf{v}$. After some manipulation the zeroth moment equation becomes

$$\frac{\partial\nu}{\partial t} + \frac{\partial}{\partial x_i}(\nu\bar{v}_i) = 0, \quad (2.3)$$

where ν is the probability density of stars. The first moment is obtained by multiplying equation 2.2 by v_j and then integrating over $d^3\mathbf{v}$. After combining the zeroth and first moment of the collisionless Boltzmann equation we arrive at

$$\nu\frac{\partial\bar{v}_j}{\partial t} + \nu\bar{v}_i\frac{\partial\bar{v}_j}{\partial x_i} = -\nu\frac{\partial\Phi}{\partial x_j} - \frac{\partial}{\partial x_i}(\nu\sigma_{ij}^2), \quad (2.4)$$

where I have introduced the stress tensor $\sigma_{ij}^2 = \overline{v_i v_j} - \bar{v}_i \bar{v}_j$. In this form, this equation resembles the Euler equation of fluid mechanics with σ_{ij}^2 playing the role of an anisotropic pressure term

Equation 2.4 in cylindrical coordinates, assuming axisymmetry and given a steady state becomes the two Jeans equations:

$$\frac{\overline{\nu v_R^2} - \nu\overline{v_\phi^2}}{R} + \frac{\partial(\overline{\nu v_R^2})}{\partial R} + \frac{\partial(\overline{\nu v_R v_z})}{\partial z} = -\nu\frac{\partial\Phi}{\partial R}, \quad (2.5)$$

$$\frac{\overline{\nu v_R v_z}}{R} + \frac{\partial(\overline{\nu v_z^2})}{\partial z} + \frac{\partial(\overline{\nu v_R v_z})}{\partial R} = -\nu\frac{\partial\Phi}{\partial z}. \quad (2.6)$$

These Jeans equations are still quite general and still depend on four unknown variables ($\overline{v_R^2}$, $\overline{v_z^2}$, $\overline{v_\phi^2}$ and $\overline{v_R v_z}$). To further reduce the problem the shape and orientation of the velocity ellipsoid is assumed, this allows two of the four variables to be expressed as a function of another one and provides a unique solution for the remaining two variables. The common ‘semi-isotropy’ condition choice is that of a spherically aligned velocity ellipsoid. This means that if the velocities of the stars are plotted in spherical coordinates (v_r, v_θ, v_ϕ) and an ellipsoid was fitted it would not be tilted relative to the axis. An alternative choice is that of a cylindrically aligned velocity ellipsoid (v_R, v_ϕ, v_z) .

[Cappellari et al. \(2007\)](#) show that a cylindrically aligned velocity ellipsoid provides a good description of fast rotator galaxies and that this may be due to the presence of discs. Therefore, the cylindrical orientation is appropriate to describe the dynamics of the disc galaxies used in Chapter 6, this is known as the Jeans Anisotropic Model.

Jeans Anisotropic Modelling (JAM)

The Jeans Anisotropic Model (JAM) requires solving the Jeans equations under the following assumptions: (i) axial symmetry and (ii) the velocity ellipsoid is aligned with the cylindrical coordinate system.

To derive the solutions for these Jeans equations [Cappellari \(2008\)](#) made the explicit choice to parameterise the stellar and the total density as a Multi Gaussian Expansion (MGE) ([Monnet et al., 1992](#); [Emsellem et al., 1994](#); [Cappellari, 2002](#)). The MGE formalism can then be used to deproject the projected surface brightness into the three-dimensional intrinsic density profile, assuming the inclination of the galaxy. [Jeans \(1922\)](#) showed that the Jeans equations can be used to model the kinematics of different dynamical tracers, as long as they move in the same potential. It is therefore possible to fit the tracer density with a MGE and write solutions to the Jeans equations for each Gaussian component of the tracer density. This allows for the modelling of anisotropy gradients or to model subcomponents of galaxies separately.

Therefore, as inputs the JAM model requires the potential density and the tracer density, both parametrised as a MGE. The potential density of a galaxy contains contributions from both the visible and dark matter. A MGE can be fitted to the luminous part directly, for the dark contribution a parameterised form must be assumed. The JAM model predicts the second moment of the velocity distribution based on the MGEs it has received as inputs. The likelihood that the assumed potential MGE can lead to the observed velocity distribution is calculated and subsequent modifications to the potential can be made. This is an iterative procedure that works to maximise the likelihood that the assumed potential produces the observed velocities. Jeans models can lead to fits that have unphysical distribution functions. However, they have the advantage that

they can be efficiently implemented allowing a wide range of models to be explored.

One major application of the JAM method was by Cappellari (2012) who used JAM to analyse 260 early-type galaxies from the ATLAS^{3D} survey and found that there is systematic variation of the initial mass function with mass-to-light ratio. Cappellari et al. (2015) combined observations from the SLUGGS and ATLAS^{3D} surveys to map out the stellar kinematics in two-dimensions. They study the total mass-density profiles of 14 fast-rotator early-type galaxies. This was the first homogeneous and detailed analysis of total-mass profiles using large-scale stellar dynamics. This was made possible through the availability of two-dimensional stellar kinematics and a fast and widely applicable dynamical modelling technique. JAM models have also been used to interpret the SAMI (Scott et al., 2015) and MaNGA (Li et al., 2018) surveys. JAM models are ideal to apply to statistically significant samples of galaxies due to their simplicity and therefore computational speed.

The JAM method makes several simplifications and assumptions, it is therefore important to know how well it represents the galaxies it models and if there are any biases in the results. Li et al. (2016) test the ability of the JAM method to recover galaxy characteristics of 1413 galaxies in the Illustris simulations. They find that within 2.5 R_e the JAM model recovers the total mass distribution within 10% (increasing to 18% for prolate galaxies). Li et al. (2016) are unable to accurately separate their total mass estimate into a dark and stellar matter component with size and shape of the galaxy determining whether there is an under- or over-estimation of the stellar mass. They also find that the accuracy of the mass recovery depends on the inclination, with galaxies with inclinations lower than 60° having high errors in the inclination and anisotropy recovery.

A limiting factor for many dynamical modelling techniques is the need to spatially bin the data and compare the velocity moments in each of the bins with the velocity moments predicted by a theoretical model. Binning methods suffer from the loss of information because in order to estimate the first and second velocity moments an average of 50 stars per bin is usually required (Watkins et al., 2013). When using GCs as tracers for a dynamical model their spatial distribution and numbers do not lend

themselves to a binned approach. However, [Watkins et al. \(2013\)](#) developed existing JAM modelling to directly fit discrete data using maximum likelihood methods. These discrete dynamical models have been used to model the resolved stellar population of some GCs and allow for the inclusion of a contaminant population (e.g. [Watkins et al. 2013](#); [Hénault-Brunet et al. 2019](#)), meaning that information is not lost by making hard cuts on kinematic or spatial properties and instead assigning a probability that the star belongs to the cluster.

For the purposes of the work in this thesis Jeans models are ideal because a tracer population that does not need to be spatially binned can be implemented and the models are computationally fast enough to apply them to a sample of galaxies.

2.3 The Markov-Chain-Monte-Carlo technique

Many dynamical modelling techniques require an iterative approach. Whereby the unknown parameters are assumed, the dynamical model is constructed with such parameters and then compared to the data. Modifications are then made to the parameters and the model is re-constructed and compared, this then continues until the model matches well to the data, usually quantified through a minimisation of the χ^2 or maximisation of the likelihood.

For the work in Chapter 6 of this thesis we use a Markov-Chain-Monte-Carlo (MCMC) technique to present the most likely parameters for the JAM model and for the work in Chapter 3 we use an MCMC to find the most likely parameters of a Schechter function. MCMC works with Bayesian statistics, which in turn works with probability distributions, where instead of just representing the values of a parameter, the distribution describes our beliefs about a parameter (e.g. [Jeffreys 1939](#); [Jaynes & Bretthorst 2003](#); [Gregory 2005](#)). There are three main distributions in a Bayesian approach: a prior, a likelihood and a posterior.

The probability distribution functions are related via Baye's theorem,

$$P(\theta|D) = \frac{P(D|\theta)P(\theta)}{P(D)}, \quad (2.7)$$

where θ is the model parameters and D is the data. The prior distribution ($P(\theta)$) is the distribution representing the beliefs about a parameter, prior to seeing any data. The likelihood distribution ($P(D|\theta)$) then summarises what the observed data is telling us, by representing a range of parameter values accompanied by the likelihood that each value explains the data. The prior distribution and the likelihood distribution can then be combined to determine the posterior distribution ($P(\theta|D)$). This tells us which parameter value maximises the probability of observing the particular data that we did, taking into account our prior beliefs. Finally, $P(D)$ is a normalisation factor, sometimes called the evidence. The set of parameters that maximise the likelihood is the parameter set that reproduces the data most closely.

Monte Carlo simulations are a way of estimating a parameter by generating many random numbers, they provide an approximation of a parameter where calculating it directly is either impossible or computationally expensive. Markov chains are sequences of events where each event comes from a set of outcomes and each outcome determines what occurs next (e.g. ([Metropolis et al., 1953](#))). Importantly, Markov chains contain everything that you would need to predict the next step in the current state, meaning that there is no need to store the history of events. Andrey Markov showed that even interdependent events, if they are subject to fixed probabilities, conform to an average. Therefore Markov chains can be used to model the general tendency of a parameter if the probabilities that govern its behaviour are well understood.

MCMC methods are then a combination of the Monte Carlo simulation technique and Markov chains ([Metropolis et al., 1953](#)). To begin, MCMC methods require a first guess at a parameter value. The Monte Carlo part then continues to generate random values, but subject to a prerequisite on what makes a good parameter value- this is the Markov chain part. It is possible to compute how likely each value is to explain the data, given the prior beliefs. If the randomly generated parameter value is more likely

than the last one, it is definitely added to the chain of parameter values and the next step is taken. However, since a posterior probability distribution function is required, sometimes a step is accepted even if the likelihood is less than the previous step. If the current parameter is θ_0 and the proposed next step is θ then the acceptance probability is calculated by dividing the two posteriors,

$$P_{\text{accept}} = \frac{P(D|\theta)P(\theta)}{P(D|\theta_0)P(\theta_0)}, \quad (2.8)$$

then even if the probability of the current parameter value is twice as large as the proposed value, there's a 50 per cent chance of moving there. So, regions of high posterior probability are visited relatively more often than those of low posterior probability.

Since the random parameter values are subject to fixed probabilities they tend to converge, after a number of steps in the Markov chain, in the region of highest probability for the parameter of interest. After convergence, MCMC sampling yields a set of points which are samples from the posterior distribution. Of particular use in multi-dimensional problems, MCMC can be used to estimate the posterior distribution of more than one parameter ([Sharma, 2017](#)).

Chapter 3

The physics governing the upper truncation mass of the globular cluster mass function

3.1 Introduction

The luminosity, or mass function of globular clusters (GCs) is one of the most fundamental observables to link the formation of star clusters to ‘normal’ star formation processes. Traditionally, the GC luminosity function has been modelled as a lognormal distribution that appears to peak at the same magnitude in all environments, corresponding to a turnover mass of $M_{\text{TO}} \approx 2 \times 10^5 M_{\odot}$ (e.g. [Brodie & Strader 2006](#)). It is found that the mass function of GCs can be described by a single power law ([Harris & Pudritz, 1994](#)) or perhaps a power law with an exponential truncation ([Schechter, 1976](#); [Burkert & Smith, 2000](#); [Portegies Zwart et al., 2010](#); [Krumholz et al., 2019](#)).

Some works have disputed the presence of a truncation (or Schechter mass) for GCs in some galaxies, instead concluding that a single power law is the preferred form of the GC mass function ([Chandar et al., 2014, 2016](#); [Mok et al., 2019](#)). On the other hand, there have been multiple works corroborating the finding of a truncation mass

in the GC mass function of many galaxies, especially for young cluster populations. For example, [Bastian et al. \(2012\)](#) used spectroscopic measurements to find GC mass functions for multiple galaxies of different morphologies and masses, all of which are consistent with having truncation in their GC mass functions. [Johnson et al. \(2017a\)](#) robustly showed that there is a truncation mass in the YMC mass function of M31 and [Messa et al. \(2018\)](#) showed, using cumulative mass functions, that a power law is a poor fit for YMCs in M51. Additionally, [Adamo et al. \(2015\)](#) find that a Schechter function best describes the shape of the initial cluster mass function of young clusters in M83. Interestingly, they also find that $M_{c,*}$ decreases with increasing galactocentric radius, showing that there is a strong environmental dependence of the truncation mass.

Observations of GC mass functions help to clarify the relative importance of early evolution versus longer-term dynamical mass loss, and how both of these are effected by galaxy mass and environment ([Elmegreen & Hunter, 2010b](#); [Kruijssen et al., 2011](#); [Kruijssen, 2015](#)). For example, young massive clusters (YMCs) have mass functions that steeply rise towards lower masses, far exceeding the number of low-mass GCs observed at $z = 0$. If we take the view that the GCs we observe today formed in a similar way to the YMCs forming in the local Universe then the mass function must have been transformed in some way at the low mass end. To explain this we have to take into account that the old GCs we observe at $z = 0$ are the surviving population of those initially formed. Therefore a strong possibility to explain the transformation in the mass function is a preferential destruction of low mass star clusters by dynamical processes (e.g. [Okazaki & Tosa 1995](#); [Baumgardt 1998](#); [Vesperini 1998](#); [Fall & Zhang 2001](#); [de Grijs et al. 2003](#); [Goudfrooij 2004](#); [Gieles et al. 2006](#); [Elmegreen 2010](#); [Kruijssen et al. 2012b](#)).

At the high-mass end of the initial cluster mass function, [Harris & Pudritz \(1994\)](#) hinted at a break in the mass function of GCs. It was also suggested that $M_{c,*}$ in a particular galaxy would change depending on the galaxy's star formation rate, meaning that $M_{c,*}$ would be greater in galaxies with higher star formation rates ([Gieles et al., 2006](#); [Larsen, 2009](#); [Bastian et al., 2012](#); [Johnson et al., 2017a](#)). [Reina-Campos & Kruijssen \(2017\)](#) predict that the high mass end of the GC mass function does not de-

pend on the absolute star formation rate, but instead is set by a combination of galactic dynamics and stellar feedback, resulting in an effective scaling with the gas and star formation rate surface densities. It is only when accounting for the interplay between both mechanisms that they can reproduce the observed trends of $M_{c,*}$ with galactocentric radius.

Many of the works in the literature focus on the initial cluster mass function and therefore fit functions to only the youngest clusters in the galaxy, whereas this chapter investigates the mass function of evolved GC populations. There are fewer observational studies on the evolved mass or luminosity functions of GCs, however many works have concluded that an evolving single power law does not describe the high-mass end well (e.g. [Fall & Zhang 2001](#); [Vesperini et al. 2003](#); [Jordán et al. 2007](#); [Kruijssen & Portegies Zwart 2009](#)).

[Jordán et al. \(2007\)](#) analysed the luminosity and mass function of evolved GCs observed by the ACS Virgo Cluster Survey to investigate the dependence of the GC luminosity and mass function on galaxy stellar mass. They find that the luminosity function of the GCs becomes narrower with decreasing galaxy stellar mass. The mass function shows a decreasing $M_{c,*}$ value with decreasing galaxy mass. They argue that the behaviour at the high mass end of the GC mass function is a consequence of systematic variations of the initial cluster mass function rather than long-term dynamical evolution.

This chapter compares the relation between $M_{c,*}$ and galaxy mass in the E-MOSAICS simulations ([Pfeffer et al. 2018](#); [Kruijssen et al. 2019a](#)) to that found by [Jordán et al. \(2007\)](#). The E-MOSAICS simulations trace the formation and evolution of GC populations alongside galaxy formation and evolution, and enables the investigation into the impact of various galaxy properties on the resulting GC observables. Specifically for this chapter, I use the simulations to explore how GC formation environment and GC mass loss play a role in initialising and evolving the GC mass function. Previously, the E-MOSAICS simulations have been shown to reproduce and provide an explanation for a range of observed properties of both young and old GCs, such as the existence of a ‘blue tilt’ in GC populations ([Usher et al., 2018](#)), as well as the fraction

of disrupted GC stars in the bulge (Hughes et al., 2020) and the halo (Reina-Campos et al., 2018, 2020) of the Milky Way. The simulations have shown that the diversity in age-metallicity relations of Milky Way-mass galaxies results from different assembly histories and can therefore be used to infer such assembly histories (Kruijssen et al., 2019a,b, 2020). The simulations have also been shown to reproduce the observed kinematics of the Galactic GC population (Trujillo-Gomez et al., 2021) and have been used to conclude that GCs associated with stellar streams will be, on average, younger than the GC population not associated with a stellar stream (Hughes et al., 2019), a result subsequently confirmed through observations of stellar streams in the halo of M31 (Mackey et al., 2019). Finally, Pfeffer et al. (2019b) showed that the simulations reproduce the properties of young cluster populations, and the simulations were subsequently used to predict when and where GCs formed (Reina-Campos et al., 2019; Keller et al., 2020). By comparing the simulation outputs to the observations of Jordán et al. (2007), this chapter serves as another test that YMCs and ancient GCs share the same formation mechanism.

Pfeffer et al. (2019b) compare the $M_{c,*}$ of young star cluster populations in the E-MOSAICS simulations with observations of local galaxies and find good agreement, though more observations of systems with young star clusters are needed to test whether the scatter found in the simulations is realistic. In this chapter I expand on the Pfeffer et al. (2019b) study to contrast the $z = 0$ $M_{c,*}$ of GC systems (with no age constraints) to that of observations. This means that the E-MOSAICS GC mass function are allowed to evolve with time (through stellar evolution and dynamical processes) and then I test whether observations are still matched. This is a test of the cluster formation physics in the simulations and also the subsequent evolution of the star clusters alongside their host galaxies.

This chapter is organised as follows. In Section 3.2, I describe the observational data and compare them to the simulations. In this section, I also justify our choice to fit Schechter functions over a single power-law function. Section 3.3 investigates the impact of considering alternative cluster formation scenarios on the mass functions. Section 3.4 describes how the mass function changes when including the initial masses

of GCs that have been completely disrupted. Finally, in Section 3.5 I will present the conclusions of this chapter.

3.2 Comparison between simulations and observations

3.2.1 Virgo Cluster Data

The data to compare the simulations with throughout this chapter are part of the ACS Virgo Cluster Survey, first presented by [Côté et al. \(2004\)](#). The survey is designed to observe 100 early-type galaxies in the Virgo Cluster, using the Advanced Camera for Surveys (ACS) on the Hubble Space Telescope. The survey used the F475W and the F850LP bandpasses (approximately equal to the Sloan g and z respectively, [Côté et al. 2004](#)). The ACS Virgo Cluster Survey is designed to probe the brightest $\approx 90\%$ of the GC luminosity function in the 100 galaxies. This yields a sample of $\approx 13,000$ GCs in the Virgo Cluster ([Côté et al., 2004](#)).

[Jordán et al. \(2007\)](#) present the luminosities of GCs belonging to early-type galaxies in the ACS Virgo Cluster Survey. They fit the luminosity functions with an evolved Schechter function (also fitting for the GC mass loss) and present the truncation luminosity in their table 3, and the corresponding truncation mass ($M_{c,*}$) as a function of galaxy mass based on the B-band galaxy magnitude in their figure 16.

[Peng et al. \(2008\)](#) present the stellar masses of the galaxies in the ACS Virgo Cluster Survey. I use their table 1 to convert the galaxy B-band magnitude in [Jordán et al. \(2007\)](#) to galaxy stellar mass. The [Jordán et al. \(2007\)](#) results in this format are presented as black stars in Fig. 3.2.

3.2.2 Simulation Data

Description of the Schechter function fits

To compare the mass functions of GCs in the E-MOSAICS simulations with those in the Virgo galaxy cluster (Jordán et al., 2007), the most massive galaxy group in the simulations is considered. In this galaxy group, $M_{200} = 5.14 \times 10^{13} M_{\odot}$ ¹. The stellar mass of the brightest cluster galaxy (BCG) is $M_* = 2.23 \times 10^{11} M_{\odot}$ and the cluster contains 154 galaxies with a stellar mass above $10^7 M_{\odot}$. The virial mass of the Virgo galaxy cluster has been estimated to be $6.3 \times 10^{14} M_{\odot}$ by Kashibadze et al. (2020) and $4.2 \times 10^{14} M_{\odot}$ by McLaughlin (1999). This places the simulated galaxy cluster at a lower mass than the Virgo galaxy cluster but periodic simulations large enough to include galaxy clusters of Virgo galaxy cluster mass are very expensive to run at the resolution of the E-MOSAICS simulations, I also show in Section 3.2.3 that halo mass does not have a strong impact on the results.

To fit Schechter functions to the GC mass functions from the simulations, I follow the methodology outlined by Pfeffer et al. (2019b), who adopt similar analyses to those used in observational studies (e.g. Johnson et al. 2017a; Messa et al. 2018). The GCs in the simulated cluster are stacked in bins of host galaxy stellar mass and use the Markov Chain Monte Carlo (MCMC) code PyMC (Fonnesbeck et al., 2015) to perform the fits and to sample the posterior distribution of the Schechter power-law index and truncation mass. The power law index is sampled with a uniform prior between -3 and -0.5, this prior is chosen to cover the full range of possibilities and to be consistent with that used by observational work (e.g. Johnson et al. 2017a). The truncation mass is sampled in log-space with a uniform prior between a minimum cluster mass (which we describe below) and $10^9 M_{\odot}$. A Gaussian likelihood is used. redOnce such Schechter function fit, with it's respective errors is shown in Fig. 3.1, where the blue line shows the cumulative distribution function of the masses of GCs in the $9.5 < \log M_*/M_{\odot} > 9.75$ galaxy mass bin.

¹The total mass contained within the radius at which the density drops to 200 times the critical density

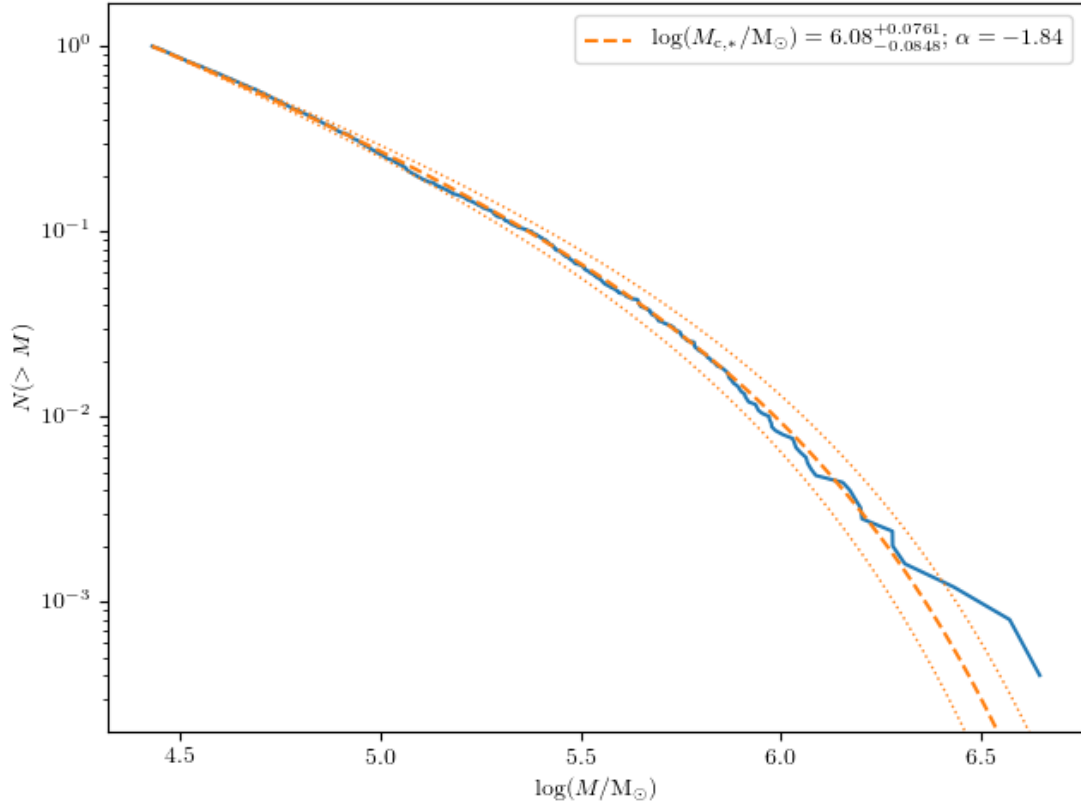


Figure 3.1: An example of a Schechter function fit to the simulation data. The blue line shows a cumulative distribution function of the GC masses. The orange dotted line shows the median Schechter function fit from the MCMC and the dotted lines show the 16th and 84th percentiles.

In the galaxy mass range of the [Jordán et al. \(2007\)](#) observations ($\log M_*/M_\odot > 9.5$) the galaxies are binned by stellar mass in bins of width 0.25 dex. Below this mass, I use galaxy stellar mass bins of width 0.5 dex to yield the best sampling. The number of galaxies and number of GCs used are presented in Table 3.1, where the ‘fiducial’, ‘no dynamical friction (DF)’ and ‘initial’ columns refer to three GC subsamples from the simulations that are described in Section 3.4. In the range of the observations ($\log M_*/M_\odot > 9.5$) the mass bins sample a similar number of galaxies as the [Jordán et al. \(2007\)](#) study, who also include just 1 galaxy in their most massive bin and 10 in their least massive. However, there are more GCs in each bin than [Jordán et al. \(2007\)](#): their sample spans a range of 193-1721 GCs, whereas the E-MOSAICS fiducial sample of GCs spans a number range of 612-2992 within the same galaxy mass range, it is a known problem that E-MOSAICS produces too many low-mass GCs (e.g. [Pfeffer](#)

et al. 2018). Additionally, the Jordán et al. (2007) are not spatially complete in their observations of the galaxies. Bastian et al. (2020) show that the fraction of galaxy mass contained in GCs in E-MOSAICS is close to the observed fraction and therefore the number of GCs at the high-mass end should be reasonably comparable.

A varying minimum cluster mass is used across the galaxy mass range. Table 1 of Jordán et al. (2007) gives the z-band magnitude limits of the GCs, and for the more massive galaxies the completeness in the z-band drops below 90 per cent at $m_z \approx 23.0$, this corresponds to a GC mass of $\approx 2 \times 10^5 M_\odot$. For the low mass galaxies ($M_* \approx 10^9 M_\odot$) the completeness drops below 90 per cent at around $m_z \approx 25.0$, corresponding to a GC mass of $\approx 3 \times 10^4 M_\odot$. This is due to massive galaxies having higher field star surface densities, such that it is more difficult to detect faint GCs. In the simulations, this is approximately equal to sampling the upper 2 dex of the mass function. I therefore fit Schechter functions to the upper 2 dex of the mass function, from the third most massive GC to account for stochasticity at the high-mass end. The minimum masses of the GCs are given in Table 3.1. Note that the lower galaxy mass bins, outside of the galaxy mass range of the Jordán et al. (2007) observations, include GCs that would be too faint to observe at the distance of the Virgo cluster, but it is still interesting from a theoretical stand point to investigate the continuation of the trend at lower galaxy stellar masses. For each galaxy mass bin the MCMC takes 10,000 steps and the first 1,000 of these steps are taken as burn-in.

Should we fit Schechter functions at all?

There is some contention in the literature as to whether Schechter functions or single power laws fit the GC mass function more accurately (Chandar et al., 2014, 2016; Mok et al., 2019). Although on a per-particle basis the mass function assumed by the E-MOSAICS fiducial model is a Schechter function with an environmentally dependent $M_{c,*}$, this does not necessarily mean that the final mass function will be best fit by a Schechter function. The GC mass function of each simulated galaxy is an accumulation of the GC populations associated with many particles; each with varying input

$M_{c,*}$, and dynamical evolution may erase the signal of any exponential truncation.

Therefore, power law functions are also fit to the GCs in each galaxy mass bin, over the same mass range and with the same MCMC method as described for the Schechter fits above. The power law index is sampled with a uniform prior between -3 and -0.5. I then calculate the Bayesian Information Criterion (BIC) value (Schwarz, 1978) for both of the fitting functions and compare.

The BIC value takes into account that a model with more free parameters is likely to fit the data better and penalises the maximum likelihood estimate of the model if there are more free parameters in the fit. The BIC value is given by,

$$\text{BIC} = k \ln(n) - 2 \ln(L) \quad (3.1)$$

where k is the number of free parameters in the fit, n is the sample size, L is the maximum likelihood estimate of the model and lower BIC values are favourable. Two models can be compared by calculating the difference in their BIC values (ΔBIC). When the BIC value of the Schechter fit is subtracted from that of the power law fit, positive values indicate that the Schechter function is preferred over the power law and vice versa. It is found that, for all galaxy mass bins, a Schechter function is strongly preferred with ΔBIC values between 18 and 133. In Section 3.4, I include two more subsamples of GCs to omit specific mass loss mechanisms. A Schechter function is also preferred over a power law function for all galaxy masses in these subsamples. For the subsample of GCs with dynamical friction omitted ΔBIC values are between 12 – 105, and for the subsample of GCs with all mass loss omitted, ΔBIC values between 2 – 129. Given that all ΔBIC values are positive the simulated globular cluster mass functions are best fit by Schechter functions.

Table 3.1: The number of galaxies and GCs in each galaxy mass bin and GC sub-population. The highest galaxy mass bins contain just one galaxy, so in this case we give the galaxy’s mass.

$\log(M_*/M_\odot)$	Galaxies	Min. GC mass [M_\odot]	Fiducial	No DF	Initial
7–7.5	41	1.63×10^3	441	476	2609
7.5–8	39	2.66×10^3	884	913	6236
8–8.5	18	3.24×10^3	1184	1211	10690
8.5–9	15	6.67×10^3	1877	1898	17958
9–9.5	10	1.60×10^4	1901	1923	14642
9.5–9.75	6	2.70×10^4	2494	2522	16624
9.75–10	4	5.45×10^4	1301	1844	21364
10–10.25	7	5.68×10^4	2465	3137	55148
10.25–10.5	2	4.21×10^4	1484	1618	33617
10.67	1	5.33×10^4	612	719	36666
10.91	1	7.16×10^4	1323	1548	47650
11.05	1	1.18×10^5	1410	1801	45898
11.35	1	1.14×10^5	2992	3332	42234

3.2.3 Model results vs. Observations

Fig. 3.2 shows $M_{c,*}$ as a function of galaxy stellar mass for the observations from [Jordán et al. \(2007\)](#) and for the most massive galaxy group in the E-MOSAICS simulations. Error bars show the 16th and 84th percentiles of the posterior distribution. Fig. 3.2 shows good agreement between the truncation masses of the observations and the E-MOSAICS simulations, particularly in the slope of the relation.

There is a systematic offset between the two distributions in Fig. 3.2: $M_{c,*}$ is consistently higher in E-MOSAICS than in the observations. This offset is smaller than the observational uncertainties, but could be due to a combination of the observations underestimating $M_{c,*}$ and the simulations over estimating it. On the simulation side, under-disruption could mean that $M_{c,*}$ is overestimated (see Appendix D of [Kruijssen et al. 2019a](#)). Alternatively, some of the difference may be due to uncertainties in the colour- M/L conversions for observed GCs.

Fig. 3.3 shows the same observational data from [Jordán et al. \(2007\)](#) as in Fig. 3.2 but I now show $M_{c,*}$ as a function of galaxy mass for all quiescent galaxies in the E-MOSAICS volume, divided by their group mass. I define ‘field galaxies’, ‘super

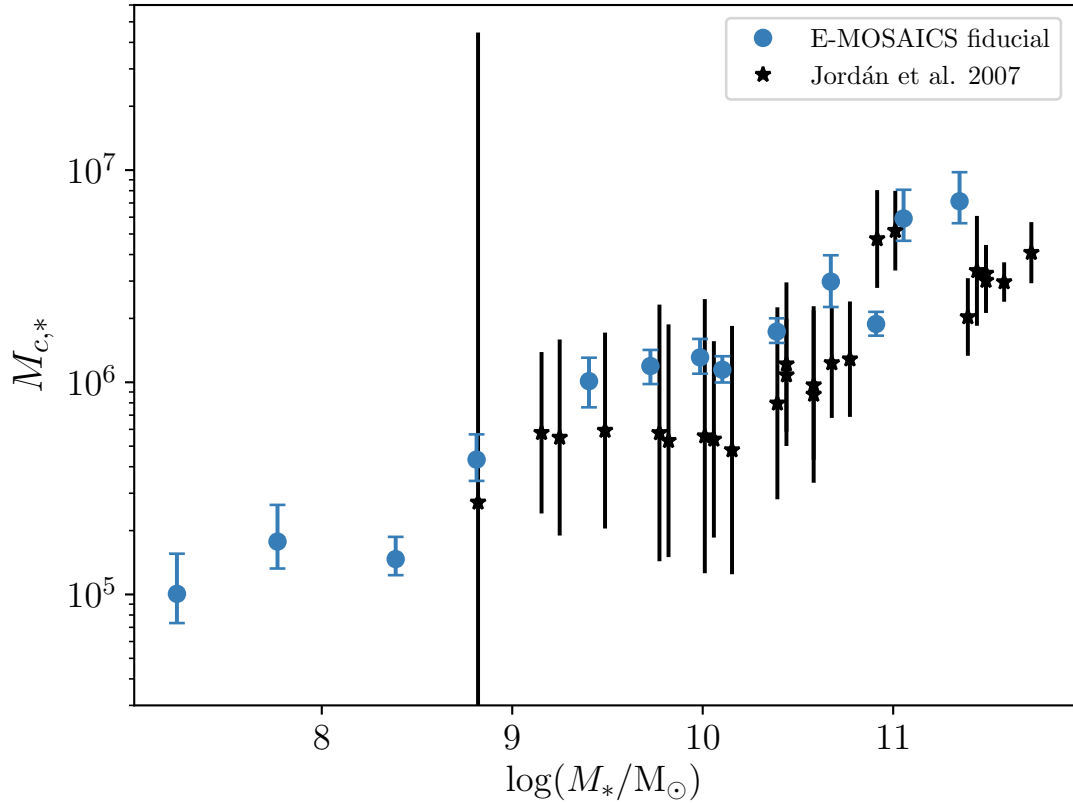


Figure 3.2: The dependence of $M_{c,*}$ on galaxy stellar mass in the Virgo galaxy cluster and the most-massive E-MOSAICS galaxy group. The black stars represent the data taken from Fig. 16 of [Jordán et al. \(2007\)](#). The blue points show the fits to the E-MOSAICS fiducial model at $z=0$, where the error bar represents the 16th-84th percentile range of the posterior distribution. The blue E-MOSAICS points match well with the [Jordán et al. \(2007\)](#) sample.

L* galaxies’ and ‘cluster galaxies’ as having total group masses $M < 10^{12}$, $10^{12} < M < 10^{13}$ and $M > 10^{13}$ respectively. Non-star forming galaxies are selected based on their specific star formation rate (sSFR) within 30kpc. Following the method in [Pfeffer et al. \(2019b\)](#) I select galaxies that are not on the star forming main sequence. The decision to exclude star-forming galaxies is two-fold: firstly, galaxies that reside in galaxy clusters (such as those used in [Jordán et al. \(2007\)](#)) are likely to be quiescent and secondly, galaxies that are forming massive GCs at $z = 0$ will bias the $M_{c,*}$ fits to high values. Fig. 3.3 shows that quiescent galaxies in the full E-MOSAICS volume also show agreement in the truncation masses with the [Jordán et al. \(2007\)](#) observed values. This analysis is confirmation that there is nothing special about the galaxies in the most massive galaxy group except that they are likely to be quiescent. Therefore the

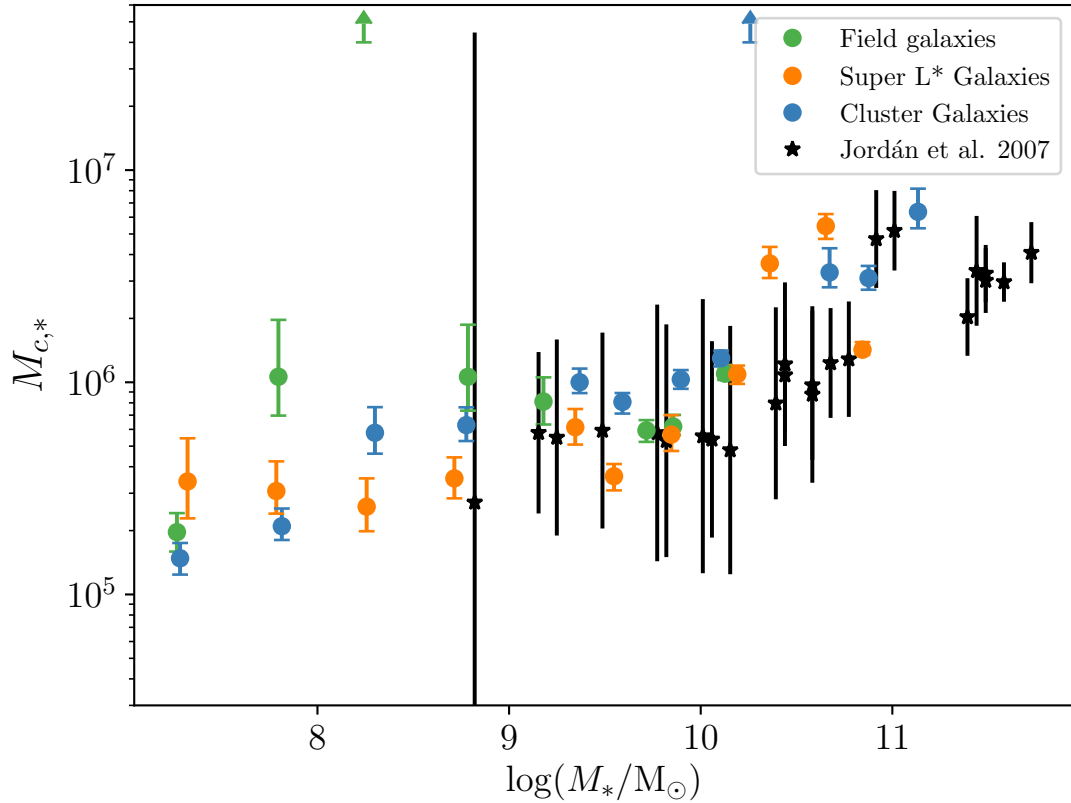


Figure 3.3: The dependence of $M_{c,*}$ on galaxy stellar mass in the Virgo galaxy cluster and the most-massive E-MOSAICS galaxy group. The black stars represent the data taken from Fig. 16 of [Jordán et al. \(2007\)](#). The coloured points show the fits to the E-MOSAICS volume, split by the group mass. We just include the quiescent galaxies from the simulations to be able to compare to the observed galaxy cluster.

rest of this work is carried out with the most massive galaxy group to ease comparison with observations and to simplify discussion.

Given the above discussion it is still fair to suggest that the E-MOSAICS simulations show mass function truncations that are a satisfactory match to the [Jordán et al. \(2007\)](#) observations and make the clear prediction that $M_{c,*}$ increases with galaxy mass. This demonstrates that the fiducial input physics of the MOSAICS model is able to reproduce a fundamental observable in GC studies. To determine which physical mechanism is the most important in setting the relation in Fig 3.2, I will examine alternative formation physics in the next section.

3.3 Alternative cluster formation physics

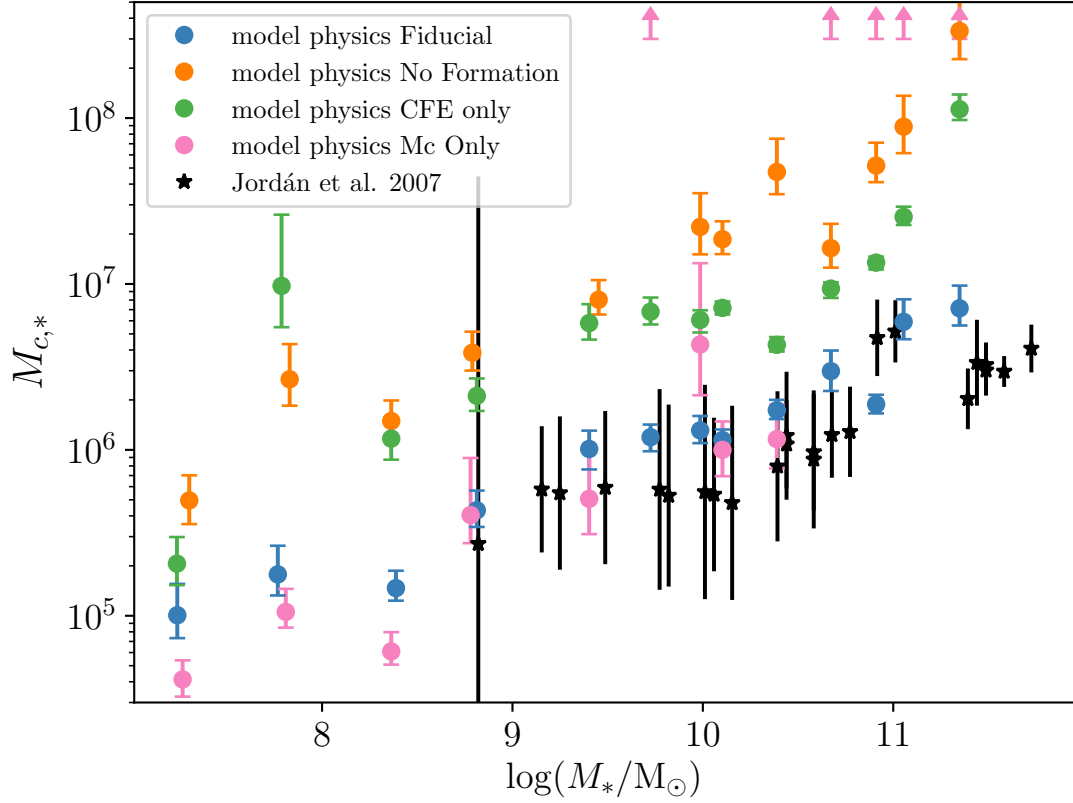


Figure 3.4: The dependence of $M_{c,*}$ on galaxy stellar mass in the Virgo galaxy cluster and the most-massive E-MOSAICS galaxy group. The fiducial model, the ‘no formation’ model, the ‘CFE only’ model and the ‘Mc only’ model are represented by blue, orange, green and pink circles respectively.

In this section three alternative cluster formation physics variants in the E-MOSAICS model are investigated to establish which of the key ingredients of the model are needed to reproduce the observations of [Jordán et al. \(2007\)](#). The differences between the models are:

- In the fiducial model, both the cluster formation efficiency and $M_{c,*}$ depend on environment (as described in Chapter 2)
- In the ‘no formation physics’ model, there is a constant cluster formation efficiency ($\Gamma = 0.1$) and no upper truncation to the mass function i.e. it is a pure power law, therefore the cluster formation is not environmentally dependent and is equivalent to a simple ‘particle tagging’ method.

- In the CFE only model, the CFE varies with environment but there is no upper truncation to the mass function.
- In the $M_{c,*}$ only model the CFE is a constant ($\Gamma = 0.1$) but $M_{c,*}$ varies with environment.

Fig. 3.4 presents the four alternative physics models in blue, orange, green and pink respectively. Firstly I will focus on the ‘no formation physics’ model (orange), where the increasing trend of $M_{c,*}$ with galaxy stellar mass is simply a size-of-sample effect. More massive galaxies form more GCs and therefore have the potential to sample more massive GCs from the power-law mass function. Dynamical friction then acts to remove some of the most massive GCs and a truncation is detected. The slope of the relation will be constant, but the relation could be shifted up or down, depending on the CFE. However, the slope of the ‘no formation physics’ model is significantly steeper than that of the observations, so even with a smaller CFE to shift the relation to lower $M_{c,*}$, it would not match the observations.

Next, I concentrate on the CFE only model, where the increasing trend of $M_{c,*}$ with galaxy stellar mass is still present and mostly follows that of the ‘no formation physics model’ except for a dip in $M_{c,*}$ at $\log(M_*/M_\odot) \approx 10$. The dip is because there is now an environmentally dependent CFE so galaxies forming most of their GCs in high pressure regions have the potential to form their most massive GCs here as well, in an environment that can subsequently disrupt them. Therefore it is likely that dynamical evolution is the cause of this slight decrease in $M_{c,*}$, which is discussed further in the context of the fiducial model in Section 3.4.

Finally, the $M_{c,*}$ only model, here upward arrows mark the galaxy mass bins where a robust Schechter fit could not be achieved. I also carry out a BIC test for all the fits in Fig. 3.4 to indicate whether a Schechter fit or a power law fit is more appropriate for the data. The BIC tests for the fits here indicate that a Schechter function is preferred in all cases except for those that are shown with an upward arrow, where a power-law fit is strongly preferred. It is interesting that in the case where a truncation mass is explicitly included in the model, a fit that does not include one is preferable in some

galaxy mass bins. In the fiducial model both $M_{c,*}$ and CFE scale with birth pressure, therefore where the $M_{c,*}$ is high, also a higher fraction of the mass of the stellar particle is available for GC formation. By contrast, in the $M_{c,*}$ only model $M_{c,*}$ scales with birth pressure and the CFE does not. As a result, there is less mass available and stellar particles are less likely to form massive GCs. In the fiducial model, high $M_{c,*}$ particles contribute more clusters to the composite cluster mass function than low $M_{c,*}$ particles due to the varying CFE but in the $M_{c,*}$ only model all particles are weighted equally. Therefore when many particles are stacked in the mass function, the power-law index (α) becomes steeper and an $M_{c,*}$ is difficult to identify.

Together, the results in this section confirm that an environmentally varying CFE and mass function truncation, as implemented in the fiducial E-MOSAICS model, is required to explain both the GC and young cluster populations (Pfeffer et al., 2018, 2019b; Usher et al., 2018; Reina-Campos et al., 2019; Bastian et al., 2020).

3.4 Dependence on GC formation and evolution

3.4.1 GC mass loss cases

As described in Section 1.5.2, the main GC mass loss mechanisms are stellar evolutionary mass loss, tidal shock heating, two body relaxation and dynamical friction. Here, I investigate the different mass loss mechanisms and how they affect the GC mass function. Again, Schechter functions are fitted to the GCs in the same galaxy mass bins as in Fig. 3.2 but now two new subsamples of GCs are included. I include the GCs from the simulations without dynamical friction applied, shown in orange in Figs. 3.5 - 3.9, and also the initial GCs that formed with a mass greater than the minimum mass given in Table 3.1, with no mass loss – stellar or dynamical– applied, shown in green in Figs. 3.5 - 3.9. Note that stellar mass loss should affect all GCs approximately equally (assuming the GCs are relatively old) and therefore will not play a part in setting the slope of the GC mass function.

The truncation mass

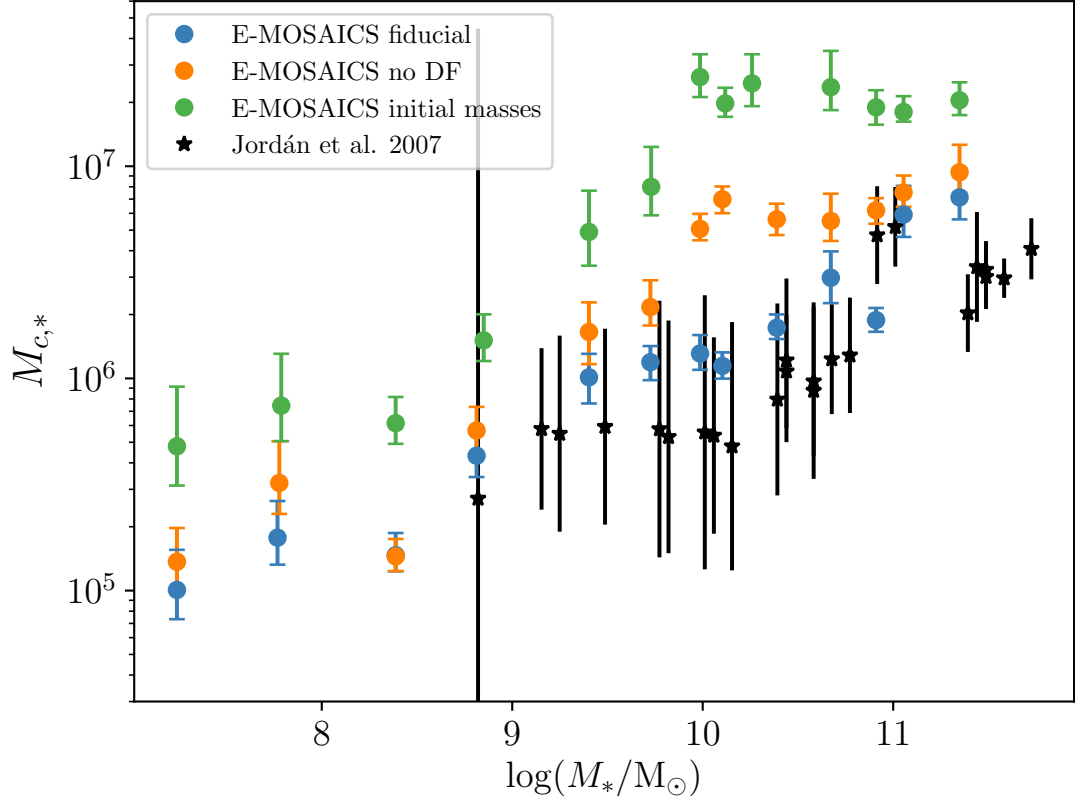


Figure 3.5: The dependence of $M_{c,*}$ on galaxy stellar mass in the Virgo galaxy cluster and the E-MOSAICS galaxy cluster. The black stars represent the data taken from Fig. 16 of [Jordán et al. \(2007\)](#). The blue points show the E-MOSAICS fiducial model at $z=0$. The orange points show the E-MOSAICS model with no dynamical friction taken into account. Finally, the green points show the E-MOSAICS with no mass loss (stellar evolution or dynamical) taken into account. Full dynamical evolution must be included in the simulation to match well with the [Jordán et al. \(2007\)](#) sample.

Fig. 3.5 shows the fitted $M_{c,*}$ as a function of galaxy stellar mass, with the fiducial, no dynamical friction (no DF) and no mass loss (initial masses) GC models shown in blue, orange and green respectively, and the [Jordán et al. \(2007\)](#) fits shown as black stars. Fig. 3.5 shows that the subsample of GCs that does not include any mass loss (initial masses) has the highest $M_{c,*}$, followed by the subsample that includes all mass-loss mechanisms except dynamical friction (no DF) and then the fiducial E-MOSAICS model exhibiting the lowest $M_{c,*}$ in a given galaxy mass bin. The $M_{c,*}$ decreases by ~ 40 per cent due to stellar evolution, however any further decrease is due to dynamical evolution. This indicates that the GC disruption time-scale is short enough to destroy

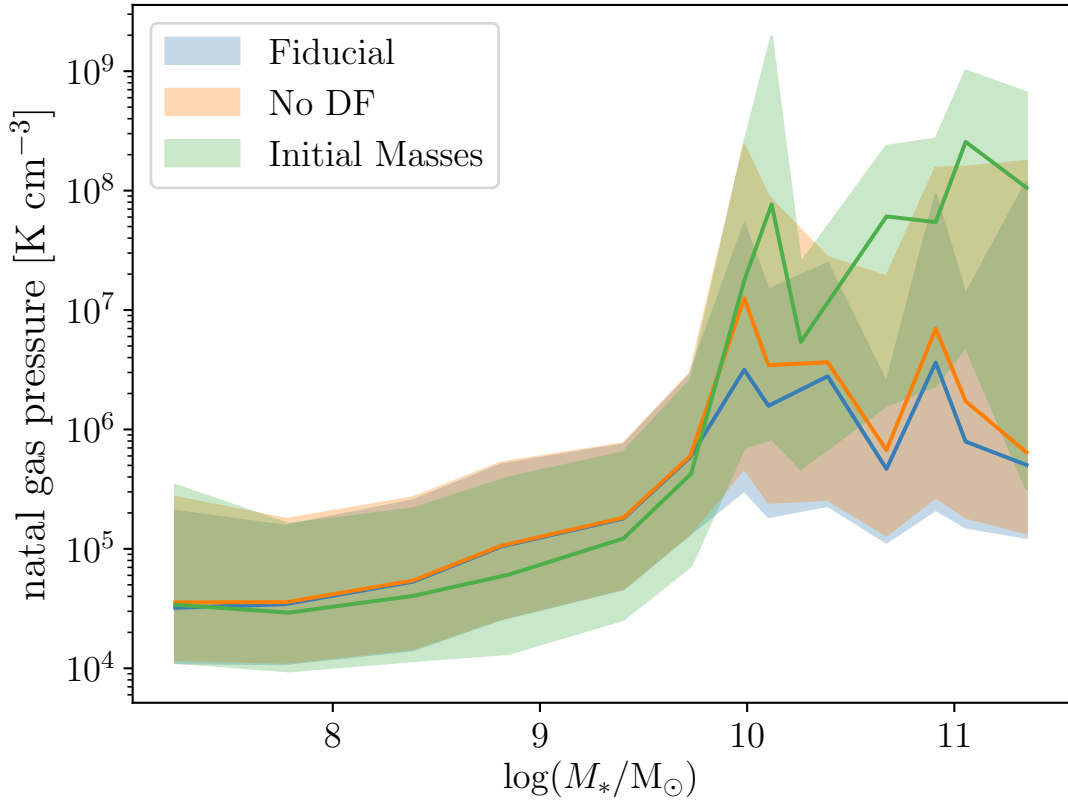


Figure 3.6: The dependence of GC birth pressure on galaxy stellar mass in the E-MOSAICS galaxy cluster. The shaded regions show the 16th-84th percentile range.

high mass GCs, and that dynamical evolution plays an important role in shaping the high mass end of the GC mass function.

The birth pressure of the GCs is shown as a function of the host galaxy mass in Fig. 3.6, which shows the birth pressure of the different subsamples of GCs in the same galaxy mass bins as in Fig. 3.5, where the solid line shows the median and the shaded region represents the 16th-84th percentile range. The birth pressures of the three subsamples are very similar up to a galaxy mass of $\approx 10^{10} M_{\odot}$, because the samples themselves are similar, i.e. there are not many GCs formed that do not survive until present day. Above a galaxy mass of $\approx 10^{10} M_{\odot}$ there is a steep increase in the initial birth pressures before a plateau. It is also at this mass where there is a separation in the median birth pressures between the ‘initial masses’ sample ($P/k \sim 10^8 \text{ K cm}^{-3}$) and the other two populations ($P/k \sim 10^6 \text{ K cm}^{-3}$).

This separation occurs because of the high birth pressures of the initial GCs. In high

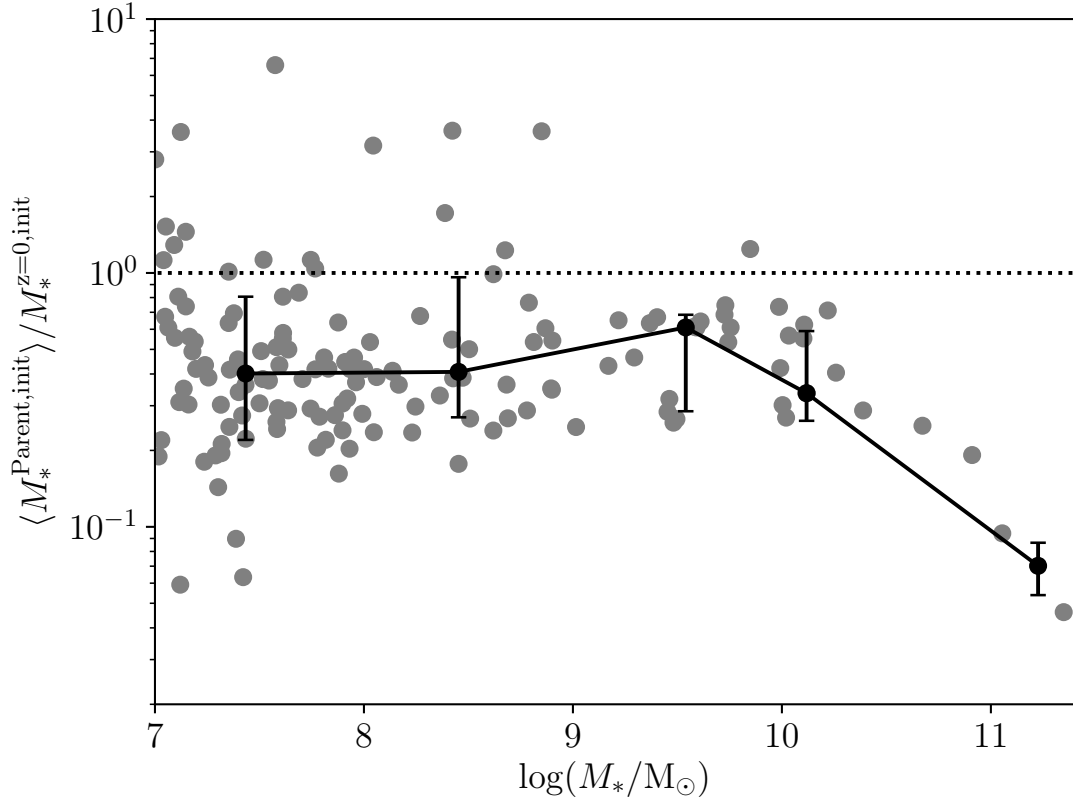


Figure 3.7: The ratio of the median initial parent galaxy stellar mass to the initial stellar mass of the $z = 0$ galaxy as a function of the $z = 0$ galaxy mass. The black points and line show the median and 16th-84th percentile ranges in galaxy mass bins of 1 dex.

pressure/high density environments, mass loss mechanisms such as tidal shocks are more prevalent and therefore quickly disrupt the newly formed GCs (termed the ‘cruel cradle effect’, [Kruijssen et al. 2012b](#); see also section 6.2 of [Pfeffer et al. 2018](#) in relation to the E-MOSAICS simulations). The tidal disruption timescale is much smaller than the dynamical friction timescale; therefore, before dynamical friction can act, GCs that have formed in the highest pressure environments have already been disrupted. Dynamical friction then becomes effective at reducing $M_{c,*}$ at a galaxy mass of $\approx 10^{10} M_\odot$ but this is not reflected in the birth pressures. This is simply because dynamical friction removes the most massive GCs that are few in number, so although this will affect the $M_{c,*}$ it will not affect the median birth pressures of the surviving GCs.

An interesting feature of Figs. 3.5 and 3.6 is that both the $M_{c,*}$ of the initial GCs and the natal birth pressure show a plateau above $\log(M_*/M_\odot) \approx 10$ while we might

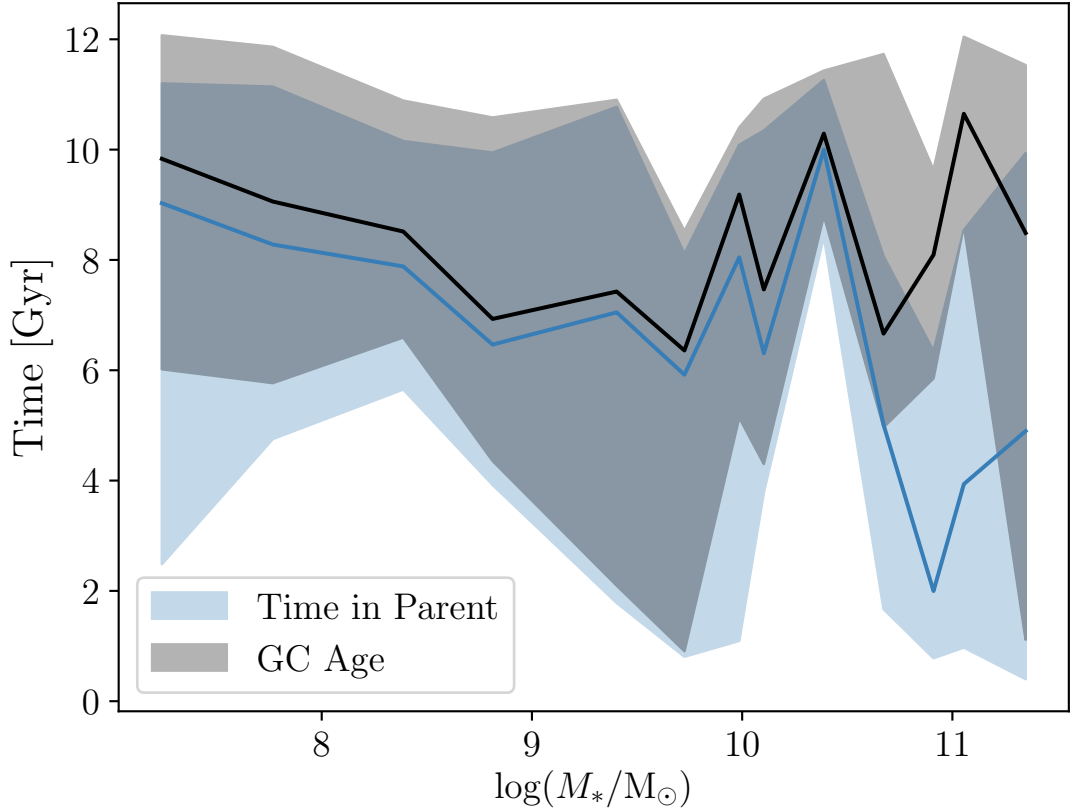


Figure 3.8: The dependence on the median time a GC spends in its parent galaxy as a function of galaxy stellar mass. The colours of the three subsamples are the same as in Fig. 3.5 and the shaded regions show the 16th-84th percentile range.

intuitively expect a continuing increase with galaxy mass, with more massive galaxies able to form a greater number of more massive GCs. However, massive galaxies grow via mergers and therefore the massive galaxy observed at $z = 0$ is an accumulation of many galaxy building blocks. Therefore, we must investigate not the galaxy mass at $z = 0$ but rather the galaxy mass at the time of GC formation. For this, I compare the median stellar mass of the galaxies in which the ‘initial’ GCs formed (the parent galaxy mass) to the $z = 0$ galaxy stellar mass, this is shown in Fig. 3.7, where each grey point represents one galaxy in the cluster and the black line shows the median for galaxy mass bins of 1 dex. Note that the y-axis shows the ratio of the stellar mass without stellar evolution taken into account, this is to remove the effect of some galaxies having more evolved stellar populations. Fig. 3.7 shows that the median GC parent galaxy mass relative to the $z = 0$ galaxy mass is broadly constant for $\log(M_*/M_\odot) < 10$, but it declines to higher masses. Above a stellar mass of $10^{10} M_\odot$

there is a higher fraction of GCs that were born in a lower mass galaxy than the $z = 0$ galaxy. Therefore, the birth pressures and subsequently $M_{c,*}$ remain constant, even with increasing $z = 0$ mass. This is because massive galaxies increasingly grow by mergers, not star formation, so they are unlikely to be forming new GCs during their late accretion-driven growth stage (e.g. [Oser et al. 2010](#); [Lee & Yi 2013](#); [Qu et al. 2017](#); [Clauwens et al. 2018](#); [Davison et al. 2020](#))

Another interesting feature of Fig. 3.5 is that the effect of dynamical evolution is not constant across all galaxy mass bins. Dynamical mass loss has the most power at reducing $M_{c,*}$ from the initial masses of all GCs to the masses at $z = 0$ at $\log(M_*/M_\odot) \approx 10$. As discussed previously, it is the addition of dynamical friction that drives the decrease in $M_{c,*}$ at these galaxy masses through the removal of the most massive GCs. Here I discuss why this is more efficient at a galaxy mass of $\log(M_*/M_\odot) \approx 10$ than for $\log(M_*/M_\odot) \approx 11$.

The first contributing factor to longer dynamical friction timescales (and therefore a higher chance of survival) is the mass ratio between the GC mass and the galaxy mass. When the mass within the GC's orbit is larger, the dynamical friction timescale is longer. In the more massive galaxies, the mass within the GC's orbit is likely to be larger at fixed radius and therefore the GC can survive for longer. The second contributing factor to longer dynamical friction timescales is the radius of the GC orbit. Importantly GCs may get pushed to wider orbits via mergers (e.g. [Kruijssen et al. 2011](#)). Mergers facilitate the means for GCs to move from their birth places (where dynamical friction timescales may be short) either by being kicked out of the inner parts of the galaxy or being deposited in the halo of a more massive galaxy (where dynamical friction timescales are very long). [Qu et al. \(2017\)](#) along with [Clauwens et al. \(2018\)](#) and [Davison et al. \(2020\)](#) showed that the EAGLE galaxies are built by mainly in-situ formation up to a stellar mass $\approx 10^{10} M_\odot$. The ex-situ fraction then increases with stellar mass, and for galaxies that reach a stellar mass $\approx 10^{11} M_\odot$ approximately 50 per cent of their mass is built through mergers. So at $\log(M_*/M_\odot) \approx 10$ significant cluster disruption is able to happen because there are few mergers to redistribute the massive GCs into a 'safer' environment. By contrast, in more massive galaxies,

mergers are common and the massive GCs have a higher chance of survival.

I now consider how long the GCs in each $z = 0$ galaxy typically spend in their parent galaxy (i.e. the time between GC formation and $z = 0$ for in-situ GCs, or the time between formation and the merger of the host galaxy in the case of accreted GCs). This contains information about whether the GC population is dominated by GCs that have survived in their parent galaxies for a long time or by GCs that have been deposited into the halo of the more massive galaxy, after spending a short amount of time in their parent galaxy. This is examined in Fig. 3.8, which shows the median age and 16-84 percentile range of the GCs and the median time and 16-84 percentile range the GCs spent in the parent galaxy (analogous to figure D2 in [Kruijssen et al., 2019a](#)). The median age of the GCs remains old (> 7 Gyr) at all galaxy masses. Note the slight decline in age between $7 < \log(M_*/M_\odot) < 10$, this is because more massive galaxies are likely to have entered the potential well of the galaxy cluster more recently, and, when they do enter the potential well of the galaxy cluster, they can hold onto their star forming gas for longer than their lower mass counter parts (see e.g. [Gunn & Gott 1972](#); [Hughes et al. 2019](#) for more details). The time spent in the parent galaxy traces the age of the GCs closely until a mass of $\log(M_*/M_\odot) \approx 10.5$ where the time spent in the parent galaxy decreases, whilst the median age still remains old. This reflects the high number of mergers in these galaxies depositing GCs into the halo of the galaxy where the dynamical timescale is long and massive GCs can survive.

In conclusion, it is the combination of more massive GC formation and then the subsequent galaxy merger histories and the effect of dynamical friction that leads to the fiducial trend between $M_{c,*}$ and galaxy mass in both the [Jordán et al. \(2007\)](#) work and the E-MOSAICS simulations.

The mass function slope

For completeness, Fig. 3.9 shows the power-law index (α) of the Schechter fit in the same galaxy stellar mass bins and the different coloured points have the same meaning as in Fig. 3.5. Note that the minimum GC mass is different in each of these

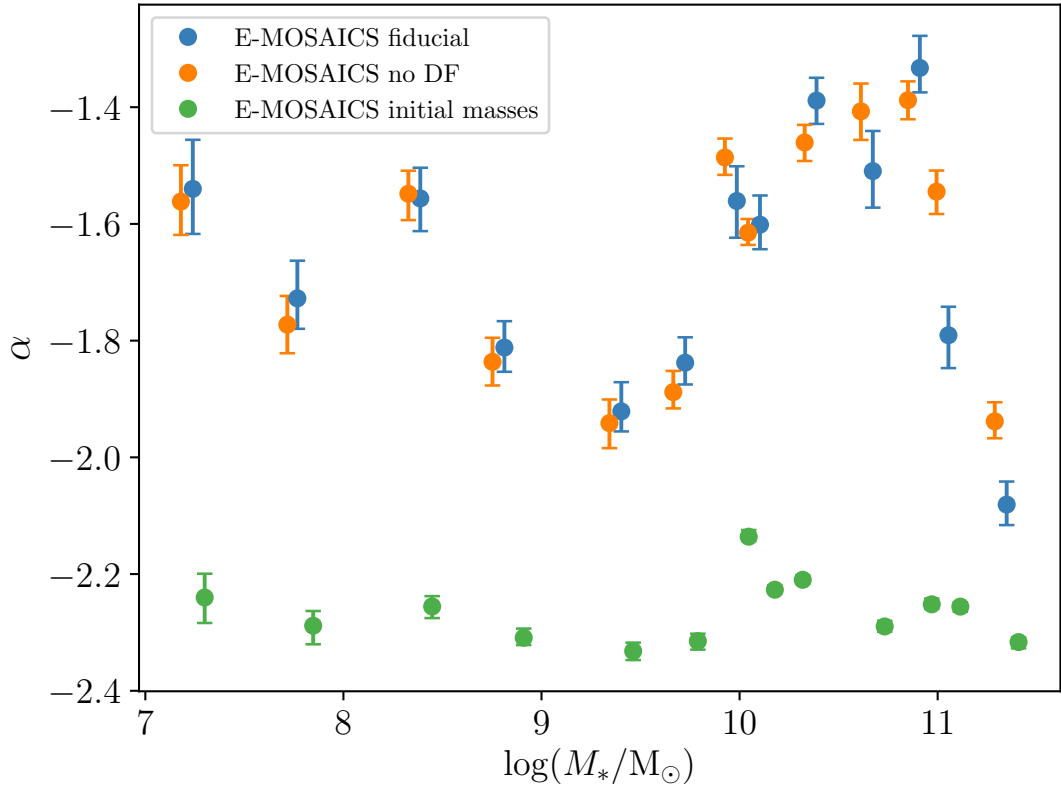


Figure 3.9: The dependence of α on galaxy stellar mass in the E-MOSAICS galaxy cluster. The blue points show the E-MOSAICS fiducial model at $z=0$. The orange points show the E-MOSAICS model with no dynamical friction taken into account. Finally, the green points show the E-MOSAICS clusters that survive to $z=0$ within our mass cut but with no mass loss (stellar evolution or dynamical) taken into account.

galaxy mass bins (see Table 6.1) because we are fitting the top two dex of the mass function. Therefore, the power law slope is from a different part of the mass function between low and high mass galaxies. This could explain the drop in α from -1.4 at $\log(M_*/M_\odot) \approx 10.5$ to -2 at $\log(M_*/M_\odot) \approx 11.5$ since the minimum GC mass changes from $\sim 10^4$ to $\sim 10^5 M_\odot$. There is a similar caveat between $\log(M_*/M_\odot) \approx 7$ and $\log(M_*/M_\odot) \approx 9.5$ where the minimum GC mass changes from $\sim 10^3$ to $\sim 10^4 M_\odot$. However, where the minimum GC mass is similar comparisons can be made. In this case this limits the discussion to galaxy masses $9.5 < \log(M_*/M_\odot) < 10.5$. I therefore refrain from commenting on any trends of α with galaxy mass across all galaxy mass bins and instead focus on the differences between the three mass-loss cases to understand how dynamical evolution plays a role.

First of all, Fig. 3.9 shows that the GC sample with no mass loss has a relatively consistent power law index, independently of galaxy mass. E-MOSAICS adopts $\alpha = -2$ for each star particle that forms a GC population. Therefore it could be expected that the subsample of GCs with no mass loss would have $\alpha = -2$, however Fig. 3.9 shows a steeper slope for this GC subsample. This is the effect of stacking many star particles; the environmentally-dependent $M_{c,*}$ means that those star particles with lower $M_{c,*}$ will contribute to a steeper α value.

Fig. 3.9 shows that dynamical friction does not play a part in shaping the slope of the $z = 0$ mass function. Dynamical friction time scales grow rapidly towards lower mass GCs as $\tau_{\text{DF}} \propto M_{\text{GC}}^{-1}$ and therefore dynamical friction takes much longer to destroy a low mass GC. By contrast tidal shocks and two-body relaxation have a less obvious scaling with galaxy mass, because they depend on many galaxy properties. Therefore, although dynamical processes do shape the slope of the GC mass function, dynamical friction is not one of them.

The galaxy mass range $9.5 < \log(M_*/M_\odot) < 10.5$ probes similar GC masses and the behaviour of α with increasing galaxy mass is informative. α increases with galaxy mass in this mass range, that is, the slope of the power-law portion of the mass function becomes flatter. This rise can be associated with a rise in the birth pressures across the same galaxy mass range. As discussed above, a higher birth pressure environment leads to effective disruption of GCs, this is particularly prevalent in the low mass GCs, thus leading to a flattening of the mass function.

3.5 Conclusions

In this chapter I investigate the origins of the shape of the GC mass function as a function of galaxy stellar mass in a galaxy cluster. To carry out this analysis, the most massive galaxy group in the E-MOSAICS 34 cMpc periodic volume is used. This choice was made to facilitate comparison to the observational results of [Jordán et al. \(2007\)](#) who fit Schechter functions to GCs binned in host galaxy mass in the Virgo

Cluster.

Firstly, I examine whether fitting Schechter functions is preferable over fitting power-law functions to the GC mass distributions. This is decided via a BIC test which penalises a maximum likelihood estimation based on the number of free parameters. For the fiducial physics model in the simulations a Schechter function is preferable and therefore a confident comparison of the truncation mass of the Schechter function in the simulations to those of the observations in [Jordán et al. \(2007\)](#) can be made. Fig. 3.2 shows excellent agreement between the $M_{c,*}$ of the simulations and the observations.

To further investigate the input physics in the simulations Schechter functions are fitted to the GCs that survive to $z = 0$ under three different sets of cluster formation physics that do not allow the CFE, $M_{c,*}$ or both, to vary with environment (Fig. 3.4). The model that does not let either the CFE or the $M_{c,*}$ vary with environment still prefers a Schechter fit to a power-law fit because of dynamical friction disrupting the most massive GCs. However, this model yields an increasing $M_{c,*}$ with galaxy mass due to a size-of-sample effect, and produces the wrong slope. The model that only allows the CFE to vary with environment again prefers a Schechter fit due to dynamical friction, but $M_{c,*}$ remains too high to match observations. Finally, the model that only allows the $M_{c,*}$ to vary with environment often prefers a power-law fit. This is because the high mass end of the mass function is not well sampled. Therefore it is only the fiducial model with an environmentally-dependent CFE and $M_{c,*}$ that matches both the absolute values and the shape of the $M_{c,*}$ trend with galaxy stellar mass. This adds to the body of work already supporting the initial physics and subsequent evolution of star clusters in the E-MOSAICS simulations. I therefore conclude that the E-MOSAICS simulations can be used to investigate the origin and shape of the observed trend.

[Jordán et al. \(2007\)](#) consider the argument that the decrease of $M_{c,*}$ with decreasing galaxy mass could be due to the stronger depletion of massive GCs in dwarf galaxies due to dynamical friction. They postulate this because the dynamical friction timescale is proportional to the galaxy's circular speed ($\tau_{DF} \propto V_c$) implying that the relevance of dynamical friction can increase in lower mass galaxies. They then rule out this hypothesis concluding that dynamical friction can only account for a small fraction of

the steepening (decreasing $M_{c,*}$) of the mass function with time. In the E-MOSAICS simulations, dynamical friction is applied in post-processing and therefore its effects can be easily disabled and I do so in Fig. 3.5 and 3.9. In the high-mass end of the GC mass function (Fig. 3.5) dynamical friction is not seen to become more important in the lower-mass galaxies. In fact dynamical friction has a very small effect in these galaxies and the effect of dynamical friction on the slope of the GC mass function is negligible across all galaxy masses (Fig. 3.9). These findings support the [Jordán et al. \(2007\)](#) claim that dynamical friction does not play an important role at low galaxy masses. However, at a galaxy stellar mass $\approx 10^{10} M_{\odot}$ dynamical friction and other mass loss mechanisms are important in setting the shape of the high-mass end of the GC mass function.

GCs are formed with increasing $M_{c,*}$ with galaxy mass until a galaxy mass $\log(M_*/M_{\odot}) \approx 10$ where $M_{c,*}$ plateaus to higher galaxy masses. This is because the birth pressure also plateaus at these galaxy masses. The birth pressure plateaus because massive galaxies grow primarily by late mergers, and their GCs form in lower mass progenitors which have correspondingly lower pressures than the present day descendant.

Although $M_{c,*}$ follows this trend at birth it is how the GCs are then nurtured by their parent galaxy that sets the final $M_{c,*}$ observed today. This depends on whether the galaxy is able to move its high-mass GCs out of their highly disruptive birth environments quickly enough for them to survive until the present day. Galaxies can redistribute their GCs when they undergo merger events. Up until a stellar mass of $10^{10} M_{\odot}$ galaxies are built by mainly in-situ formation and therefore do not undergo enough mergers to re-distribute their GCs and their high-mass GCs get destroyed. This means that disruption of all kinds is most efficient at reducing $M_{c,*}$ at a stellar mass of around $10^{10} M_{\odot}$ where the pressures are high enough to form and then subsequently destroy high-mass GCs and there is not enough merger activity to redistribute them.

In conclusion, it is a combination of both nature and nurture that sets the $z = 0$ $M_{c,*}$ trend with galaxy mass. It is in the galaxy's nature to form more massive GCs if the galaxy itself is massive, but these GCs must be nurtured and redistributed via mergers if they are to survive until $z = 0$.

Chapter 4

Fossil stellar streams and their globular cluster populations in the E-MOSAICS simulations

4.1 Introduction

In the current galaxy formation paradigm, galaxies grow hierarchially through the accretion of diffuse gas and dark matter via filaments and mergers with other galaxies (e.g. [White & Rees 1978](#); [White & Frenk 1991](#)). Mergers with other galaxies can be in the form of a major merger: where two galaxies of similar mass collide; or a minor merger: where a galaxy of lower mass is accreted onto a more massive galaxy. Signatures of both types of mergers can be observed in the local Universe today in the form of substructure in a galaxy's gas, stars and globular cluster (GC) population. Substructure comes in a variety of forms such as shells, streams and planes. An abundance of substructure has been observed in our galaxy, both in the form of overdensities of stars and kinematically ([Majewski et al., 1996](#); [Newberg et al., 2002](#); [Belokurov et al., 2006](#); [Starkenburg et al., 2009](#); [Martin et al., 2014](#); [Shipp et al., 2018](#)), in M31 ([Ibata et al., 2001](#); [McConnachie et al., 2003](#); [Kalirai et al., 2006](#)) and other nearby galaxies ([Shang et al., 1998](#); [Martínez-Delgado et al., 2008](#); [Cohen et al., 2014](#); [Merritt et al.,](#)

2016; Abraham et al., 2018). This chapter focuses on substructure in the form of stellar streams.

Perhaps the most-studied substructure is the Sagittarius stream, which originates from the Sagittarius dwarf galaxy and currently resides in the halo of the Milky Way (MW, Ibata et al. 1995). The Sagittarius dwarf galaxy is our closest satellite galaxy with its nucleus just 16 kpc from the Galactic centre (Ibata et al., 1995). It is also the brightest Galactic dwarf spheroidal galaxy and has an estimated current total mass of $\approx 2.5 \times 10^8 M_{\odot}$ (Law & Majewski, 2010a). Sagittarius is elongated along the direction towards the MW centre which suggests it is undergoing strong tidal distortion before being integrated into our galaxy (Majewski et al., 2003). The Sagittarius stream is thought to host 7-11 globular clusters and open clusters with high to moderate confidence (Bellazzini et al., 2003; Forbes & Bridges, 2010; Law & Majewski, 2010b), although the distinction between open clusters and GCs is somewhat arbitrary. Overall, between 25 – 40% of the MW’s GC population are thought to have been accreted from dwarf galaxies (Forbes & Bridges, 2010; Kruijssen et al., 2019a,b). In M31, there is a striking spatial correlation between stellar substructure and GCs beyond 30 kpc from the galactic centre (Mackey et al., 2010). It was concluded that there is a less than 1% chance that these GCs are in their spatial configuration by chance (Mackey et al., 2010; Veljanoski et al., 2014) and are therefore likely to have been accreted with the stars comprising the substructure.

It has been postulated that substructures in a galaxy’s halo will present different stellar ages and metallicities than the bulk of the stellar halo because of their late infall onto the central galaxy and their smaller stellar mass (Ferguson et al., 2002; Johnston et al., 2008). Therefore, we might also expect tangible differences between the halo population of GCs and those which are associated with stellar streams. GCs associated with stellar streams, by construction, formed in a galaxy with a different star formation history, and hence a different GC formation history, than the galaxy in which they currently reside. Therefore stars and GCs associated with a particular stellar stream are expected to exhibit a different age-metallicity relationship to those formed in the central galaxy (Forbes & Bridges, 2010; Dotter et al., 2011; Leaman et al., 2013; Kruijssen

et al., 2019a). Mackey et al. (2013) estimate that 2 of the GCs (PA-7 and PA-8) associated with the M31 substructure known as the South West Cloud have ages of 6-10 Gyr, which makes them at least 3 Gyr younger than the oldest MW GCs. However, there is no evidence that GCs associated with stellar streams are in general younger than the rest of the GC population. In fact, some GCs associated with the Sagittarius stream are classified as old halo clusters (Mackey & van den Bergh, 2005), and from proper motion estimates of MW GCs it has also been suggested that young clusters are also formed in-situ (Sohn et al., 2018).

GCs form in tandem with the field stars comprising galaxies (Reina-Campos et al., 2019), taking part in merger events alongside their parent galaxies. With photometry and regular spectroscopy it is difficult to find stars from a tidally disrupted galaxy, therefore the greater surface brightness of its associated GCs renders them more readily identifiable against the background of field stars. This makes a galaxy's GC population a powerful means of inferring a picture of its formation (e.g. Harris, 1991; Forbes et al., 1997; Brodie & Strader, 2006; Kruijssen et al., 2019a,b).

This chapter uses simulations from the E-MOSAICS project (Pfeffer et al., 2018; Kruijssen et al., 2019a) to investigate properties of the GCs associated with stellar streams at $z = 0$. E-MOSAICS houses a suite of 25 zoom-in simulations of MW-mass galaxies. They are selected solely on the basis of their halo mass, meaning they span a wide range of formation histories. This makes the E-MOSAICS galaxies well suited to investigate the properties of GCs associated with stellar streams in a range of environments. I want to only include galaxies with a disc-like morphology, i.e. somewhat similar to the MW, so we exclude any which have undergone a major merger (a merger with a stellar mass ratio greater than 1/4) at $z \approx 0$ or are in the process of undergoing a major merger, since this would greatly disrupt the present day configuration of star particles. I also exclude galaxies which are not of disc-like morphology or do not contain any stellar streams. Therefore we finally have a set of 15 zoom simulations of MW-like galaxies which contain streams to carry out our analysis (these are MW01, MW02, MW03, MW05, MW06, MW07, MW08, MW09, MW10, MW12, MW13, MW17, MW20, MW23 and MW24 in Table 1 of Kruijssen et al. 2019a).

This chapter is organised as follows; in Section 4.2 I discuss how I identify stellar streams in the simulations. In Section 4.3 I examine the ages and the metallicities of the GCs associated with stellar streams relative to those of other GCs associated with the host galaxy and relate these properties to the GC parent galaxy mass and infall time. In Section 4.4 I investigate the relationship between the GC formation history, galaxy mass and infall time to provide a method to estimate the infall time of the Sagittarius dwarf galaxy and in Section 4.5 I compare the results in this paper to observables. Section 4.6 contains the conclusions to this chapter.

4.2 Identifying stellar streams and their associated GCs in E-MOSAICS

4.2.1 Stellar stream identification

The first step towards being able to describe the GC population in stellar streams requires the identification of such structures and their associated GCs in the suite of simulations. The following describes the method I implemented.

The simulations record the history of particles, enabling the user to trace star particles and their associated GCs from formation until $z = 0$. This means I can assign a parent galaxy to the stellar particles and GCs. If their parent galaxy is not the main galaxy then they must have been accreted onto the main galaxy via a merger. This allows the user to view the current positions of the stars and GCs associated with each individual accretion event throughout the main galaxy's formation history, without the contamination from any other stars or GCs in the main galaxy. From this, I can determine whether or not the stars are in a stream like configuration.

The $z = 0$ positions of the stars from each accreted galaxy that contain more than 100 star particles at $z = 0$, corresponding to a stellar mass of $\approx 10^7 M_{\odot}$, is shown in a stellar density map in three projections. Below 100 stellar particles it comes difficult to identify whether an accreted galaxy is in a stream like configuration or not. Al-

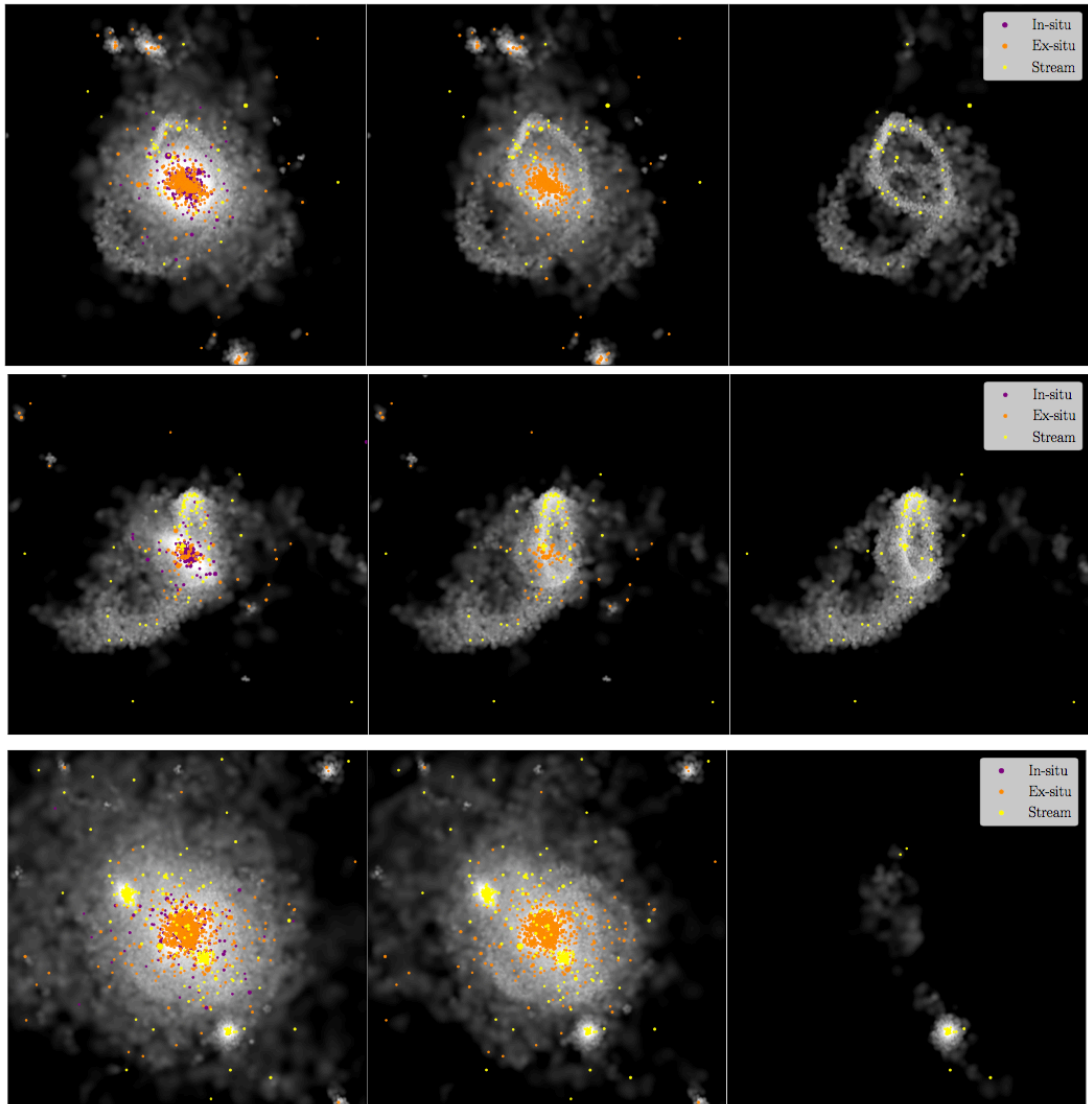


Figure 4.1: Stellar density plots of 3 of the haloes which show clear streams. From top to bottom, we show galaxies MW03, MW09 and MW17. From left to right, the plots show the main galaxy, the accreted component (everything that did not form in the central galaxy) and one clear stream. Each panel is 200 kpc on a side.

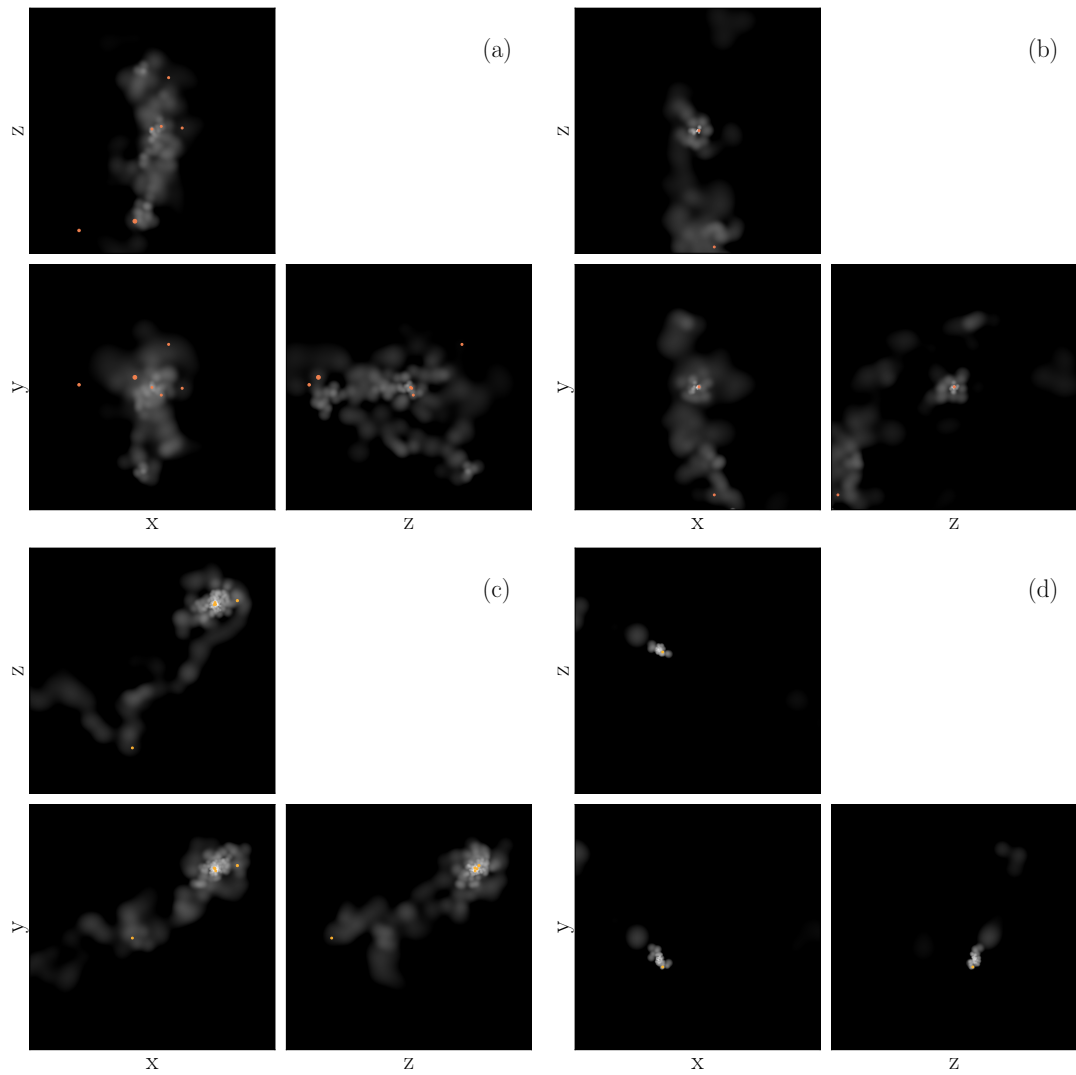


Figure 4.2: Examples of stellar substructure generated during the accretion of a single galaxy. These panels highlight the high diversity in the classification of a stellar stream. All of these events were placed into the stream category. From panel (a)–(d) these are accretion events from MW12, MW17, MW05 and MW13.

though observed stellar streams can have lower masses than the limiting mass of these simulations.

Fig. 4.1 shows three of the galaxies with clear stellar streams (MW03, MW09 and MW17 from top to bottom). The coloured points in this plot represent all of the GCs with a mass greater than $2 \times 10^4 M_{\odot}$. The left hand panels show all the stars and GCs in the main galaxy, the middle panels show just the accreted stars and GCs and the right hand panels show the stars and GCs from just one of the accreted galaxies whose current configuration is classified as stream-like. All of these figures show structures which are unambiguously classified as stellar streams.

Fig. 4.2 shows the stellar density map in three projections of stream-like accretion events, it is from these three 2-D projections of individual accretion events that I identify stream-like substructures. Fig. 4.2 illustrates that there is a considerable diversity of substructures. This makes categorising the accretion events difficult in a minority of cases. In order to combat this, four researchers partook in the classification of streams. A universal classification method was developed for all researchers to follow. For the event to be classified as stream-like the stellar density had to be elongated in at least two of the projections. The identification of streams is complicated by the presence of gravitationally bound, spheroidal relics of accreting satellites, as well as shell-like structures. If the bound object is considered to have a significant tail-like structure then it is classified as a stream. Shell-like structures are more difficult to categorise and therefore I exclude them from the stream sample. Over the 15 galaxies, 3-7 streams are identified per halo with a mean number of streams per halo of 4.5. The percentage of accreted galaxies with a mass greater than $10^7 M_{\odot}$ which leave streams varies between 14-36 % with a mean of 21.4%.

Furthermore, all GCs formed in a galaxy generating a stellar stream were included in the ‘on stream’ category, regardless of their projection onto the stream. Therefore, any GCs that formed in the accreted galaxy, but are not currently visually associated with it, have been included regardless. This is done to account for observers potentially having chemo-kinematic information about the GCs. For example, Palomar 12 is thought to have once been associated with the Sagittarius dwarf galaxy, yet it now sits at a wide

separation from Sagittarius on the sky (Cohen, 2004; Sohn et al., 2018). There are also a handful of other GCs which are candidates for once being related to the Sagittarius dwarf even though they are no longer spatially associated with the stellar component (Forbes & Bridges, 2010).

Once all of the GCs have been classified either into the stream or non-stream category, the analysis includes a selection on GC properties. First of all, a lower mass limit of $2 \times 10^4 M_{\odot}$ is imposed to alleviate the under disruption of low mass clusters in E-MOSAICS. This mass corresponds to a luminosity of $M_V \approx -5$ at old ages (> 10 Gyr). The PAndAS survey begins to suffer from incompleteness at $M_V \approx -6$ and is 50% complete at $M_V \approx -4.1$ (Huxor et al., 2014), therefore this mass limit is reasonable for comparison with the MW and M31. A radius cut of $R > 10$ kpc from the main galaxy’s centre is imposed on all GCs to excise most of the disc GC population. When observing an external galaxy, the central substructure is lost due to the high surface brightness of the main galaxy. This also makes finding GCs in this central region difficult. The radius cut also helps to alleviate the underestimated disruption rate in the centre of the galaxy due to the lack of cold interstellar medium in E-MOSAICS, as discussed in Section 2.1.2.

4.2.2 Definitions

I now define several terms that will be used frequently throughout the rest of this chapter. In-situ and ex-situ define whether the GCs were formed in the main galaxy or not. This is defined as where the gas particle was prior to forming a stellar particle. Figure 10 in Pfeffer et al. (2018) and figure 6 in Kruijssen et al. (2019a) show examples of the merger trees. In these figures, the main branch is highlighted by the thick black line and represents the evolution of the central galaxy. If the gas particle is in a subhalo on the main branch of the merger tree before it becomes a star/cluster population, then this is in-situ star/cluster formation, whereas if the gas particle is on a different branch of the merger tree, then it is ex-situ star/cluster formation. I define GCs that are formed whilst bound to the central galaxy but from the gas that has been accreted as in-situ.

This may affect a minority of cases where a GC forms just after the satellite galaxy has merged with the main galaxy and the gas particle gets assigned to the main galaxy instead of the satellite.

The GCs that are referred to as ‘stream’ are ex-situ GCs by definition, because they had to be formed in a halo other than the main galaxy to be accreted along with the stellar component that then forms a stream. Non-stream GCs are a combination of both in-situ and ex-situ, because they are simply defined as the GCs which are not associated with a stream at $z = 0$.

For reference, properties which are named in the form X_c refer to the GC properties. More specifically, $X_{c,\text{stream}}$ relates to the median of this particular property of all the GCs on this particular stream and $X_{c,\text{non-stream}}$ relates to the median of this particular property of all the GCs, not including those on the stream in question, but still including those from other streams. Properties which are named in the form X_{sat} refer to the accreted galaxy properties. The properties of the GCs we consider are the metallicity ($[\text{Fe}/\text{H}]$) and the age. The properties of the accreted galaxies considered are the stellar mass (M_{sat}) and the infall time (T_{infall}). The infall time is defined as the last time the galaxy enters the halo of the main galaxy¹ and is measured in terms of lookback time. The mass of the stream progenitor galaxy is measured when the stellar mass is at a maximum, before the galaxy is affected by tidal stripping.

4.3 GCs in stellar streams

4.3.1 Properties of GCs associated with stellar streams

I first examine the median ages and metallicities of the GCs on all streams, and GCs not on streams, for each halo. Fig. 4.3 shows these median ages and metallicities for the 15 haloes along with their 16th and 84th percentile bars. The GCs associated with streams exhibit diverse properties. The mean difference in the ages of the stream and

¹Some galaxies undergo multiple crossings of the virial radius.

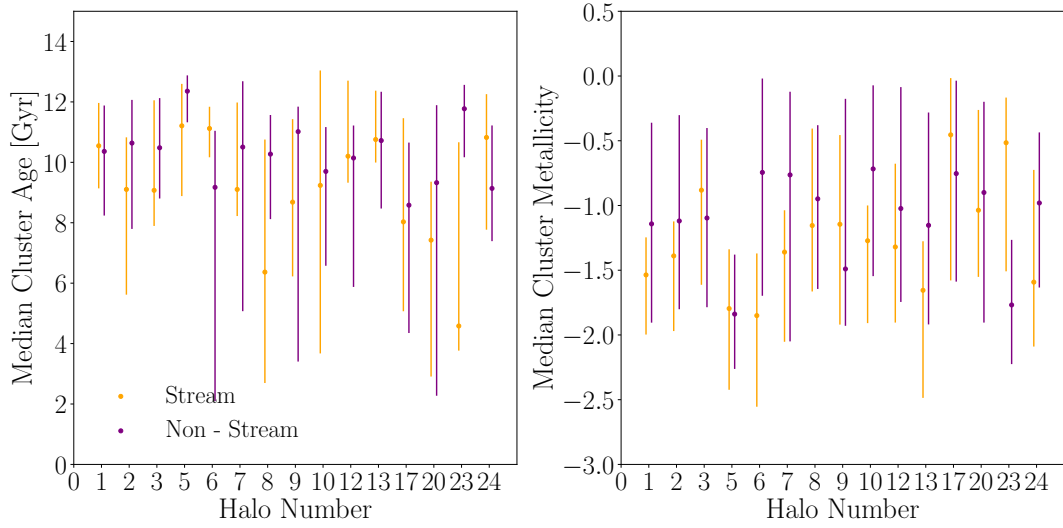


Figure 4.3: Median ages and metallicities of GCs on and off the streams shown with their 16th and 84th percentile bars. Each pair of points represents one simulated halo, where ‘stream’ refers to the median of all the GCs which are associated with all of the streams in a given halo, and ‘non-stream’ refers to the median of all the GCs which are not associated with a stream in this halo. The GCs have undergone the mass, age and radius cuts mentioned previously. Note the large variation from halo to halo.

non-stream populations is -1.19 Gyr (i.e. stream GCs are typically younger) with a standard deviation of 2.15 Gyr. The mean difference in the metallicity of the stream and non-stream population is -0.17 dex (i.e. stream GCs are typically less metal-rich) with a standard deviation of 0.53 dex. This diversity motivates a closer scrutiny of the progenitors of the streams.

Fig. 4.4 shows the relationship between infall time and stellar mass of the stream progenitor galaxies and the median age and metallicity of the GCs they bring into the main halo. The median age of GCs on streams increases with the satellite infall time and decreases with galaxy mass. The median metallicity of GCs on streams decreases with galaxy infall time and increases with galaxy mass. The Pearson r and p coefficients are shown for each of the panels and all the panels show reasonably strong trends. The strongest of these trends is between GC metallicity and galaxy mass (Fig. 4.4, top right). Peng et al. (2006) also investigate the relation between GC metallicity and galaxy mass for the GCs in 100 early type galaxies. The relation of Peng et al. (2006) (their figure 13) for all GCs is shown in this panel by the blue line and I find that the

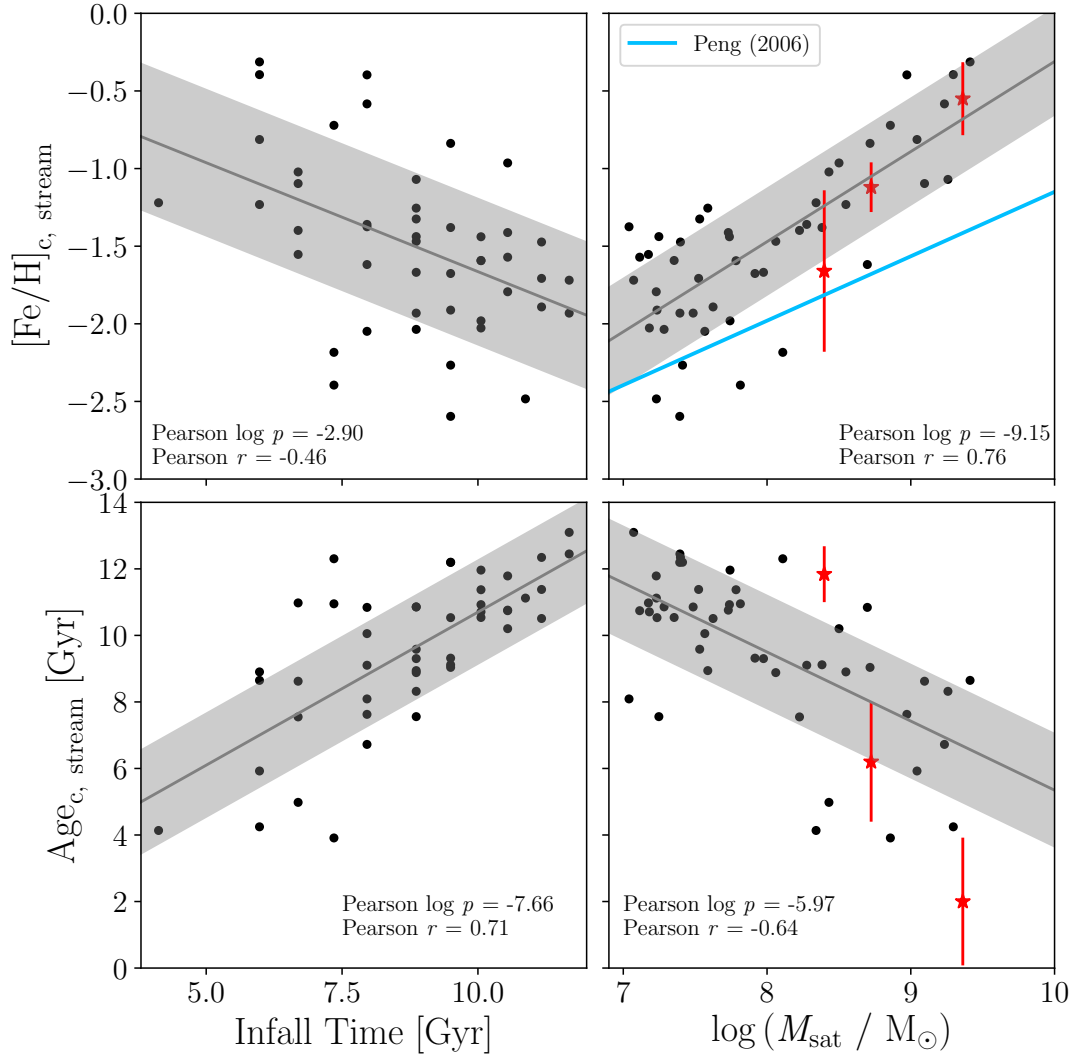


Figure 4.4: Host galaxy properties (lookback time of the crossing of the virial radius, i.e. the 'infall time', and stellar mass) are plotted against the GC properties (median metallicity and median age) in order to highlight key trends. Here, each point represents an individual stream progenitor galaxy across all simulated haloes. The black lines represent the fit and the grey band represents the 1σ scatter of the data around the fit. The red stars represent where the Sagittarius dwarf, the SMC and the LMC (from low to high mass) lie in this parameter space – see the text for age and metallicity references. The mass-metallicity relation of Peng et al. (2006) for all GCs is shown by the light blue line in the top right panel- this has been extrapolated below stellar masses of $5 \times 10^8 M_{\odot}$. Age and metallicity show a clear dependence on the parent galaxy properties, indicated by the Pearson coefficients quoted in each panel.

relation from the simulations is steeper than theirs. The shallower relation of Peng et al. (2006) is potentially caused because they study galaxies which are in a cluster environment, whereas the galaxies we are using for this work occupy less dense environments and we resolve much lower galaxy and GC masses. Galaxies which reside in cluster environments are likely to have been quenched and therefore dwarf galaxies around MW-like galaxies have more extended star formation histories and therefore contain higher metallicity clusters. Also, galaxies in clusters are more likely to grow via the accretion lower mass galaxies which bring with them lower metallicity GCs. The steeper relation could also be a simulation effect in that we do not disrupt enough higher metallicity clusters, although this is partially ruled out by confirming that the local group dwarf galaxies lie within our steeper relation.

I compare these results with observations by placing the Sagittarius dwarf, the SMC and the LMC in this figure. I take the GCs most likely to be associated with the Sagittarius stream from Law & Majewski (2010b) and find a median $[\text{Fe}/\text{H}] = -1.5$ and a median age of 11.84 Gyr (using the average ages and metallicities from Forbes & Bridges 2010; Dotter et al. 2010, 2011 and VandenBerg et al. 2013)². The LMC and SMC are also currently falling into the halo of the MW and are beginning produce a stellar stream-like structure (e.g. D’Onghia & Fox 2016). The LMC and SMC GCs have a median GC metallicity and age of $[\text{Fe}/\text{H}] = -0.55$ and 2 Gyr (Suntzeff et al., 1992; Gilmozzi et al., 1994; Hunter et al., 1995; Da Costa, 1998; Olsen et al., 1998; Dirsch et al., 2000; Hill et al., 2000; Geisler et al., 2003; Piatti et al., 2003; Mackey & Gilmore, 2004; Mackey & Broby Nielsen, 2007; Ferraro et al., 2006; Kerber et al., 2007; Mucciarelli et al., 2008; Mucciarelli, 2009; Mucciarelli et al., 2011, 2012; Palma et al., 2013; Li et al., 2013; Mackey et al., 2013; Mucciarelli et al., 2014; Wagner-Kaiser et al., 2017) and $[\text{Fe}/\text{H}] = -1.12$ and 6.2 Gyr (Da Costa & Hatzidimitriou, 1998; Sirianni et al., 2002; Glatt et al., 2008; Dalessandro et al., 2016), respectively. With a stellar mass of $\approx (2 - 3) \times 10^8 M_{\odot}$ (Niederste-Ostholt et al., 2010) this would place Sagittarius slightly lower than the relation in the top right panel but still within the scatter. The SMC and LMC have masses of $2.3 \times 10^9 M_{\odot}$ and $5.3 \times 10^8 M_{\odot}$,

²I have excluded Berkley 29 and Whiting 1 from this analysis to be consistent with our mass cut.

respectively (James & Ivory, 2011), they also lie within the mass-metallicity relation for satellites of late type galaxies. I can also place Sagittarius, the SMC and the LMC in the bottom right panel. The LMC lies much lower than the relation here. However, the black points in this figure represent satellite galaxies which are now streams, and the SMC and the LMC have not yet formed a stream like structure owing to their relatively recent accretion. The comparison here with the progenitors of streams in the simulations may therefore may not be wholly like-for-like.

There is a wide range in the properties of the stellar streams shown in Fig. 4.4, causing the large scatter in the global GC properties of each halo as shown in Fig. 4.3. Streams with more massive progenitors contain younger and more metal-rich GCs than streams with less massive progenitors. Streams that fell into the main galaxy more recently also have younger and more metal-rich GCs. In the following sections I investigate mass and the infall time of the galaxies and the properties of their GCs.

Finally, note that the infall time is discreet due to the snapshot resolution of the simulations.

4.3.2 Comparisons of GC properties on and off streams

I now investigate the properties of the GCs on one particular stream relative to the rest of the GC population (the GCs not associated with this particular stream), and then, relate it to the mass and infall time of the stream progenitor galaxy. The motivation for this investigation is that in some observational cases we may be able to associate a given set of GCs with a stellar stream but do not know where the rest of the GCs in the halo came from. In Fig. 4.5 each point represents a single stream. The x -axis represents the median $[\text{Fe}/\text{H}]$ of the GCs on the stream relative to the median $[\text{Fe}/\text{H}]$ of the rest of the population. The y -axis represents the median age of the GCs on the stream relative to the median age of the rest of the GC population. The points in the left panel are coloured by the maximum stellar mass of the satellite galaxy before infall and the colours in the right panel represent the infall lookback time of the stream progenitor galaxy. Streams that have younger GCs also have more metal rich GCs and

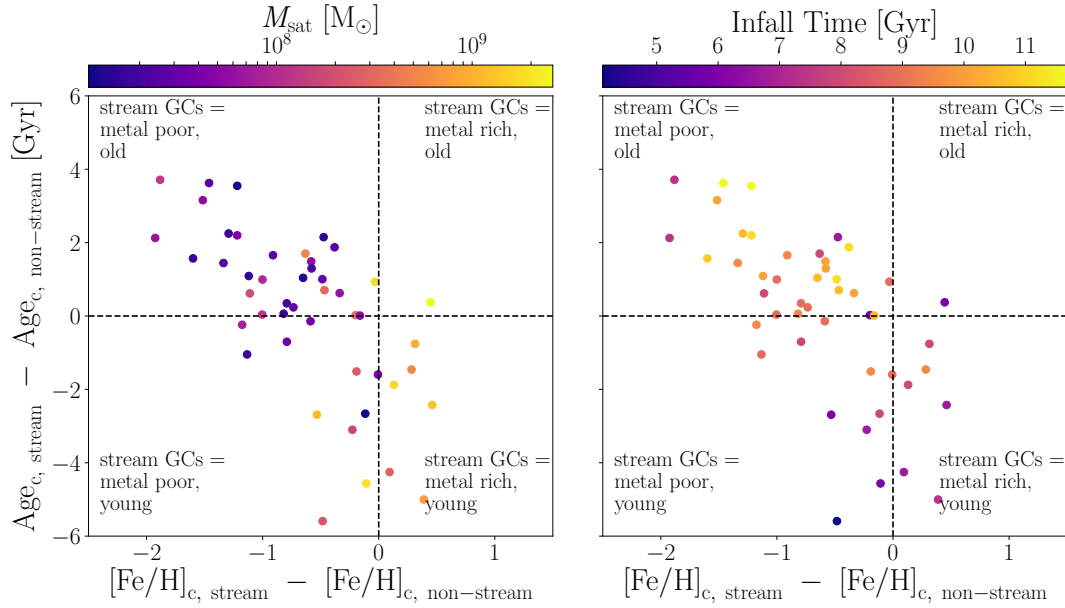


Figure 4.5: The difference in the median GC ages between the stream and non stream GCs, within the same halo, plotted as a function of the difference in their median metallicities. Each point represents one stream. The non-stream population refers to all the GCs which survive the various property cuts which do not lie on this particular stream; it therefore includes GCs which lie on other streams in this halo, GCs which have been accreted but do not lie on a stream and GCs formed in the main galaxy. Left panel: the colours represent the host galaxy’s stellar mass. Right panel: the colours represent the virial radius crossing time. There is an anti correlation between age and metallicity. More massive galaxies which crossed the virial radius more recently are more likely to have GCs on streams which are younger and more metal rich.

come from more massive progenitor stream galaxies that are accreted later. It is these two competing effects that cause the variation among galaxies we see in Fig. 4.3.

Using Fig. 4.5, I can restrict the sample to only the most massive streams that fell into the halo recently, since these are those that are readily observable. These streams present younger and more metal rich GCs than the rest of the population. This can also be seen in M31, where the observable streams do show younger GCs (Mackey et al., 2019). Lower mass streams that fell into the halo of the main galaxy longer ago tend to harbour GCs that are older and more metal poor than the rest of the population.

Note the lack of GCs in the top right quadrants of Fig. 4.5: there are no satellite galaxies that bring with them relatively old and metal-rich GCs. In order to populate this region of the plot, the GC host galaxy would have had to self-enrich faster than

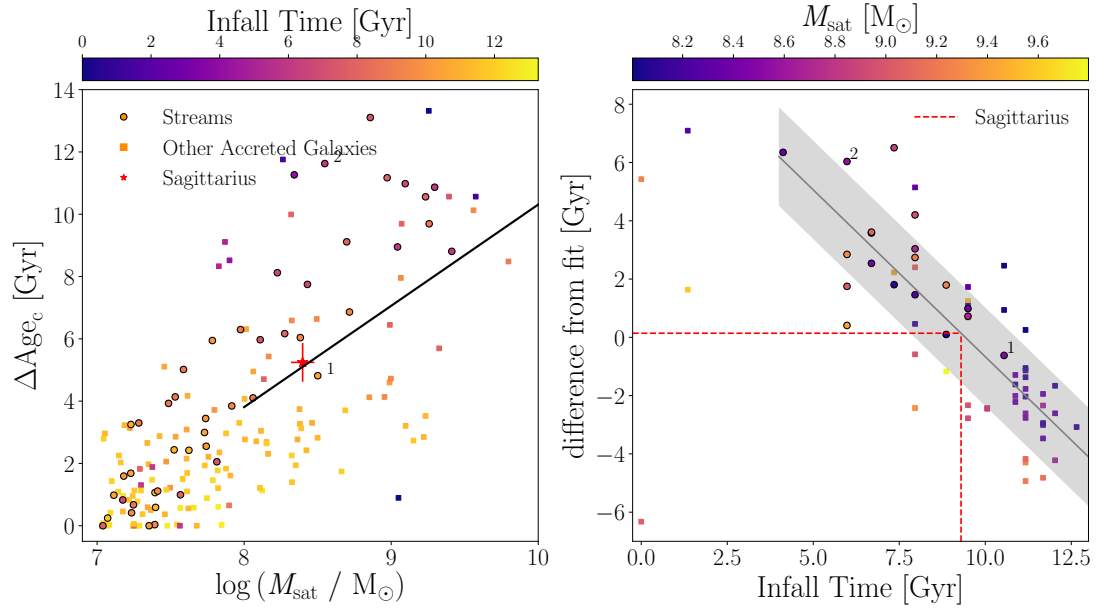


Figure 4.6: Left panel: the age range of the GCs which have been accreted with a satellite galaxy as a function of the parent galaxy’s stellar mass, the solid black line represents the best fit line for satellite galaxies with a stellar mass greater than $10^8 M_{\odot}$, the red symbol with error bar represents the position of the Sagittarius dwarf galaxy. Right panel: the difference from the line of best fit for each satellite galaxy above $10^8 M_{\odot}$, the solid grey line represents the best fit line and the grey band represents the 1σ scatter of the data around the fit, the red dotted line represents the method for estimating an infall time for the Sagittarius dwarf galaxy, discussed in Section 6.6. Each point represents an accreted galaxy, those accretion events that are seen as streams at $z = 0$ are represented by circles and the rest of the accreted galaxies are represented by squares. The points labelled 1 and 2 will be used in Fig. 4.7 to investigate the star formation histories of two galaxies at the same mass but with different age ranges.

the present day central galaxy. But the enrichment history and metallicity depends on galaxy mass (Petropoulou et al., 2012), so for a galaxy which forms a stream in the halo of the main galaxy, this is unlikely.

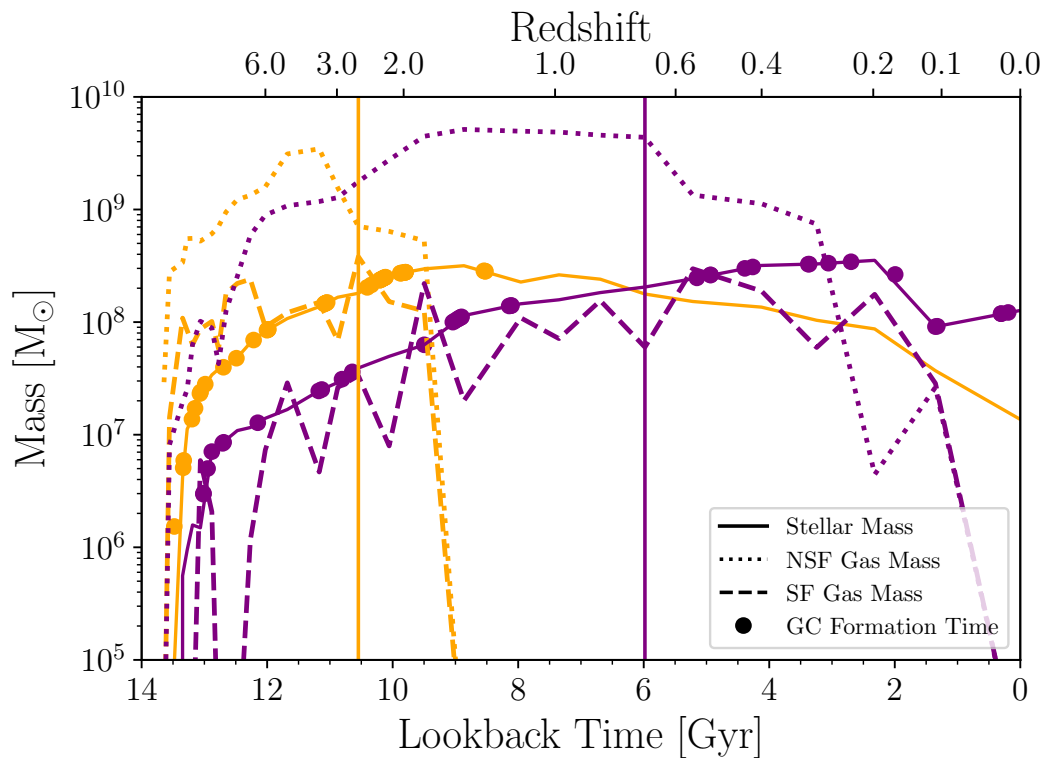


Figure 4.7: The star formation histories of two accreted galaxies that produce streams. The orange lines correspond to the galaxy labelled 1 in Fig. 4.6 and the purple lines correspond to the galaxy labelled 2 in Fig. 4.6. The gas is split up into star forming (dashed lines) and non star forming (dotted lines). Note how the galaxy which crossed the virial radius (shown by the vertical lines) longer ago also stopped forming GCs longer ago, which is due to gas stripping.

4.4 The Relationship Between GC Formation History, Galaxy Mass and Infall Time

4.4.1 Total age range of GCs

The GC age range is a direct probe of the GC formation history: a greater GC age range indicates a more extended GC formation history. The left panel of Fig. 4.6 shows that, on average, more massive satellite galaxies have greater GC age ranges than lower mass satellite galaxies. In Fig. 4.6 I separately show all galaxies that have been accreted, to assess whether the accretion events producing streams form a distinct group. Interestingly, the satellite galaxies that produce streams have a large GC age

4.4. *The Relationship Between GC Formation History, Galaxy Mass and Infall Time*

range for their mass. To understand this, we have to consider the reason why we see a stream – the galaxy must have produced a stream-like structure as it fell into the main galaxy halo and the stars must have then stayed in this configuration for long enough for us to observe a stream at $z = 0$. Therefore, a galaxy which causes an observable stream at present day is more likely to have fallen into the halo of the main galaxy more recently and has not had as long to disrupt. As I will discuss in Section 4.4, galaxies that entered the halo of the main galaxy more recently at a given mass have a greater GC age range, which would cause the streams to reside near the top of this distribution.

Even though the relation is relatively tight, at a given galaxy mass, there is a large scatter in the GC age range – up to 10 Gyr for the more massive satellites. I select two galaxies of approximately equal stellar mass but different GC age ranges, the two galaxies which are labelled as 1 and 2 in Fig. 4.6. I show the time evolution of their stellar and gas masses in Fig. 4.7. The points on the line representing the stellar mass show the formation epochs of the GCs that survive until present day (44 and 37 respectively). In both cases, the mass of the gas and stellar component increases until the galaxy enters the halo of the main galaxy - shown by the vertical lines in Fig. 4.7. Note here that we are limited by the snapshot time resolution of the simulation, so the fact that galaxy 1 starts to lose its non-star forming gas (NSF) before infall is not necessarily a real effect, but is in fact because it entered the halo of the main galaxy at a time between the two snapshots. After infall, both galaxies start to lose NSF gas immediately and galaxy 1 also starts to lose its star forming (SF) gas. Galaxy 2 holds onto its SF gas for longer after infall, but in both cases there is a rapid and complete loss of all gas and a truncation in GC formation. Therefore, at a fixed galaxy mass, the age range of the clusters associated with a satellite galaxy is potentially dependent on the infall time. Galaxy 1 has a smaller GC age range in Fig. 4.6 than galaxy 2 because it fell into the halo of the main galaxy much earlier, shortening the GC formation history.

The low mass galaxies (i.e. $M_{\text{sat}} < 10^8 M_{\odot}$) may have their GC formation truncated due to a variety of physical processes (such as stellar feedback), meaning that their infall time may not be well traced by their GC formation histories. To alleviate this, I do not include galaxies with masses lower than $10^8 M_{\odot}$ in the rest of this analysis. I

4.4. *The Relationship Between GC Formation History, Galaxy Mass and Infall Time*

investigate the infall time being the reason for the scatter in the left panel of Fig. 4.6 by subtracting off the mean relation of ΔAge_c as a function of satellite galaxy stellar mass (solid line in top panel) and showing the residual against the infall time in the right panel of Fig. 4.6. There is a strong correlation between difference from the line of best fit and infall time, indicating that the scatter in the age range at a given galaxy mass is indeed due to the satellite infall time. The galaxies that cross the virial radius of the main galaxy later build up their mass more slowly and have longer to form clusters free from severe environmental influences than those which build up their mass and fall into the halo of the main galaxy early in their evolution. This leads to a smaller cluster age range for satellites accreted early on. The fit to the data in the right panel is shown by the grey solid line. I do not include the four points with infall time less than 2 Gyr ago, for two reasons. The satellite galaxy with a difference from fit of below -6 is considered an outlier because it is a 'backsplash' galaxy (Gill et al., 2005) i.e. it is an earlier crossing of the virial radius which causes this galaxy to stop forming GCs (this is discussed in section 4.4.2). The other three galaxies with infall time < 2 Gyr are outliers due their recent infall – their ΔAge_c is not yet fixed and could potentially continue to grow if the simulation was to continue running.

4.4.2 GC formation after infall

As discussed above, infall into the main galaxy halo and subsequent gas stripping is the main reason for the truncation of GC formation in satellite galaxies. However, some galaxies continue to form clusters after they have entered the halo of the main galaxy, this is seen in the SMC and the LMC. I now investigate how long GCs continue to form after the satellite has fallen into the main group ($T_{\text{infall}} - \min(\text{Age}_c)$) with respect to the galaxy mass and infall lookback time (Fig. 4.8).

I present the time for which GCs continue to form after the satellite galaxy has entered the halo of the main galaxy as a function of the satellite galaxy stellar mass in Fig. 4.8 and find that more massive galaxies can continue to form GCs for longer after entering the halo of the main galaxy. I can investigate this effect in relation to the time of infall

4.4. The Relationship Between GC Formation History, Galaxy Mass and Infall Time

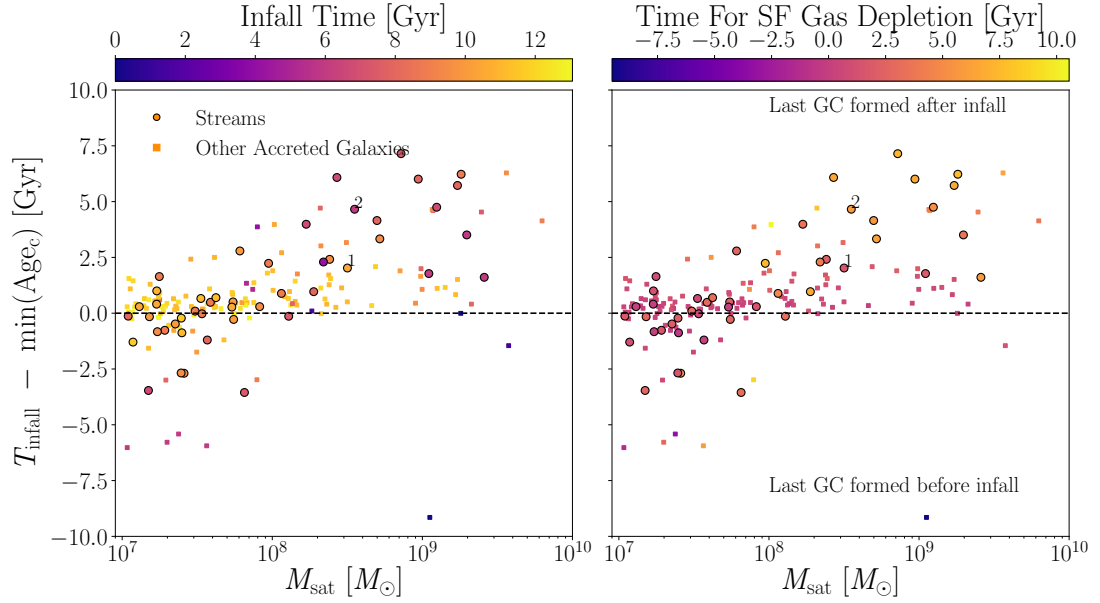


Figure 4.8: Time for which GCs continue to form after they have crossed the virial radius as a function of galaxy mass. The points are coloured by the infall time (left panel) and the time for which the galaxy retains its star forming gas after falling into the halo of the main galaxy (right panel) .

(Fig. 4.8, left panel) and the time for which the galaxy retains its star forming gas after infall (Fig. 4.8, right panel). I will divide this discussion into whether the last GC forms during, after or before infall, that is when $T_{\text{infall}} - \min(\text{Age}_c) \approx 0, \gg 0$ or $\ll 0$ respectively.

Those satellites that stop forming GCs during infall are accreted early in the formation of the main galaxy, and lose their star forming gas almost immediately upon infall. In the early universe, when these galaxies are accreted, all halos are smaller. This means mergers happen on shorter time-scales and, consequently, star-forming gas gets stripped and GC formation truncates faster, which leads to a smaller GC age range after infall. This is demonstrated in Fig. 4.9, where we present the time for which the satellite continues to form clusters after infall against the time it takes for the satellite to merge with the main galaxy after infall ($T_{\text{infall}} - T_{\text{merger}}$). I find that a quick truncation of GC formation after infall ($T_{\text{infall}} - \min(\text{Age}_c) \approx 0$) is due to a quick merger time and these quick mergers typically happen in early accretion events. Fig. 4.9 only shows satellite galaxies with a mass greater than $10^8 M_{\odot}$ because, as discussed above, below

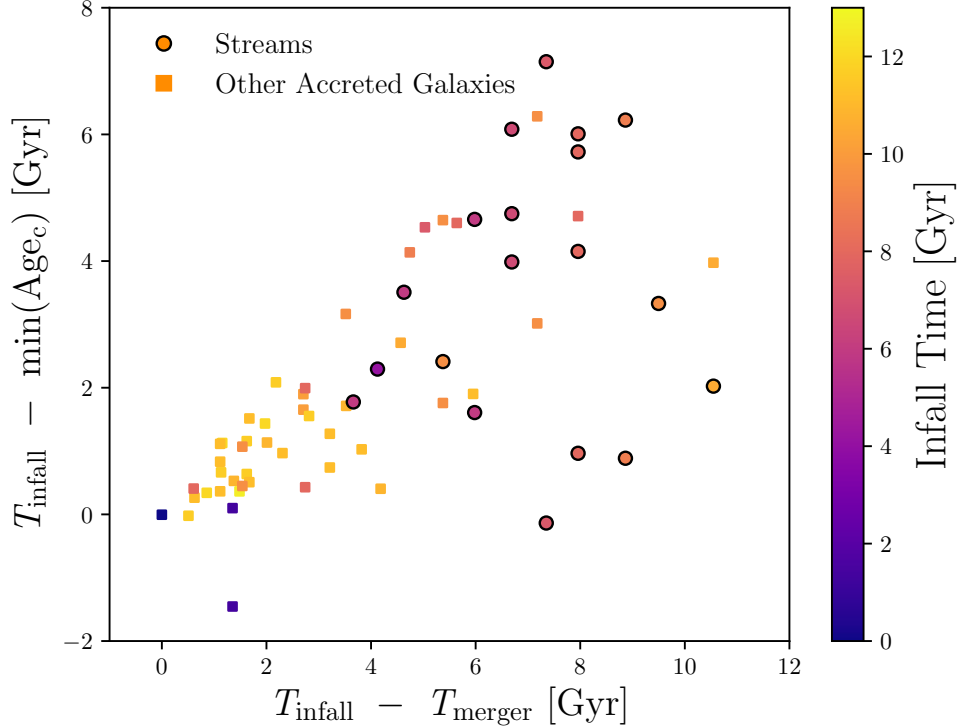


Figure 4.9: Time for which GCs continue to form after they have crossed the virial radius as a function of how long the satellite galaxy takes to completely merge with the main galaxy after it has crossed the virial radius. Only galaxies with $M > 10^8 M_{\odot}$ are shown. The points are coloured by infall time. We see that faster mergers happen at earlier times.

this mass some satellite galaxies stop forming GCs due to reasons other than infall into the main halo. This population of galaxies at $T_{\text{infall}} - \min(\text{Age}_c) \approx 0$ does not contain many stellar streams due to their early infall times, i.e. if a stream is produced, it is unlikely to survive until present day.

Those satellites that continue to form GCs after their infall are accreted later in the formation of the main galaxy. They show a dependency on their stellar mass. At greater masses, these galaxies can retain their star-forming gas for a longer time and retain high enough pressures to continue to form clusters. Many of the satellite galaxies in this population produce streams because the galaxies were accreted later and so the stream survives until present day.

Those satellites that stop forming GCs before their infall are accreted later in the forma-

tion of the main galaxy but stop forming clusters before they cross the central galaxy's virial radius. These are low mass galaxies ($M_{\text{gal}} < 10^8 M_{\odot}$) that formed all of their GCs within a few Gyr (Fig. 4.6 shows lower GC age ranges for lower mass galaxies). The low masses and densities of these galaxies imply that even the feedback from a burst of star formation can cause GC formation to cease. Many of these satellite galaxies also produce streams due to their later infall.

Finally, it is important to note here that I define infall time as the last time the satellite galaxy crossed the virial radius of the main galaxy. For most galaxies the last time they crossed the virial radius is an accurate representation of the interaction that caused the most change to the galaxy. However, in a few cases it is an earlier interaction with the main galaxy that causes the loss of star-forming gas and the truncation of GC formation – these are known as backplash galaxies (Gill et al., 2005). This affects the very blue point that has $T_{\text{infall}} - \min(\text{Age}_c) \approx -9$ and a mass $M_{\text{gal}} \approx 10^9 M_{\odot}$ in Fig. 4.8. It is an interaction with the main galaxy 9 Gyr ago that causes this galaxy to lose star forming gas and stop forming GCs.

4.5 Comparisons With Observations

Observations of streams in the MW and other galaxies will be biased towards the most massive and recent accretion events, as these events are easier to observe both by overdensities of stars and kinematically. If I focus the stream sample in this chapter on relatively high mass galaxies that were accreted recently, from Fig. 4.4 I find that they should host GC populations that are statistically younger, have a larger age range and are more metal-rich than the median across the entire accreted satellite population.

GCs on extragalactic stellar streams are much easier to study than individual stars, due to their higher surface brightness. Observations of the GC population outside 30 kpc of the centre of M31 have shown that a large fraction of these GCs are situated on streams (Mackey et al., 2010) and this has also been found to be the case for other galaxies outside the Local Group (e.g. Romanowsky et al. 2012; Powalka et al. 2018). As is

the case for the Sagittarius dwarf, the simulations predict that the mean age of these GCs is younger than the other GCs associated with these galaxies. Age dating GCs at these distances (where colour-magnitude diagrams generally do not reach the main sequence turn-off) can be difficult. However, if these GCs are younger than 9–10 Gyr, they would not be expected to have an extended blue horizontal branch. Instead, they should have a compact red clump (or red horizontal branch) (e.g. [Gratton et al., 2010](#)). Deep HST and/or ground based images will be able to test this prediction. In addition, relative ages between GC (sub)populations may be obtained by combining multi-band photometry with spectroscopy ([Usher et al., 2018](#)). With ages and metallicities of these GCs, parent galaxy mass and infall time could also be predicted for external galaxies.

Throughout this chapter, I have compared various results to the GCs found in the Sagittarius dwarf galaxy, which is currently generating a large stellar stream in the halo of the MW. I show that the median metallicity and the median age of the clusters which have been associated with this stream are consistent with those found for the streams in this chapter at similar galaxy stellar masses. I can use Fig. 4.6 to estimate the time at which the Sagittarius dwarf galaxy began its infall into the MW halo. Sagittarius was relatively massive before it fell into the halo of the MW with a stellar mass of $\approx (2 - 3) \times 10^8 M_{\odot}$, (e.g. [Niederste-Ostholt et al. 2010](#)). Considering the GCs that have a high to moderate confidence of being associated with the Sagittarius stream from [Forbes & Bridges \(2010\)](#)³ and the average ages from [Forbes & Bridges \(2010\)](#); [Dotter et al. \(2010, 2011\)](#) and [VandenBerg et al. \(2013\)](#), (see the compilation in Appendix A of [Kruijssen et al. 2019b](#)) the GCs likely to be associated with the Sagittarius stream have an age range of 5.24 Gyr, shown in the left panel of Fig. 4.6. I can then find the difference of Sagittarius from the line of best fit, which can be used in the right panel of Fig. 4.6 to estimate the infall time of Sagittarius – shown by the red dotted line in this figure. The uncertainty on the infall time is calculated by first considering the uncertainty on the difference of Sagittarius from the fit in the left panel. This includes the difference in the ΔAge_c from the uncertainty on the stellar mass and the difference in the ΔAge_c from the uncertainty on the age of the youngest and the oldest Sagittarius

³As in our previous analysis we exclude Berkley 29 and Whiting 1 based on their mass.

cluster. The uncertainty in the difference from fit is then propagated through to the bottom panel and is combined with the dispersion in the difference from fit against infall time parameter space to calculate a final uncertainty on the infall time. I estimate an infall lookback time (time of virial radius crossing) of 9.3 ± 1.8 Gyr. [Dierickx & Loeb \(2017\)](#) predict an infall lookback time of the Sagittarius dwarf of 8 ± 1.5 Gyr based on the age of the M giants in the stream calculated by [Bellazzini et al. \(2006\)](#), which is consistent (albeit somewhat lower than) the value predicted by this analysis.

4.6 Conclusions

I present the GC properties of 15 MW-like haloes of the E-MOSAICS simulations. I specifically investigate the properties of GCs that are associated with stellar streams relative to the rest of each galaxy's GC population. I find a large variation in the median ages and metallicities of the clusters on individual streams. It is found that more massive and recently accreted galaxies host GCs that are more metal rich and younger than the rest of the population, whereas less massive and earlier accreted galaxies harbour GCs that are older and more metal poor than the rest of the population. Applying this to M31, where massive and recent accretion events are easier to detect, I expect that GCs associated with stellar streams are, on average, younger than the rest of the population. This is consistent with observed GCs in M31 where GCs on streams are indeed found to be younger, on average, than GCs not on streams ([Mackey et al., 2019](#)).

Two effects contribute to the GC age ranges of satellite galaxies. The first is that more massive streams host younger and more metal rich GCs because they entered the halo of the main galaxy more recently – this allowed the satellites to continue form GCs for a longer time without being subject to strong environmental effects, resulting in a more extended GC formation history and younger GCs. Using the E-MOSAICS simulations, I find that the GC age range is more extended for more massive satellites, but there is a relatively large scatter at a given satellite mass. This scatter is determined by the infall time (i.e. the last time a galaxy enters the virial radius of the main galaxy, see Fig. 4.6). Galaxies that enter the halo of the main galaxy more recently have longer to evolve in

isolation and therefore have a more extended GC formation history than galaxies of the same mass which entered the halo of the main galaxy early in cosmic history. The second effect is that more massive galaxies have more extended GC formation histories because they retain their star-forming gas for longer after infall into the main galaxy.

With a reliable way of associating observed GCs with stellar streams, it would be possible to take all of the GCs associated with a stellar stream and use their median metallicity and the relation between median GC metallicity and galaxy stellar mass shown in Fig. 4.4 to estimate a mass of their parent galaxy. Using this derived mass and the age range of the GCs, I could then place this galaxy in Fig. 4.6 to estimate its infall time. In this chapter, this is done for Sagittarius and an infall time of 9.3 ± 1.8 Gyr ago is calculated. [Kruijssen et al. \(2019b\)](#) predict the existence of three main satellites of the Milky Way, the least massive of which is Sagittarius. The other two satellites (the ‘Sausage’ identified by [Myeong et al. 2018](#) and the enigmatic galaxy ‘Kraken’ inferred by [Kruijssen et al. 2019b](#)) are indistinguishable in the age-metallicity relation of the Milky Way, but [Kruijssen et al. \(2019b\)](#) predict that they were accreted at $z < 2$, i.e. more recently than ≈ 10 Gyr ago. This suggests that all three of the major satellites of the Milky Way were accreted after $z = 2$.

Observations of GCs on streams are biased to massive stream progenitors, such as the Sagittarius stream, which explains why GCs observed to be on streams are younger on average than the rest of the GC population. The E-MOSAICS simulations show that when moving down to lower mass stream progenitor galaxies it is possible to probe earlier accretion events, which contribute older GCs. However, to be able to probe these masses and infall times, better stellar stream detection and GC association methods are needed – both of which will be facilitated within the Milky Way by current and future Gaia data releases.

Chapter 5

The $[\alpha/\text{Fe}]$ - $[\text{Fe}/\text{H}]$ relation in the E-MOSAICS simulations: its connection to the birth place of globular clusters and the fraction of globular cluster field stars in the bulge

5.1 Introduction

The element abundances of stars and globular clusters (GCs) are powerful tools with which to extract information about the time and place of their formation, giving us an insight into how galaxies form and assemble. The element abundances of Milky Way (MW) GCs are often used to assess whether they formed in the MW or in a satellite galaxy that was later accreted. A powerful set of abundances are those of the α elements. The abundance ratio of α elements to iron, $[\alpha/\text{Fe}]$, is an important tracer of the relative contributions of Type II/Ia supernovae (SN), since only Type II SN contribute to the production of α elements whereas both contribute to iron ([Wheeler et al., 1989](#)). This makes $[\alpha/\text{Fe}]$, together with $[\text{Fe}/\text{H}]$, a good tracer of the enrichment history of a

galaxy. For example, a star or GC with a high $[\alpha/\text{Fe}]$ at fixed $[\text{Fe}/\text{H}]$ indicates that its progenitor gas was enriched primarily with α elements synthesised and promptly released by Type II supernovae, whilst incorporating relatively little iron synthesised by Type Ia supernovae (Wheeler et al., 1989; McWilliam, 1997). In many galaxies, low $[\text{Fe}/\text{H}]$ stars that formed before Type Ia SN enriched the interstellar medium (ISM) show a relatively constant $[\alpha/\text{Fe}]$. There is then a ‘knee’ in the $[\alpha/\text{Fe}]$ - $[\text{Fe}/\text{H}]$ distribution, where stars begin to form from the Type Ia SN enriched material, followed by a downwards trend of decreasing $[\alpha/\text{Fe}]$ as the ISM continues to be enriched by Type Ia SN. Lower mass galaxies do not self enrich as fast as higher mass galaxies and therefore the position of the ‘knee’ is shifted to lower $[\text{Fe}/\text{H}]$ (e.g. Pritzl et al. 2005; Tolstoy et al. 2009).

The $[\alpha/\text{Fe}]$ - $[\text{Fe}/\text{H}]$ distribution of field stars in cosmological simulations has been addressed in several recent studies. Mackereth et al. (2018) used the EAGLE simulations to investigate the $[\alpha/\text{Fe}]$ - $[\text{Fe}/\text{H}]$ distribution around the solar neighbourhood of 133 MW-like galaxies in terms of their stellar mass and kinematics. They found a diversity in the shape of the distributions, noting that only five per cent of them show a bimodal $[\alpha/\text{Fe}]$ distribution, similar to that exhibited by the MW. The simulations indicate that this bimodality, in particular the appearance of a high- α sequence, occurs in galaxies that experience rapid growth at early epochs ($1 < z < 2$) in response to a period of vigorous star formation triggered by the atypically early formation of their dark matter halo. The low- α sequence is then formed by a subsequent prolonged period of less intense star formation. The non-bimodal galaxies in their sample tend to have a more consistent growth across all epochs and a period of rapid growth is not present. The authors therefore concluded that the MW also underwent a rapid early growth, making it an atypical L^* galaxy. Grand et al. (2018) found $[\alpha/\text{Fe}]$ bimodality in the disc populations of six MW-sized halos in the Auriga simulations. Consistent with Mackereth et al. (2018), they attribute bimodality in the inner disc to a central starburst (caused by a gas rich merger), followed by less intense star formation. In the outer disc, they further attribute $[\alpha/\text{Fe}]$ bimodality to early α -rich star formation in a gas disc, followed by a shrinking of the disc that lowers the star formation rate. It is of particular interest

that both studies attribute a high- α sequence to an early, rapid star formation episode (also see [Kruijssen et al., 2019b](#)).

In the MW GCs exhibit similar $[\alpha/\text{Fe}]$ to field stars at fixed $[\text{Fe}/\text{H}]$ (e.g. [Pritzl et al. 2005](#)). However, there are some Galactic GCs, such as Ruprecht 106 (Rup 106) and Palomar 12 (Pal 12) that have relatively low $[\alpha/\text{Fe}]$ ratios for their $[\text{Fe}/\text{H}]$ values with respect to both the MW field stars and other GCs. It has been hypothesised that these GCs have been captured from dwarf galaxies with a different chemical enrichment history to the MW ([Lin & Richer, 1992](#); [Snedden, 2004](#); [Pritzl et al., 2005](#); [Forbes & Bridges, 2010](#)). A similar offset is also seen when comparing stars in dwarf galaxies with the MW field stars ([Pritzl et al., 2005](#); [Tolstoy et al., 2009](#)).

In the field stars, element abundances can be useful for finding groups of stars that were born in the same molecular cloud: this is called ‘chemical tagging’, a concept introduced by [Freeman & Bland-Hawthorn \(2002\)](#). Finding the stars that once belonged to bound clusters has become a major topic with the recent advances in Galactic surveys such as APOGEE ([Majewski et al., 2017](#)), Gaia-ESO ([Gilmore et al., 2012](#)), RAVE ([Steinmetz et al., 2006](#); [Zwitter et al., 2008](#); [Siebert et al., 2011](#)) and GALAH ([De Silva et al., 2015](#); [Buder et al., 2018](#)). With these surveys it is possible to tag chemically hundreds of thousands of stars, making it possible to identify stars likely to have once been members of the same star cluster (e.g. [Price-Jones & Bovy 2019](#)). This same technique may be used to identify stars that once belonged to the same dwarf galaxy, providing an insight into the accretion history of the MW. On a larger scale, chemical tagging to find disrupted GCs and dwarf galaxies gives some clues about the early star formation process of the galaxy and its dynamical history ([Ting et al., 2015](#)).

In addition to identifying stars that were born in the same molecular cloud, it is also interesting to consider more broadly the fraction of field stars that originated in GCs. If the fraction of stars formed in bound star clusters varies with the surface density of star formation (e.g. [Kruijssen, 2012](#)), then the disrupted GC contribution to the thin disk, thick disc and bulge offers clues as to how each of these components formed. Stars that have formed within GCs can be identified by exploiting star-to-star abundance variations within GCs (e.g. [Fernández-Trincado et al. 2019](#)), known as multiple

populations (e.g. Gratton et al. 2004; Bastian & Lardo 2018). This has been carried out in the halo of the MW, where 2-3 per cent of halo stars were found to exhibit chemical signatures seen in GC stars (Martell et al., 2011; Carollo et al., 2013; Martell et al., 2016; Reina-Campos et al., 2020). These studies then attribute 4-17 per cent of halo stars as once being part of a GC, depending on the GC formation mechanism and the fraction of enriched stars initially within GCs. Schiavon et al. (2017) carried out a similar analysis in the Milky Way bulge in a specific metallicity range of $[\text{Fe}/\text{H}] < -1$ and, by finding nitrogen-enriched stars, concluded that 14 percent of the stellar mass of the bulge came from disrupted GCs.

Alongside the work presented in this chapter, I investigate the GC contribution to the halo of the 25 simulated MW-mass galaxies from the E-MOSAICS simulations in another publication which I contributed to. We find a median of 0.3 per cent of the mass in halo field stars formed in GCs, indicating that the disruption of GCs plays a sub-dominant roll in the build-up of galaxy stellar haloes (Reina-Campos et al., 2020).

In this chapter I continue the study of α abundances in cosmological simulations using the 25 zoom-in E-MOSAICS simulations described by Pfeffer et al. (2018) and Kruijssen et al. (2019a), which enable me to follow the formation, evolution and disruption of GCs alongside the evolution of their host galaxy. I discuss the differences and similarities between the field stars and GCs and the in-situ and ex-situ GCs in Section 5.2. In Section 5.3, I investigate the formation and disruption of GCs in the $[\alpha/\text{Fe}]-[\text{Fe}/\text{H}]$ plane. In Section 5.4, I present how the amount of GC disruption (particularly that in the bulge) can be related to the shape of the field star $[\alpha/\text{Fe}]-[\text{Fe}/\text{H}]$ distribution and subsequently the formation time of the galaxy. Finally, in Section 5.5 I present the conclusions of this chapter.

5.2 The α abundances of globular clusters and field stars

The α element abundances of GCs have been used to establish whether a GC is likely to have been formed in-situ or ex-situ, under the assumption that a GC with low $[\alpha/\text{Fe}]$ at

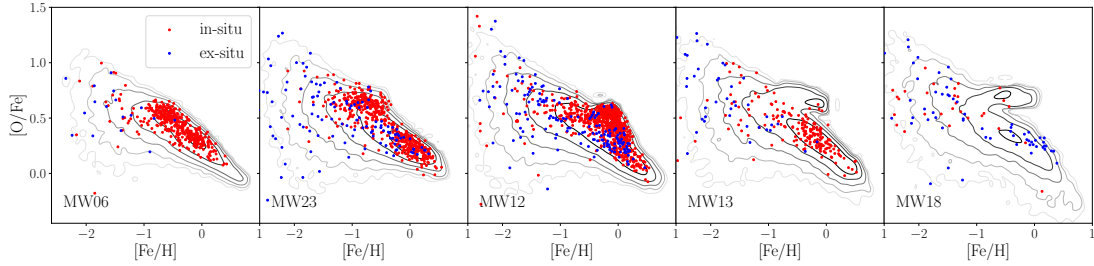


Figure 5.1: Five of the E-MOSAICS galaxies in $[\alpha/\text{Fe}]-[\text{Fe}/\text{H}]$ space, chosen to illustrate the diversity of the $z = 0$ $[\alpha/\text{Fe}]-[\text{Fe}/\text{H}]$ distributions. The contours represent the field stars and the points represent the in-situ (red) and ex-situ (blue) GCs.

a fixed $[\text{Fe}/\text{H}]$ (relative to the MW’s field stars) indicates an ex-situ origin (e.g. [Pritzl et al. 2005](#)). The motivation for this follows from the assumption that GCs formed ex-situ did so in a satellite galaxy with a longer gas consumption timescale than the main progenitor. In particular, low mass dwarf galaxies are expected to transition to low $[\alpha/\text{Fe}]$ at lower $[\text{Fe}/\text{H}]$ than more massive galaxies ([Matteucci & Brocato, 1990](#); [Tolstoy et al., 2009](#)). The underlying assumption to this classification is that the GC formation history is broadly representative of the field star formation history in all galaxies.

[Pritzl et al. \(2005\)](#) used a compilation of Galactic GCs with high-fidelity stellar abundance measurements and compared their $[\alpha/\text{Fe}]$ abundances with those of the field stars. They find that GCs follow the abundances of field stars reasonably well, with a few exceptions. In particular, they suggest that Ter 7, Pal 12 and Rup 106 have an extra-galactic origin based on their lower $[\alpha/\text{Fe}]$ abundances. This is also suggested in other studies where Ter 7 ([Da Costa & Armandroff, 1995](#)) and Pal 12 ([Dinescu et al., 2000](#)) are inferred to be associated with the tidally disrupting Sagittarius dwarf galaxy. It has been suggested that Rup 106 is of extragalactic origin although its parent galaxy is still debated ([Bellazzini et al., 2003](#); [Law & Majewski, 2010a](#); [Forbes & Bridges, 2010](#); [Massari et al., 2019](#)). Other MW GCs with low $[\alpha/\text{Fe}]$ suggesting extragalactic origin include NGC 5694 ([Lee et al., 2006](#); [Mucciarelli et al., 2013](#)) and Pal 1 ([Monaco et al., 2011](#); [Sakari et al., 2011](#)). There is also evidence that the GCs in the Fornax dwarf galaxy have lower $[\alpha/\text{Fe}]$ when compared to the MW GCs ([Larsen et al., 2012](#)). Also, [Cohen \(2004\)](#) and [Tautvaišienė et al. \(2004\)](#) concluded that the

known Sagittarius GCs follow the $[\alpha/\text{Fe}]$ trend of the known Sagittarius field stars.

I present in Fig. 5.1 a subset of the E-MOSAICS galaxies with a range of shapes in $[\alpha/\text{Fe}] - [\text{Fe}/\text{H}]$ to highlight key points in the differences and similarities between galaxies. These are MW06, MW12, MW13, MW18 and MW23 in Table 1 of [Kruijssen et al. \(2019a\)](#). The contours represent the field stars, and the GCs are overplotted as red or blue points depending if they formed in-situ or ex-situ respectively. Unless otherwise stated, when I refer to ‘field stars’ in this work I am referring to all stellar particles that are bound to the main subhalo. When calculating the mass of the field stars, the mass of the globular cluster population associated with the stellar particle is omitted. In all the galaxies, both the field stars and the GCs show a decline of $[\alpha/\text{Fe}]$ with increasing $[\text{Fe}/\text{H}]$. From left to right, the panels show field star distributions ranging from a smooth decline to being clearly bimodal at fixed metallicity (in the range $-1 < [\text{Fe}/\text{H}] < 0$). [Mackereth et al. \(2018\)](#) used the EAGLE simulations to investigate the $[\alpha/\text{Fe}]$ abundances of the field stars around the solar radius (thus excluding stars in the bulge) in a sample of MW-like galaxies. They also found bimodality in 5 per cent of their galaxies and attribute the appearance of bimodality to a phase of rapid growth early in the galaxy’s formation history - we investigate this explanation and its relation to GCs in Section 5.4.

The first thing to note is that the abundances of the GCs closely trace the abundances of the field star population; however, similarly to the MW there are some clear exceptions. All of the galaxies shown in Fig. 5.1 host a small population of GCs that have low $[\alpha/\text{Fe}]$ for a given $[\text{Fe}/\text{H}]$. However, contrary to what is assumed for the MW, this population of GCs is not universally ex-situ. In E-MOSAICS GCs follow the abundance trends of the field stars by construction (there cannot be a GC without a star particle), but where the GCs form and how they evolve in the simulation may impart biases on the properties of the star particles that still hold a GC at $z = 0$. I investigate these points further by stacking all 25 MW-like galaxies and looking for systematic trends in Fig. 5.2.

To test whether GCs follow the abundance trends of the field stars in our simulations, I show the median $[\text{O}/\text{Fe}]$ for fixed bins of $[\text{Fe}/\text{H}]$ of the in-situ (red) and ex-situ

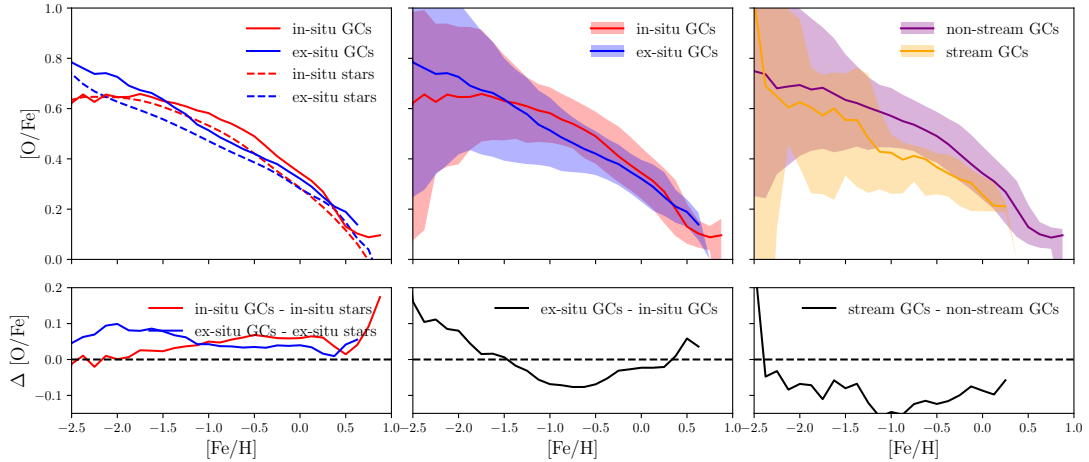


Figure 5.2: Top left: the median $[\text{O}/\text{Fe}]$ as a function of metallicity of the in-situ and ex-situ field stars and GCs in all 25 galaxies. Top middle: the median $[\text{O}/\text{Fe}]$ as a function of metallicity of the in-situ and ex-situ GCs in all 25 galaxies. Top right: the median $[\text{O}/\text{Fe}]$ as a function of metallicity of the GCs on streams and not on streams in the 15 MW-like galaxies identified in [Hughes et al. \(2019\)](#). The shaded regions show the 16th and 84th percentiles and the lines are a running median of $[\text{O}/\text{Fe}]$ in $[\text{Fe}/\text{H}]$ bins of 0.5 dex with a difference of 0.125 dex between each bin. The bottom panels show the differences in $[\text{O}/\text{Fe}]$ between the subsets of stars or GCs for each $[\text{Fe}/\text{H}]$ bin. All panels only include bins with more than 5 GCs to avoid poor sampling issues.

(blue) GCs and field stars of the 25 galaxies (top left panel of Fig. 5.2). Both field stars (dashed lines) and GCs (solid lines) show a decrease in the median $[\text{O}/\text{Fe}]$ with increasing $[\text{Fe}/\text{H}]$, a similar trend to that seen in the MW field stars and GCs (e.g. [Hayden et al., 2015](#)). We also find that the GCs follow the general trend of the field stars, but they are offset to higher $[\text{O}/\text{Fe}]$. We quantify this difference in the bottom left panel, where we show the difference in median $[\text{O}/\text{Fe}]$ between stars and GCs for both the in-situ and ex-situ populations. This panel shows that the GC $[\text{O}/\text{Fe}]$ is always greater than that of the field stars by ~ 0.05 dex. We expect GCs to show higher $[\text{O}/\text{Fe}]$ because, in the MOSAICS model, GCs are formed in high density environments, and high density environments induce shorter gas consumption times ([Tacconi et al., 2018](#); [Mackereth et al., 2018](#)) which in turn leads to higher $[\text{O}/\text{Fe}]$. The gas consumption time is an estimate of the time a star-forming gas particle resides in the ISM before becoming a star particle. It can vary significantly across a single galaxy due to variations in pressure. A correlation between gas consumption time and $[\alpha/\text{Fe}]$ is not necessary, because such correlation only arises if a parcel of gas is self-enriched (i.e., there is no

dilution from gas infall, the Fe and α elements produced by stellar evolution are not ejected to large distances, and there is no large-scale radial mixing of gas within the galaxy). In the EAGLE simulation, a correlation between gas consumption time and $[\alpha/\text{Fe}]$ has been demonstrated by [Mackereth et al. \(2018\)](#) (their fig. 4). This arises because metals produced by stellar evolution are returned locally (using the SPH kernel), and because gas consumption timescales are similar to the timescales of the Type IaSNe delay time distribution.

To further study the difference in the α abundances of the in-situ and ex-situ GCs, I show their median $[\text{O}/\text{Fe}]$ values as a function of $[\text{Fe}/\text{H}]$ in the middle panel of Fig. 5.2, where the shaded region shows the 16th and 84th percentile range. Although the ex-situ GCs show, on average, systematically lower $[\text{O}/\text{Fe}]$, the distributions heavily overlap and the difference between the medians is smaller than the 1σ ranges. The middle bottom panel of Fig. 5.2 shows the difference between the in-situ and ex-situ GC median $[\text{O}/\text{Fe}]$. There is a range of $[\text{Fe}/\text{H}]$ ($-1.2 < [\text{Fe}/\text{H}] < -0.25$) in which ex-situ GCs have a lower median $[\text{O}/\text{Fe}]$ than in-situ GCs, but outside of this range $[\text{O}/\text{Fe}]$ is similar or ex-situ GCs have higher α enhancement (particularly for $[\text{Fe}/\text{H}] < -1.8$). Therefore it is not definitively shown that ex-situ GCs show lower α abundances at all $[\text{Fe}/\text{H}]$. However, the ex-situ GCs in these simulations are identified as any GC which has been accreted onto a central galaxy over its full formation history. This means that some of the ex-situ GCs were formed in progenitors that were accreted very early on in the galaxy's formation history, and consequently they would most likely be identified as in-situ GCs in chemical and kinematic studies. Dwarf galaxies accreted early tend to have more rapid formation histories (in terms of the time it takes them to reach a maximum mass) than those accreted late ([Mistani et al., 2016](#)), therefore we would expect them to have higher $[\alpha/\text{Fe}]$ abundances. Therefore, it would be prudent for us to examine an alternative definition of an ex-situ GC to facilitate a more direct comparison with observations of GCs in the Milky Way.

The most direct evidence for accretion in the Milky Way comes in the form of stellar streams, therefore we complement the in-situ/ex-situ comparison with a stream/non-stream comparison. For this, I use the sample of stellar streams in 15 of the E-

MOSAICS MW-mass galaxies from [Hughes et al. \(2019\)](#) and the previous chapter in this thesis, which were visually identified in 2D projections of the stellar particles of accreted galaxies. I show their $[\text{O}/\text{Fe}]$ abundances in the right panel of Fig. 5.2 and quantify the differences in the bottom right panel. This panel shows that the stream GCs have consistently lower $[\text{O}/\text{Fe}]$ abundances than the non-stream GCs. At $[\text{Fe}/\text{H}] = -1$ the difference between the stream and the non-stream GCs is double that of the difference between the ex-situ and the in-situ GCs. Therefore I can conclude that if a GC is observed in the halo of a galaxy that belongs to a stream, there is a high probability that it will be α -poor relative to the main GC population. This supports the conclusion of works that state that ex-situ GCs should exhibit lower $[\alpha/\text{Fe}]$ at fixed $[\text{Fe}/\text{H}]$ than in-situ GCs (e.g. [Pritzl et al. 2005](#)), however I would revise this conclusion to state that we can distinguish *recently* accreted GCs this way, i.e. that high $[\alpha/\text{Fe}]$ does not necessarily imply that a GC formed in-situ, as at low metallicity most GCs form with high $[\alpha/\text{Fe}]$. I can also conclude that if there is a low $[\alpha/\text{Fe}]$ GC in the halo of a galaxy it is likely to have been accreted relatively recently and could be a signpost for the presence of an associated disrupting dwarf galaxy. The lower α abundance of these accreted stars and GCs is not driven by their ex-situ origin in itself, but by the fact that they formed and accreted recently.

5.3 The $[\alpha/\text{Fe}] - [\text{Fe}/\text{H}]$ distribution of field stars and its connection to the formation and disruption of globular clusters

5.3.1 Cluster formation and disruption across the $[\alpha/\text{Fe}]$ - $[\text{Fe}/\text{H}]$ plane

Section 5.2 shows us that the α abundances of a galaxy's GCs encode information about the formation and assembly of the galaxy's GC population. I now focus on what we may learn about the contribution of disrupted GCs to the galaxy's field star popu-

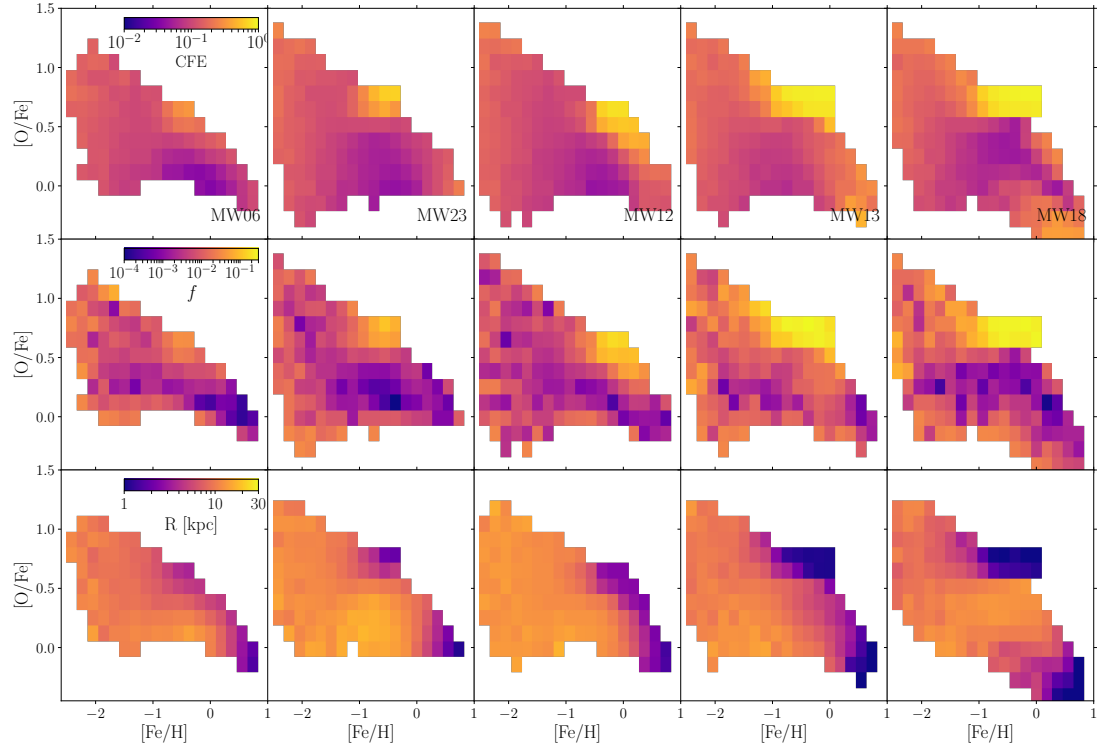


Figure 5.3: The $[\text{O}/\text{Fe}] - [\text{Fe}/\text{H}]$ relation for five of the simulated galaxies. Each panel shows a 2D histogram of the stars in the galaxy coloured by, the cluster formation efficiency (CFE), the fraction of stars which were born in GCs but now reside in the field (f) and the galactocentric radius of the stars at $z = 0$ (R). In the last row, only the stars from the inner 30 kpc are shown.

lation from their α abundances. In Fig. 5.1 MW13 and MW18 show a bimodal $[\text{O}/\text{Fe}]$ distribution in their field stars at $[\text{Fe}/\text{H}] \approx -0.25$, however, there are relatively few GCs in the high $[\alpha/\text{Fe}]$ sequence compared to the low $[\alpha/\text{Fe}]$ sequence. This motivates investigation of the $[\alpha/\text{Fe}] - [\text{Fe}/\text{H}]$ plane in terms of GC formation and disruption.

GC formation

I first focus on the formation of GCs through the CFE. The CFE governs the fraction of star formation that yields bound clusters (see [Adamo & Bastian 2018](#) for a recent review). The CFE increases with star formation rate surface density ([Adamo et al., 2015](#)) and in the E-MOSAICS simulations it scales with the natal gas pressure. E-MOSAICS uses the environmentally dependent description of the CFE from the [Kruijssen \(2012\)](#) model, which relates the fraction of star formation into bound stellar clusters to the

properties of the interstellar medium (ISM) - bound clusters form most efficiently at the high density end of the hierarchically structured ISM.

The first row of Fig. 5.3 shows a 2D histogram of the stellar particles in the $[\text{O}/\text{Fe}] - [\text{Fe}/\text{H}]$ space coloured by the CFE associated with their birth cloud (or ‘natal gas’). The CFE ranges from a few percent to 80 percent, depending on the location in $[\alpha/\text{Fe}] - [\text{Fe}/\text{H}]$ space. As the stellar $[\alpha/\text{Fe}] - [\text{Fe}/\text{H}]$ distribution becomes more bimodal (Fig. 5.1, from left to right), the high CFE feature in the galaxy (Fig. 5.3, second row) becomes more pronounced in the high- α sequence. The CFE is dependent on the density of the natal gas of the stellar particle (through the natal pressure, due to the equation of state imposed on dense, star forming gas), with higher densities leading to a higher CFE. Therefore the high- α sequence must form from material with increased natal gas pressure, meaning that the stars form from gas with short gas consumption times (see later discussion and [Mackereth et al. 2018](#) for details).

However, as discussed earlier, the bimodal galaxies MW13 and MW18 have a lack of GCs in their high $[\alpha/\text{Fe}]$ sequence, even though this is the same area of $[\alpha/\text{Fe}] - [\text{Fe}/\text{H}]$ space where the CFE is the highest. This means that although there is a clearly defined area in this plane where the galaxy is forming a large number of GCs, these GCs do not survive to $z = 0$. Therefore, I now investigate GC disruption across the $[\alpha/\text{Fe}] - [\text{Fe}/\text{H}]$ plane.

The link between bimodality and the gas consumption time

In a high density (pressure) environment, the gas consumption timescale of the natal gas is short, and therefore the natal gas is consumed before it can be enriched with the Fe nucleosynthesised by Type Ia supernovae. [Mackereth et al. \(2018\)](#) shows that the amount of α enhancement correlates with the gas consumption timescale (t_g) of field stars. I now test this for the GCs and field stars in the 25 E-MOSAICS galaxies. The consumption time of the natal gas from which the GC formed is calculated, following

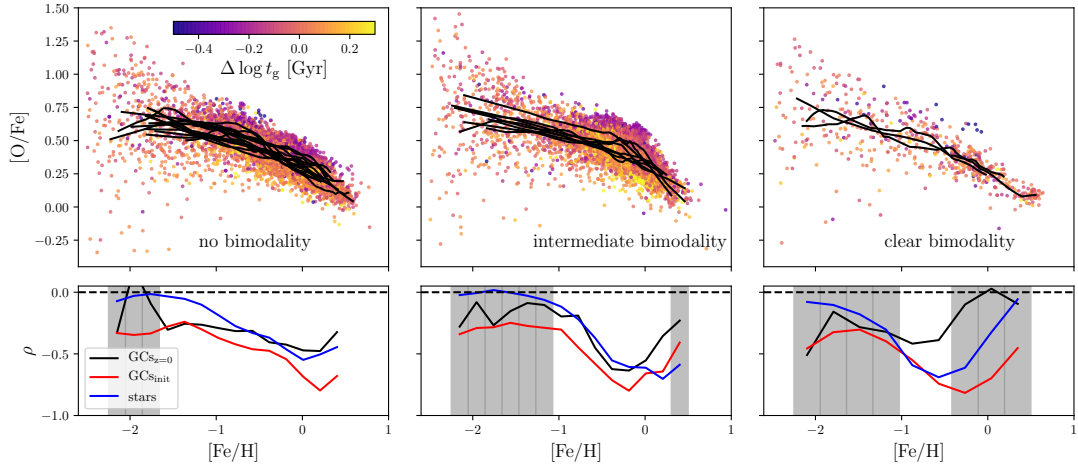


Figure 5.4: Top row: the $[\text{O}/\text{Fe}]$ - $[\text{Fe}/\text{H}]$ relation for GCs grouped by their galaxy’s degree of bimodality. The solid black lines represent the running medians of the individual galaxies, computed using the LOWESS method. Each point represents one $z = 0$ GC coloured by its difference from the running median of the t_g - $[\text{Fe}/\text{H}]$ relation of its host galaxy. Bottom row: the Spearman rank correlation coefficient of the Δt_g - $\Delta[\text{O}/\text{Fe}]$ relation. Each line represents present day GCs ($\text{GCS}_{z=0}$, black), any GC that formed (GCS_{init} , red) and the field stars (blue). The shaded regions highlight the metallicity bins in which the Spearman correlation coefficient for $\text{GCS}_{z=0}$ is not significant (Spearman p-value > 0.01). The other populations have significant correlations in all $[\text{Fe}/\text{H}]$ bins. The $[\text{Fe}/\text{H}]$ bins are wider in the clearly bimodal case to account for lower number statistics.

the description in [Schaye & Dalla Vecchia \(2008\)](#) (eq. 11), as

$$t_g = A^{-1} (1 M_{\odot} \text{pc}^{-2})^n \left(\frac{\gamma}{G} f_g P_{\star} \right)^{(1-n)/2}. \quad (5.1)$$

Here, the parameters $A = 1.515 \times 10^{-4} M_{\odot} \text{yr}^{-1} \text{kpc}^{-2}$ and $n = 1.4$ are specified by observations, see [Schaye et al. \(2015\)](#) for details. $\gamma = 5/3$ is the ratio of specific heats for an ideal gas, f_g is the local gas fraction (assumed to be unity) and P_{\star} is the pressure of the natal gas. t_g provides an estimate of the amount of time a star forming gas particle resides in the ISM before becoming a star particle (though I note this is an over-estimate since it neglects ejection of the ISM in winds), a low t_g therefore indicates vigorous star formation.

Following the methodology used by [Davies et al. \(2019\)](#), for each of the galaxies I compute the running median of the $[\text{O}/\text{Fe}]$ - $[\text{Fe}/\text{H}]$ relation and the t_g - $[\text{Fe}/\text{H}]$ rela-

tion using the locally weighted scatter plot smoothing method (LOWESS, Cleveland 1979). The running medians are calculated separately for the stars, GCs and initial GCs. I then compute the difference from these running medians for each GC and star, i.e. $\Delta t_{g,\text{GC}} = t_{g,\text{GC}} - t_{g,\text{GC,median}}$. The correlation between $\Delta[\text{O}/\text{Fe}]$ and Δt_g is computed as a Spearman rank correlation coefficient (ρ), the significance of this correlation coefficient is given by the Spearman p-value. A correlation is not significant if the p-value is greater than 0.01.

The top row of Fig. 5.4 shows the $z = 0$ GCs along with the running medians (black lines) for each of the galaxies. Each GC is coloured by the consumption time of its natal gas (t_g). The bottom panels of Fig. 5.4 show the Spearman- ρ values for the $z = 0$ GCs shown in the top panels and also the initial GCs and the field stars. Here the $z = 0$ GCs are those that survive until present day with a mass $> 10^5 M_\odot$, the initial GCs are those that were formed with a mass $> 10^5 M_\odot$ but do not necessarily survive until $z = 0$.

In the left and the middle panels of Fig. 5.4 the ρ -values are calculated in 15 equally sized bins from $-2.5 < [\text{Fe}/\text{H}] < 0.5$. In the right panel the ρ -values are calculated in 10 equally sized bins across the same metallicity range, to account for lower number statistics. The Spearman p-value is indicative as to whether a correlation is significant as it depends on the strength of the correlation and the sample size. I calculate the p-value for each of the bins and shade the bins to highlight where the $\Delta[\text{O}/\text{Fe}]$ - Δt_g correlation is not significant (the Spearman-p value exceeds 0.01). For the $z = 0$ GCs, the correlation for the initial GCs and the stars is significant everywhere. The galaxies are grouped by the shape of their field star contours in $[\text{O}/\text{Fe}]$ - $[\text{Fe}/\text{H}]$ space (as discussed in Section 5.4) and from left to right show: no bimodality, intermediate bimodality and clear bimodality.

Inspection by eye shows that, in the top panels of 5.4, the GCs that have a higher than average $[\text{O}/\text{Fe}]$ have a lower than average t_g . Hence, the recovered relation is negatively correlated ($\rho < 0$) for much of the range in $[\text{Fe}/\text{H}]$. This section discusses how the high $[\text{O}/\text{Fe}]$ field star sequence in the bimodal galaxies is formed in high pressure environments that induce a short gas consumption time. This is seen directly in Fig.

5.4, the field stars show a negative correlation everywhere above an $[\text{Fe}/\text{H}] > -1$. However, the correlation is stronger in the intermediate and clearly bimodal galaxies. The initial GCs show the strongest correlation. They show a stronger correlation than the field stars because some stars that form with fast consumption times are α -poor, this therefore weakens the field star correlation.

The high pressures that create the most α -rich stars in the clearly bimodal galaxies creates the perfect environment to form and then subsequently destroy high α GCs. Again this can be seen directly in Fig. 5.4. In the lower right panel the initial GCs show a strong negative correlation between their α enhancement and relative t_g . However, the GCs that survive until the present day do not show such a relation, because many of the GCs with the shortest t_g have been destroyed. All galaxies show a weaker correlation between $\Delta[\text{O}/\text{Fe}]$ and Δt_g in their $z = 0$ GCs when compared to their initial GCs, but the difference is most pronounced in the most bimodal galaxies. At $[\text{Fe}/\text{H}] = -0.5$ (where the correlation is significant in all galaxies) we calculate the difference in the Spearman- ρ value between the initial GCs and final GCs for the 'clearly bimodal' and 'no bimodality' galaxies. The clearly bimodal galaxies have a ρ -value difference of 0.44 whereas the galaxies with no bimodality have a difference of 0.11.

GC disruption

The region of high CFE in the $[\alpha/\text{Fe}]-[\text{Fe}/\text{H}]$ plane tells us that the stars and GCs which form in this region do so in a high density environment. However, tidal shocks are also more prevalent in high density environments and can efficiently disrupt the nascent cluster. This is the 'cruel cradle effect' described by [Kruijssen et al. \(2012a\)](#) and means that where a galaxy is likely to form many clusters, it is also likely to disrupt them. Dynamical friction also removes many of the most massive clusters that are not disrupted by tidal shocks, particularly in the centres of galaxies. The combination of the cruel cradle effect and dynamical friction explains the absence of GCs in the same location in $[\alpha/\text{Fe}]-[\text{Fe}/\text{H}]$ space where the CFE is high in Fig. 5.3.

I can make a measurement of the fraction of the stars that formed in bound massive

clusters similar to present day GCs but now reside in the field. For this purpose I revise slightly the definition of a GC to that of a star cluster with an *initial mass* greater than $10^5 M_{\odot}$ and an age greater than 2 Gyr. The second row of Fig. 5.3 shows a 2D histogram of all the stellar particles in the galaxy weighted by the fraction of their mass that once belonged to a GC that has since dissolved into the field star population,

$$f = \frac{\sum_i^{N_*} (M_{\text{GC},\text{init}} \times \text{SML} - M_{\text{GC},\text{final}})}{\sum_i^{N_*} M_{*,\text{field}}}, \quad (5.2)$$

where $M_{\text{GC},\text{init}}$ is the initial total mass in GCs, $M_{\text{GC},\text{final}}$ is the final total mass in GCs, $M_{*,\text{field}}$ is the final total mass field star population in the stellar particles and the factor $\text{SML} = M_{*,\text{final}}/M_{*,\text{init}}$ corrects the initial total mass in GCs for stellar evolutionary mass loss (such that I am only considering dynamical mass loss). I include mass loss from tidal shocks and two-body relaxation but not the complete removal of clusters by dynamical friction. Dynamical friction is omitted since I assume that this mass will quickly sink to the centre of the galaxy potentially contributing to the nuclear star cluster¹ (e.g. [Antonini 2013](#)). Therefore these stars would not be easily identifiable through chemical tagging studies of the field star population of the Galaxy.

Some of the galaxies show a clearly defined region of $[\text{O}/\text{Fe}] - [\text{Fe}/\text{H}]$ space where up to 30 per cent of the field stars were born in GCs. This region of high f is the same as the region of high CFE and overlaps with the high $[\text{O}/\text{Fe}]$ sequence in the galaxies which show bimodality in the top row. Therefore, I show that in some galaxies, some stars are born in high density regions of star forming gas, which means that for a given $[\text{Fe}/\text{H}]$ their $[\text{O}/\text{Fe}]$ will be high. Due to the high densities it is likely that these stars will form in bound clusters, but because of the ‘cruel cradle effect’ a high fraction of these clusters will also be fully or partially disrupted. Hence, in some galaxies, there is expected to be a region in $[\alpha/\text{Fe}] - [\text{Fe}/\text{H}]$ space where a high fraction of field stars were originally born in GC-like clusters. This has implications for chemical tagging studies and will be discussed in detail in Section 5.4.

¹Any potential increase in tidal disruption due to a shrinking orbit cannot be captured in the present model.

5.3.2 Galactocentric position in the $[\alpha/\text{Fe}]$ - $[\text{Fe}/\text{H}]$ plane

I investigate whether there is a radial dependence on where stellar particles will be distributed in $[\alpha/\text{Fe}]$ - $[\text{Fe}/\text{H}]$ space. In the bottom row of Fig. 5.3 I show a 2D histogram of the stellar particles within 30kpc of the centre of the galaxy, coloured by their galactocentric (spherical) radius. The region of $[\text{O}/\text{Fe}]$ - $[\text{Fe}/\text{H}]$ space that shows the highest fraction of disrupted GC stars (f) resides at the centre, or bulge, of the galaxy. This is expected since the centres of galaxies usually show the highest pressures due to the radial pressure gradient of the gas (see e.g. fig. 8 of [Crain et al., 2015](#)). Due to the high $[\alpha/\text{Fe}]$ sequence of interest being concentrated towards the centre of these galaxies, I consider just the bulge of the galaxy in Section 5.4.

5.4 The fraction of field stars in the bulge originating in GCs

5.4.1 Bulge stars from disrupted GCs in E-MOSAICS

I found in Section 5.3 that the high $[\alpha/\text{Fe}]$ sequence of stellar particles shown in Fig. 5.3 mostly reside close the centre of the galaxies. I therefore target the bulges of the 25 E-MOSAICS galaxies in the rest of this analysis, with a focus on the contribution of disrupted GCs to the formation of the bulge. Since the size of the bulge varies for each galaxy I make a radius and orbital circularity cut. I define the orbital circularity as in [Abadi et al. \(2003\)](#), $\epsilon_J = J_z/J_c(E)$ (i.e. the angular momentum relative to the angular momentum of a circular orbit), where $\epsilon = 1$ describes a perfectly circular orbit. The field stars in the bulge are therefore defined as the stellar particles within the stellar half mass radius with $\epsilon_J < 0.5$ ([Sales et al., 2015](#)).

I can now determine the contribution of disrupted GCs to the stellar population of the bulge, in the form of the fraction of field stars in the bulge that were born in a GC (f_{bulge}). The E-MOSAICS galaxies host too many GCs at $z = 0$ due to under dis-

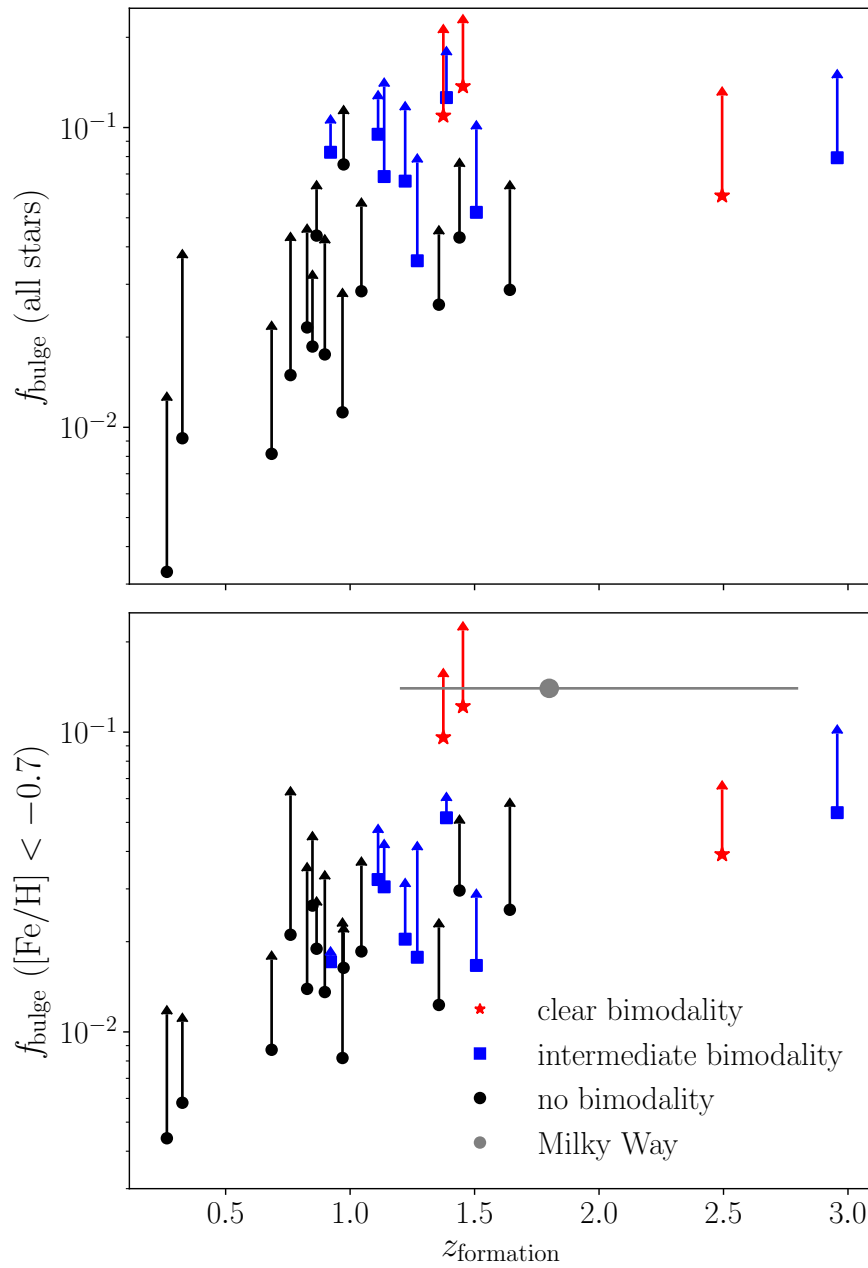


Figure 5.5: The fraction of field stars in the bulge which were born in GCs (f_{bulge}) as a function of the redshift ($z_{\text{formation}}$) at which all progenitors together have attained half of the $z = 0$ stellar mass (this is effectively the median age or median formation redshift of all stars in the galaxy at $z = 0$). The different symbols represent the degree of bimodality the field stars show in the $[\text{O}/\text{Fe}] - [\text{Fe}/\text{H}]$ plane, from definite bimodality (stars), to intermediate bimodality (squares) to no bimodality at all (circles). The data are shown as lower limits due to the under disruption of GCs in E-MOSAICS. The upper limits (at the tips of the arrows) show the extreme assumption that no GC survives in the bulge. Top panel: f_{bulge} across all field stars in the bulge. Bottom panel: f_{bulge} for field stars below $[\text{Fe}/\text{H}] < -0.7$ to match the selection when deriving f_{bulge} for the MW. The grey data point indicates the bulge mass fraction from GCs derived by [Schiaon et al. \(2017\)](#) for the formation redshift of the Milky Way inferred from the age-metallicity distribution of its GC population by [Kruijssen et al. \(2019b\)](#).

ruption (Pfeffer et al., 2018; Kruijssen et al., 2019a). For this reason, these fractions should be considered as lower limits. Therefore I also show the extreme upper limits on f_{bulge} , where I assume that every GC formed in the bulge of the galaxy becomes disrupted i.e. no GC survives to the present day in the bulge. Such an extreme assumption does not affect the general trend of the simulations.

I show f_{bulge} for all 25 galaxies in the left panel of Fig. 5.5 and see that there is a large range in the value of f_{bulge} , from 0.3-14 per cent. This fraction is dependent on the time at which the total stellar mass of all progenitors of that galaxy reaches half of the $z = 0$ mass ($z_{\text{formation}}$, De Lucia et al. 2006; Qu et al. 2017), such that galaxies that formed faster have higher f_{bulge} .

I also group the galaxies by the shape of their stellar contours in $[\alpha/\text{Fe}]-[\text{Fe}/\text{H}]$ space (like those shown in Fig. 5.1). I place each galaxy into one of three categories:

- No bimodality, where there is a smooth decline in $[\text{O}/\text{Fe}]$ for increasing $[\text{Fe}/\text{H}]$ (e.g. MW06).
- Intermediate bimodality, where there is a small bump or a slight increase in $[\text{O}/\text{Fe}]$ for a given metallicity (e.g. MW23 and MW12).
- Clear bimodality, where there are two distinct $[\text{O}/\text{Fe}]$ sequences at a given metallicity (e.g. MW13 and MW18).

I conclude that the most bimodal galaxies have a high f_{bulge} and also formed at the early end of the distribution. This is to be expected since, from Section 5.3, the high $[\alpha/\text{Fe}]$ sequence in the bimodal galaxies is formed from a high pressure environment close to the centre of the galaxy where GCs are efficiently formed and subsequently disrupted.

As a small aside here I will comment on the two bimodal galaxies with $z_{\text{formation}} \approx 1.5$. These two galaxies, although at the early side of $z_{\text{formation}}$ are still consistent with other galaxies that do not present bimodal $[\text{O}/\text{Fe}]$ distributions. Upon further investigation I find that they are significant outliers in the distribution of median stellar ages for stars

in the bulge. The stars residing in their bulge formed much earlier than average for the Milky Way-mass galaxies presented in this work. I continue this work with the $z_{\text{formation}}$ metric because it is more readily comparable with observations.

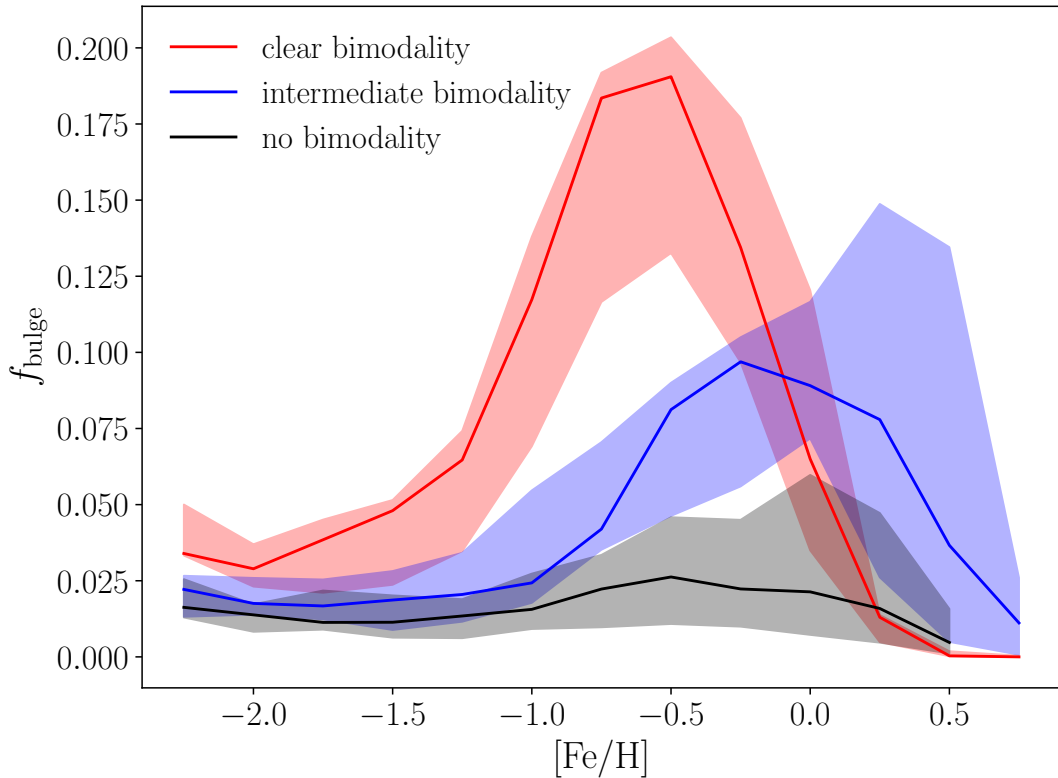


Figure 5.6: The fraction of field stars in the bulge which were contributed by GCs (f_{bulge}) in 0.5 dex $[\text{Fe}/\text{H}]$ bins. The solid lines show the running median and the shaded regions represent the 16th-84th percentile range. The galaxies are stacked by the level of bimodality their stars show in the $[\alpha/\text{Fe}]-[\text{Fe}/\text{H}]$ plane, coloured as in Fig. 5.5. f_{bulge} peaks higher and at lower metallicities in galaxies with clear $[\alpha/\text{Fe}]$ bimodality.

I also present the metallicity dependent f_{bulge} in Fig. 5.6. Here, f_{bulge} is calculated in $[\text{Fe}/\text{H}]$ bins of 0.5 dex and the median and the 16th-84th percentile range of the galaxies grouped by their level of bimodality is shown. For all galaxies, GC disruption and the contribution of GCs to the field star population increases towards higher metallicities for $[\text{Fe}/\text{H}] < -0.5$. The clearly bimodal galaxies show the highest and most metal-poor peak. The intermediate bimodal galaxies show a smaller and slightly more metal-rich peak and the galaxies with no bimodality show a relatively flat f_{bulge} with increasing $[\text{Fe}/\text{H}]$. Fig. 5.5 shows that the MW has a high fraction of disrupted

GCs in its bulge, consistent with the most bimodal simulated galaxies. I therefore use the most bimodal galaxies in Fig. 5.6 to predict that the stars from disrupted GCs in the bulge of the MW will show the highest fraction around $[\text{Fe}/\text{H}] \approx -1$.

5.4.2 Comparison with the Milky Way

Searching for stars from disrupted GCs in the bulge of the MW is something that has been done with large scale surveys of galactic stars. These searches mainly focus on finding populations of nitrogen rich stars ([Schiavon et al., 2017](#)).

Whilst some stars in GCs show the same chemical abundances as those found in the field (first population, FP), others show enhancements or depletions in some elements, such as a nitrogen enhancement (second population, SP, e.g. [Carretta et al. 2009](#), for a recent review see [Bastian & Lardo 2018](#)).

It is interesting here to address the effect the formation time-scales of multiple populations may have on our comparison with the MW bulge. The main theories for the origin of multiple populations in GCs suggest that the formation of SP stars happens on timescales < 300 Myr. For scenarios invoking enrichment by massive stars, the timescales for SP star formation are $< 5 - 10$ Myr (e.g. [Gieles et al. 2018](#)). For the asymptotic giant branch (AGB) scenario, the timescale to form SP stars is < 100 Myr, as this is the timescale for the first Type Ia SNe to stop further generations of stars forming within the cluster ([D’Ercole et al., 2008](#)). Furthermore, observations also give some constraint on the relative formation times of FP and SP stars. Ancient GCs show that the age difference between the two populations is < 200 Myr and consistent with 0 Myr ([Marino et al., 2012](#)). Younger GCs also show a similar difference with an age difference calculated for NGC 1978 of 1 ± 20 Myr ([Martocchia et al., 2018](#)). Therefore, both theoretical and observational evidence suggest that GC disruption happens after multiple populations form and I can therefore directly compare the nitrogen rich stars in the MW with disrupted GCs in the simulations without adding any extra calculations for the formation times of the nitrogen rich stars.

[Schiavon et al. \(2017\)](#) used APOGEE to find a population of nitrogen rich stars in the bulge of the MW. Restricting their selection to stars below $[\text{Fe}/\text{H}] = -1$, they found that 7 percent of the field stars in the bulge are nitrogen enhanced. Although they advance multiple explanations for the origin of these stars, their preferred explanation is that they are remnants of disrupted GCs. [Schiavon et al. \(2017\)](#) then assume equal numbers of first and second population stars are lost from GCs and calculate that 14 percent of field stars in the bulge (within this metallicity selection) formed in a GC.

In order to fairly compare the results from the E-MOSAICS simulation to that of the MW, I also make a metallicity selection for the stars in the bulges of the simulations. Due to the metallicities in the EAGLE simulations being overestimated ([Schaye et al., 2015](#)) I make a metallicity cut of $[\text{Fe}/\text{H}] < -0.7$ to compare with the metallicity cut of $[\text{Fe}/\text{H}] < -1$ in [Schiavon et al. \(2017\)](#). I show this in the bottom panel of Fig. 5.5, using for the MW, $z_{\text{formation}} = 1.8_{-0.6}^{+1.0}$ ([Kruijssen et al., 2019b](#)). Although the metallicity cut reduces the f_{bulge} calculation for most galaxies, the MW is consistent with the subset of E-MOSAICS galaxies with a bimodal $[\alpha/\text{Fe}]$ distribution, fitting with the observation that the MW also exhibits an $[\alpha/\text{Fe}]$ bimodality ([Fuhrmann, 1998](#); [Adibekyan et al., 2012](#); [Hayden et al., 2015](#)). I note here that [Schiavon et al. \(2017\)](#) did not make any orbital cuts in their selection, however when I do not include the circularity cut, there is no significant change in Fig. 5.5 and therefore I keep this in our analysis for consistency.

[Schiavon et al. \(2017\)](#) also present the metallicity distribution of their sample of nitrogen enriched stars. The metallicity distribution function (MDF) peaks at $[\text{Fe}/\text{H}] \sim -1$ whereas the MDF of the bulge field stars begins to decline at this metallicity ([Schiavon et al. 2017](#), fig. 9). Therefore I conclude that for the MW f_{bulge} will indeed peak at $[\text{Fe}/\text{H}] \sim -1$ as predicted from the simulations in the previous section. In Fig. 5.7, I present the metallicity distribution function of field stars in the bulge of the three galaxies in our sample that are classified as bimodal in their $[\alpha/\text{Fe}]$ distributions (MW13, MW18 and MW21). The field stars are coloured by whether they were once bound to GC (blue lines) or not (red lines). [Schiavon et al. \(2017\)](#) present a similar figure in which they show the metallicity distributions of nitrogen-rich and nitrogen-normal

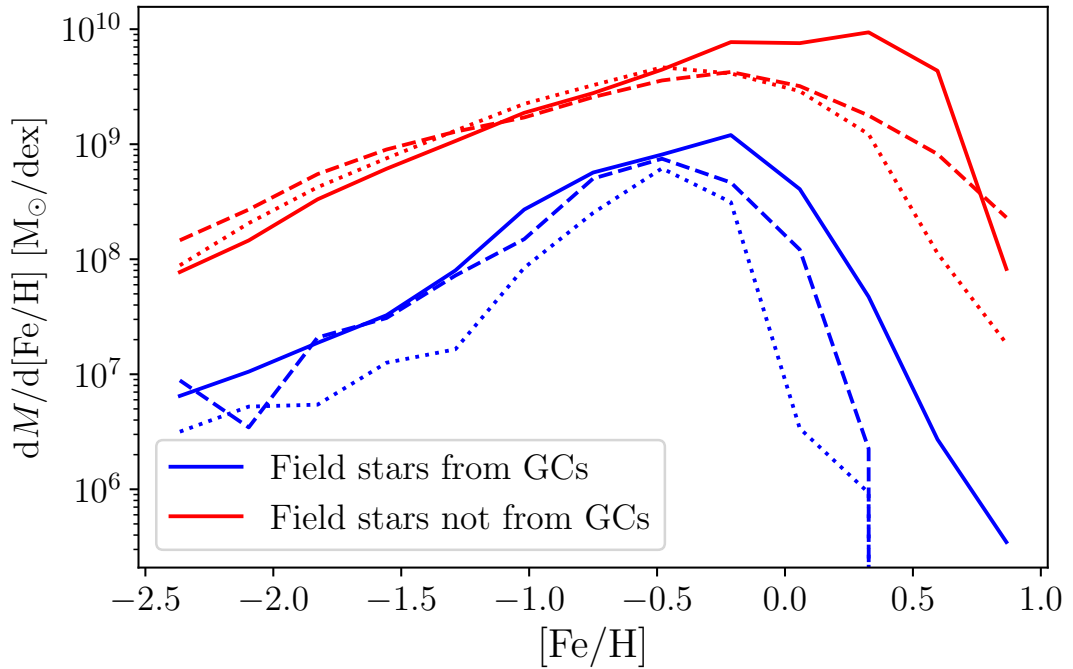


Figure 5.7: The metallicity distribution function of field stars in the bulges of the three E-MOSAICS galaxies that show bimodal $[\alpha/\text{Fe}]$ at a given $[\text{Fe}/\text{H}]$, these are MW13 (solid line), MW18 (dashed line) and MW21 (dotted line). The stars are split by whether they were born in a GC (blue lines) or not (red lines).

stars. Similar to the distribution shown in [Schiavon et al. \(2017\)](#) the ex-GC stars in the E-MOSAICS simulations show a more peaked distribution than that of the field stars not from GCs. Also similar to [Schiavon et al. \(2017\)](#) the ex-GC stars peak at a lower metallicity than the stars not born in GCs (albeit at a higher metallicity than the MW).

These findings therefore corroborate the conclusion of [Schiavon et al. \(2017\)](#) that the population of nitrogen enriched stars found in the bulge of the Milky Way are likely to be from disrupted clusters. However, such a large fraction (14 percent) of stars in the bulge originating in clusters is rare in the E-MOSAICS simulations, with only 2 of the galaxies showing fractions greater than 10 per cent. In the context of these findings, such a high nitrogen-enhanced fraction of bulge stars constitutes further evidence that the MW formed unusually early in cosmic history, given its halo mass (also see [Mackereth et al. 2018](#) and [Kruijssen et al. 2019b](#)).

5.5 Conclusions

This chapter uses the E-MOSAICS simulations to investigate the $[\alpha/\text{Fe}]-[\text{Fe}/\text{H}]$ distribution of a galaxy's field stars and GCs. Fig. 5.1 reveals many interesting features in the $[\alpha/\text{Fe}]-[\text{Fe}/\text{H}]$ space of the E-MOSAICS galaxies, namely, bimodal distributions and a lack of GCs in the high α sequence. Therefore, I use 25 MW-like galaxies and their GC populations to understand what their $[\alpha/\text{Fe}]-[\text{Fe}/\text{H}]$ distribution can reveal about the formation of the galaxy, both in terms of the α abundance ratios of individual GCs and where in $[\alpha/\text{Fe}]-[\text{Fe}/\text{H}]$ space we should look for remnants of disrupted GCs.

Many works present the hypothesis that GCs should follow the $[\alpha/\text{Fe}]-[\text{Fe}/\text{H}]$ distribution of field stars and those GCs which have been accreted should show relatively low $[\alpha/\text{Fe}]$ for their $[\text{Fe}/\text{H}]$. I show in Fig. 5.2 that the GCs do follow the general trend of the field stars and if a GC has a low $[\alpha/\text{Fe}]$ abundance, then it is likely that this GC has been recently accreted alongside a dwarf galaxy. However, it is impossible to distinguish between in-situ GCs and GCs that were accreted early in the formation history of the galaxy based on α enhancement alone.

When focusing on the field star $[\alpha/\text{Fe}]-[\text{Fe}/\text{H}]$ distribution, there is a wide range of shapes, from a smooth decline to clearly bimodal (Fig. 5.1). The high- α field star sequence present in some of the E-MOSAICS galaxies is made up of a large fraction of disrupted GCs (Fig. 5.3). This is due to the high pressure environment that is necessary to create a high $[\alpha/\text{Fe}]$ sequence. This environment creates very short gas consumption times (T_g), making it ideal for GC formation and, due to the 'cruel cradle effect', subsequent destruction. This area of high $[\alpha/\text{Fe}]$ is located close to the centre of the galaxy and I therefore calculate the fraction of disrupted GCs contributing to the bulge of each of the 25 galaxies (f_{bulge}).

Fig. 5.5 shows that the galaxies which show the strongest bimodality also show rapid early growth of their progenitors. It is also the most bimodal galaxies that have the highest contribution from disrupted clusters, f_{bulge} . Mackereth et al. (2018) showed that a high- α sequence in MW-like galaxies is formed via a phase of rapid early formation, a conclusion that is corroborated by a comparison of the $f_{\text{bulge}}-z_{\text{formation}}$ relation

with the high f_{bulge} fraction inferred by [Schiavon et al. \(2017\)](#). I also add that galaxies that formed, on average, earlier than typical galaxies of that mass, are likely to have a relatively high fraction of stars in the bulge that originated in GCs. It is the high- α sequence in these galaxies are likely to contain a high fraction of stars that were born in GCs.

I compare the f_{bulge} of the E-MOSAICS galaxies to that of the Milky Way and find that the Milky Way has an unusually high f_{bulge} , comparable to only 2 out of the 25 E-MOSAICS galaxies. This is consistent with the conclusions of previous works that the Milky Way underwent a period of rapid growth early in its formation, suggesting that its mass assembly history is atypical of L_* galaxies (e.g. [Mackereth et al. 2018](#); [Kruijssen et al. 2019b](#)).

Chapter 6

What to expect when using globular clusters as tracers of the total mass distribution in Milky Way-mass galaxies

6.1 Introduction

The distribution of mass within a galaxy contains information about its formation and evolution. It also helps us to understand how the dark and baryonic matter are linked (e.g. [Blumenthal et al. 1986](#); [Remus et al. 2017](#)). Mass distributions may be obtained via a variety of techniques such as strong gravitational lensing (e.g. [Auger et al. 2010](#); [Sonnenfeld et al. 2013](#)), the virial theorem (e.g. [Watkins et al. 2019](#)) and dynamical modelling (e.g. [Tortora et al. 2014](#); [Poci et al. 2017](#)). Dynamical models are used to connect the motion of a set of tracers to the gravitational potential. This allows kinematic data sets to be turned into information not only about the distribution of mass within a galaxy (including the DM content) but also the intrinsic shape (e.g. [van den Bosch et al. 2008](#)), the stellar initial mass function of its composite stellar population (e.g. [Thomas et al. 2011](#); [Posacki et al. 2015](#); [Tortora et al. 2016](#); [Li et al.](#)

2017b), the baryonic to dark-matter mass ratio (e.g. [Thomas et al. 2011](#); [Zhu et al. 2016a](#)), the merger history of the galaxy (e.g. [Schulze et al. 2020](#)) and the intrinsic properties of the tracer population (e.g. [Schuberth et al. 2010](#)).

Jeans models ([Jeans, 1915](#); [Binney, 1980](#); [Merritt, 1985](#); [Dejonghe & Merritt, 1992](#)) involve solving the Jeans equations (spherical, axisymmetric or triaxial) for the kinematics of a galaxy based on a parameterisation of the galaxy mass distribution. Jeans models are commonly used to provide initial insights for computationally slower (but more sophisticated) models, such as Schwarzschild models ([Schwarzschild, 1979](#)) and made-to-measure models ([Syer & Tremaine, 1996](#)). They also have the advantage that no functional form has to be assumed for the underlying distribution functions. Jeans models have been used to determine the distribution of the DM of all kinds of galaxies, from dwarfs (e.g. [Kleyna et al. 2001](#); [Battaglia et al. 2008](#); [Strigari et al. 2008](#); [Łokas 2009](#); [Walker et al. 2009](#)) to ellipticals (e.g. [Napolitano et al. 2009](#); [Schuberth et al. 2010](#); [Deason et al. 2012](#); [Agnello et al. 2014](#)). In early-type galaxies the GC velocities obtained by the SLUGGS survey (e.g. [Forbes et al. 2017](#)) has been combined IFU kinematic maps from the ATLAS^{3D} survey to model the total-mass profiles of a sample of 21 galaxies in the stellar mass range $10^{10} < M_*/M_\odot < 10^{11.6}$ ([Bellstedt et al., 2018](#)). [Bellstedt et al. \(2018\)](#) find that the mass and density profile slope measured through the Jeans modelling are consistent with those measured in the inner regions of galaxies by other studies and using other techniques.

[Leung et al. \(2018\)](#) combined stellar kinematics from CALIFA ([Sánchez et al., 2016](#)) with gas kinematics from the EDGE ([Bolatto et al., 2017](#)) survey and found that the Jeans models, along with the Schwarzschild models and Asymmetric Drift Correction can recover the dynamical mass within 1Re to within 20 per cent, but cautioned that assumptions may break down in the inner regions. In addition [Scott et al. \(2015\)](#) used Jeans models to calculate the dynamical masses of 106 SAMI ([Croom et al., 2012](#)) galaxies. Jeans models have also been used in the ATLAS^{3D} and the MaNGA ([Bundy et al., 2015](#)) surveys to find variations in the stellar initial mass functions of early type and late type galaxies ([Cappellari, 2012](#); [Li et al., 2017b](#)).

In the Jeans-Anisotropic-MGE (JAM) modelling technique ([Cappellari, 2008, 2012](#);

D'Souza & Rix, 2013; Watkins et al., 2013), the potential and tracer densities are given as inputs in the form of multi-gaussian-expansions (MGE) (Emsellem et al., 1994; Cappellari, 2002). Watkins et al. (2013) extended the JAM model by removing the need for binning and working directly with the discrete data. Fitting each tracer particle individually means that quality cuts in the data are no longer needed and the likelihoods can be extended to easily incorporate further information such as the metal abundances. Watkins et al. (2013) applied these models to resolved stars in the GC ω Centauri to find the velocity anisotropy, the inclination angle, a V -band mass-to-light ratio and a distance that are all in agreement with the values found in previous studies. Based on the dynamical models of Watkins et al. (2013), den Brok et al. (2014) constructed dynamical models of the GC M15, again using the discrete fitting method. They were able to show that the models reproduced the radial variation of the mass-to-light ratio found in other studies and theoretical predictions.

Zhu et al. (2016b) extended the models by Watkins et al. (2013) to include multiple populations in a new chemo-dynamical axisymmetric Jeans model. They applied this model to several mock data sets for the dwarf spheroidal galaxy Sculptor, where they considered different stellar populations tracing the same potential. Where most Jeans modelling techniques compute a likelihood in the kinematics, in this case a combined likelihood in position, metallicity and kinematics is used to constrain the mass profile, velocity anisotropy and internal rotation of the dwarf galaxy. This type of model allowed Zhu et al. (2016b) to show that stars in Sculptor naturally separated into two populations - metal rich and metal poor. The two populations have different spatial distributions, velocity dispersions and rotation. Zhu et al. (2016a) further extended the axisymmetric Jeans model to include three dynamical tracer populations and also fit the integrated light stellar kinematic data in the inner region of the giant elliptical galaxy NGC 5846. The three dynamical tracer populations were the planetary nebulae (PNe) and two GC subpopulations. Using this method they constrained the mass distribution including the DM fraction and the internal dynamics of each tracer population.

It is clear that dynamical modelling techniques can reveal a lot about a stellar or galactic system. It is therefore important to test these kinds of models on hydrodynamical

simulations to fully understand what biases may be present when they are applied to real systems. These biases may be driven by the sample size of the dynamical tracers, the data quality or the intrinsic properties of the stellar or galactic system being modelled.

JAM has been extensively tested on > 1000 simulated galaxies by [Li et al. \(2016\)](#). They used the Illustris project ([Genel et al., 2014](#); [Vogelsberger et al., 2014](#); [Nelson et al., 2015](#)) to select massive galaxies and constructed a dynamical model for each galaxy. In this study, [Li et al. \(2016\)](#) construct kinematic maps and brightness maps of the galaxies, which are then used as inputs for the JAM modelling. They find that the total mass enclosed within $2.5 R_e$ is constrained to within 10 per cent. They also find that the 1σ scatter in the recovered stellar mass-to-light ratio M^*/L is 30-40 per cent of the true value and this accuracy depends on the triaxial shape of the galaxy.

Similarly, [El-Badry et al. \(2017\)](#) used simulations from the FIRE project to test the reliability of Jeans models on low-mass galaxies. [El-Badry et al. \(2017\)](#) use the stellar radial velocity profile and number density profile as inputs into their Jeans models. They connect the results from the Jeans models to the gas inflow and outflow of these low-mass galaxies and find that the Jeans model overestimates a galaxy's dynamical mass during periods of post-starburst gas outflow and underestimates it during periods of net inflow. They place a lower limit of 20 per cent uncertainty in the mass measurements of gas-rich galaxies, but this is reduced to 10% in gas-free galaxies.

The [Li et al. \(2016\)](#) study is based on the assumption that we have a kinematic map for a full galaxy, and the study of [El-Badry et al. \(2017\)](#) is based on the assumption that we can extract a radial velocity profile of the stars. However, the dynamics of the full galaxy halo must be used to obtain as much information as possible about the properties and formation of a galaxy. This includes the very outskirts of the galaxy, where the most information about the merger history is contained. With the advent of large surveys (e.g. SLUGGS, Fornax 3D, [Sarzi et al. 2018](#); [Fahrion et al. 2020](#)) it is an opportune time to take full advantage of the GC and planetary nebulae (PNe) survey data. GCs and PNe are bright tracers in distant galaxies that probe far out into a galaxy's halo and therefore are particularly useful for constraining the radial

distribution and mass of the DM halo (Schuberth et al., 2010) and the merger history of the galaxy (Schulze et al., 2020; Trujillo-Gomez et al., 2021).

The suite of E-MOSAICS simulations (Pfeffer et al., 2018; Kruijssen et al., 2019a) forms and evolves GCs fully self consistently alongside their host galaxies. I use the volume-limited sample of 25 MW-mass galaxies from the high-resolution 25 cMpc volume EAGLE simulation (Recal-L025N0752; Schaye et al. 2015). The sample is chosen solely based on a total mass cut of $7 \times 10^{11} < M_{200}/M_{\odot} < 3 \times 10^{12}$ and therefore probes a variety of formation histories and is a representative sample of MW-mass galaxies. This allows for the unique opportunity of using these simulated GCs as tracers in the JAM model to test their ability to recover the mass profile of a galaxy using just the line-of-sight velocities of the GCs. I test this method on 25 zoom-in simulations of MW-mass galaxies and their associated GC populations. For the majority of this analysis, I use a fiducial sample of GCs defined as all star clusters with a present ($z = 0$) mass $> 10^5 M_{\odot}$, old ages (> 8 Gyr), and excluding the innermost clusters (projected $R > 2$ kpc). The mass cut is made to be consistent with what is likely to be observable (in external galaxies) with current telescope facilities. In addition I note that although the high mass end of the simulated GC mass function is in good agreement with that of the MW and M31, E-MOSAICS produces too many low mass clusters (likely due to under disruption, Pfeffer et al. 2018; Kruijssen et al. 2019a). Thus, the mass cut also works towards mitigating this effect. The age cut is made to be consistent with what is considered a ‘traditional’ GC, i.e. an old and massive bound star cluster. Also, this age cut will remove young disc clusters, which are often excised from spectroscopic studies because of extinction in the disc. Finally, the inner radius cut is made since this is the region where most observational studies are likely to be affected by crowding (although see e.g. Fahrion et al. 2020 for an example of GCs being identified and velocities extracted in the inner parts of a galaxy using MUSE), therefore making it difficult to identify and get reliable velocity measurements for GCs. In addition to the fiducial sample, I also test the effect of not including cuts on the age and the radius. However, overall the results are not systematically affected by these selections. For reference, I show the number of GCs in each simulated galaxy, for each selection in

Table 6.1: The total and stellar mass of each galaxy simulation along with the number of GCs in each of the 25 simulated galaxies for 3 different GC parameter restrictions. Note that the radius cut is based on projected x and y coordinates after the galaxy has been aligned as edge-on.

Simulation	$\log M_{200}$	$\log M_*$	All GCs	Age>8 Gyr	Age > 8 Gyr , R >2kpc
MW00	11.95	10.28	252	245	101
MW01	12.12	10.38	642	382	186
MW02	12.29	10.56	841	817	400
MW03	12.17	10.42	547	534	206
MW04	12.02	10.11	264	251	99
MW05	12.07	10.12	951	949	340
MW06	11.96	10.31	441	328	125
MW07	11.86	10.16	251	117	58
MW08	11.87	10.12	200	75	18
MW09	11.87	10.16	255	178	93
MW10	12.36	10.48	1012	494	295
MW11	12.15	10.06	205	134	66
MW12	12.34	10.44	1013	810	394
MW13	12.38	10.37	280	168	109
MW14	12.34	10.59	827	239	179
MW15	12.16	10.15	551	37	30
MW16	12.32	10.54	504	442	341
MW17	12.29	10.49	337	108	97
MW18	12.25	10.00	121	61	51
MW19	12.20	9.93	108	73	31
MW20	11.97	10.10	385	137	59
MW21	12.12	10.03	181	146	122
MW22	12.15	10.43	365	252	200
MW23	12.19	10.53	711	395	241
MW24	12.06	10.29	340	102	77

Table 6.1, keeping in mind that the clusters are always restricted to be more massive than $10^5 M_\odot$.

This paper is organised as follows, Section 6.2 describes the Jeans model used for this chapter and the inputs. Section 6.3 contains the outputs of the model and the first steps to interpret them, including the enclosed mass profiles. In Section 6.4 I discuss how the properties of the GC system, such as the spatial distribution, number and line-of-sight velocity error may affect the recovery of the DM mass profiles. In Section 6.5 I

correlate the DM profile recovery with other galaxy properties and discuss the resulting correlations and finally I summarise and conclude in Section 6.6.

6.2 The Jeans Model

6.2.1 Introducing the coordinate system

This chapter uses the cylindrical version of the Jeans equations and therefore works in cylindrical polar coordinates (R, θ, z) . However, for most of the equations presented here I work in projected Cartesian coordinates, where (x', y', z') represent the projected coordinates on the plane of the sky. The x' -axis is aligned with the galaxy's projected major axis, the y' -axis with the projected minor axis and the z' -axis lies along the line-of-sight such that the vector is positive in the direction away from the observer. I also perform the calculations using the line-of-sight velocity ($v_{z'}$) such that the vector is also positive in the direction away from the observer. The $v_{z'}$ is calculated by subtracting the mean line-of-sight velocity of the galaxy from that of the star particle.

6.2.2 Jeans-Anisotropic-MGE

To determine the DM halo density distribution I use a Jeans model with parameterised potential and tracer densities and maximise the likelihood of each parameter by comparing the velocity outputs with the measured line-of-sight velocity at multiple positions in the galaxy. In conjunction with the Jeans theorem, I assume a steady-state, time-independent form of the potential for each galaxy.

I model the simulated data-set using the extended version of the axisymmetric Jeans Anisotropic MGE formalism. This particular formalism takes the potential and tracer densities in the form of a multi-gaussian-expansion (Emsellem et al., 1994; Cappellari, 2002). The MGE is a series of 2D gaussians that provide information about the shape and intensity of a distribution. The MGE method developed by Emsellem et al. (1994)

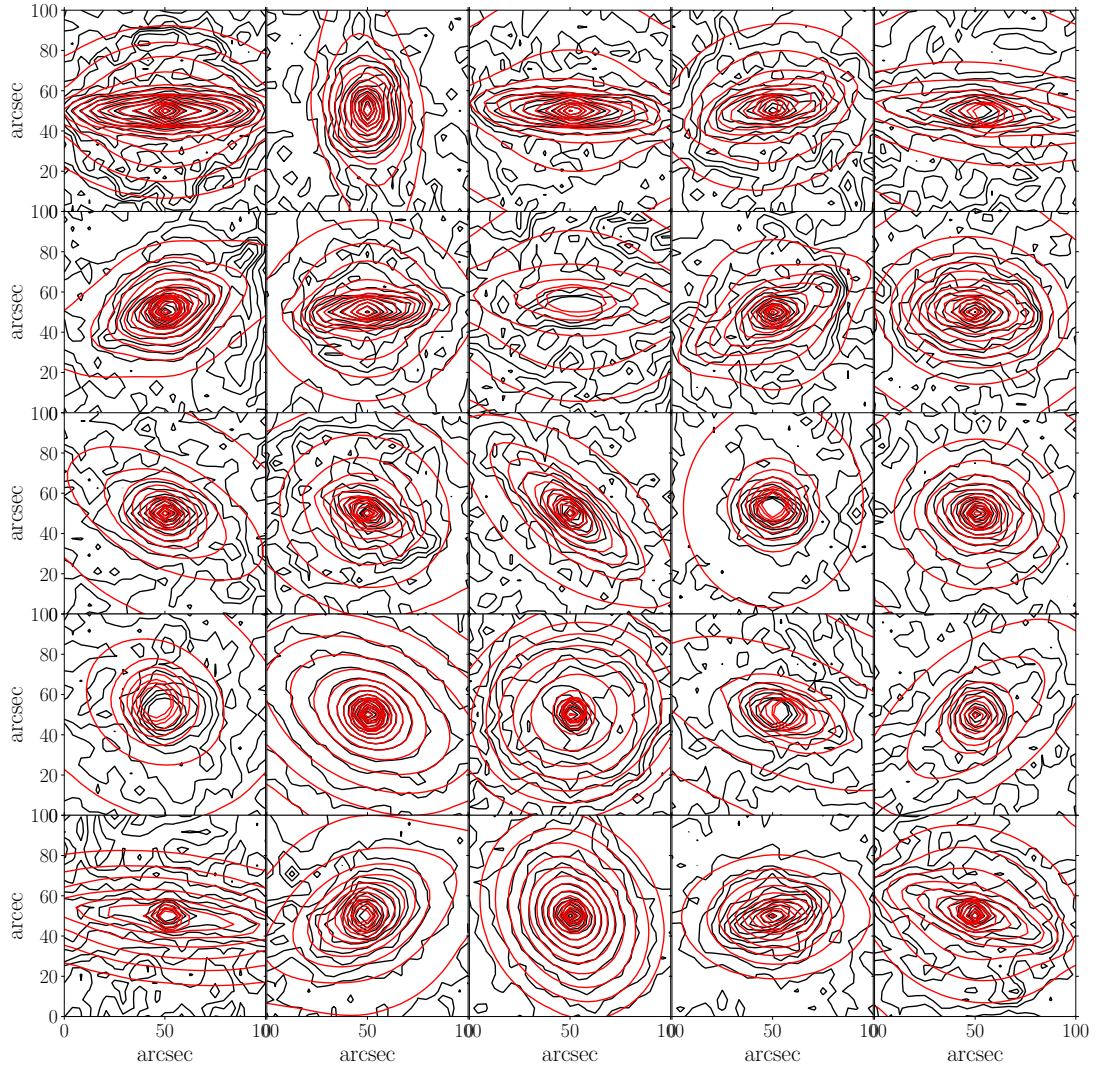


Figure 6.1: MGE fits for all 25 galaxies. The black contours show the distribution of baryons in the galaxies and the red ellipses show the MGE fits to the simulations. The galaxies are ordered from left to right and then top to bottom in increasing number, with MW00 in the top left and MW24 in the bottom right. The galaxies are projected at a distance of 1Mpc and we show the inner 100 arcsec square (100 arcsec equates to ≈ 480 pc).

(based on [Monnet et al. 1992](#)) has the benefit of being able to perform deprojection analytically and efficiently. I use the [Watkins et al. \(2013\)](#) implementation of the JAM formalism as it removes the need to spatially bin data. This means I can directly pass in the line-of-sight velocities and positions of each GC as a discrete data point.

The goal of this work is to determine how well the JAM model recovers the radial distribution and the mass of the DM halo when using GCs as the tracer population. I use the version of the JAM code made publicly available by ([Watkins et al. 2013](#), <https://github.com/lauralwatkins/cjam.git>) to calculate the first- and second-moments of the line-of-sight velocity. The code requires as inputs:

- The tracer density, characterised as a MGE. In this case I am using GCs as tracers and assume a spherical distribution for the GC population (i.e. I assume the system is not flattened in any direction). Therefore a 1D MGE is fitted to the projected $r' = \sqrt{x'^2 + y'^2}$ GC positions. I investigate the effect of assuming a spherical distribution in Section 6.4.1.
- The galaxy density, characterised as a MGE. The galaxy potential is split into two components. Firstly, the baryonic component, for which I use the MGE FIT SECTORS software (which is on the python package index, [Cappellari 2002](#)) to fit a 2D axisymmetric MGE directly to the x' and y' positions of the star and gas particles in the simulations. Here I fit directly to the baryonic masses so removing the need to factor in the mass-to-light ratio degeneracies. I show the MGE fits in Fig. 6.1 and see that for most galaxies the software outputs 2D gaussians that describe the baryonic distribution well. Secondly, the DM component is characterised by a generalised Navarro-Frenk-White (gNFW, [Navarro et al. \(1996\)](#)) profile

$$\rho(r) = \frac{\rho_0}{(r/r_s)^\gamma (1 + r/r_s)^{3-\gamma}}, \quad (6.1)$$

where r represents the galactocentric spherical radius) where the scale density (ρ_0), scale length (r_s) and inner slope (γ) are free parameters. This allows the profile to choose between cusps ($\gamma > 1$) and cores ($\gamma = 0$) while still becoming gNFW-like ($\rho \propto r^{-3}$ at large radii).

- The measured line-of-sight velocities of each GC. Having the luxury of simulated data means I know the exact present day velocity for every GC and choose to use a 10 km s^{-1} line-of-sight velocity uncertainty. To obtain the GC line-of-sight velocity including observational errors a normal distribution is randomly sampled with a mean of 0 km/s and a standard deviation of 10 km/s and added to the true velocity from the simulation. I then include the 10 km/s uncertainty in the calculation of the likelihood. However, I discuss this choice and how different errors may affect the results in Sections 6.4.3 and 6.4.4.
- The distance and inclination angle of the galaxy. For this work I project our simulated galaxies at a distance of 1Mpc and at an inclination angle of 90° (edge-on).
- The rotation parameter (κ) of the GC system. This sets the relative contributions of random and ordered motion to the root mean squared velocities. In these models I assume the rotation parameter to be 0.
- The velocity anisotropy parameter ,

$$\beta_z = 1 - \frac{\overline{v_z^2}}{v_R^2}, \quad (6.2)$$

calculated in cylindrical polar coordinates. I leave the velocity anisotropy to be free but constant i.e. a single value for the entire GC population. Parameterised this way, β_z takes values in the range $-\infty$ (tangentially biased) to 1 (radially biased). This large range of possible values can be difficult to work with. To deal with this, I re-parameterise as $\beta' = \beta/(2 - \beta)$, which takes values between -1 (vertical bias) and 1 (radial bias).

I highlight here that we are using JAM models which assume cylindrical alignment of the velocity ellipsoid. An alternative would have been to consider models with a spherically aligned velocity ellipsoid. [Cappellari \(2020\)](#) provides such JAM models along with accompanying software implementation. When choosing between the assumptions of cylindrical or spherical alignment, however, it is not a-priori obvious

which choice is more suitable for this problem, despite the GC systems being close to spherical in their spatial distribution. This is because spherical distributions can still have cylindrically aligned velocity ellipsoids. Thankfully, there is reason to believe that this choice will not greatly affect the results presented in this chapter. [Cappellari \(2020\)](#) also shows that inferred density slopes are statistically indistinguishable when using the axisymmetric or spherically aligned assumptions. Since the main goal of this chapter is to reconstruct mass profiles, this suggests that similar results would be obtained if the spherically aligned assumption was used.

To summarise, I have four free parameters in our model. These are three parameters from the DM distribution: the scale density, the scale length and the inner slope (ρ_0, r_s, γ) and a reparameterised version of the velocity anisotropy (β') . Aligning the galaxies edge-on removes the need for an inclination angle in the free parameters, but also adds an extra assumption to the rest of this chapter that should be kept in mind. However, for realistic disc galaxies, this work is best carried out in edge-on systems because these are the systems where the GC population is most readily observed and there are no uncertainties when deprojecting the MGE. I use a Markov-chain-Monte-Carlo (MCMC) method to explore this multi-dimensional parameter space.

6.2.3 Markov-chain-Monte-Carlo

The major improvement to previous JAM models, made by [Watkins et al. \(2013\)](#), is that there is no need to bin the data since the model takes discrete kinematic tracers. Previously, [Gerssen et al. \(2002\)](#) used individual stars with measured line-of-sight velocities to construct a discrete spherical Jeans model for the GC M15. [Chanamé et al. \(2008\)](#) extended the Schwarzschild dynamic models to also include discrete data sets and [van der Marel & Anderson \(2010\)](#) used line-of-sight velocities and proper motions of individual stars in the GC ω -Centauri to find the presence of a possible intermediate-mass black hole in its centre. For small data sets such as the GC systems of MW-mass galaxies being able to use discrete data is a huge advantage, I can compare models against the data-set on a GC-by-GC basis by defining a discrete likelihood. For this,

I use Bayes' theorem, where the posterior probability distribution function of any free parameter in a model can be written as

$$P(\theta|D) = \frac{P(D|\theta)P(\theta)}{P(D)}, \quad (6.3)$$

where $\theta = (\rho_0, r_s, \beta, \gamma)$ represents the model parameter set and $D = (x', y', v_{z'})$ represents the data set. $P(D|\theta)$ is the likelihood of an observation, given a model, $P(\theta)$ is the prior and $P(D)$ is a normalisation factor, sometimes called the evidence. The set of parameters that maximise the likelihood is the parameter set that reproduces the data most closely. In this case this means that this is the set of parameters that produce a DM halo that, together with the baryons, reproduces the GC velocities in the simulated galaxies.

The total likelihood of observing GC i given model θ is the product of the model likelihoods for each individual GC:

$$P(D|\theta) = \prod_{i=1}^{N_{\text{GC}}} \frac{1}{\sqrt{2\pi}\sigma_{i\theta}} \exp\left(-\frac{(\bar{v}_{z',i} - \bar{v}_{z',i\theta})^2}{2\sigma_{i\theta}^2}\right), \quad (6.4)$$

where

$$\sigma_{i\theta}^2 = \overline{v_{z',i\theta}^2} - \bar{v}_{z',i\theta}^2 + e^2, \quad (6.5)$$

where $\bar{v}_{z',i\theta}$ and $\overline{v_{z',i\theta}^2}$ are the predicted first and second moments respectively, for a given GC position i , given the model parameters θ . The error on the measurement of the true value is given by e . I also note here that this equation is only rigorously correct if the line-of-sight velocity dispersion is described by a Gaussian. The evaluation of the line-of-sight velocity dispersion is beyond the scope of this thesis.

I set flat priors given by:

- $5 \times 10^5 < \rho_0 / [\text{M}_\odot \text{kpc}^{-1}] < 5 \times 10^7$
- $0 < R_s / [\text{kpc}] < 50$
- $0 < \gamma < 3$

- $-1 < \beta' < 1$

I explore parameter space using the Markov-Chain-Monte-Carlo (MCMC) package, EMCEE, developed by [Foreman-Mackey et al. \(2013\)](#). EMCEE uses a number of independent walkers to explore the parameter space. Every walker takes a specified number of steps. At each step, an gNFW profile is calculated, for which a 1D spherical MGE can be fitted. This MGE is combined with the baryonic MGE (obtained by fitting the projected mass map directly from the simulation) to create the JAM potential density input. The JAM model then calculates the predicted first- and second-moments for the line-of-sight velocity at each GC position in this potential. I compare the JAM velocity moments with the true velocity moments (including the given velocity error) to return a likelihood value. 100 walkers are used, each taking 500 steps. The MCMC converges well in 500 steps, I checked this by eye and saw that the walkers settled down to a stable state. I burn in the chain at step 50 and therefore use 450 steps to produce the posterior distributions.

6.3 JAM outputs

6.3.1 Recovery of free parameters

As discussed in Section 6.2.3 the JAM model, when combined with an MCMC, returns a posterior distribution of the four free parameters in the model. These are three free parameters in the gNFW halo and the velocity anisotropy of the GCs. To understand whether the JAM model is performing well I would like to compare the results from the model to the 'true' values of the free parameters in the gNFW halo. However, I must also acknowledge that a range of parameter combinations may produce the same DM radial profile. To quantify this degeneracy in the 'true' parameter values, I perform an MCMC parameter exploration directly on density profiles from the simulation.

I first calculate a 1D DM density profile directly from the DM particles in the simulation using 100 logarithmically-spaced spherical shells. I then fit a gNFW profile to the

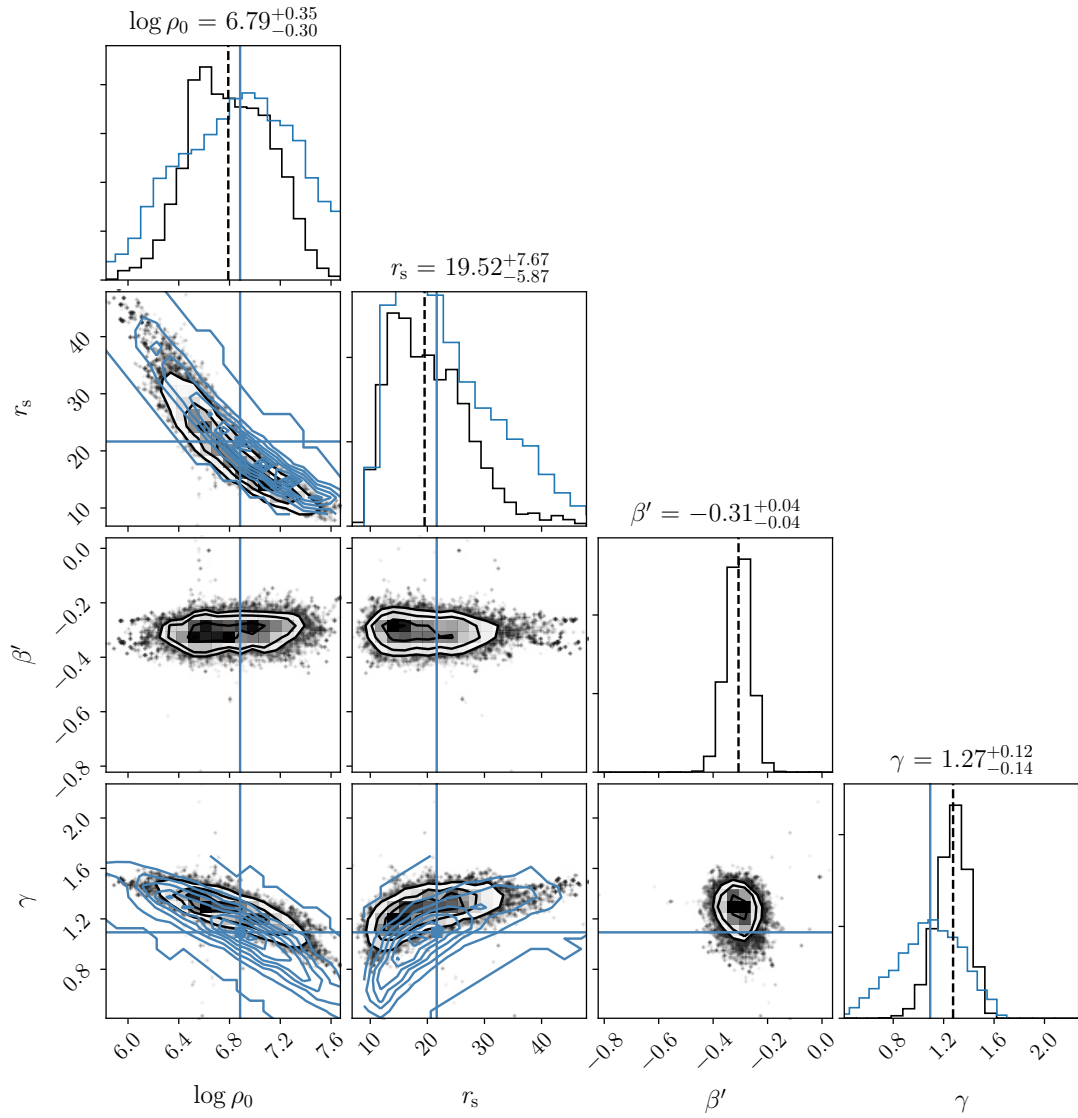


Figure 6.2: The posterior distributions for the four free parameters shown for one of the simulated galaxies (MW02). The grey 1D and 2D histograms represent the recovered values from the JAM model and the blue 1D histograms and vertical lines represent the fit directly to the simulated data.

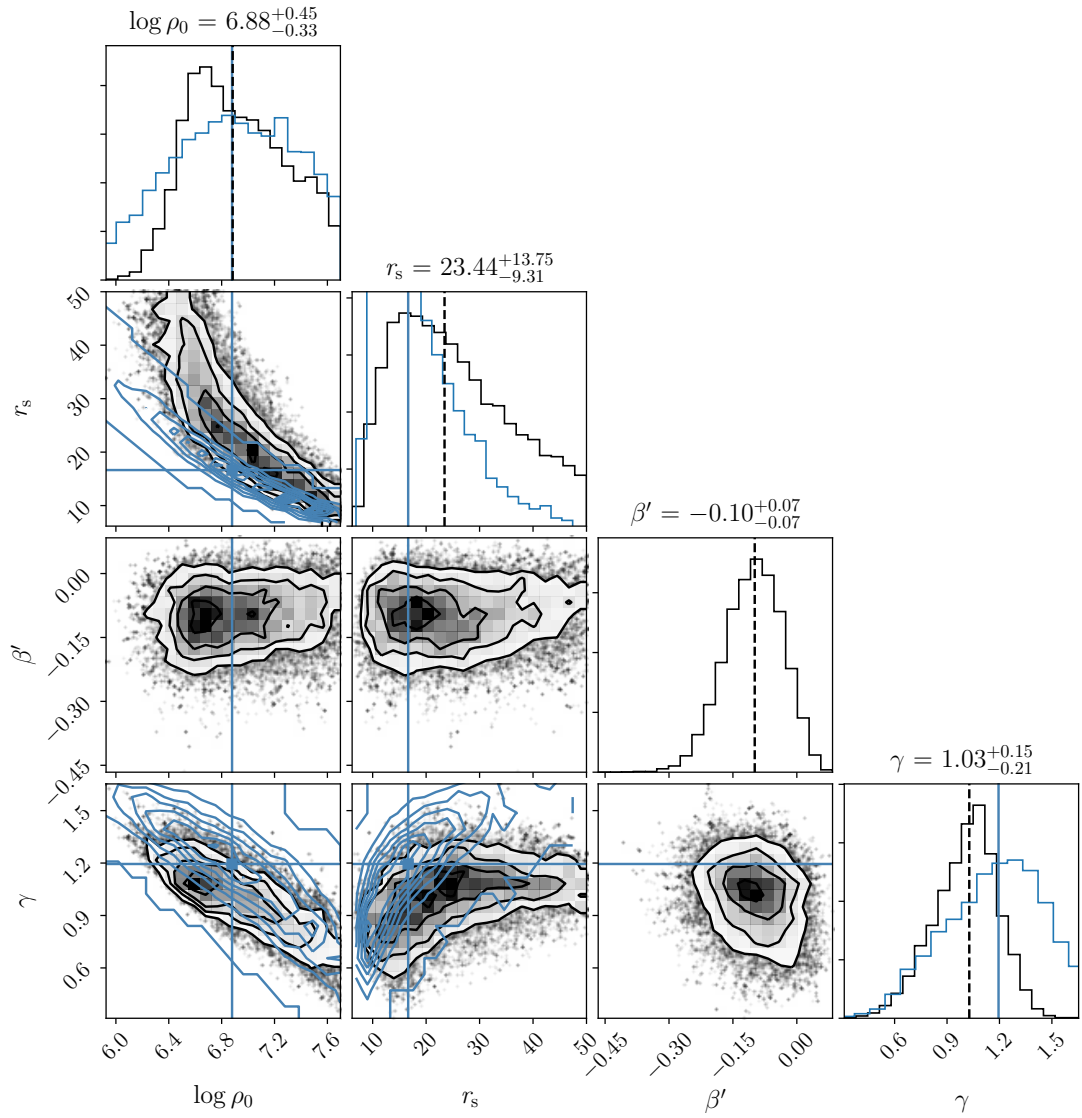


Figure 6.3: The posterior distributions for the four free parameters shown for one of the simulated galaxies (MW04). The grey 1D and 2D histograms represent the recovered values from the JAM model and the blue 1D histograms and vertical lines represent the fit directly to the simulated data.

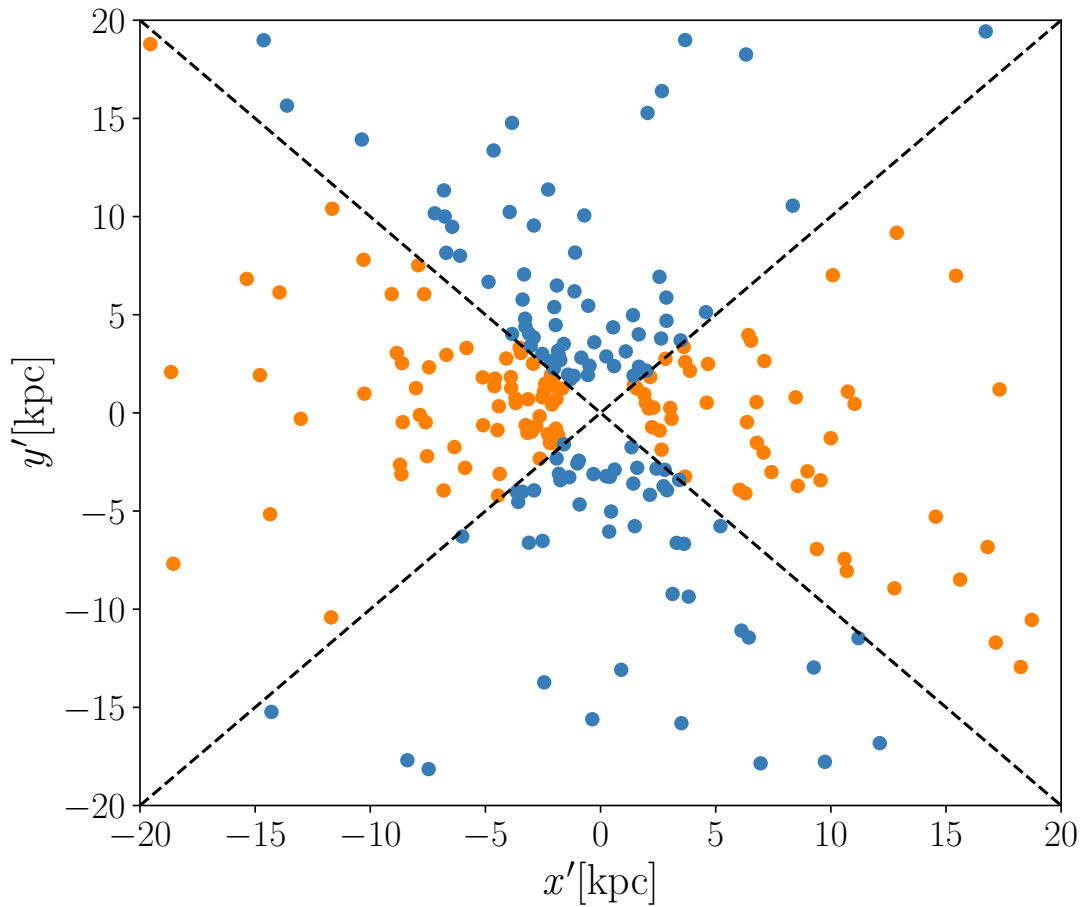


Figure 6.4: A demonstration of how we assign GCs to the major or minor axes for MW16. Each point represents one GC, coloured by whether it belongs to the major or minor axis population, with the minor axis shown in blue and the major axis shown in orange. The void in the centre is due to the inner 2 kpc radius cut.

true density distribution using the same free parameters, priors, number of walkers and number of steps as used for the JAM model. This then gives a posterior distribution for the true parameters that I can directly compare to the posterior distribution from the model. I include this step because the E-MOSAICS simulations are fully cosmological simulations and therefore their density profiles are only approximated by the gNFW parameterisation, so there will always be some uncertainty in the gNFW fit.

The 1D and 2D posterior distributions for two galaxies (MW02 and MW04) are shown in Figs. 6.2 and 6.3 where the black data shows the outputs from the JAM model and the blue data shows the outputs from the gNFW fit applied directly to the DM particles from the simulation. A β' could not be directly calculated from the simulations due to

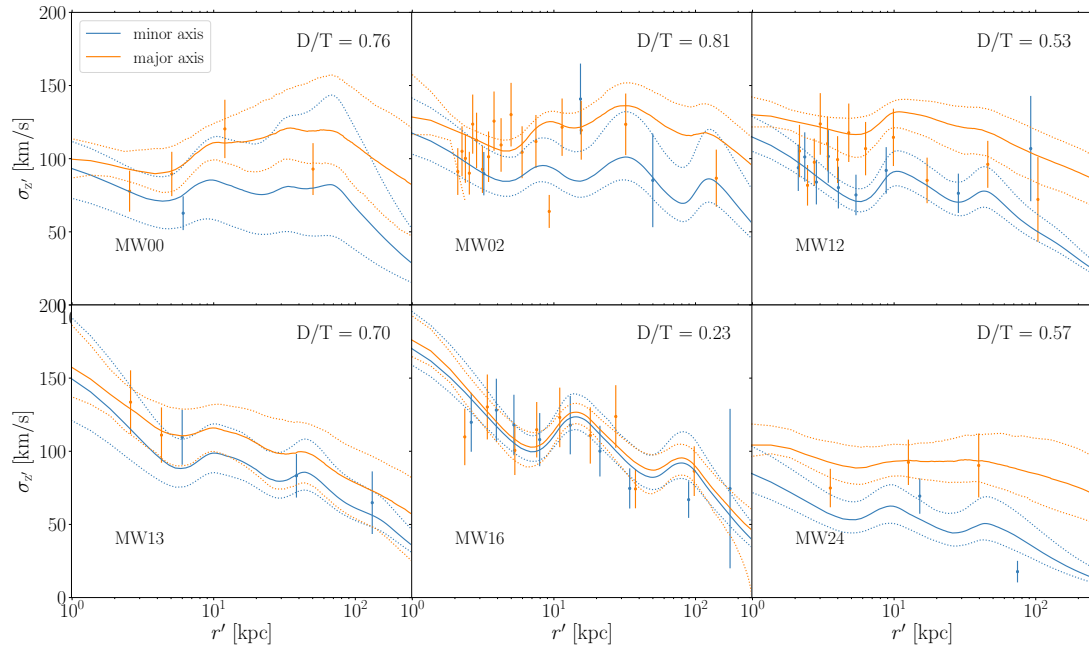


Figure 6.5: The line of sight velocity dispersion ($\sigma_{z'}$) recovered from JAM and directly from the simulations as a function of projected radius for 6 of the simulated galaxies. The continuous solid line shows the median JAM output and the dotted lines represent the 1σ spread in the predictions. The points with error bars show the true $\sigma_{z'}$ calculated directly from the simulations. To calculate the true GC $\sigma_{z'}$ we binned the GCs in groups of 20. In the top right corner I indicate the disc to total mass ratio (D/T) for each galaxy.

the low numbers of GCs. I exclude a small percentage of the walkers from this analysis as they diverged from the majority. The first thing to note is that there are significant degeneracies in the recovery of the true parameters: $\log \rho_0$ anti-correlates with r_s and γ , and r_s correlates with γ . This means that although there are most-likely values, there are multiple combinations of these parameters that will produce the same fit to the DM particles. Therefore, it is good to be wary of comparing the absolute values of the free parameters given by the JAM model and the fit directly to the DM particles. I discuss our chosen method of comparison in the next section.

In the contour plot for MW02 (Fig. 6.2) I see that the posterior distributions for the JAM model almost lie on top of that for the true fit, meaning that the recovered values for each DM halo parameter are close to that of the true value and that the degeneracies encountered in the JAM model are explained by the intrinsic degeneracies in the parameters. The 1D histograms show the posterior distributions for each parameter individually. The blue histogram and solid blue vertical line represent the posterior

distribution and the median value of the ‘true’ fit and the black histogram and vertical dotted line represents the same for the JAM fit. In Fig. 6.2 the posterior distributions for the true fits and the JAM model are similar in shape and the median values are reasonably close. However, for MW04 (Fig. 6.3) the posteriors for the JAM model are offset slightly from those of the true fit, this is also evident in the shape of the posterior distributions for each parameter, although the median values for the free parameters are still recovered well. Also note that the posterior distributions are wider in shape for MW04 (Fig. 6.3) than for MW02 (Fig. 6.2), which means that the JAM model cannot get as good constraints on the DM distribution in MW04. These two galaxies were chosen because they represent two different cases of the DM distribution recovery. Table 6.1 shows that MW04 has almost 4 times fewer GCs than MW02 and therefore this could be the driving factor for the difference in the constraints for the two galaxies. This is discussed further in Section 6.4.2, but for now this is a good demonstration of how well the JAM model is performing in general and, after inspecting all the recovered parameters for all galaxies, there are no JAM recoveries that differ too greatly from the true recovered parameters.

6.3.2 Recovery of velocity moments

The JAM model calculates the first and second velocity moments at any given position in the galaxy. It is therefore possible to compare the line of sight velocity dispersion ($\sigma_{z'}$) as given by JAM to that calculated directly from the simulations. Since this is an axisymmetric model, I first divide the galaxy into a major (x') and minor (y') axis. For the JAM predictions, this is relatively straightforward since I can just calculate the velocity moments directly along the $y' = 0$ axis and the $x' = 0$ axis to obtain predictions for the minor and major axis respectively. I divide the x-y plane into quadrants using the $x = y$ and $x = -y$ lines, and assign GCs to the major or minor axis according to the quadrant where they are located, as demonstrated by Fig. 6.4. The blue points represent the minor axis GCs and the orange points represent the major axis GCs. The void in the centre is the 2 kpc inner radius cut.

The calculation of the true first- and second-moments of the velocity directly from the simulations is reasonably straightforward. The first moment is simply the $v_{z'}$ outputted directly from the simulation. However, for the second moment we must bin the GCs. The GCs are binned along each axis in groups of 20 and the second moment is given by

$$\overline{v^2_{z'}} = \frac{1}{N_{\text{GC}}} \sum_{i=1}^{N_{\text{GC}}} \overline{v^2_{z',i}} \quad (6.6)$$

where N_{GC} is the number of GCs in the bin. From the first- and second-moments the final line-of-sight velocity dispersion is given by

$$\sigma_{z'} = \sqrt{\overline{v^2_{z'}} - \overline{v_{z'}}^2}. \quad (6.7)$$

The JAM predictions and simulation calculations for $\sigma_{z'}$ are shown for six galaxies in Fig. 6.5, where the solid and dotted lines represent the median and 1σ spreads from the JAM model respectively and the points represent the velocity dispersion calculated directly from the simulation. Each point is calculated using 20 GCs, with the x-axis position representing the centre of the 20 GC bin (for example we see that MW02 has many GCs in its central 10 kpc). I fold the galaxy about the minor axis, this is done because the first moment of the velocity is squared, so it removes the need to keep the sign of the velocity. The error bars are calculated via a Monte-Carlo error calculation.

Fig. 6.5 shows that the $\sigma_{z'}$ from the JAM model matches that calculated from the simulations reasonably well within the errors. This is a good demonstration of how good dynamical models of galaxies can be constructed using just the GCs as tracers, even for galaxies such as MW13 where there are a limited number of tracers. I do notice however that in MW12, although the JAM model does a good job at predicting the velocity dispersion along the minor axis it over predicts the velocity dispersion along the major axis particularly in the outskirts.

Fig. 6.5 also shows that there is variation in the shape of the JAM predictions between galaxies. I particularly take note of the difference between some galaxies, such as MW16 and MW12, where the predictions for the minor and major axis are very similar and reasonably different, respectively. The number in the top right corner of each panel

represents the disc to total mass ratio (D/T). D/T is calculated by assigning stellar particles to the disc or halo component of the galaxy. This is done by calculating the fraction of angular momentum that is in the disc plane for each particle, also known as the circularity parameter $\epsilon_J = J_z/J_c(E)$ (Abadi et al., 2003) where $\epsilon_J = 1$ describes a perfectly circular orbit. The stellar particles that belong to the disc component have $\epsilon_J > 0.5$ (Sales et al., 2015).

MW16 is likely to have velocity dispersion profiles that are similar along the minor and major axis due to the fact that this galaxy is not very disc dominated and is therefore more elliptical in shape, making the galaxy more spherically symmetric. In addition, MW16 also has a similar number of tracers along its major and minor axis so the data quality is similar in both cases. The rest of the galaxies in Fig. 6.5 have $D/T > 0.5$ and therefore are in the disc-dominated regime. In these cases there is a clear difference between the major and the minor axis velocity dispersions, with the major axis being dominated by the disc component always having higher velocity dispersion. This is because, in a disc galaxy orientated edge-on the major axis constitutes a thicker component and there are particles on different stages of their orbits.

6.3.3 Recovery of dark matter mass distribution

As it is shown and discussed in Section 6.3.1, there are significant degeneracies between the free parameters in the gNFW profile. Therefore it is better not to compare the true and JAM-recovered individual parameters, but to compare the DM distribution and mass enclosed within a chosen radius given by the simulations and recovered by the JAM model. This mitigates the need to take parameter degeneracies into account. I therefore convert the gNFW profile parameters into enclosed mass profiles. For the JAM outputs I calculate a realisation of the profile for each MCMC run and plot the 1 and 2σ spread of the mass enclosed at each radius. The DM enclosed mass profiles for the 25 simulated MW-mass galaxies are shown in Fig. 6.6, where the black solid line represents the DM mass calculated directly from the DM particles in the simulation. The blue shaded regions represent the 1 and 2σ recovered DM mass from the JAM

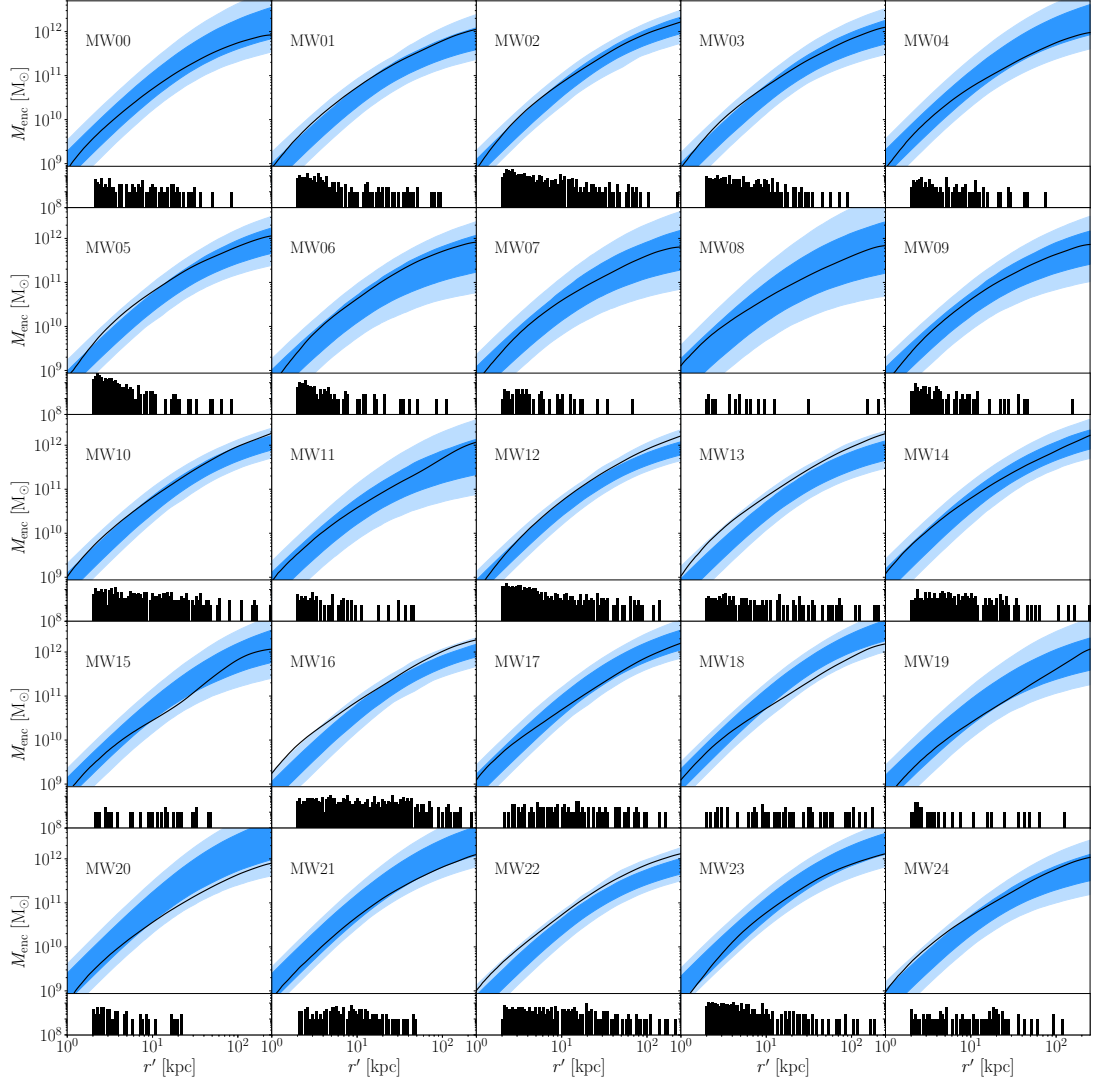


Figure 6.6: Projected radial profiles of the mass enclosed for the 25 galaxies, using all clusters at $z = 0$ with a mass $> 10^5 M_{\odot}$, an age $> 8\text{Gyr}$ and a galactocentric radius $R > 2\text{kpc}$. The solid black line represents the true mass calculated directly from the simulations. The blue-shaded regions represent the 1 and 2σ bounds on the recovered mass from the JAM model. Each panel also contains a histogram of the 2D projected GC positions.

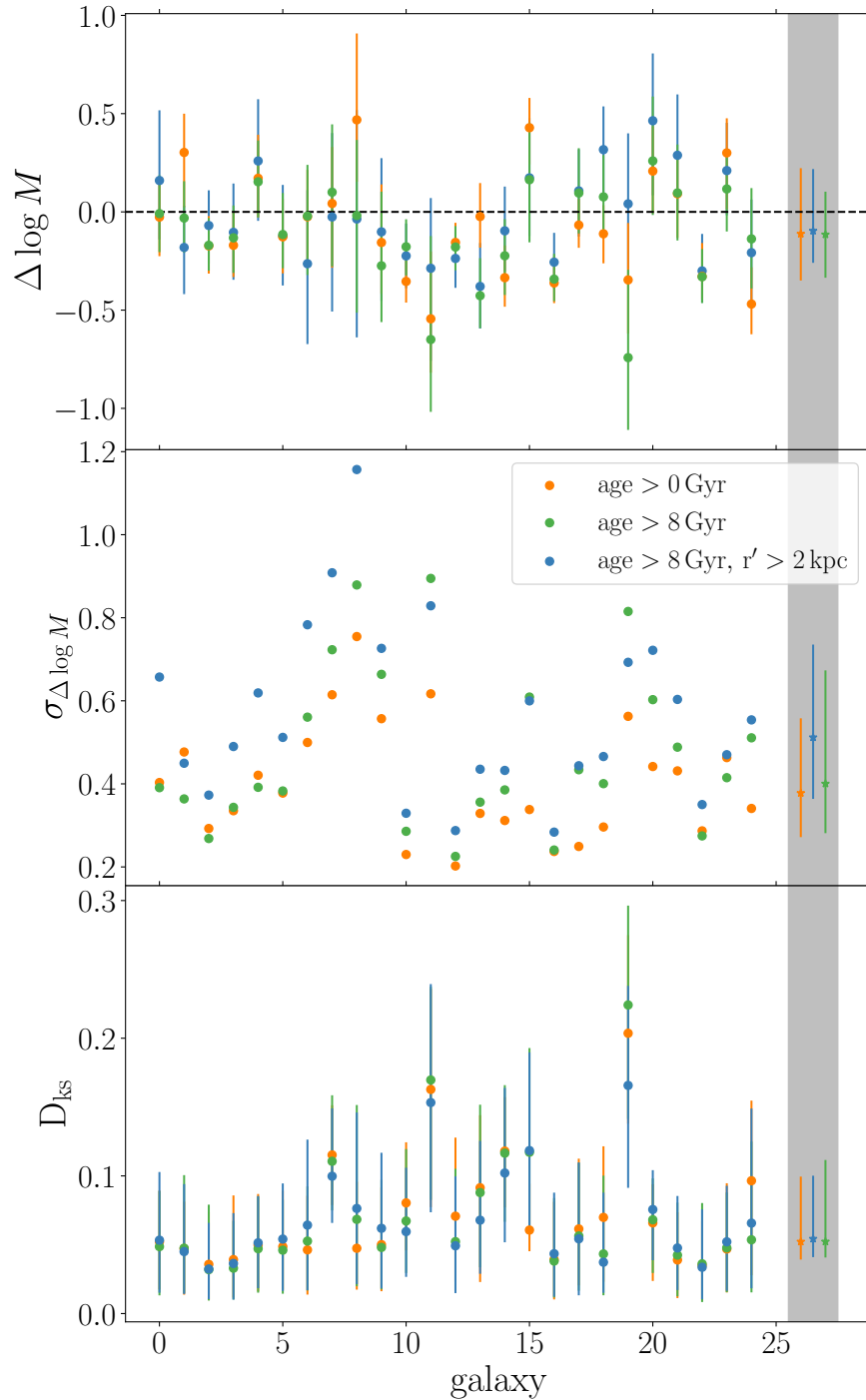


Figure 6.7: Estimators of the performance of the JAM model. From top to bottom, they quantify the DM mass difference, the spread in the DM mass difference and the maximum values of the KS test, for all the galaxies in the suite of 25 Milky Way-mass zoom simulations. Data points correspond to different samples of GC tracers as indicated in the legend. The grey-shaded region contains the averages and 1σ spreads for each of the GC sub-samples, indicated by the stars with errorbars.

model. At the bottom of each panel, I also show a histogram of the GC positions, plotted as a function of projected spherical coordinate R' . This is useful to understand how the GCs are distributed in 2D projected $x' - y'$ space. Fig. 6.6 shows that the radial distributions of the recovered and true DM distributions are similar for all galaxies, with no obvious outliers. However, I do notice that there are clear differences between how well the JAM model performs for each galaxy. For example, when comparing MW16 with MW07, the JAM model under predicts the DM mass in MW16 but the 1σ and 2σ spread are very small. However, the true DM mass in MW07 is almost in the middle of the 1σ spread, its precision is much larger. To compare quantitatively the results for different simulated galaxies I use three quantities: the recovered vs the true mass enclosed at the maximum GC radius, the 1σ spread in this mass and a cumulative distribution test.

To quantify the difference between the recovered DM mass from JAM and the true DM mass within the maximum GC radius I use the log difference,

$$\Delta \log M = \log(M_{\text{JAM}}/M_{\text{true}}), \quad (6.8)$$

where M_{JAM} is the median of the posterior of the JAM fits. This means that JAM model over- or under-predicts the mass when $\Delta \log M > 0$ and $\Delta \log M < 0$, respectively.

The second test I use is the spread in $\Delta \log M$ due to the 1σ spread in the recovered mass from JAM,

$$\sigma_{\Delta \log M} = \log(M_{\text{JAM},84}/M_{\text{true}}) - \log(M_{\text{JAM},16}/M_{\text{true}}) \quad (6.9)$$

where $M_{\text{JAM},16}$ and $M_{\text{JAM},84}$ represent the 16th and 84th percentiles of the JAM-recovered enclosed mass. These two values are informative about how close to the true value and how well constrained the JAM-recovered mass is.

The previous two parameters inform us about the mass of DM at a given radius. However, the free parameters in the JAM model also describe the radial profile of the DM distribution, therefore I also test how the radial profile of the DM from the JAM model

compares to the true profile. For this, I use a Kolmogorov-Smirnov (KS) test, which is a nonparametric test of whether two cumulative distributions differ. The KS test determines whether the null-hypothesis that the two distributions are from independent samples drawn from the same underlying form is likely to be true or not. The KS D value (D_{KS}) represents the maximum value of the absolute difference between the two cumulative distribution functions and therefore the lower this number, the more likely it is that the two distributions match. I calculate D_{KS} for each simulated galaxy by calculating the difference between the normalised cumulative distribution functions of the DM radial profiles directly from the simulations and the JAM output. I do this at 100 radii logarithmically spaced between 2 kpc and the maximum GC radius, and find the maximum difference.

To summarise, I have now described three parameters that we use to quantify how well the JAM model performs, two that describe how well the mass at the maximum GC radius is recovered ($\Delta \log M$, $\sigma_{\Delta \log M}$) and one that quantifies how well we recover the radial profile of the DM distribution (D_{KS}).

Fig. 6.7 shows these three parameters for all 25 galaxies. I show, for each galaxy, three variations on the selection of GCs (which I include in all steps of the model setup, and given in Table 6.1). The orange points represent the case where I use all of the star clusters with $M > 10^5 M_{\odot}$, the green points represent the case where I restrict the sample to the classical ancient GCs ($M > 10^5 M_{\odot}$, age > 8 Gyr) and the blue points represent the case where I also exclude the inner-most GCs ($M > 10^5 M_{\odot}$, age > 8 Gyr, $r' > 2$ kpc). In Fig. 6.7 I also show the median of each of the three values, represented by the stars within the grey shaded region. Fig. 6.7 shows that in all GC sub-samples the JAM model marginally underestimates the DM mass, but is consistent with not showing any biases. The middle panel of Fig. 6.7 shows that the subset of GCs with $M > 10^5 M_{\odot}$, age > 8 Gyr, and $r' > 2$ kpc have the largest $\sigma_{\Delta \log M}$. However, in the D_{KS} test, which quantifies the recovery of the DM radial distribution, none of the three GC sub-samples performs consistently better than the others. The radial profile recovery is reasonably consistent between galaxies, with two potential outliers. Galaxies MW11 and MW19 (along with MW15) have a massive companion

galaxy that is distorting the shape of the DM halo and causing it to no longer be well parameterised by an gNFW halo. The mass of the DM halo is still well recovered in these galaxies and I therefore keep them in the rest of the analysis.

For the rest of the analysis I use the GC selection that includes the radius and the age cut, motivated by previous discussions about observational constraints. Therefore, in the rest of this chapter, I define a GC as a star cluster with $M > 10^5 M_{\odot}$, $\text{age} > 8 \text{ Gyr}$ and $r' > 2 \text{ kpc}$. I now look into the different properties of the GC populations and investigate which galaxy properties may be affecting the variations in the recovery of the DM profile.

6.4 Investigation of the effects of the GC system

6.4.1 Effect of GC distribution sphericity

In the JAM model I force the GC distribution to be spherical because I model it with a spherical MGE. However, it is interesting to see how spherical these distributions are in the simulations and how deviations from sphericity affects the recovery of the DM distribution.

A ‘sphericity’ parameter (s) is obtained for the GC spatial distribution using the methodology described in [Thob et al. \(2019\)](#). The 3D spatial distribution of GCs is modelled with an ellipsoid with major, intermediate and minor axes a , b and c . The sphericity of this distribution can then be defined as,

$$s = \frac{c}{a}. \quad (6.10)$$

For spherical distributions, $s = 1$. The axis lengths are defined by the square root of the eigenvalues of a matrix that describes the three-dimensional GC distribution. The matrix is chosen to be the tensor of the quadrupole moments of the spatial distribution (often referred to as the moment of inertia tensor). I direct the interested reader to [Thob et al. \(2019\)](#) for more details.

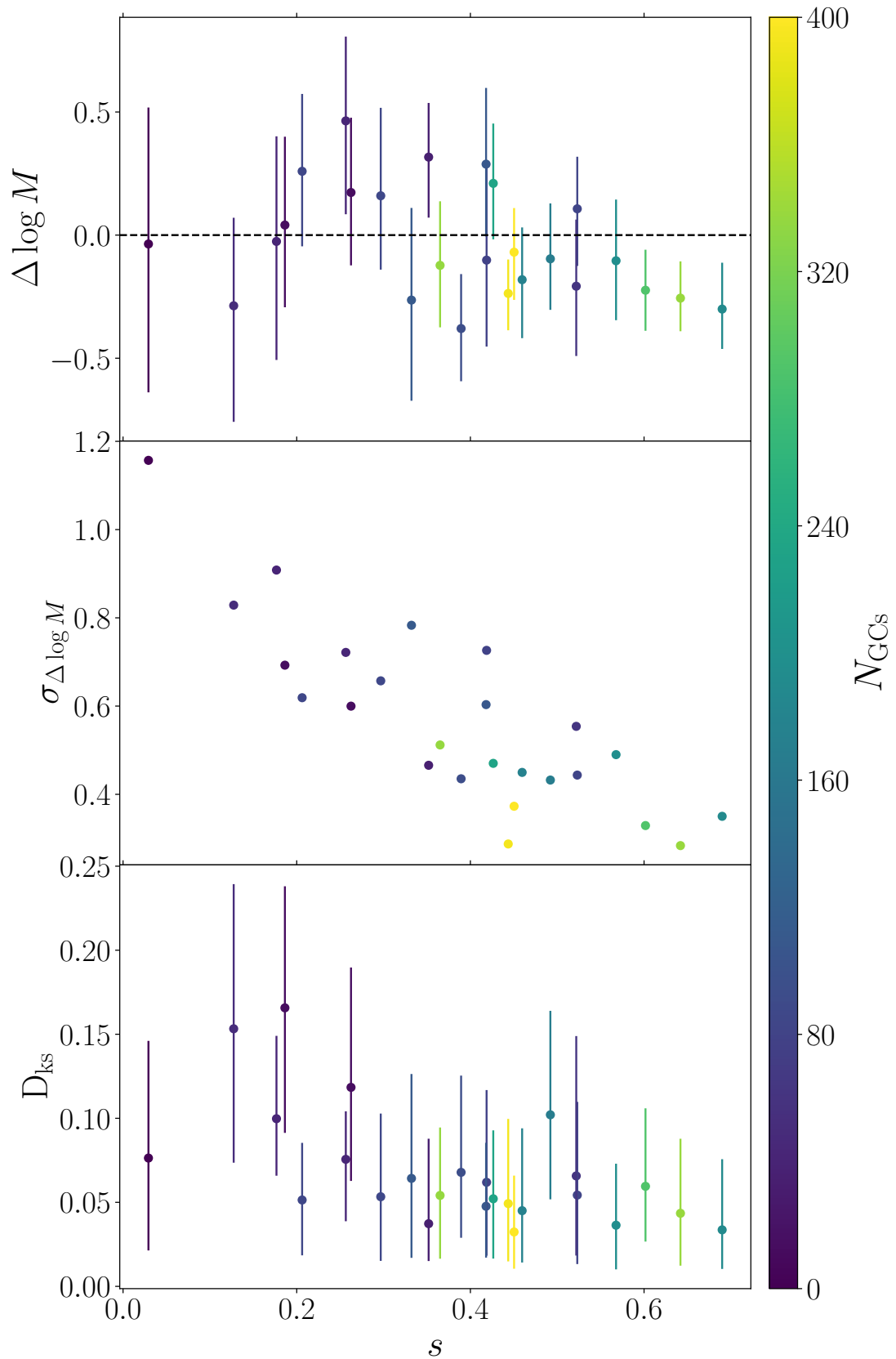


Figure 6.8: Estimators of the performance of the JAM model as in Fig. 6.7, as a function of the sphericity (s) of the GC distribution, with $s = 1$ being a spherical distribution. The points are also coloured by the number of GCs used in the JAM model.

In Fig. 6.8 I show the mass and radial profile recovery of the DM distribution as a function of s . Each point represents one galaxy and the points are coloured by the number of GCs in each galaxy. First of all, I note that although we are modelling the GC distributions as spherical, they often deviate from this assumption. This could be due to sparse sampling in the calculation of this parameter. I perform Monte Carlo simulations to estimate the axis ratio of 2D ellipsoids and find that the error will increase with increasing sphericity. I calculate a maximum error of 0.06 for $s > 0.6$.

I first focus on the recovered mass ($\Delta \log M$ and $\sigma_{\Delta \log M}$). Importantly, the sphericity does not have an effect on the absolute value of $\Delta \log M$ i.e. the sphericity does not bias the recovery of the mass enclosed. As expected, as s increases (the GC distribution becomes more spherical), the recovered mass becomes more constrained, as shown by $\sigma_{\Delta \log M}$ becoming smaller. Next, I focus on the radial profile of the distributions, D_{KS} shows that as s tends towards 1 the radial profile of the recovered DM becomes closer to the true radial profile. However, those galaxies with GC systems with a sphericity parameter greater than ≈ 0.3 have similar D_{KS} values.

Fig. 6.8 shows that there tends to be more GCs in more spherical systems. For example, the galaxy that has the least spherical GC distribution (MW18) also has the least number of GCs, at just 18. This could simply be because with less GCs the system appears less spherical because it is not well-sampled. Alternatively, it could be related to another correlation between assembly history and richness of the GC system, with galaxies with fewer minor mergers have fewer GCs (Kruijssen et al., 2019a). Therefore, the galaxies with fewer GCs also underwent fewer minor mergers and therefore could not uniformly populate the halo volume with GCs. I would expect that galaxies with fewer GCs would also have flatter distributions because their GC population is made up of a higher fraction of in-situ GCs which formed in the disc. Above a sphericity of 0.3 it seems that the two properties of the GC system (number and sphericity) work together to affect the output of the JAM model. $\sigma_{\Delta \log M}$ is, on average, continuously decreasing with s , however at a given s (above 0.3) $\sigma_{\Delta \log M}$ depends on the number of GCs. This is also apparent in the radial profile recovery – the two galaxies that have the best match in the DM distribution are also the two galaxies with the most

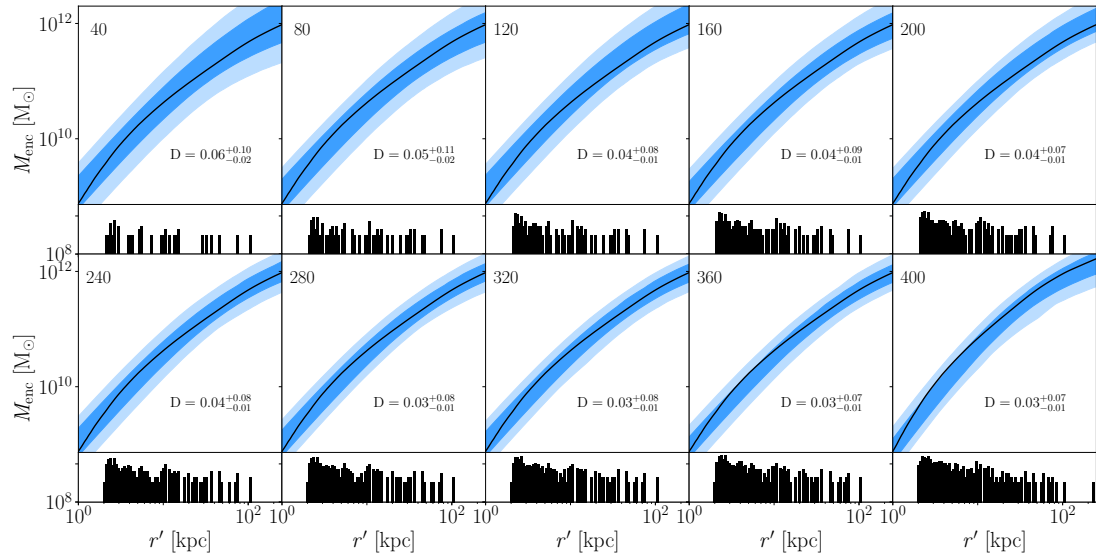


Figure 6.9: Mass enclosed profiles for MW002 with its GCs randomly sampled to include 10-100 percent of them. We show the D_{KS} value of each JAM model in the relevant panel. The number in the top left of each panel shows the number of GCs used in the JAM model. The lines and shaded regions correspond to the description in Fig. 6.6

GCs.

Therefore, I conclude that both the sphericity and the number of GCs impact how well the DM profile can be recovered. However, within the models, I note a strong correlation between the sphericity and GC number, hence observations limited to large GC systems are less likely to be affected by non-sphericity of their GC systems. I investigate the impact of the number of GCs in the next section.

I also note here that we find that the concentration of the GC system ($r'_{\text{median}}/r'_{\text{max}}$) plays no role in the recovery of the DM mass or overall radial profile.

6.4.2 Number of GCs

I now investigate how the number of dynamical tracers used as an input to the JAM model affects how well the JAM model can recover the DM mass profile. I do this in two ways: first by varying the number of GCs in one galaxy and then a comparison between the number of GCs in different galaxies. Note that in this subsection we keep

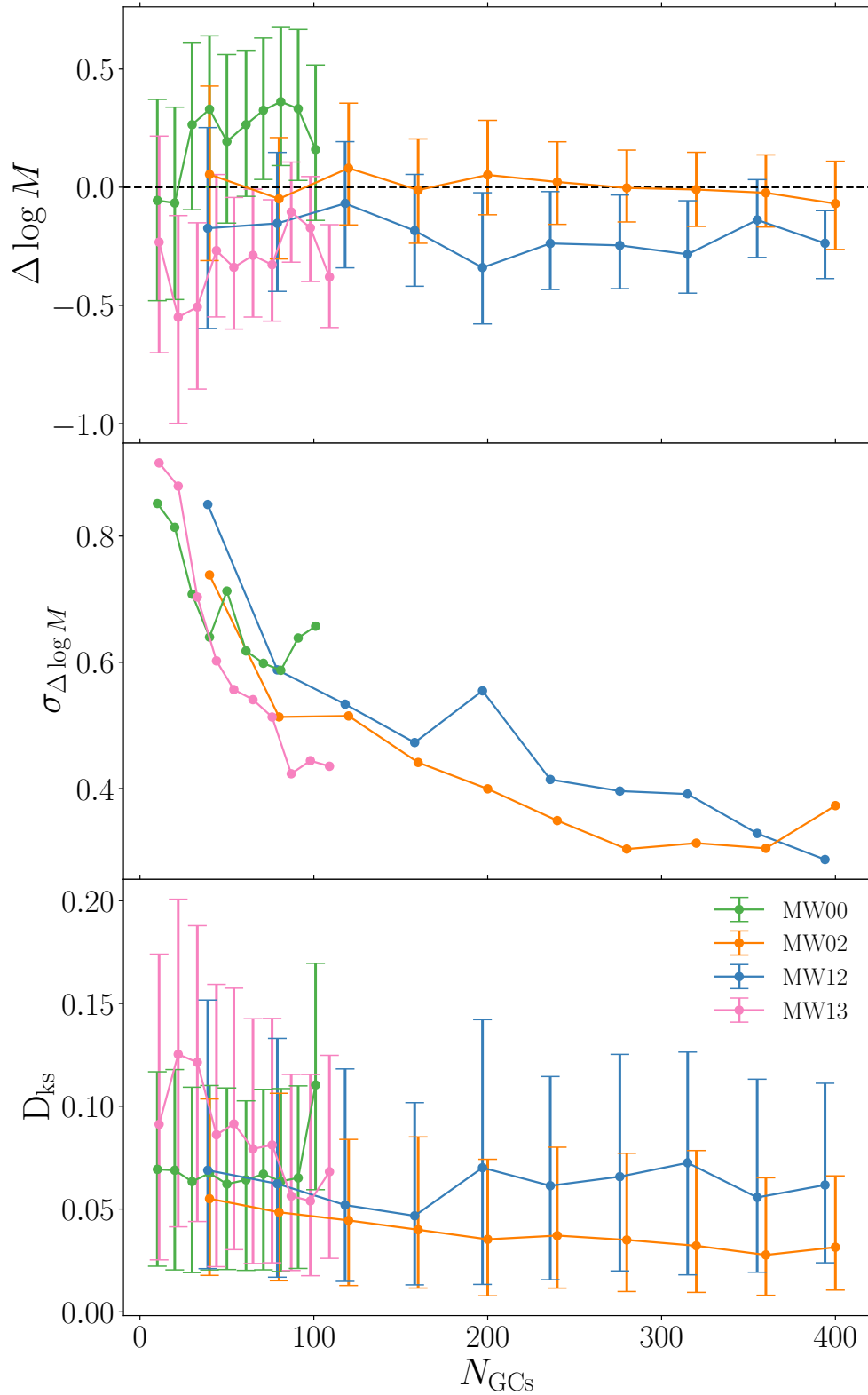


Figure 6.10: Estimators of the performance of the JAM model as in Fig. 6.7, as a function of the number of GCs used in the model. Here we show four galaxies: MW00, MW02, MW12 and MW13 indicated by the legend.

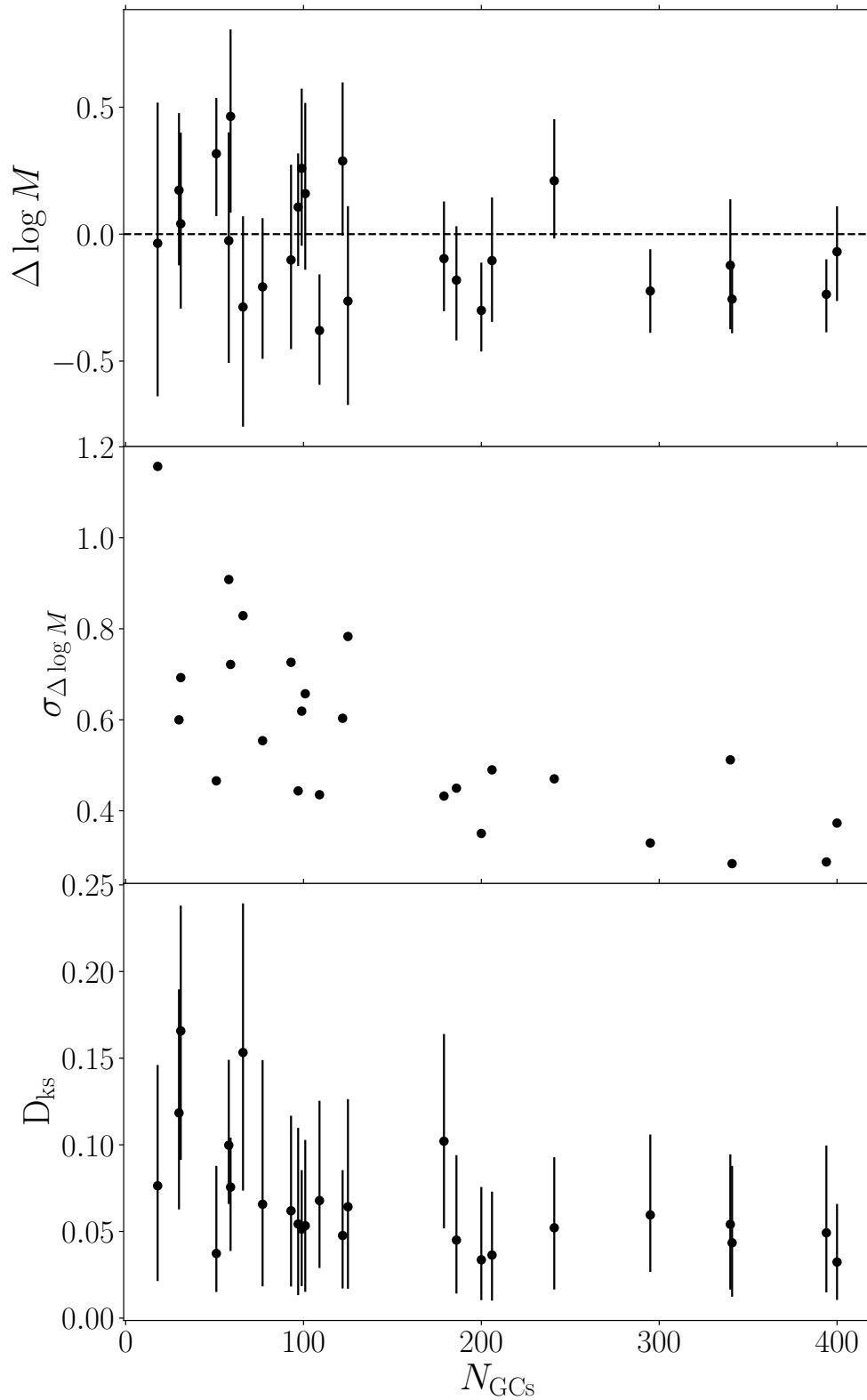


Figure 6.11: Estimators of the performance of the JAM model as in Fig. 6.7, as a function of the total number of GCs in the galaxy and used in the JAM model. Each point represents one of the 25 simulated galaxies.

the velocity error $\Delta v_{z'} = 10 \text{ km s}^{-1}$.

First, I randomly sample the GCs in one galaxy, to select 10, 20, 30, 40, 50, 60, 70, 80 and 90 per cent of their GCs as inputs to the JAM model. I use just the randomly sampled GC throughout the whole JAM model, including the initial MGE fit to their positions. I then carry out our analysis in the same way as before. Fig. 6.9 shows the enclosed mass profiles for MW02 for each subset of GCs. Here the plots are the same as described for Fig. 6.6. From left to right and top to bottom the number of GCs used is increased in steps of 10 per cent and the number in the top left corner is the number of GCs used. In the bottom right of each panel the KS statistic is quoted. As can be seen in the top panels, the uncertainty in the recovered DM radial profile decreases as the number of GCs is increased from 40 to 200. Not much further improvement is gained by increasing the number of GCs to 400 (bottom panels). It is particularly encouraging that in this galaxy, the radial profile is well recovered even with only 40 GCs, with errors less than 6 per cent.

I follow the same method of randomly sampling GCs in three more galaxies. I chose these simulated galaxies because their mass profiles are recovered similarly well when all their GCs are used, but they have a different total number of GCs. The mass and radial profile recovery for these four galaxies, as a function of the number of GCs used (N_{GCs}) is shown in Fig. 6.10. The recovery of the radial profile of the DM improves when a higher fraction of a galaxy's GCs is used, as shown by the average D_{KS} value decreasing with increasing N_{GCs} . There is no systematic trend in $\Delta \log M$ with the fraction of GCs used, but there is a consistent offset for each galaxy, meaning that if the model underestimates the mass when using 100 per cent of its GCs, it does when using a smaller fraction of its GCs. This shows that the number of GCs does not cause an estimate of the enclosed DM mass to be an over- or under-estimation. The one sigma spread ($\sigma_{\Delta \log M}$) decreases as the fraction of GCs increases. This forms a narrow negative correlation. An increasing number of GCs are needed to get the JAM models as well constrained and as close to the shape of the true DM profile as possible.

I now plot every galaxy as a function of the total number of GCs used in the Jeans model. This is shown in Fig. 6.11, where each point now represents an individual

galaxy, with all of its GCs. Here I see that the Jeans models produce consistently lower $\sigma_{\Delta \log M}$ in galaxies with more than 150 GCs compared to those with fewer than 150 GCs. The Jeans models in the galaxies with increased number of GCs also recover the overall radial profile of the DM consistently well. However, it does not mean that in galaxies with fewer than 150 GCs, models systematically fail at recovering the mass and radial distribution of the halo, but instead that there is a lot of scatter in the recovered mass and profile. To guarantee that the JAM model will perform well, I would suggest that more than 150 GCs are needed for a Jeans model of a Milky Way-mass galaxy. As previously mentioned, the mean accuracy in the recovered mass ($\Delta \log M$) for all the galaxies is 0.21 dex with a precision ($\sigma_{\Delta \log M}$) of 0.57 dex. However, when considering galaxies with more than 150 GCs, although the accuracy only improves by 0.03 to 0.18 dex, the precision increases to 0.38 dex, almost a 0.2 dex improvement in precision. We conclude that with fewer than 150 GCs, the Jeans model could be recovering the mass profile accurately without bias. However, to obtain a precise constraint more than 150 GCs are needed.

The analysis so far assumed a line-of-sight velocity error of 10 km s^{-1} . However, the number of GCs needed may be impacted by the quality of the data. I therefore investigate the effect of data quality by increasing the line-of-sight velocity error in the next section of this chapter.

6.4.3 Line-of-sight velocity error

So far, this analysis has been performed using a 10 km s^{-1} line-of-sight velocity error. This, although achievable with surveys such as the Fornax 3D survey, is not always the error reached for all GCs (e.g. [Fahrion et al. 2020](#)). I therefore investigate the impact of increasing the error to 60 km s^{-1} in increments of 10 km s^{-1} . For this, I take a similar approach to the previous section: I take the same four galaxies and rerun the JAM model using line-of-sight velocity errors $\Delta v_z = 20, 30, 40, 50$ and 60 km s^{-1} . I then carry out our analysis in the same way as before for each of the runs.

The top panel of Fig. 6.12 shows the mass recovery. Similarly to Fig. 6.10 there is no

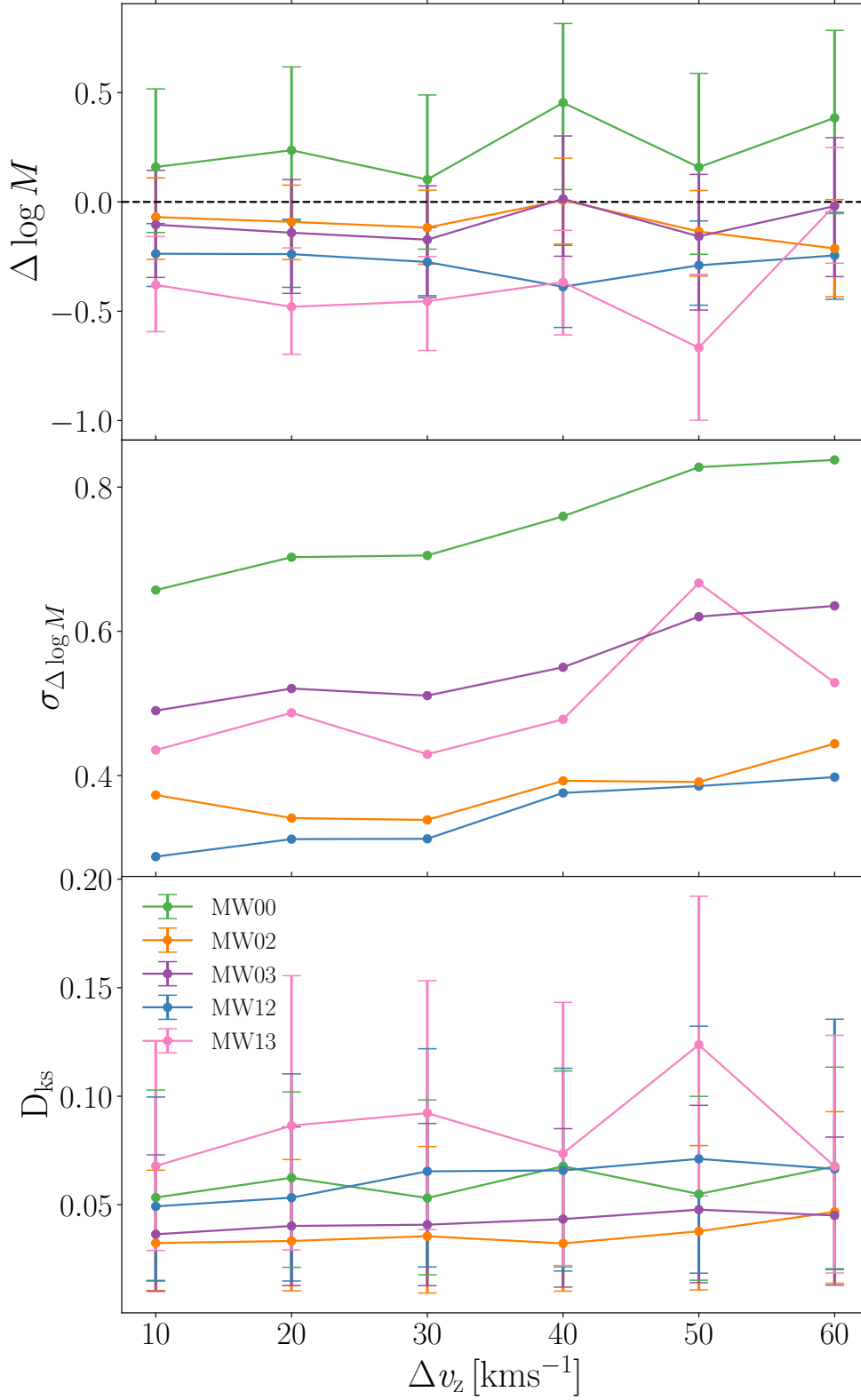


Figure 6.12: Estimators of the performance of the JAM model as in Fig. 6.7, as a function of the line-of-sight velocity error. Here we show five galaxies: MW00, MW02, MW03, MW12 and MW13 as indicated by the legend.

systematic variation of $\Delta \log M$ with increasing Δv_z but again there is a consistent offset, indicating that the model consistently over or underestimates the mass, regardless of Δv_z value. The 1σ spread in the recovered mass ($\sigma_{\Delta \log M}$) tells a different story: it increases as Δv_z increases. It also seems to be reasonably stable until $\Delta v_z = 30$ km/s and then the increase steepens towards $\Delta v_z = 60$ km/s. However, there is an offset between the galaxies, with MW02 and MW12 (orange and blue points) always at lower $\sigma_{\Delta \log M}$ than MW03 and MW13 (purple and pink points). These galaxies always have lower $\sigma_{\Delta \log M}$ than MW00 (green points). Again, this is due to the number of GCs in each of these galaxies. Table 6.1 shows that MW02 and MW12 have the most GCs with $N_{\text{GCs}} \approx 400$. MW03 has half this number with $N_{\text{GCs}} \approx 200$ and MW13 and MW00 have a quarter with $N_{\text{GCs}} \approx 100$. Therefore, although the velocity error does of course play a part in the recovery of the mass profile, it is the number of GCs that is the most important factor for the mass recovery.

6.4.4 Number of GCs and velocity error combined

The previous two sections have shown that it is often a combination of factors that determine whether the JAM model is a good fit or not. Therefore, I now combine the effects of the number of GCs and the line-of-sight velocity error in Fig. 6.13, which shows the mass enclosed recovery for the 25 galaxies as a function of the number of GCs in the galaxy and with three different velocity errors ($v_z = 10, 30, \text{ and } 60 \text{ km s}^{-1}$). The panels show the accuracy (i.e. how far from the true value they are, top panel) and the precision (i.e. the size of the error bar, bottom panel) of the enclosed DM mass at the maximum GC radius for each galaxy. In the top panel I do not see an obvious trend between the accuracy and number of GCs, therefore I fit a linear model to each of the three Δv_z groups. The lines confirm that there is little to no improvement in the accuracy with increasing number of GCs. However, particularly for the galaxies with small numbers of GCs, the accuracy improves with smaller Δv_z .

In the bottom panel of Fig. 6.13, I show that the precision improves, as the number of

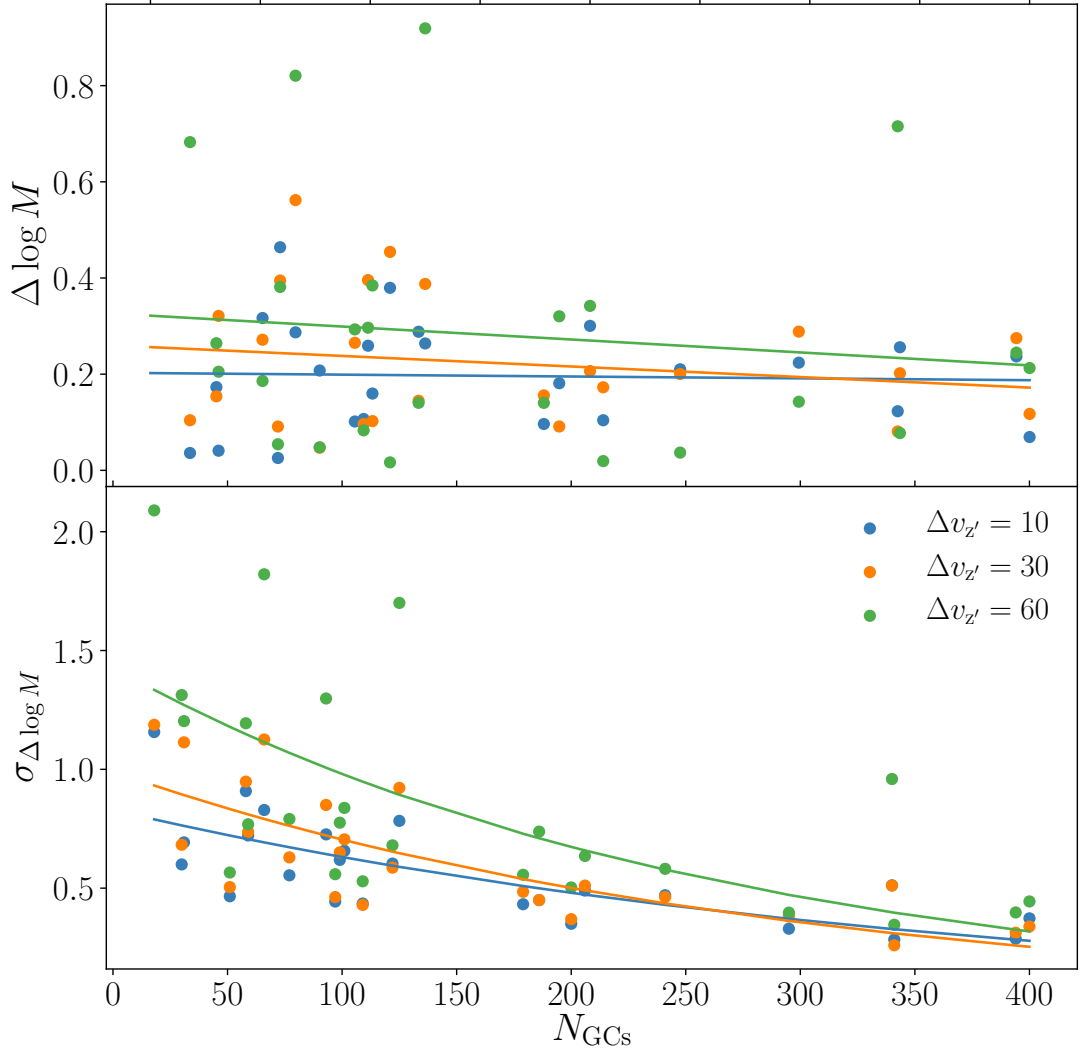


Figure 6.13: The accuracy and precision of the mass enclosed at the maximum GC radius for all 25 galaxies plotted as a function of the number of GCs in that galaxy. Each colour represents the results for three different line of sight velocity errors.

GCs increases. I therefore fit each Δv_z group with an exponential

$$\sigma_{\Delta \log M} = ae^{-N_{\text{GCs}}/b}, \quad (6.11)$$

where a and b are free parameters. All three curves show decreasing values of precision (therefore smaller error bars and better constraints on the mass enclosed) as the number of GCs increases. The exponential fits are:

$$\sigma_{\Delta \log M} = 0.83e^{-N_{\text{GCs}}/367}, \quad (6.12)$$

$$\sigma_{\Delta \log M} = 0.99e^{-N_{\text{GCs}}/293}, \quad (6.13)$$

$$\sigma_{\Delta \log M} = 1.43e^{-N_{\text{GCs}}/266}, \quad (6.14)$$

for the $\Delta v_z = 10, 30, 60 \text{ km s}^{-1}$ velocity errors respectively.

The $\Delta v_z = 60 \text{ km s}^{-1}$ (green) points are always higher than the $\Delta v_z = 30 \text{ km s}^{-1}$ (orange) points, which are always higher or the same as the $\Delta v_z = 10 \text{ km s}^{-1}$ points. This is true for the exponential fits and for each individual galaxy, meaning that the JAM models with the lower line-of-sight velocity errors constrain the mass better than the models with higher velocity error, as is expected. I also note that the blue and the orange points ($\Delta v_z = 10$ and 30 km s^{-1} respectively) show less scatter around their exponential fit than the green ($\Delta v_z = 60 \text{ km s}^{-1}$) points do. What is particularly interesting about this panel is that the curves converge at the highest number of GCs, showing that as long as you have a high enough number of GCs it does not necessarily matter what the line-of-sight velocity error is. However, if you have a smaller number of GCs it will be of great benefit to reduce the line-of-sight velocity errors to obtain the best constraints on the mass enclosed. Finally, there is already a significant improvement in reducing the errors from 60 km s^{-1} to 30 km s^{-1} and there isn't a huge amount to be gained by improving the precision to 10 km s^{-1} . But of course this depends on the exact system being modelled, 10 km/s is around one tenth of the velocity dispersion of these systems. But for a galaxy cluster a higher error may suffice and for a lower mass galaxy higher precision measurements may be needed.

6.5 Dependence on additional galaxy properties

There are many properties of a galaxy that could affect the performance of dynamical modelling. Therefore, I also carry out a similar analysis to [Kruijssen et al. \(2019a\)](#) and search for statistical correlations between all galaxy assembly and formation properties with $\Delta \log M$, $\sigma_{\Delta \log M}$, D_{KS} and $\sigma_{D_{\text{KS}}}$. We do this by calculating the Spearman

rank-order correlation r and p values. We do not find significant correlations that are surprising or cannot be explained through a secondary correlation. For example, the number of mergers with a mass ratio $<1:100$, the number of leaves in the merger tree and the number of branches in the merger tree all anti-correlate somewhat with $\sigma_{\Delta \log M}$, with an increase in the number of tiny mergers, leaves or branches resulting in a better constraint on the mass. All of these properties relate to the number of minor mergers, and [Kruijssen et al. \(2019a\)](#) showed the number of minor mergers correlates with the number of GCs, therefore we interpret it as follows: the mass of a galaxy is better constrained when it has more minor mergers because this means that the galaxy has more GCs. We also find that $\sigma_{\Delta \log M}$ and $\sigma_{D_{KS}}$ all correlate with the virial mass (M_{200}), the virial radius (R_{200}) and the maximum velocity (V_{max}), where an increase in the galaxy property means a better constraint on the mass and the radial profile of the DM halo. Again this can be explained in terms of the number of GCs because more massive haloes host more GCs and therefore the larger these particular galaxy properties are, the better constrained the properties of the DM halo become.

There are no correlations between how well the DM mass and profile is constrained and any other galaxy property. This means that the time of the last major merger does not have an effect on the JAM model. This is somewhat surprising since the JAM model assumes that the tracers and the potential are in equilibrium and a major merger would violate this assumption. The 25 galaxies span a broad range of lookback times for a major merger, from never experiencing one to having just undergone one. The lack of correlation could be explained by the relaxation time of the galaxy being relatively short- the galaxy returns to equilibrium within a short timescale after the final coalescence of the two progenitors.

6.6 Summary and Conclusions

This work uses the E-MOSAICS suite of 25 zoom-in simulations of Milky Way-mass galaxies to understand the extent to which different galaxy and GC properties, and data quality properties affect the outcomes of the axisymmetric Jeans model JAM ([Cappel-](#)

lari, 2008) using the approach for discrete tracers by Watkins et al. (2013). This formalism of a Jeans model takes Multi Gaussian Expansion fits to the tracer population and the potential of the baryonic components as inputs and obtains a fit to the DM density profile within the radial range probed by the tracers. In this case the tracer population is the GCs and the potential of the baryons is obtained by fitting a Multi Gaussian Expansion to the stellar mass distribution. The DM component is parametrised using a gNFW profile. The gNFW profile has three free parameters and the JAM model adds one more in the form of the cylindrical velocity anisotropy (β), therefore there are four free parameters in the model. The parameter space is explored using an MCMC analysis.

I discuss in section 6.3.1 and show in Figs. 6.2 and 6.3 that there are degeneracies between the DM halo parameters, even when fitting directly to the DM particle distribution from the simulation. Therefore, I choose not to compare the recovery of the free parameters directly to the simulation DM profile fits. Instead I quantify how well the JAM model is performing with two quantities that probe the mass recovery and one quantity that probes the recovery of the DM radial profile. The enclosed DM mass recovery is quantified by the logarithmic difference between the DM mass within the maximum GC radius recovered by JAM and the truth from the simulation ($\Delta \log M$) and the 1σ spread in this log difference from the spread in the posterior distributions from the JAM model ($\sigma_{\Delta \log M}$). The radial profile recovery is quantified using a KS test where the maximum difference between two cumulative mass distributions (D_{KS}) is calculated.

Although all dynamical models perform well, some perform much better than others, as shown by the three diagnostics. There is no effect on the DM profile recovery with the concentration or maximum radius of the GCs, but there is some effect due to the sphericity of the GC system. The GC spatial distribution is fitted with a spherical MGE but it is clear from Fig. 6.8 that most of the GC systems are not spherical. More spherical GC systems result in a better constraint on the mass and DM profile. However, there is also another effect at play. The least spherical GC systems are also those with the fewest number of GCs and at a given sphericity the galaxies with the

most GCs are also those with the best constraints.

Therefore, how the number of GCs in the galaxy affects the recovery of the enclosed DM mass and radial distribution is investigated. Figs. 6.9-6.11 show that there is a strong dependency of the precision of the JAM model on the number of GCs. The number of GCs has no effect on $\Delta \log M$ but a strong effect on $\sigma_{\Delta \log M}$ and also impacts the ability to constrain the DM halo profile. The dependency is exponential, where galaxies with fewer than 150 GCs show significant scatter in their mass and radial distribution recovery, but galaxies with more than 150 GCs consistently constrain the mass and distribution well.

I also investigate the impact of the data quality on the performance of the JAM model. This is done through increasing the line-of-sight velocity error. Fig.6.12 shows that increasing the line-of-sight velocity error from 10 km s^{-1} to 60 km s^{-1} mainly has an impact on $\sigma_{\Delta \log M}$: the larger the error, the less well constrained the mass is. It also has a small effect on how well the DM halo radial profile is constrained. However, Fig. 6.12 also shows that the number of GCs plays a role in the recovery of the enclosed DM mass. Therefore, I combine the number of GCs and the velocity error in Fig. 6.13 and find that $\Delta \log M$ does not change with number of GCs, but becomes slightly worse when increasing Δv_z . While $\sigma_{\Delta \log M}$ decreases exponentially with increasing number of GCs. When increasing Δv_z from 10 to 30 to 60 km/s there is a large difference in the recovery of the mass at low GC number, however, when large enough GC numbers are used the line-of-sight velocity error no longer plays a significant role in the recovery of the DM mass. Therefore, if GC numbers are low in a spiral galaxy it is important for data to be of high quality.

The JAM model performs well for all of the 25 simulated galaxies. This is a promising result since the E-MOSAICS galaxies probe a wide range of formation and assembly histories and the JAM model can successfully deal with all of these. It also shows that GCs are effective as tracers in dynamical models and therefore it is possible to construct dynamical models of galaxies at higher redshift where stellar kinematics become problematic at large radii, but GCs remain bright tracers of the outer halo. The limitations of the JAM model come with the need to set a pre-defined geometry for the

potential and - perhaps more importantly for a GC system - to assume a fixed orientation of the velocity ellipsoid. Some of these limitations can be alleviated by using more sophisticated dynamical modelling methods, e.g. higher order Jeans equations, distribution function based methods, and Schwarzschild orbit-based modelling techniques. Schwarzschild models, for example, allow the most flexibility in the geometry of the potential and the tracer distribution function enabling for a more rigorous dynamical description of the galaxies. It is unclear, however, how much data would be needed to well constrain these more sophisticated models which come with more free parameters. For this problem, where some galaxy halos are sampled with as few as 18 GC tracers, I decided to use simple axisymmetric Jeans models. For galaxies with more abundant data, revisiting this problem with more sophisticated techniques is highly desirable in the future.

Chapter 7

Summary

The aim of this thesis is to place globular clusters (GCs) in the context of galaxy formation and evolution. Chapter 1 discusses the multiple ways in which the properties of the $z = 0$ GC system can be related to the $z = 0$ properties and the formation and evolution of their host galaxy. This thesis uses the state of the art E-MOSAICS simulations (described in Chapter 2) to investigate the intimate relationship between GC systems and galaxies, with novel results that contribute to answering four main questions:

- How are the mass functions of GCs related to the stellar mass of their host galaxy?
- How do the age and metallicity distributions of GCs on stellar streams differ from other GCs in a galaxy halo?
- How does the distribution of stars and GCs in the $[\alpha/\text{Fe}]-[\text{Fe}/\text{H}]$ plane relate to the formation history of the galaxy?
- How can GCs be used to infer the mass and radial distribution of dark matter?

In Chapter 3, I examine the mass function of GC populations. Specifically, I investigate the physics that governs the truncation mass ($M_{c,*}$) of the mass function, when it can be described by a Schechter function. [Jordán et al. \(2007\)](#) fit Schechter functions

to the mass distributions of GCs in galaxy stellar mass bins and find an increasing $M_{c,*}$ with galaxy stellar mass. The E-MOSAICS simulations reproduce this trend with excellent agreement and therefore Chapter 3 serves as another confirmation of the input physics to the simulations. This chapter then investigates the reason for such a trend in the observations and the simulations. It is found to be a combination of both nature and nurture that contributes to the form of the relation. Firstly, the nature of star cluster formation is that more massive clusters can be formed in denser, higher pressure environments. More massive galaxies are able to contain higher pressure environments and therefore more massive clusters can form. The caveat of this is that as galaxies become more massive their growth becomes dominated by the accretion of less massive galaxies and so there is a limit to how high $M_{c,*}$ can reach. This then leaves an increasing trend of $M_{c,*}$ with galaxy mass until a galaxy stellar mass of $\approx 10^{10} M_{\odot}$, after which galaxies become accretion dominated and $M_{c,*}$ does not grow any further as galaxy mass increases. However, this is not the trend observed at $z = 0$ where we see a constantly increasing $M_{c,*}$ with galaxy stellar mass. This is where the nurture of the massive star clusters becomes important. In the accretion dominated galaxies of stellar masses $\approx 10^{11} M_{\odot}$, mergers are able to move stellar clusters from their disruptive birth environments so they can survive a Hubble time and $M_{c,*}$ remains high. At a galaxy stellar mass of $\approx 10^{10}$, there are not enough mergers to redistribute the massive GCs to safer environments and they get destroyed, resulting in the reduction of $M_{c,*}$. Chapter 3 highlights the complicated relationship the GC system has with the mass build-up of its host galaxy.

Chapter 4 contrasts the ages and metallicities of GCs associated with stellar streams with other GCs in the galaxy halo. Stellar streams are the most direct evidence for dwarf galaxy accretion onto a Milky Way-mass halo and can be observed in local group galaxies such as M31. Chapter 4 shows that GCs associated with the most massive and recently accreted stellar streams are, on average, younger and more metal-rich than the other GCs in the halo of the galaxy. This is a result that was later confirmed by [Mackey et al. \(2019\)](#) who observed GCs on stellar streams in the halo of M31. Dwarf galaxies that have been recently accreted evolve in isolation for a long time and continue to

form GCs. The galaxy stops forming GCs when it enters the halo of the Milky Way-mass galaxy and its star forming gas gets stripped. This means that the age range of GCs associated with stellar streams can be used to place constraints on accretion time.

Chapter 5 also shows that GCs associated with stellar streams have lower $[\alpha/\text{Fe}]$ for a given $[\text{Fe}/\text{H}]$ than the rest of the GC population, again this due to their different star formation history in a lower mass galaxy that has been recently accreted. Also in Chapter 5 I investigate the $[\alpha/\text{Fe}]-[\text{Fe}/\text{H}]$ distribution of field stars. It is found that galaxies show very different distributions. Of particular note is that some galaxies exhibit a bimodal distribution with a high- $[\alpha/\text{Fe}]$ and a low $[\alpha/\text{Fe}]$ sequence. [Mackereth et al. \(2018\)](#) attribute this particular shape to an early formation of the galaxies, a conclusion that is supported in this Chapter. Additionally, I find a lack of GCs in the high- $[\alpha/\text{Fe}]$ sequence, which is attributed mainly to the inner parts of the galaxy. This motivates the investigation into the disruption of GCs in the bulge and it is found that in the galaxies with a bimodal $[\alpha/\text{Fe}]$ - there is a higher than average fraction of field stars that were born in a GC. Using chemical tagging ([Schiavon et al., 2017](#)) and ([Horta et al., 2021b](#)) find a similarly high fraction of field stars that were born in a GC in the bulge of the Milky Way. The Milky Way has also been postulated to have formed earlier than average L^* galaxies.

Finally, Chapter 6 reveals the power of the simulations to be used as a test case for other modelling techniques. In this case, the simulation data is used as inputs to Jeans dynamical modelling (described in Chapter 2) and I examine the outputs to understand how well GCs act as tracers for a dynamical model. This Chapter helps users of dynamical models to understand what kind of data is needed for this problem. It also points out any biases the modelling technique may have.

7.1 Future prospects

With the exception of Chapter 3, the work in this thesis is carried out using the 25 zoom-in simulations of Milky Way-mass galaxies in the E-MOSAICS suite. However,

a 34 Mpc volume simulation is now available with the same resolution as the Milky Way-mass zooms. Therefore, it would now be possible to extend some of the analysis in this thesis to other galaxy masses (from dwarfs through to massive ellipticals) and environments (in isolation and a range of galaxy groups and clusters, up to the mass of the Fornax galaxy cluster).

For example, it would be interesting to understand how the field stars in the $[\alpha/\text{Fe}]$ - $[\text{Fe}/\text{H}]$ plane behave in more massive galaxies and whether bimodality exists at all galaxy masses. Additionally, it would be interesting to see if there is still a space in this plane where the GCs are preferentially disrupted and how this relates to the galaxy's formation.

Much observational work is available that investigates the GC properties as a function of radius and is beginning to put constraints on how this can be used to infer formation histories of galaxies (e.g. [Forbes et al. 2011](#); [Peng et al. 2016](#); [Fahrion et al. 2020](#); [Villaume et al. 2020](#)). This is something that can be explicitly tested with the E-MOSAICS volume simulation and a statistical sample could be compiled. With the wealth of E-MOSAICS data now available, galaxies can be placed into subgroups to investigate the effects of environment and morphology on the GC properties as a function of radius.

Another interesting avenue to explore with the E-MOSAICS volume simulation is testing more complicated dynamical modelling techniques. Chapter 6 represents a relatively simple case of dynamical modelling, with just one tracer population in well-behaved edge on spiral galaxies. However, more massive galaxies come with more GCs and therefore more tracers as inputs to the dynamical models. Dynamical models can be extended to include more than one dynamical tracer and have been shown to separate the red and blue GC population into two separate dynamical components (e.g. [Schuberth et al. 2010](#); [Zhu et al. 2016a](#)). A statistical sample of test galaxies could help the users of the JAM model understand how well the model performs with more than one tracer population and if there are any biases introduced into the model.

Although there has been large steps forward in recent years, the exact formation mech-

anism of GCs is still under some debate (e.g. [Forbes et al. 2018](#)). However, there is agreement that the bulk of GC formation occurs before the peak of cosmic star formation ([Fall & Rees, 1985](#); [Ashman & Zepf, 1992](#); [Fall & Zhang, 2001](#); [Griffen et al., 2010](#); [Li et al., 2017b](#); [Reina-Campos et al., 2019](#)), which occurs at $z \approx 2$ ([Madau & Dickinson, 2014](#)). This implies that proto-GC formation is likely to be observed in lensed galaxies at $z \approx 2 - 3$. However, [Pfeffer et al. \(2019a\)](#) showed that galaxies are unlikely to host GCs bright enough to be observed with the Hubble Space Telescope (HST), due to rapidly fading young stellar populations in the UV. Moving to redder filters (e.g. JWST) lessens the bias of observing only the youngest GCs, instead observing those slightly older, but that no longer have their surrounding cluster complex and so individual clusters could be identified. Alternatively, the upcoming generation of 30m-class telescopes will provide the resolution ($< 10 - 20\text{pc}$) to observe individual proto-GCs at redshifts between 1 and 3.

The direct detection of individual proto-GCs will help to inform the future generation of GC formation models, which in turn can be implemented into hydrodynamical, cosmological simulations of galaxy formation. Until that time however, there are still some issues with the current generation of models that can be attended to. Due to the lack of resolution of the cold ISM in the EAGLE simulations, there is an under-disruption of GCs in E-MOSAICS. A new generation of cosmological simulations, with a higher resolution and the ability to resolve the cold ISM are on the way. The MOSAICS model of star cluster formation will be implemented into these simulations in the same way as in E-MOSAICS but the resulting GC populations are likely to be more refined. The results in Chapters 3, 4 and 5 are potentially impacted by this under-disruption and the steps taken to reduce the effects are discussed in the relevant chapters. With the new generation of simulations, there will be less need for such mitigating steps and more confidence can be placed into some results.

Until recently, observations of GC populations were ahead of the theoretical framework and simulations to complement them. Now, with the advent of fully hydrodynamical cosmological simulations of GC system formation alongside galaxy formation the true intimate relationship between the two is appreciated.

Bibliography

- Abadi M. G., Navarro J. F., Steinmetz M., Eke V. R., 2003, [ApJ](#), **597**, 21
- Abraham R., et al., 2018, [Research Notes of the American Astronomical Society](#), **2**, 16
- Adamo A., Bastian N., 2018, *The Lifecycle of Clusters in Galaxies*. p. 91, [doi:10.1007/978-3-319-22801-3_4](#)
- Adamo A., Kruijssen J. M. D., Bastian N., Silva-Villa E., Ryon J., 2015, [MNRAS](#), **452**, 246
- Adibekyan V. Z., Sousa S. G., Santos N. C., Delgado Mena E., González Hernández J. I., Israelian G., Mayor M., Khachatryan G., 2012, [A&A](#), **545**, A32
- Agertz O., Kravtsov A. V., 2016, [ApJ](#), **824**, 79
- Agnello A., Evans N. W., Romanowsky A. J., Brodie J. P., 2014, [MNRAS](#), **442**, 3299
- Alabi A. B., et al., 2017, [MNRAS](#), **468**, 3949
- Alves-Brito A., Hau G. K. T., Forbes D. A., Spitler L. R., Strader J., Brodie J. P., Rhode K. L., 2011, [MNRAS](#), **417**, 1823
- Anders E., 1959, [ApJ](#), **129**, 327
- Anders P., de Grijs R., Fritze-v. Alvensleben U., Bissantz N., 2004, [MNRAS](#), **347**, 17
- Antonini F., 2013, [ApJ](#), **763**, 62
- Armandroff T. E., 1989, [AJ](#), **97**, 375

- Arnold J. A., Romanowsky A. J., Brodie J. P., Chomiuk L., Spitler L. R., Strader J., Benson A. J., Forbes D. A., 2011, *ApJ*, **736**, L26
- Arp H., Sandage A., 1985, *AJ*, **90**, 1163
- Ashman K. M., Zepf S. E., 1992, *ApJ*, **384**, 50
- Auger M. W., Treu T., Bolton A. S., Gavazzi R., Koopmans L. V. E., Marshall P. J., Moustakas L. A., Burles S., 2010, *ApJ*, **724**, 511
- Bacon R., et al., 2010, in McLean I. S., Ramsay S. K., Takami H., eds, Society of Photo-Optical Instrumentation Engineers (SPIE) Conference Series Vol. 7735, Ground-based and Airborne Instrumentation for Astronomy III. p. 773508, doi:10.1117/12.856027
- Balogh M. L., Pearce F. R., Bower R. G., Kay S. T., 2001, *MNRAS*, **326**, 1228
- Barmby P., Huchra J. P., Brodie J. P., Forbes D. A., Schroder L. L., Grillmair C. J., 2000, *AJ*, **119**, 727
- Barnes J. E., 1998, in Kennicutt R. C. J., Schweizer F., Barnes J. E., Friedli D., Martinet L., Pfenniger D., eds, Saas-Fee Advanced Course 26: Galaxies: Interactions and Induced Star Formation. p. 275
- Bassino L. P., Faifer F. R., Forte J. C., Dirsch B., Richtler T., Geisler D., Schuberth Y., 2006, *A&A*, **451**, 789
- Bastian N., 2008, *MNRAS*, **390**, 759
- Bastian N., 2016, in Moraux E., Lebreton Y., Charbonnel C., eds, EAS Publications Series Vol. 80, EAS Publications Series. pp 5–37 (arXiv:1606.09468), doi:10.1051/eas/1680002
- Bastian N., Lardo C., 2018, *ARA&A*, **56**, 83
- Bastian N., Konstantopoulos I. S., Tranco G., Weisz D. R., Larsen S. S., Fouesneau M., Kaschinski C. B., Gieles M., 2012, *A&A*, **541**, A25

- Bastian N., Pfeffer J., Kruijssen J. M. D., Crain R. A., Trujillo-Gomez S., Reina-Campos M., 2020, *MNRAS*, **498**, 1050
- Battaglia G., Helmi A., Tolstoy E., Irwin M., Hill V., Jablonka P., 2008, *ApJL*, **681**, L13
- Battistini P., Bonoli F., Braccesi A., Federici L., Fusi Pecci F., Marano B., Borngen F., 1987, *A&AS*, **67**, 447
- Baumann D., 2009, arXiv e-prints, p. [arXiv:0907.5424](https://arxiv.org/abs/0907.5424)
- Baumgardt H., 1998, *A&A*, **330**, 480
- Baumgardt H., Hilker M., 2018, *MNRAS*, **478**, 1520
- Baumgardt H., Makino J., 2003, *MNRAS*, **340**, 227
- Beasley M. A., 2020, *Globular Cluster Systems and Galaxy Formation*. pp 245–277, [doi:10.1007/978-3-030-38509-5_9](https://doi.org/10.1007/978-3-030-38509-5_9)
- Beasley M. A., Baugh C. M., Forbes D. A., Sharples R. M., Frenk C. S., 2002, *MNRAS*, **333**, 383
- Beasley M. A., Bridges T., Peng E., Harris W. E., Harris G. L. H., Forbes D. A., Mackie G., 2008, *MNRAS*, **386**, 1443
- Beasley M. A., Romanowsky A. J., Pota V., Navarro I. M., Martinez Delgado D., Neyer F., Deich A. L., 2016, *ApJL*, **819**, L20
- Bellazzini M., Ferraro F. R., Ibata R., 2003, *AJ*, **125**, 188
- Bellazzini M., Correnti M., Ferraro F. R., Monaco L., Montegriffo P., 2006, *A&A*, **446**, L1
- Bellstedt S., et al., 2018, *MNRAS*, **476**, 4543
- Belokurov V., et al., 2006, *ApJL*, **642**, L137
- Belokurov V., Erkal D., Evans N. W., Koposov S. E., Deason A. J., 2018, *MNRAS*, **478**, 611

- Bender R., Burstein D., Faber S. M., 1992, *ApJ*, 399, 462
- Bennett C. L., et al., 1996, *ApJL*, 464, L1
- Bennett C. L., et al., 2003, *ApJS*, 148, 1
- Bennett C. L., et al., 2013, *ApJS*, 208, 20
- Bernard E. J., et al., 2016, *MNRAS*, 463, 1759
- Bernardi M., Shankar F., Hyde J. B., Mei S., Marulli F., Sheth R. K., 2010, *MNRAS*, 404, 2087
- Binney J., 1980, *MNRAS*, 190, 873
- Binney J., Tremaine S., 1987, Galactic dynamics
- Binney J., Wong L. K., 2017, *MNRAS*, 467, 2446
- Blake C., et al., 2010, *MNRAS*, 406, 803
- Blakeslee J. P., 1999, *AJ*, 118, 1506
- Blanton M. R., Moustakas J., 2009, *ARA&A*, 47, 159
- Blumenthal G. R., Faber S. M., Primack J. R., Rees M. J., 1984, *Nature*, 311, 517
- Blumenthal G. R., Faber S. M., Flores R., Primack J. R., 1986, *ApJ*, 301, 27
- Bolatto A. D., et al., 2017, *ApJ*, 846, 159
- Booth C. M., Schaye J., 2009, in Heinz S., Wilcots E., eds, American Institute of Physics Conference Series Vol. 1201, American Institute of Physics Conference Series. pp 21–24, doi:10.1063/1.3293041
- Bower R. G., Benson A. J., Malbon R., Helly J. C., Frenk C. S., Baugh C. M., Cole S., Lacey C. G., 2006, *MNRAS*, 370, 645
- Boylan-Kolchin M., 2017, *MNRAS*, 472, 3120
- Boylan-Kolchin M., Ma C.-P., Quataert E., 2008, *MNRAS*, 383, 93

- Brodie J. P., Strader J., 2006, [ARA&A](#), **44**, 193
- Brodie J. P., et al., 2014, [ApJ](#), **796**, 52
- Buder S., et al., 2018, [MNRAS](#), **478**, 4513
- Bundy K., et al., 2015, [ApJ](#), **798**, 7
- Burkert A., Smith G. H., 2000, [ApJL](#), **542**, L95
- Burstein D., Bender R., Faber S., Nolthenius R., 1997, [AJ](#), **114**, 1365
- Caldwell N., Harding P., Morrison H., Rose J. A., Schiavon R., Kriessler J., 2009, [AJ](#), **137**, 94
- Caldwell N., Schiavon R., Morrison H., Rose J. A., Harding P., 2011, [AJ](#), **141**, 61
- Cappellari M., 2002, [MNRAS](#), **333**, 400
- Cappellari M., 2008, [MNRAS](#), **390**, 71
- Cappellari M., 2012, arXiv e-prints, p. [arXiv:1211.7009](#)
- Cappellari M., 2020, [MNRAS](#), **494**, 4819
- Cappellari M., et al., 2007, [MNRAS](#), **379**, 418
- Cappellari M., et al., 2009, [ApJL](#), **704**, L34
- Cappellari M., et al., 2015, [ApJL](#), **804**, L21
- Carollo D., Martell S. L., Beers T. C., Freeman K. C., 2013, [ApJ](#), **769**, 87
- Carretta E., et al., 2009, [A&A](#), **505**, 117
- Carretta E., Bragaglia A., Gratton R., Lucatello S., Bellazzini M., D’Orazi V., 2010, [ApJL](#), **712**, L21
- Chanamé J., Kleyna J., van der Marel R., 2008, [ApJ](#), **682**, 841
- Chandar R., Whitmore B. C., Calzetti D., O’Connell R., 2014, [ApJ](#), **787**, 17

- Chandar R., Whitmore B. C., Dinino D., Kennicutt R. C., Chien L. H., Schinnerer E., Meidt S., 2016, [ApJ](#), **824**, 71
- Chandrasekhar S., 1943, [ApJ](#), **97**, 255
- Chantereau W., Usher C., Bastian N., 2018, [MNRAS](#), **478**, 2368
- Choksi N., Gnedin O. Y., Li H., 2018, [MNRAS](#), **480**, 2343
- Clauwens B., Schaye J., Franx M., Bower R. G., 2018, [MNRAS](#), **478**, 3994
- Cleveland W. S., 1979, [Journal of the American Statistical Association](#), **74**, 829
- Cohen J. G., 2004, [AJ](#), **127**, 1545
- Cohen S. A., Hickox R. C., Wegner G. A., Einasto M., Vennik J., 2014, [ApJ](#), **783**, 136
- Colless M., et al., 2001, [MNRAS](#), **328**, 1039
- Colpi M., Mayer L., Governato F., 1999, [ApJ](#), **525**, 720
- Correnti M., Goudfrooij P., Bellini A., Kalirai J. S., Puzia T. H., 2017, [MNRAS](#), **467**, 3628
- Côté P., Marzke R. O., West M. J., 1998, [ApJ](#), **501**, 554
- Côté P., et al., 2001, [ApJ](#), **559**, 828
- Côté P., et al., 2004, [ApJS](#), **153**, 223
- Courteau S., Dutton A. A., van den Bosch F. C., MacArthur L. A., Dekel A., McIntosh D. H., Dale D. A., 2007, [ApJ](#), **671**, 203
- Cox T. J., Dutta S. N., Di Matteo T., Hernquist L., Hopkins P. F., Robertson B., Springel V., 2006, [ApJ](#), **650**, 791
- Crain R. A., et al., 2015, [MNRAS](#), **450**, 1937
- Crampton D., Cowley A. P., Schade D., Chayer P., 1985, [ApJ](#), **288**, 494
- Croom S. M., et al., 2012, [MNRAS](#), **421**, 872

- Croton D. J., et al., 2006, [MNRAS](#), **365**, 11
- Crowther P. A., et al., 2016, [MNRAS](#), **458**, 624
- D’Ercole A., Vesperini E., D’Antona F., McMillan S. L. W., Recchi S., 2008, [MNRAS](#), **391**, 825
- D’Onghia E., Fox A. J., 2016, [ARA&A](#), **54**, 363
- D’Souza R., Rix H.-W., 2013, [MNRAS](#), **429**, 1887
- Da Costa G. S., 1998, in Aparicio A., Herrero A., Sánchez F., eds, *Stellar astrophysics for the local group: VIII Canary Islands Winter School of Astrophysics*. p. 351
- Da Costa G. S., Armandroff T. E., 1995, [AJ](#), **109**, 2533
- Da Costa G. S., Hatzidimitriou D., 1998, [AJ](#), **115**, 1934
- Dalessandro E., Lapenna E., Mucciarelli A., Origlia L., Ferraro F. R., Lanzoni B., 2016, [ApJ](#), **829**, 77
- Dalla Vecchia C., Schaye J., 2012, [MNRAS](#), **426**, 140
- Davies J. J., Crain R. A., McCarthy I. G., Oppenheimer B. D., Schaye J., Schaller M., McAlpine S., 2019, [MNRAS](#), **485**, 3783
- Davis M., Efstathiou G., Frenk C. S., White S. D. M., 1985, [ApJ](#), **292**, 371
- Davison T. A., Norris M. A., Pfeffer J. L., Davies J. J., Crain R. A., 2020, [MNRAS](#), **497**, 81
- De Lucia G., Springel V., White S. D. M., Croton D., Kauffmann G., 2006, [MNRAS](#), **366**, 499
- De Silva G. M., et al., 2015, [MNRAS](#), **449**, 2604
- Deason A. J., Belokurov V., Evans N. W., McCarthy I. G., 2012, [ApJ](#), **748**, 2
- Dejonghe H., Merritt D., 1992, [ApJ](#), **391**, 531

- Dekel A., Birnboim Y., 2006, [MNRAS](#), **368**, 2
- Dekel A., Sari R., Ceverino D., 2009, [ApJ](#), **703**, 785
- Dierickx M. I. P., Loeb A., 2017, [ApJ](#), **836**, 92
- Dinescu D. I., van Altena W. F., Girard T. M., López C. E., 1999, [AJ](#), **117**, 277
- Dinescu D. I., Majewski S. R., Girard T. M., Cudworth K. M., 2000, [AJ](#), **120**, 1892
- Dirsch B., Richtler T., Gieren W. P., Hilker M., 2000, [A&A](#), **360**, 133
- Djorgovski S., Davis M., 1987, [ApJ](#), **313**, 59
- Dolag K., Borgani S., Murante G., Springel V., 2009, [Monthly Notices of the Royal Astronomical Society](#), 399, 497
- Dotter A., et al., 2010, [ApJ](#), **708**, 698
- Dotter A., Sarajedini A., Anderson J., 2011, [ApJ](#), **738**, 74
- Eisenstein D. J., Hu W., 1998, [ApJ](#), **496**, 605
- El-Badry K., Wetzel A. R., Geha M., Quataert E., Hopkins P. F., Kereš D., Chan T. K., Faucher-Giguère C.-A., 2017, [ApJ](#), **835**, 193
- El-Badry K., Quataert E., Weisz D. R., Choksi N., Boylan-Kolchin M., 2019, [MNRAS](#), **482**, 4528
- Elmegreen B. G., 2010, [ApJl](#), **712**, L184
- Elmegreen B. G., Efremov Y. N., 1997, [ApJ](#), **480**, 235
- Elmegreen B. G., Hunter D. A., 2010a, [ApJ](#), **712**, 604
- Elmegreen B. G., Hunter D. A., 2010b, [ApJ](#), **712**, 604
- Emsellem E., Monnet G., Bacon R., 1994, [A&A](#), **285**, 723
- Faber S. M., Jackson R. E., 1976, [ApJ](#), **204**, 668

- Faber S. M., Dressler A., Davies R. L., Burstein D., Lynden Bell D., Terlevich R., Wegner G., 1987, in Faber S. M., ed., *Nearly Normal Galaxies. From the Planck Time to the Present.* p. 175
- Fahrion K., et al., 2020, [A&A](#), **637**, A26
- Faifer F. R., et al., 2011, [MNRAS](#), **416**, 155
- Fakhouri O., Ma C.-P., Boylan-Kolchin M., 2010, [MNRAS](#), **406**, 2267
- Fall S. M., Efstathiou G., 1980, [MNRAS](#), **193**, 189
- Fall S. M., Rees M. J., 1985, [ApJ](#), **298**, 18
- Fall S. M., Zhang Q., 2001, [ApJ](#), **561**, 751
- Fan Z., de Grijs R., Zhou X., 2010, [ApJ](#), **725**, 200
- Farouki R., Shapiro S. L., 1981, [ApJ](#), **243**, 32
- Farouki R. T., Shapiro S. L., 1982, [ApJ](#), **259**, 103
- Ferguson A. M. N., Irwin M. J., Ibata R. A., Lewis G. F., Tanvir N. R., 2002, [The Astronomical Journal](#), **124**, 1452
- Fernández-Trincado J. G., et al., 2019, [ApJL](#), **886**, L8
- Ferraro F. R., Mucciarelli A., Carretta E., Origlia L., 2006, [ApJL](#), **645**, L33
- Filippenko A. V., 1997, [ARA&A](#), **35**, 309
- Fonnesbeck C., Patil A., Huard D., Salvatier J., 2015, *PyMC: Bayesian Stochastic Modelling in Python* (ascl:1506.005)
- Forbes D. A., Bridges T., 2010, [MNRAS](#), **404**, 1203
- Forbes D. A., Brodie J. P., Grillmair C. J., 1997, [AJ](#), **113**, 1652
- Forbes D. A., Spitler L. R., Strader J., Romanowsky A. J., Brodie J. P., Foster C., 2011, [MNRAS](#), **413**, 2943

- Forbes D. A., Ponman T., O'Sullivan E., 2012, [MNRAS](#), **425**, 66
- Forbes D. A., Pastorello N., Romanowsky A. J., Usher C., Brodie J. P., Strader J., 2015, [MNRAS](#), **452**, 1045
- Forbes D. A., et al., 2017, [AJ](#), **153**, 114
- Forbes D. A., et al., 2018, [Proceedings of the Royal Society of London Series A](#), **474**, 20170616
- Foreman-Mackey D., Hogg D. W., Lang D., Goodman J., 2013, [PASP](#), **125**, 306
- Forte J. C., Faifer F., Geisler D., 2007, [MNRAS](#), **382**, 1947
- Freeman K., Bland-Hawthorn J., 2002, [ARA&A](#), **40**, 487
- Fuhrmann K., 1998, [A&A](#), **338**, 161
- Fujii M., Funato Y., Makino J., 2006, [PASJ](#), **58**, 743
- Gaia Collaboration et al., 2018, [A&A](#), **616**, A12
- Gajda G., Gerhard O., Blaña M., Zhu L., Shen J., Saglia R. P., Bender R., 2021, [A&A](#), **647**, A131
- Gallagher John S. I., Ostriker J. P., 1972, [AJ](#), **77**, 288
- Geisler D., Lee M. G., Kim E., 1996, [AJ](#), **111**, 1529
- Geisler D., Piatti A. E., Bica E., Clariá J. J., 2003, [MNRAS](#), **341**, 771
- Genel S., et al., 2014, [MNRAS](#), **445**, 175
- Gerssen J., van der Marel R. P., Gebhardt K., Guhathakurta P., Peterson R. C., Pryor C., 2002, [AJ](#), **124**, 3270
- Gieles M., 2009, [MNRAS](#), **394**, 2113
- Gieles M., Baumgardt H., 2008, [MNRAS](#), **389**, L28

- Gieles M., Portegies Zwart S. F., Baumgardt H., Athanassoula E., Lamers H. J. G. L. M., Sipior M., Leenaarts J., 2006, [MNRAS](#), **371**, 793
- Gieles M., Athanassoula E., Portegies Zwart S. F., 2007, [MNRAS](#), **376**, 809
- Gieles M., et al., 2018, [MNRAS](#), **478**, 2461
- Gill S. P. D., Knebe A., Gibson B. K., 2005, [MNRAS](#), **356**, 1327
- Gilmore G., et al., 2012, *The Messenger*, **147**, 25
- Gilmozzi R., Kinney E. K., Ewald S. P., Panagia N., Romaniello M., 1994, [ApJL](#), **435**, L43
- Glatt K., et al., 2008, [AJ](#), **136**, 1703
- Gnedin O. Y., Ostriker J. P., 1997, [ApJ](#), **474**, 223
- Gnedin O. Y., Lee H. M., Ostriker J. P., 1999, [ApJ](#), **522**, 935
- Goudfrooij P., 2004, in Lamers H. J. G. L. M., Smith L. J., Nota A., eds, *Astronomical Society of the Pacific Conference Series Vol. 322, The Formation and Evolution of Massive Young Star Clusters*. p. 469 ([arXiv:astro-ph/0404189](#))
- Governato F., Willman B., Mayer L., Brooks A., Stinson G., Valenzuela O., Wadsley J., Quinn T., 2007, [MNRAS](#), **374**, 1479
- Grand R. J. J., et al., 2018, [MNRAS](#), **474**, 3629
- Gratton R., Sneden C., Carretta E., 2004, [ARA&A](#), **42**, 385
- Gratton R. G., Carretta E., Bragaglia A., Lucatello S., D’Orazi V., 2010, [A&A](#), **517**, A81
- Gregory P. C., 2005, *Bayesian Logical Data Analysis for the Physical Sciences: A Comparative Approach with ‘Mathematica’ Support*
- Griffen B. F., Drinkwater M. J., Thomas P. A., Helly J. C., Pimbblet K. A., 2010, [MNRAS](#), **405**, 375

- Grillmair C. J., Dionatos O., 2006a, [ApJ](#), 641, L37
- Grillmair C. J., Dionatos O., 2006b, [ApJ](#), 643, L17
- Gunn J. E., Gott J. Richard I., 1972, [ApJ](#), 176, 1
- Gustafsson B., Church R. P., Davies M. B., Rickman H., 2016, [A&A](#), 593, A85
- Halbesma T. L. R., Grand R. J. J., Gómez F. A., Marinacci F., Pakmor R., Trick W. H., Busch P., White S. D. M., 2020, [MNRAS](#), 496, 638
- Harris W. E., 1991, [ARA&A](#), 29, 543
- Harris W. E., 1996, [AJ](#), 112, 1487
- Harris W. E., 1999, in *Globular Clusters*. pp 325–355
- Harris W. E., 2009, [ApJ](#), 703, 939
- Harris W. E., 2010, arXiv e-prints, p. [arXiv:1012.3224](#)
- Harris W. E., Pudritz R. E., 1994, [ApJ](#), 429, 177
- Harwit M., Spaans M., 2003, [ApJ](#), 589, 53
- Hayden M. R., et al., 2015, [ApJ](#), 808, 132
- Helmi A., 2008, [A&A Rev.](#), 15, 145
- Helmi A., White S. D. M., de Zeeuw P. T., Zhao H., 1999, [Nature](#), 402, 53
- Helmi A., Babusiaux C., Koppelman H. H., Massari D., Veljanoski J., Brown A. G. A., 2018, [Nature](#), 563, 85
- Hénault-Brunet V., Gieles M., Sollima A., Watkins L. L., Zocchi A., Claydon I., Pancino E., Baumgardt H., 2019, [MNRAS](#), 483, 1400
- Herschel W., 1786, *Philosophical Transactions of the Royal Society of London Series I*, 76, 457

- Herschel W., 1789, *Philosophical Transactions of the Royal Society of London Series I*, [79](#), [212](#)
- Herschel W., 1802, *Philosophical Transactions of the Royal Society of London Series I*, [92](#), [477](#)
- Hilker M., Infante L., Richtler T., 1999, *A&AS*, [138](#), [55](#)
- Hill V., François P., Spite M., Primas F., Spite F., 2000, *A&A*, [364](#), [L19](#)
- Hodge P. W., Lee S. O., 1984, *ApJ*, [276](#), [509](#)
- Holtzman J. A., et al., 1992, *AJ*, [103](#), [691](#)
- Hopkins P. F., Cox T. J., Kereš D., Hernquist L., 2008, *ApJS*, [175](#), [390](#)
- Horta D., Hughes M. E., Pfeffer J. L., Bastian N., Kruijssen J. M. D., Reina-Campos M., Crain R. A., 2021a, *MNRAS*, [500](#), [4768](#)
- Horta D., et al., 2021b, *MNRAS*, [500](#), [5462](#)
- Hoyle F., Fowler W. A., 1960, *ApJ*, [132](#), [565](#)
- Hubble E. P., 1926, *ApJ*, [64](#), [321](#)
- Hudson M. J., Harris G. L., Harris W. E., 2014, *ApJl*, [787](#), [L5](#)
- Hughes M. E., Pfeffer J., Martig M., Bastian N., Crain R. A., Kruijssen J. M. D., Reina-Campos M., 2019, *MNRAS*, [482](#), [2795](#)
- Hughes M. E., Pfeffer J. L., Martig M., Reina-Campos M., Bastian N., Crain R. A., Kruijssen J. M. D., 2020, *MNRAS*, [491](#), [4012](#)
- Hunter D. A., 1992, *ApJS*, [79](#), [469](#)
- Hunter D. A., Shaya E. J., Holtzman J. A., Light R. M., O’Neil Jr. E. J., Lynds R., 1995, *ApJ*, [448](#), [179](#)
- Huxor A. P., Tanvir N. R., Ferguson A. M. N., Irwin M. J., Ibata R., Bridges T., Lewis G. F., 2008, *MNRAS*, [385](#), [1989](#)

- Huxor A. P., et al., 2014, [MNRAS](#), **442**, 2165
- Ibata R. A., Gilmore G., Irwin M. J., 1995, [Monthly Notices of the Royal Astronomical Society](#), **277**, 781
- Ibata R., Irwin M., Lewis G., Ferguson A. M. N., Tanvir N., 2001, *Nature*, **412**, 49
- Ibata R., Martin N. F., Irwin M., Chapman S., Ferguson A. M. N., Lewis G. F., McConnachie A. W., 2007, [ApJ](#), **671**, 1591
- James P. A., Ivory C. F., 2011, [MNRAS](#), **411**, 495
- Janes K., 2000, *Star Clusters*. p. 1871, [doi:10.1888/0333750888/1871](https://doi.org/10.1888/0333750888/1871)
- Jaynes E. T., Bretthorst G. L., 2003, *Probability Theory*
- Jeans J. H., 1915, [MNRAS](#), **76**, 70
- Jeans J. H., 1922, [MNRAS](#), **82**, 122
- Jeffreys H., 1939, *The Theory of Probability*
- Jiang L., Helly J. C., Cole S., Frenk C. S., 2014, [MNRAS](#), **440**, 2115
- Johnson L. C., et al., 2016, *VizieR Online Data Catalog*, 182
- Johnson L. C., et al., 2017a, [ApJ](#), **839**, 78
- Johnson T. L., et al., 2017b, [ApJ](#), **843**, 78
- Johnston K. V., Zhao H., Spergel D. N., Hernquist L., 1999, [ApJ](#), **512**, L109
- Johnston K. V., Bullock J. S., Sharma S., Font A., Robertson B. E., Leitner S. N., 2008, [The Astrophysical Journal](#), **689**, 936
- Jones D. H., et al., 2004, [MNRAS](#), **355**, 747
- Jordán A., et al., 2007, [ApJS](#), **171**, 101
- Kalirai J. S., Guhathakurta P., Gilbert K. M., Reitzel D. B., Majewski S. R., Rich R. M., Cooper M. C., 2006, [ApJ](#), **641**, 268

- Kashibadze O. G., Karachentsev I. D., Karachentseva V. E., 2020, *A&A*, **635**, A135
- Kassin S. A., et al., 2007, *ApJ*, **660**, L35
- Katz N., Gunn J. E., 1991, *ApJ*, **377**, 365
- Katz H., Ricotti M., 2014, *MNRAS*, **444**, 2377
- Kauffmann G., et al., 2003, *MNRAS*, **341**, 54
- Keller B. W., Kruijssen J. M. D., Pfeffer J., Reina-Campos M., Bastian N., Trujillo-Gomez S., Hughes M. E., Crain R. A., 2020, *MNRAS*, **495**, 4248
- Kennicutt Robert C. J., 1998, *ApJ*, **498**, 541
- Kerber L. O., Santiago B. X., Brocato E., 2007, *A&A*, **462**, 139
- Kereš D., Katz N., Weinberg D. H., Davé R., 2005, *MNRAS*, **363**, 2
- Kim J.-h., et al., 2018, *MNRAS*, **474**, 4232
- Kinman T. D., 1959, *Monthly Notices of the Astronomical Society*, **119**, 538
- Kirby E. N., Cohen J. G., Guhathakurta P., Cheng L., Bullock J. S., Gallazzi A., 2013, *ApJ*, **779**, 102
- Kleyna J. T., Wilkinson M. I., Evans N. W., Gilmore G., 2001, *ApJ*, **563**, L115
- Kormendy J., 1977, *ApJ*, **218**, 333
- Kormendy J., Ho L. C., 2013, *ARA&A*, **51**, 511
- Kormendy J., Fisher D. B., Cornell M. E., Bender R., 2009, *ApJS*, **182**, 216
- Kravtsov A. V., Gnedin O. Y., 2005, *ApJ*, **623**, 650
- Kruijssen J. M. D., 2012, *MNRAS*, **426**, 3008
- Kruijssen J. M. D., 2014, *Classical and Quantum Gravity*, **31**, 244006
- Kruijssen J. M. D., 2015, *MNRAS*, **454**, 1658

- Kruijssen J. M. D., Portegies Zwart S. F., 2009, [ApJ](#), **698**, L158
- Kruijssen J. M. D., Pelupessy F. I., Lamers H. J. G. L. M., Portegies Zwart S. F., Icke V., 2011, [MNRAS](#), **414**, 1339
- Kruijssen J. M. D., Maschberger T., Moeckel N., Clarke C. J., Bastian N., Bonnell I. A., 2012a, [MNRAS](#), **419**, 841
- Kruijssen J. M. D., Pelupessy F. I., Lamers H. J. G. L. M., Portegies Zwart S. F., Bastian N., Icke V., 2012b, [MNRAS](#), **421**, 1927
- Kruijssen J. M. D., Pfeffer J. L., Crain R. A., Bastian N., 2019a, [MNRAS](#), **486**, 3134
- Kruijssen J. M. D., Pfeffer J. L., Reina-Campos M., Crain R. A., Bastian N., 2019b, [MNRAS](#), **486**, 3180
- Kruijssen J. M. D., et al., 2020, [MNRAS](#), **498**, 2472
- Krumholz M. R., McKee C. F., Bland-Hawthorn J., 2019, [ARA&A](#), **57**, 227
- L’Huillier B., Combes F., Semelin B., 2012, [A&A](#), **544**, A68
- Lahén N., Naab T., Johansson P. H., Elmegreen B., Hu C.-Y., Walch S., 2019, [ApJ](#), **879**, L18
- Lahén N., Naab T., Johansson P. H., Elmegreen B., Hu C.-Y., Walch S., Steinwandel U. P., Moster B. P., 2020, [ApJ](#), **891**, 2
- Lamers H. J. G. L. M., Gieles M., 2006, [A&A](#), **455**, L17
- Lamers H. J. G. L. M., Gieles M., Bastian N., Baumgardt H., Kharchenko N. V., Portegies Zwart S., 2005, [A&A](#), **441**, 117
- Larsen S. S., 2000, [MNRAS](#), **319**, 893
- Larsen S. S., 2009, [A&A](#), **494**, 539
- Larsen S. S., Brodie J. P., Huchra J. P., Forbes D. A., Grillmair C. J., 2001, [AJ](#), **121**, 2974

- Larsen S. S., Brodie J. P., Strader J., 2012, [A&A](#), **546**, [A53](#)
- Larson R. B., Tinsley B. M., Caldwell C. N., 1980, [ApJ](#), **237**, [692](#)
- Law D. R., Majewski S. R., 2010a, [ApJ](#), **714**, [229](#)
- Law D. R., Majewski S. R., 2010b, [ApJ](#), **718**, [1128](#)
- Leaman R., VandenBerg D. A., Mendel J. T., 2013, [MNRAS](#), **436**, [122](#)
- Lee J., Yi S. K., 2013, [ApJ](#), **766**, [38](#)
- Lee J.-W., López-Morales M., Carney B. W., 2006, [ApJL](#), **646**, [L119](#)
- Lee M. G., Park H. S., Kim E., Hwang H. S., Kim S. C., Geisler D., 2008, [ApJ](#), **682**, [135](#)
- Lee M. G., Park H. S., Hwang H. S., Arimoto N., Tamura N., Onodera M., 2010, [ApJ](#), **709**, [1083](#)
- Leroy A. K., Walter F., Brinks E., Bigiel F., de Blok W. J. G., Madore B., Thornley M. D., 2008, [AJ](#), **136**, [2782](#)
- Leung G. Y. C., et al., 2018, [MNRAS](#), **477**, [254](#)
- Li H., Gnedin O. Y., 2014, [ApJ](#), **796**, [10](#)
- Li Y., Mo H. J., van den Bosch F. C., Lin W. P., 2007, [MNRAS](#), **379**, [689](#)
- Li C., de Grijs R., Deng L., 2013, [MNRAS](#), **436**, [1497](#)
- Li H., Li R., Mao S., Xu D., Long R. J., Emsellem E., 2016, [MNRAS](#), **455**, [3680](#)
- Li H., Gnedin O. Y., Gnedin N. Y., Meng X., Semenov V. A., Kravtsov A. V., 2017a, [ApJ](#), **834**, [69](#)
- Li H., et al., 2017b, [ApJ](#), **838**, [77](#)
- Li H., Mao S., Cappellari M., Graham M. T., Emsellem E., Long R. J., 2018, [ApJL](#), **863**, [L19](#)

- Libeskind N. I., Knebe A., Hoffman Y., Gottlöber S., Yepes G., Steinmetz M., 2011, [MNRAS](#), **411**, 1525
- Lin D. N. C., Richer H. B., 1992, [ApJ](#), **388**, L57
- Łokas E. L., 2009, [MNRAS](#), **394**, L102
- Longmore S. N., et al., 2014, [Protostars and Planets VI](#), pp 291–314
- Lotz J. M., Jonsson P., Cox T. J., Primack J. R., 2008, [MNRAS](#), **391**, 1137
- Ma X., et al., 2020, [MNRAS](#), **493**, 4315
- Mackereth J. T., Crain R. A., Schiavon R. P., Schaye J., Theuns T., Schaller M., 2018, [MNRAS](#), **477**, 5072
- Mackey A. D., Broby Nielsen P., 2007, [MNRAS](#), **379**, 151
- Mackey A. D., Gilmore G. F., 2004, [MNRAS](#), **352**, 153
- Mackey A. D., van den Bergh S., 2005, [MNRAS](#), **360**, 631
- Mackey A. D., et al., 2010, [The Astrophysical Journal](#), **717**, L11
- Mackey A. D., et al., 2013, [Monthly Notices of the Royal Astronomical Society](#), **429**, 281
- Mackey A. D., et al., 2019, [MNRAS](#), **484**, 1756
- Madau P., Dickinson M., 2014, [ARA&A](#), **52**, 415
- Madau P., Lupi A., Diemand J., Burkert A., Lin D. N. C., 2020, [ApJ](#), **890**, 18
- Majewski S. R., 1994, [ApJ](#), **431**, L17
- Majewski S. R., Munn J. A., Hawley S. L., 1996, [ApJ](#), **459**, L73
- Majewski S. R., Skrutskie M. F., Weinberg M. D., Ostheimer J. C., 2003, [ApJ](#), **599**, 1082
- Majewski S. R., et al., 2017, [AJ](#), **154**, 94

- Malumuth E. M., Richstone D. O., 1984, *ApJ*, 276, 413
- Marín-Franch A., et al., 2009, *ApJ*, 694, 1498
- Marinacci F., Pakmor R., Springel V., 2014, *MNRAS*, 437, 1750
- Marino A. F., et al., 2012, *ApJ*, 746, 14
- Martell S. L., 2018, in Chiappini C., Minchev I., Starkenburg E., Valentini M., eds, Vol. 334, *Rediscovering Our Galaxy*. pp 38–42 ([arXiv:1710.03858](https://arxiv.org/abs/1710.03858)), [doi:10.1017/S1743921317007487](https://doi.org/10.1017/S1743921317007487)
- Martell S. L., Smolinski J. P., Beers T. C., Grebel E. K., 2011, *A&A*, 534, A136
- Martell S. L., et al., 2016, *ApJ*, 825, 146
- Martin N. F., et al., 2014, *ApJ*, 787, 19
- Martínez-Delgado D., Peñarrubia J., Gabany R. J., Trujillo I., Majewski S. R., Pohlen M., 2008, *ApJ*, 689, 184
- Martocchia S., et al., 2018, *MNRAS*, 477, 4696
- Massari D., Bellini A., Ferraro F. R., van der Marel R. P., Anderson J., Dalessandro E., Lanzoni B., 2013, *ApJ*, 779, 81
- Massari D., Koppelman H. H., Helmi A., 2019, *A&A*, 630, L4
- Matteucci F., Brocato E., 1990, *ApJ*, 365, 539
- Matzner C. D., McKee C. F., 2000, in *American Astronomical Society Meeting Abstracts #195*. p. 135.07
- McConnachie A. W., Irwin M. J., Ibata R. A., Ferguson A. M. N., Lewis G. F., Tanvir N., 2003, *MNRAS*, 343, 1335
- McConnachie A. W., et al., 2009, *Nature*, 461, 66
- McCrea W. H., 1961, *Proceedings of the Royal Society of London Series A*, 260, 152

- McLaughlin D. E., 1999, [ApJl](#), 512, L9
- McLaughlin D. E., Harris W. E., Hanes D. A., 1994, [ApJ](#), 422, 486
- McWilliam A., 1997, [ARA&A](#), 35, 503
- Melnick J., Moles M., Terlevich R., 1985, [A&A](#), 149, L24
- Meneguzzi M., Audouze J., Reeves H., 1971, in Dauber P. M., ed., *Isotopic Composition of the Primary Cosmic Radiation*. p. 147
- Merritt D., 1985, [AJ](#), 90, 1027
- Merritt A., van Dokkum P., Abraham R., Zhang J., 2016, [ApJ](#), 830, 62
- Messa M., et al., 2018, [MNRAS](#), 477, 1683
- Metropolis N., Rosenbluth A. W., Rosenbluth M. N., Teller A. H., Teller E., 1953, [J. Chem. Phys.](#), 21, 1087
- Miholics M., Kruijssen J. M. D., Sills A., 2017, [MNRAS](#), 470, 1421
- Mihos J. C., Hernquist L., 1996, [ApJ](#), 464, 641
- Milgrom M., 1983, [ApJ](#), 270, 365
- Minniti D., 1995, [AJ](#), 109, 1663
- Mistani P. A., et al., 2016, [MNRAS](#), 455, 2323
- Mitchell P. D., Schaye J., Bower R. G., Crain R. A., 2020, [MNRAS](#), 494, 3971
- Mok A., Chandar R., Fall S. M., 2019, [ApJ](#), 872, 93
- Monaco L., Saviane I., Correnti M., Bonifacio P., Geisler D., 2011, [A&A](#), 525, A124
- Monnet G., Bacon R., Emsellem E., 1992, [A&A](#), 253, 366
- Moore B., Katz N., Lake G., Dressler A., Oemler A., 1996, [Nature](#), 379, 613
- Moore B., Diemand J., Madau P., Zemp M., Stadel J., 2006, [MNRAS](#), 368, 563

- Moretti A., Held E. V., 2007, in Vazdekis A., Peletier R., eds, Vol. 241, *Stellar Populations as Building Blocks of Galaxies*. pp 455–456, [doi:10.1017/S1743921307008769](https://doi.org/10.1017/S1743921307008769)
- Mucciarelli A., 2009, *Mem. Soc. Astron. Italiana*, **80**, 89
- Mucciarelli A., Ferraro F. R., Origlia L., Fusi Pecci F., 2007, *AJ*, **133**, 2053
- Mucciarelli A., Ferraro F. R., Origlia L., Carretta E., Fusi Pecci F., 2008, *Mem. Soc. Astron. Italiana*, **79**, 529
- Mucciarelli A., et al., 2011, *MNRAS*, **413**, 837
- Mucciarelli A., Origlia L., Ferraro F. R., Bellazzini M., Lanzoni B., 2012, *ApJL*, **746**, L19
- Mucciarelli A., Bellazzini M., Catelan M., Dalessandro E., Amigo P., Correnti M., Cortés C., D’Orazi V., 2013, *MNRAS*, **435**, 3667
- Mucciarelli A., Dalessandro E., Ferraro F. R., Origlia L., Lanzoni B., 2014, *ApJL*, **793**, L6
- Muratov A. L., Gnedin O. Y., 2010, *ApJ*, **718**, 1266
- Myeong G. C., Evans N. W., Belokurov V., Sanders J. L., Koposov S. E., 2018, *ApJL*, **863**, L28
- Myeong G. C., Vasiliev E., Iorio G., Evans N. W., Belokurov V., 2019, *MNRAS*, **488**, 1235
- Naab T., Jesseit R., Burkert A., 2006, *MNRAS*, **372**, 839
- Napolitano N. R., et al., 2009, *MNRAS*, **393**, 329
- Navarro J. F., Benz W., 1991, *ApJ*, **380**, 320
- Navarro J. F., Frenk C. S., White S. D. M., 1996, *ApJ*, **462**, 563
- Negroponte J., White S. D. M., 1983, *MNRAS*, **205**, 1009

- Nelson D., et al., 2015, [Astronomy and Computing](#), **13**, 12
- Newberg H. J., et al., 2002, [ApJ](#), **569**, 245
- Niederste-Ostholt M., Belokurov V., Evans N. W., Peñarrubia J., 2010, [ApJ](#), **712**, 516
- Nomoto K., Kobayashi C., Tominaga N., 2013, [ARA&A](#), **51**, 457
- Norris M. A., et al., 2012, [MNRAS](#), **421**, 1485
- O'Connell R. W., Gallagher John S. I., Hunter D. A., 1994, [ApJ](#), **433**, 65
- Ocvirk P., Pichon C., Teyssier R., 2008, [MNRAS](#), **390**, 1326
- Odenkirchen M., et al., 2001, [ApJl](#), **548**, L165
- Okazaki T., Tosa M., 1995, [MNRAS](#), **274**, 48
- Olsen K. A. G., Hodge P. W., Mateo M., Olszewski E. W., Schommer R. A., Suntzeff N. B., Walker A. R., 1998, [MNRAS](#), **300**, 665
- Osborn W., 1971, *The Observatory*, **91**, 223
- Oser L., Ostriker J. P., Naab T., Johansson P. H., Burkert A., 2010, [ApJ](#), **725**, 2312
- Ostriker J. P., Tremaine S. D., 1975, [ApJl](#), **202**, L113
- Palma T., Clariá J. J., Geisler D., Piatti A. E., Ahumada A. V., 2013, [A&A](#), **555**, A131
- Peebles P. J. E., 1984, [ApJ](#), **277**, 470
- Peng E. W., et al., 2006, [ApJ](#), **639**, 95
- Peng E. W., et al., 2008, [ApJ](#), **681**, 197
- Peng E. W., Zhang H.-X., Liu C., Liu Y., 2016, in Bragaglia A., Arnaboldi M., Rejkuba M., Romano D., eds, Vol. 317, *The General Assembly of Galaxy Halos: Structure, Origin and Evolution*. pp 153–158, [doi:10.1017/S1743921315009837](https://doi.org/10.1017/S1743921315009837)
- Penzias A. A., Wilson R. W., 1965, [ApJ](#), **142**, 419

- Perlmutter S., et al., 1999, [ApJ](#), 517, 565
- Petropoulou V., Vílchez J., Iglesias-Páramo J., 2012, [ApJ](#), 749, 133
- Pfeffer J., Kruijssen J. M. D., Crain R. A., Bastian N., 2018, [MNRAS](#), 475, 4309
- Pfeffer J., Bastian N., Crain R. A., Kruijssen J. M. D., Hughes M. E., Reina-Campos M., 2019a, [MNRAS](#), 487, 4550
- Pfeffer J., Bastian N., Kruijssen J. M. D., Reina-Campos M., Crain R. A., Usher C., 2019b, [MNRAS](#), 490, 1714
- Piatti A. E., Bica E., Geisler D., Clariá J. J., 2003, [MNRAS](#), 344, 965
- Planck Collaboration et al., 2014, [A&A](#), 571, A1
- Planck Collaboration et al., 2016, [A&A](#), 594, A1
- Planck Collaboration et al., 2020, [A&A](#), 641, A6
- Poci A., Cappellari M., McDermid R. M., 2017, [MNRAS](#), 467, 1397
- Poci A., McDermid R. M., Zhu L., van de Ven G., 2019, [MNRAS](#), 487, 3776
- Portegies Zwart S. F., McMillan S. L. W., Gieles M., 2010, [ARA&A](#), 48, 431
- Posacki S., Cappellari M., Treu T., Pellegrini S., Ciotti L., 2015, [MNRAS](#), 446, 493
- Pota V., et al., 2013, [MNRAS](#), 428, 389
- Pota V., et al., 2018, [MNRAS](#), 481, 1744
- Powalka M., et al., 2016, [ApJL](#), 829, L5
- Powalka M., et al., 2018, [ApJ](#), 856, 84
- Press W. H., Schechter P., 1974, [ApJ](#), 187, 425
- Price-Jones N., Bovy J., 2019, [MNRAS](#), 487, 871
- Prieto J. L., Gnedin O. Y., 2008, [ApJ](#), 689, 919

- Pritzl B. J., Venn K. A., Irwin M., 2005, *AJ*, **130**, 2140
- Qu Y., et al., 2017, *MNRAS*, **464**, 1659
- Ramos-Almendares F., Sales L. V., Abadi M. G., Doppel J. E., Muriel H., Peng E. W., 2020, *MNRAS*, **493**, 5357
- Read J. I., Wilkinson M. I., Evans N. W., Gilmore G., Kleyna J. T., 2006, *MNRAS*, **366**, 429
- Recio-Blanco A., 2018, *A&A*, **620**, A194
- Rees M. J., Ostriker J. P., 1977, *MNRAS*, **179**, 541
- Reina-Campos M., Kruijssen J. M. D., 2017, *MNRAS*, **469**, 1282
- Reina-Campos M., Kruijssen J. M. D., Pfeffer J., Bastian N., Crain R. A., 2018, *MNRAS*, **481**, 2851
- Reina-Campos M., Kruijssen J. M. D., Pfeffer J. L., Bastian N., Crain R. A., 2019, *MNRAS*, **486**, 5838
- Reina-Campos M., Hughes M. E., Kruijssen J. M. D., Pfeffer J. L., Bastian N., Crain R. A., Koch A., Grebel E. K., 2020, *MNRAS*, **493**, 3422
- Remus R.-S., Dolag K., Naab T., Burkert A., Hirschmann M., Hoffmann T. L., Johansson P. H., 2017, *MNRAS*, **464**, 3742
- Renaud F., Agertz O., Gieles M., 2017, *MNRAS*, **465**, 3622
- Richstone D. O., 1976, *ApJ*, **204**, 642
- Riess A. G., et al., 1998, *AJ*, **116**, 1009
- Roberts M. S., Haynes M. P., 1994, *ARA&A*, **32**, 115
- Rockosi C. M., et al., 2002, *AJ*, **124**, 349
- Rodighiero G., et al., 2011, *ApJl*, **739**, L40

- Romanowsky A. J., Strader J., Spitler L. R., Johnson R., Brodie J. P., Forbes D. A., Ponman T., 2009, [AJ](#), **137**, 4956
- Romanowsky A. J., Strader J., Brodie J. P., Mihos J. C., Spitler L. R., Forbes D. A., Foster C., Arnold J. A., 2012, [ApJ](#), **748**, 29
- Rosas-Guevara Y. M., et al., 2015, [MNRAS](#), **454**, 1038
- Rubin V. C., Ford W. Kent J., 1970, [ApJ](#), **159**, 379
- Rubin V. C., Ford W. K. J., Thonnard N., 1980, [ApJ](#), **238**, 471
- Sakari C., Venn K., Arimoto N., Aoki W., Irwin M., 2011, in American Astronomical Society Meeting Abstracts #217. p. 434.48
- Sales L. V., et al., 2015, [MNRAS](#), **447**, L6
- Sánchez S. F., et al., 2016, [A&A](#), **594**, A36
- Sarzi M., et al., 2018, [A&A](#), **616**, A121
- Schaller M., Dalla Vecchia C., Schaye J., Bower R. G., Theuns T., Crain R. A., Furlong M., McCarthy I. G., 2015, [MNRAS](#), **454**, 2277
- Schaye J., Dalla Vecchia C., 2008, [MNRAS](#), **383**, 1210
- Schaye J., et al., 2015, [MNRAS](#), **446**, 521
- Schechter P., 1976, [ApJ](#), **203**, 297
- Schiavon R. P., et al., 2017, [MNRAS](#), **465**, 501
- Schuberth Y., Richtler T., Hilker M., Dirsch B., Bassino L. P., Romanowsky A. J., Infante L., 2010, [A&A](#), **513**, A52
- Schulze F., Remus R.-S., Dolag K., Bellstedt S., Burkert A., Forbes D. A., 2020, [MNRAS](#),
- Schwarz G., 1978, *Annals of Statistics*, **6**, 461

- Schwarzschild M., 1979, *ApJ*, 232, 236
- Scott N., et al., 2015, *MNRAS*, 451, 2723
- Sérsic J. L., 1963, Boletín de la Asociación Argentina de Astronomía La Plata Argentina, 6, 41
- Sersic J. L., 1968, Atlas de Galaxias Australes
- Shang Z., et al., 1998, *ApJ*, 504, L23
- Shapiro K. L., Genzel R., Förster Schreiber N. M., 2010, *MNRAS*, 403, L36
- Shapley H., 1917, *Proceedings of the National Academy of Science*, 3, 479
- Shapley H., 1918a, *PASP*, 30, 42
- Shapley H., 1918b, *ApJ*, 48, 89
- Shapley H., 1918c, *ApJ*, 48, 154
- Shapley H., 1918d, Contributions from the Mount Wilson Observatory / Carnegie Institution of Washington, 155, 1
- Shapley H., 1930, Star Clusters. Vol. 2
- Sharma S., 2017, *ARA&A*, 55, 213
- Shen S., Mo H. J., White S. D. M., Blanton M. R., Kauffmann G., Voges W., Brinkmann J., Csabai I., 2003, *MNRAS*, 343, 978
- Shipp N., et al., 2018, *ApJ*, 862, 114
- Siebert A., et al., 2011, *AJ*, 141, 187
- Silk J., 1977, *ApJ*, 211, 638
- Silk J., Rees M. J., 1998, *A&A*, 331, L1
- Silva-Villa E., Adamo A., Bastian N., 2013, *MNRAS*, 436, L69

- Sinnott B., Hou A., Anderson R., Harris W. E., Woodley K. A., 2010, *AJ*, **140**, 2101
- Sirianni M., Nota A., De Marchi G., Leitherer C., Clampin M., 2002, *ApJ*, **579**, 275
- Smoot G. F., et al., 1992, *ApJl*, **396**, L1
- Snedden C., 2004, *Mem. Soc. Astron. Italiana*, **75**, 267
- Sohn S. T., Watkins L. L., Fardal M. A., van der Marel R. P., Deason A. J., Besla G., Bellini A., 2018, preprint, ([arXiv:1804.01994](https://arxiv.org/abs/1804.01994))
- Solanes J. M., Perea J. D., Valentí-Rojas G., 2018, *A&A*, **614**, A66
- Sonnenfeld A., Treu T., Gavazzi R., Suyu S. H., Marshall P. J., Auger M. W., Nipoti C., 2013, *ApJ*, **777**, 98
- Spitzer Lyman J., 1940, *MNRAS*, **100**, 396
- Spitzer L., 1987, *Dynamical evolution of globular clusters*
- Spitzer Lyman J., Harm R., 1958, *ApJ*, **127**, 544
- Springel V., 2005, *MNRAS*, **364**, 1105
- Springel V., White S. D. M., Tormen G., Kauffmann G., 2001, *MNRAS*, **328**, 726
- Starkenburger E., et al., 2009, *ApJ*, **698**, 567
- Steinmetz M., et al., 2006, *AJ*, **132**, 1645
- Strader J., Brodie J. P., Cenarro A. J., Beasley M. A., Forbes D. A., 2005, *AJ*, **130**, 1315
- Strader J., Beasley M. A., Brodie J. P., 2007, *AJ*, **133**, 2015
- Strader J., et al., 2011, *ApJS*, **197**, 33
- Strigari L. E., Bullock J. S., Kaplinghat M., Simon J. D., Geha M., Willman B., Walker M. G., 2008, *Nature*, **454**, 1096
- Suntzeff N. B., Schommer R. A., Olszewski E. W., Walker A. R., 1992, *AJ*, **104**, 1743

- Swinbank A. M., et al., 2011, [ApJ](#), 742, 11
- Syer D., Tremaine S., 1996, [MNRAS](#), 282, 223
- Tacconi L. J., et al., 2018, [ApJ](#), 853, 179
- Tamura N., Sharples R. M., Arimoto N., Onodera M., Ohta K., Yamada Y., 2006, [MNRAS](#), 373, 601
- Tautvaišienė G., Wallerstein G., Geisler D., Gonzalez G., Charbonnel C., 2004, [AJ](#), 127, 373
- Thob A. C. R., et al., 2019, [MNRAS](#), 485, 972
- Thomas J., 2010, [Reviews in Modern Astronomy](#), 22, 143
- Thomas J., et al., 2011, [MNRAS](#), 418, 2815
- Ting Y.-S., Conroy C., Goodman A., 2015, [ApJ](#), 807, 104
- Tolstoy E., Hill V., Tosi M., 2009, [ARA&A](#), 47, 371
- Tonini C., 2013, [ApJ](#), 762, 39
- Toomre A., 1964, [ApJ](#), 139, 1217
- Toomre A., 1977, in Tinsley B. M., Larson Richard B. Gehret D. C., eds, *Evolution of Galaxies and Stellar Populations*. p. 401
- Tortora C., Napolitano N. R., Saglia R. P., Romanowsky A. J., Covone G., Capaccioli M., 2014, [MNRAS](#), 445, 162
- Tortora C., La Barbera F., Napolitano N. R., 2016, [MNRAS](#), 455, 308
- Tremonti C. A., et al., 2004, [ApJ](#), 613, 898
- Trujillo-Gomez S., Kruijssen J. M. D., Reina-Campos M., Pfeffer J. L., Keller B. W., Crain R. A., Bastian N., Hughes M. E., 2021, [MNRAS](#), 503, 31
- Trujillo I., et al., 2006, [ApJ](#), 650, 18

- Trumpler R. J., 1931, *PASP*, **43**, 145
- Tsujikawa S., 2003, arXiv e-prints, pp hep-ph/0304257
- Tully R. B., Fisher J. R., 1977, *A&A*, **500**, 105
- Usher C., et al., 2012, *MNRAS*, **426**, 1475
- Usher C., Pfeffer J., Bastian N., Kruijssen J. M. D., Crain R. A., Reina-Campos M., 2018, *MNRAS*,
- VandenBerg D. A., Brogaard K., Leaman R., Casagrande L., 2013, *ApJ*, **775**, 134
- Vanzella E., et al., 2017, *MNRAS*, **467**, 4304
- Vasiliev E., 2019, *MNRAS*, **484**, 2832
- Veljanoski J., et al., 2013, *MNRAS*, **435**, 3654
- Veljanoski J., et al., 2014, *Monthly Notices of the Royal Astronomical Society*, **442**, 2929
- Vesperini E., 1998, *MNRAS*, **299**, 1019
- Vesperini E., Zepf S. E., Kundu A., Ashman K. M., 2003, *ApJ*, **593**, 760
- Villaume A., Foreman-Mackey D., Romanowsky A. J., Brodie J., Strader J., 2020, *ApJ*, **900**, 95
- Vogelsberger M., et al., 2014, *MNRAS*, **444**, 1518
- Wagner-Kaiser R., et al., 2017, *MNRAS*, **468**, 1038
- Walker M. G., Mateo M., Olszewski E. W., Peñarrubia J., Evans N. W., Gilmore G., 2009, *ApJ*, **704**, 1274
- Walsh D., Carswell R. F., Weymann R. J., 1979, *Nature*, **279**, 381
- Wang Q., Peng E. W., Blakeslee J. P., Côté P., Ferrarese L., Jordán A., Mei S., West M. J., 2013, *ApJ*, **769**, 145

- Wannier P., Wrixon G. T., 1972, *ApJ*, **173**, L119
- Watkins L. L., van de Ven G., den Brok M., van den Bosch R. C. E., 2013, *MNRAS*, **436**, 2598
- Watkins L. L., van der Marel R. P., Sohn S. T., Evans N. W., 2019, *ApJ*, **873**, 118
- Webb J. J., Sills A., Harris W. E., Hurley J. R., 2014, *MNRAS*, **445**, 1048
- Webb J. J., Reina-Campos M., Kruijssen J. M. D., 2019, *MNRAS*, **486**, 5879
- Wen Z. Z., Zheng X. Z., 2016, *ApJ*, **832**, 90
- Wheeler J. C., Sneden C., Truran Jr. J. W., 1989, *ARA&A*, **27**, 279
- White S. D. M., Frenk C. S., 1991, *ApJ*, **379**, 52
- White S. D. M., Rees M. J., 1978, *MNRAS*, **183**, 341
- Whitmore B. C., Schweizer F., 1995, *The Astrophysical Journal*, **109**, 960
- Whitmore B. C., Schweizer F., Leitherer C., Borne K., Robert C., 1993, *AJ*, **106**, 1354
- Wiersma R. P. C., Schaye J., Theuns T., Dalla Vecchia C., Tornatore L., 2009, *MNRAS*, **399**, 574
- Williams J. P., Blitz L., McKee C. F., 2000, in Mannings V., Boss A. P., Russell S. S., eds, *Protostars and Planets IV*. p. 97 ([arXiv:astro-ph/9902246](https://arxiv.org/abs/astro-ph/9902246))
- Yoon S.-J., Yi S. K., Lee Y.-W., 2006, *Science*, **311**, 1129
- Yoon S.-J., et al., 2011, *ApJ*, **743**, 150
- York D. G., et al., 2000, *AJ*, **120**, 1579
- Zepf S. E., Beasley M. A., Bridges T. J., Hanes D. A., Sharples R. M., Ashman K. M., Geisler D., 2000, *AJ*, **120**, 2928
- Zhu L., et al., 2014, *ApJ*, **792**, 59
- Zhu L., et al., 2016a, *MNRAS*, **462**, 4001

- Zhu L., van de Ven G., Watkins L. L., Posti L., 2016b, [MNRAS](#), **463**, 1117
- Zinn R., 1985, [ApJ](#), **293**, 424
- Zwicky F., 1937, [ApJ](#), **86**, 217
- Zwitter T., et al., 2008, [AJ](#), **136**, 421
- de Grijs R., Bastian N., Lamers H. J. G. L. M., 2003, [ApJl](#), **583**, L17
- den Brok M., van de Ven G., van den Bosch R., Watkins L., 2014, [MNRAS](#), **438**, 487
- van Gorkom J. H., 2004, in Mulchaey J. S., Dressler A., Oemler A., eds, Clusters of Galaxies: Probes of Cosmological Structure and Galaxy Evolution. p. 305 ([arXiv:astro-ph/0308209](#))
- van den Bosch R. C. E., van de Ven G., Verolme E. K., Cappellari M., de Zeeuw P. T., 2008, [MNRAS](#), **385**, 647
- van der Marel R. P., Anderson J., 2010, [ApJ](#), **710**, 1063
- van der Wel A., et al., 2014, [ApJ](#), **788**, 28